Doctoral Dissertation
Doctoral Program in Mechanical Engineering (31th Cycle)

Suspension lower control arm case study: enhancing lightweight and vibration reduction

by

Alessandro Messana

* * * * * *

Supervisor
Prof. Massimiliana Carello

Doctoral Examination Committee:
Prof. P. Beomonte Zobel , Referee, Università de L'Aquila
Prof. R. Serra, Referee, Institut National des Sciences Appliqeés
Prof. D. Hughes, Co-examiner, Teesside University
Prof. A. Fasana, Co-examiner, Politecnico di Torino

Politecnico di Torino
April 30, 2019

Declaration

I hereby declare that, the contents and organisation of this dissertation constitute my own original work and does not compromise in any way the rights of third parties, including those relating to the security of personal data.

Alessandro Messana
Turin, April 30, 2019

Ad maiora semper

Summary

The E.U. has issued recently regulations ordering the necessity of the 40% reduction of polluting emissions and of the greenhouse gases produced by vehicles. This target is to be achieved by 2030. It is an ambitious goal asking car industry for the development of “lightweight” solutions in order to allow a consumption reduction, an overall efficiency increase and a vehicles wider sustainability: so it is necessary to optimize all mechanical systems. Since the suspension systems build up the 25% of the whole mass of a vehicle, their optimization would cause advantages both in handling and vibro-acoustic comfort. The innovative materials use, such as Carbon Fibres Reinforced Plastic (CFRP), hybrid laminate and high-damping elastomers, meet the lightness and strength requirements but they imply, at the same time, a greater complexity both in design and virtual modelling.

In this context, the aim of this thesis dissertation consisting in studying, development and testing a multi-material (carbon fibre and steel) Lower Control Arm (LCA) of a McPherson suspension for a C segment vehicle. An innovative viscoelastic material has been used to join carbon fiber with steel that works as passive constrained layer damper and adhesive simultaneously. In particular, it has been developed a specific methodology that combines both virtual and experimental procedures to face the hybridization challenges of mechanical coupling, damping and lightweight.

For these reasons, the multi-material lower control arm represents a noticeable case study in which this methodology has been applied, correlated and validated.

First of all, a multibody model of the vehicle has been made in MSC-AdamsCar and particularly of the front and rear suspension systems, in order to evaluate the forces acting on the LCA. Therefore, six main manoeuvers have been defined for evaluating the behaviour and afterwards basing the multi-material component design. Particularly, three manoeuvers concern the “special events” that are all those situations in which the arm has to assure its working in the elastic range. On the contrary, the other three manoeuvers are defined as “misuse events” that are all

those situations where the arm can exceed the material elastic limit without breaking.

Subsequently, the arm CAD model has been generated through a reverse engineering activity in which it has been carried out the final geometry starting from the component 3D laser scan. In such a way, the FEM model of the original arm (also called *baseline*) has been created in Altair Hypermesh in order to evaluate the overall mechanical performances and to define the design target as regards the multi-material one (also called *hybrid*). As far as the FEM simulations are concerned, it has been considered five load cases for evaluating: the stiffness: the behaviour for special events and misuse events, the frequency response and the longitudinal strength test.

Although the arm has been perceived as a unique prototype, a set of design constraints has been defined concerning the LCA geometry and mechanical coupling in order to be replaceable on the vehicle and compliant to standard manufacturing process. Hence, the suspension packaging analysis has been conducted and the external arm envelop has been identified as maximum design volume for the hybrid LCA. An innovative technology consisting on a calibrate Visco-Elastic Material (VEM) foil has been used to join carbon fiber with steel to satisfy the requirement of lightweight, vibration damping, stiffness and safety.

For the purpose of investigating the mechanical properties of the suspension arms materials, the experimental characterization has been conducted. As regards the viscoelastic materials, it has been evaluated two different compound in such a way to compare their stiffness, damping and adhesion properties. These tests have been performed according to the ASTM E756-05 standard for the dynamic and damping properties, and according to D5868-01, D5528, and D7905 standards for the properties of fracture toughness and strength of the adhesive joint. In addition, the VEMs have been subjected both to a test at temperature (between -20°C and 60°C) according to the SAE J 1637 and at ageing cycle of 750 h according to the IEC 60068.

As concerns the carbon fiber materials, it has been carried out the characterization of the fabric and the unidirectional CFRP following the standards ASTM D3039, D3410 and D790 for the tensile, compression and bending tests along the principal directions. Also for the steel making up the arm baseline, it has been tested according to the ASTM E8/E8m-16A.

The experimental tests results carried out on the specimens were essential for the creation of the material card, necessary to carry out the Finite Element Analysis (FEA) and to correlate the virtual models with the real behaviour.

After obtaining a very good correlation with the virtual specimen models, it has been created the FEM model for the “hybrid” arm optimization, with the main objective of reducing the mass safeguarding the stiffness and reducing vibration than the “baseline” arm. The optimization result has allowed to work out the feasible plybook in order to go on to the achievement of the hybrid component through hand lay-up and vacuum bag technologies. Finally, the mass obtained of the hybrid LCA is 1,68 kg that means 23% less than the baseline.

The last phase of the thesis has been focused on testing the two arms to obtain the frequency response and the longitudinal strength. Firstly, the experimental modal analysis has been performed and the hybrid LCA reported a sensible improvement of damping ratio of 3,5 times for each eigenmode than the baseline. Then, it has been carried out the correlation among the virtual modal analysis models and the experimental FRFs (Frequency Response Function) by comparing frequencies and MAC (Modal Assurance Criterion) index. As results, it has been obtained a very good correlation between the FRFs and a high MAC index value for both the models.

Secondly, the longitudinal strength test has been conducted to evaluate the characteristic curves of the arms. The test has been limited at 10 kN to preserve the structural integrity of the components. The test reported a stiffness difference between the arms of only 6%, and a very high correlation has also obtained with the FEM models. Subsequently, the data of experimental force and displacement have been compared with the ones obtained by the virtual models, obtaining a very good fitting for both arms with negligible differences between the curves.

In conclusion, the methodological approach applied from specimen to component has been validated by the prediction and robustness level of the FEM models and the experimental comparison done on modal analysis and strength tests. In the end, the hybrid lower control arm achieved a 23% mass reduction, a total damping increase equal to about 3,5 times and a final stiffness lower than 6% compared with the “baseline” arm values.

Acknowledgment

After these three-years PhD, I firmly convinced that limits do not exist. Limits are just superstructures we use to justify our fear of failure, our fear of unknown. This is why I love research and I think this thesis is a clear example in which I put my heart and soul over every obstacle.

My research group is a young and complex “entity”: every day we literally fight against those superstructures, against our limits just to fill our thirst of knowledge.

Therefore, in order to thank all the IEHV people who gave their contribution to the success of my research work, I will use a special analogy comparing them to a LMP1 team. The “team boss” is obviously Prof. Massimiliana Carello: she trusted in me since I was a bachelor student and she gave the possibility to express my whole potential guiding me to the final goal. Then, the “technical directors” are Dr. Alessandro Ferraris and Dr. Andrea Airale: they followed me every time, especially when I was in trouble, giving me the tools to improve my professional skills and personal capabilities. Finally, there are all the “drivers” that are Lorenzo, Davide, Corinne, Luca and Andrea, which ran with me in these three years “Le Mans” supporting whenever I need. To all of them and to the other guys not cited, my special thanks goes.

However, this work would not have seen the light without the precious support of Prof. Alessandro Fasana, who introduced me to the “obscure art” of vibration mechanics (that I personally like to call “fasanesimo”) and Prof. Ugo Icardi, who tried to explain me all the composite material secrets with a lot of patience. I would also like to thank all the DISEG technicians who helped me with great enthusiasm. Last but not least, a special mention goes to Altair Italia Engineering especially to Roberto D’Aria and Francesco Russo for their fundamental advices on FEM models.

I would to say a particular thanks to all the companies and people that help me in different moments for their fundamental support to my research: SFC Compositi, OPAC group, 3VU Compositi, Officina Massola, Gruppo Progetto (in particular Mr. Sabatino), Gruppo SCAR (in particular Mr. Puzzo), eng. J. Cavallo, eng. A. Pizzuto and eng. L. Piano.

But the most important “thanks” go to my parents Giuseppe and Rosalba, to my brother Davide, to my aunt Angela and, above all, to Serena who took care of me in these last “demanding” three years both in success and in failure.

To my beloved niece Clara,
the future of my family

Content

1. Lightweight lower control arm scenario 1

1.1. The future of the urban mobility 1
1.2. Lightweight strategy to tackle CO_2 targets 2
1.3. Benefit of lightweight suspension system 5
1.4. MacPherson suspension system 9
1.5. The lower control arm case study 12
1.5.1. Noise Vibration and Harshness 12
1.5.2. Mechanical coupling 14
1.5.3. Suspension safety standards 15
1.6. Lightweight lower control arm state of art 16
1.7. Research aim and workflow 23

2. LCA case study definition 27

2.1. Reference vehicle 28
2.2. Vehicle load case configurations 31
2.3. Multibody model on ADAMS/Car 31
2.3.1. Front McPherson suspension modelling 32
2.3.2. Rear McPherson suspension modelling 34
2.4. Full vehicle assembly and simulation 34
2.4.1. Skid-pad test 36
2.4.2. Maximum acceleration test 38
2.4.3. Maximum braking test 38
2.4.4. Obstacle misuse test: Crossbeam 39
2.4.5. Obstacle misuse test: Hump 40
2.4.6. Obstacle misuse test: Drain 41
2.5. Final consideration on MBD simulations 42
2.6. Lower control arm CAD file creation 43
2.7. Finite element simulation set 45
2.8. Optistruct FE model 46

2.9. Stiffness simulation on Baseline LCA 50
2.10. Special and misuse event simulations on Baseline LCA 52
2.11. Simulation results on Baseline LCA 53
2.12. Target definition for Hybrid lower control arm 57
3. Multi-material LCA concept 59
3.1. Design constraints and solutions 59
3.2. Innovative application 61
3.3. Suspension Packaging 65
3.4. Carbon fiber material cover 67
4. Viscoelastic material testing and correlation 75
4.1. Oberst test method 76
4.2. Thermal test SAE J1637 79
4.3. Aging test IEC 60068 80
4.4. Single Lap Joint Test (SLJ) 80
4.5. Double Cantilever Beam test (DCB) 81
4.6. End-Notched Flexure test (ENF) 82
4.7. Experimental results: damping behavior 83
4.8. Experimental results: joint properties 89
4.8.1. Single lap joint results 90
4.8.2. Double cantilever beam results 91
4.8.3. End-notched flexure results 93
4.9. Synthesis of the experimental results on viscoelastic materials 95
4.10. Virtual-Experimental correlation on Oberst beam test 95
4.10.1. Structural beam correlation results 98
4.10.2. One side beam correlation results 100
4.11. Final considerations on VEMs characterization 103
5. Mechanical characterization on hybrid LCA materials 105
5.1. Tensile test ASTM D3039 106
5.2. Compression test ASTM D3410 106
5.3. Bending test ASTM D790 107
5.4. Tensile test ASTM E8/E8M-16A 108
5.5. Experimental results 108
5.6. Virtual-Experimental correlation on carbon fibers and steel 111
5.6.1. Correlation on CFRP mechanical tests 111
5.6.2. Fitting results on CFRP UD M46J 114
5.6.3. Fitting results on CFRP T300-GG245T 115
5.6.4. Fitting results on CFRP T700-GG430T 116
5.6.5. Correlation on steel mechanical tests 117
5.6.6. Fitting results on steel S420MC 118

5.7. Final considerations on materials characterization 118
6. Hybrid LCA optimization and manufacturing 120
6.1. Composite optimization in Optistruct 120
6.2. FE Optimization model 123
6.3. Phase I: Free-Size 125
6.4. Phase II: Size 128
6.5. Phase III: Shuffling 129
6.6. Hybrid lower control arm performance 130
6.7. Manufacturing process 138
7. Virtual experimental correlation on lower control arms 143
7.1. Experimental modal analysis set up 143
7.2. Model parameters extraction algorithm 146
7.3. Experimental data processing 148
6.3.1. Baseline Experimental modal analysis 149
6.3.2. Hybrid experimental modal analysis 152
6.3.3. Synthesis of experimental modal analysis results 155
7.4. FE model for modal analysis 156
7.5. Correlation on modal analysis 158
7.6. Strength analysis: bending load case 162
7.7. RADIOSS FE model 164
7.8. Experimental results and correlation 166
7.9. Correlation on strength tests 168
8. Conclusions 171

List of Tables

Table 1.1 - General properties of aluminium and composite materials [44]...20
Table 2.1 – Fiat 500X technical data....30
Table 2.2 – Front bushing stiffness values....33
Table 2.3 – Set of multibody simulations for LCA forces estimation....35
Table 2.4 – Input force for skid-pad FEM simulation....37
Table 2.5 – Input force for maximum acceleration FEM simulation....38
Table 2.6 – Input force for maximum braking FEM simulation....39
Table 2.7 – Input values for FEM crossbeam simulation....40
Table 2.8 - Input values for FEM hump simulation....41
Table 2.9 - Input values for FEM drain simulation....42
Table 2.10 – Multibody simulation results summary....42
Table 2.11 – Finite element simulation set....46
Table 2.12 – Datasheet values for S420MC....49
Table 2.13 - Resultant forces due to special and misuse events....52
Table 2.14 – Results summary for Baseline lower control arm....57
Table 3.1 – Vehicle data for packaging analysis....66
Table 4.1 – Experimental test set-up on VEMs....76
Table 4.2 – HVV specimen tested....86
Table 4.3 – HAA specimen tested....87
Table 4.4 – HVV specimens tested....90
Table 4.5 – HAA specimens tested....90
Table 4.6 – DCB specimen tested for HVV....92
Table 4.7 - DCB specimen tested for HAA....92
Table 4.8 - ENF specimen tested for HVV....93
Table 4.9 – ENF specimen tested for HAA....94
Table 4.10 – Structural beam model dimension....99
Table 4.11 – CFRP frequency correlation....99
Table 4.12 – One side beam models data....100

Table 4.13 – HVV frequency correlation 101
Table 4.14 – HAA frequency correlation 101
Table 5.1 – Experimental test set-up on CFRP and steel 105
Table 5.2 - Mechanical properties of T300 epoxy GG245T 108
Table 5.3 - Mechanical properties of T700 epoxy GG430T 109
Table 5.4 - Mechanical properties of UD M46J epoxy 110
Table 5.5 – Mechanical properties of steel S420MC 110
Table 5.6 – UD specimens dimensions and set up for FE analysis 114
Table 5.7 – GG245T specimens dimensions and set up for FE analysis 116
Table 5.8 – GG430T specimens dimensions and set up for FE analysis 116
Table 5.9 - Steel specimen dimensions and set up for FE analysis 118
Table 5.10 - Experimental mechanical properties of arms CFRP and steel .. 119
Table 6.1 – Material data used in hybrid LCA FEM model 125
Table 6.2 - Baseline and Hybrid LCA mass and stiffness comparison 134
Table 6.3 – Baseline and Hybrid LCA stress comparison 138
Table 7.1 – Load cell characteristics 144
Table 7.2 – Accelerometers characteristics 144
Table 7.3 – Experimental data comparison between baseline and hybrid LCA 156
Table 7.4 – Correlation between FEM and EXP data for baseline LCA arm 160
Table 7.5 - Correlation between FEM and EXP data on hybrid LCA 161
Table 7.6 – Result summary on longitudinal strength tes 169

List of Figures

Figure 1.1 - Weight evolution of Volkswagen Golf from 1975 to 2009.....2
Figure 1.2 - Audi A8 spaceframe material composition.....3
Figure 1.3 - Mercedes-Benz C-Class body.....4
Figure 1.4 - Mercedes-Benz SL body in white.....4
Figure 1.5 - BMW i3: Life module (top) and Drive Module (bottom).....5
Figure 1.6 - Side view of BMW 7 Series BIW with CFRP components.....5
Figure 1.7 - Mass repartition in a generic vehicle.....6
Figure 1.8 - Corvette C6 rear leaf spring.....6
Figure 1.9 - Peugeot 208 Hybrid FE: powertrain and suspension system.....7
Figure 1.10 - Rear GFRP leaf spring of Volvo XC90.....7
Figure 1.11 - ZF rear suspension layout for small cars.....8
Figure 1.12 - MacPherson suspension scheme.....9
Figure 1.13 - The banana-like shape of a lower control arm.....10
Figure 1.14 - Example of cast iron LCA.....11
Figure 1.15 - Example of welded clamshell LCA.....11
Figure 1.16 - Example of single stamped shell LCA.....12
Figure 1.17 - Noise level trend vs. speed.....13
Figure 1.18 - Noise sources accordingly to the frequencies.....14
Figure 1.19 - Bottom view of a vehicle [35].....15
Figure 1.20 - LCA shape from [40].....17
Figure 1.21 - Clamshell design.....18
Figure 1.22 - The I-Beam design.....18
Figure 1.23 - Forged Design.....19
Figure 1.24 - Thermoplastic CFRP lower control arm by PSA group.....19
Figure 1.25 - Lamborghini LCA with thinned flange to increase stiffness.....20

Figure 1.26 - Magneti Marelli Sistemi Sospensivi LCA....21
Figure 1.27 - Shunt circuit model 22
Figure 1.28 - Fraunhofer LCA laminate....22
Figure 1.29 - Modal analysis results and piezo positioning....23
Figure 1.30 - Research workflow....25
Figure 2.1 - LCA load case definition workflow 27
Figure 2.2 - FEM virtual model workflow....27
Figure 2.3 – Fiat 500X 28
Figure 2.4 – Fiat 500X lower control arms 29
Figure 2.5 – LCA total mass (left) and without bushings and lower ball joint (right) 29
Figure 2.6 – LCA dimensions [mm] 30
Figure 2.7 Front McPherson suspension with powertrain modification 33
Figure 2.8 – Dampers characteristic curves 34
Figure 2.9 - Rear McPherson suspension with powertrain modification....34
Figure 2.10 - Full vehicle assembly in ADAMS/Car....35
Figure 2.11 - LBJ force orientation for FE calculations 36
Figure 2.12 – Skid-pad test configuration....37
Figure 2.13 - Skid-pad test simulation results....37
Figure 2.14 – Maximum acceleration simulation results 38
Figure 2.15 - Maximum braking simulation results....39
Figure 2.16 - Crossbeam obstacle design....39
Figure 2.17 – Crossbeam simulation results 40
Figure 2.18 - Hump obstacle design....40
Figure 2.19 - Hump test simulation results 41
Figure 2.20 – Drain obstacle design....41
Figure 2.21 - Drain test simulation results 42
Figure 2.22 - Impact force for obstacle (left) and impact force on LBJ (right) 43
Figure 2.23 - Anthropomorphous laser arm....44
Figure 2.24 – Surfaces generation from *.stl* scan 44
Figure 2.25 – Render of final lower control arm CAD model 45
Figure 2.26 – CAD model assembly....46
Figure 2.27 – Surface subdivision and defeaturing....47
Figure 2.28 – Meshed model....47
Figure 2.29 – Front bushing modellization 48
Figure 2.30 – Particular of welding lines on FE model 48
Figure 2.31 – Section of tetrahedral elements on LBJ support 49

Figure 2.32 – Contact area between LBJ and LCA....49
Figure 2.33 – Stiffness model configuration....50
Figure 2.34 – Bushing constraints: numbers represent the DOF fixed....51
Figure 2.35 – LBJ reference system (green) oriented as in MBD model....51
Figure 2.36 – Special events configuration....52
Figure 2.37 – Misuse events configuration....53
Figure 2.38 – Displacement for bending case....54
Figure 2.39 – Displacement for buckling case....54
Figure 2.40 – Stress distributions (MPa) on stiffness simulations....55
Figure 2.41 – Stress distribution (MPa) for special events simulations....55
Figure 2.42 – Deformed shape caused by braking load....56
Figure 2.43 – Deformed shape caused by acceleration load....56
Figure 2.44 - Stress distribution for misuse events case....56
Figure 3.1 – Main modification on metal shape....60
Figure 3.2 - Fillet details on bushings seats....61
Figure 3.3 - Section detail on bolt connection....61
Figure 3.4 - Kraibon damping properties (left) and specific mass (right)....62
Figure 3.5 – Formula student front nose CFRP crash....63
Figure 3.6 - Advantages on application of Kraibon in hybrid material....64
Figure 3.7 - Kraibon compound: HAA (left) and HVV (right)....64
Figure 3.8 – Hybrid LCA design proposal....65
Figure 3.9 – Wheel assembly (left) and its simplified CAD model (right)....65
Figure 3.10 - Enlarged lower control arm....66
Figure 3.11 – Packaging analysis at different configuration....66
Figure 3.12 – Building block approach....67
Figure 3.13 – Stress vs. strain for different fiber types....68
Figure 3.14 – Strength vs. modulus for fibers classification....68
Figure 3.15 - M46J Unidirectional carbon fiber....69
Figure 3.16 – Example of Young modulus variation along fiber orientation....69
Figure 3.17 - Transversely isotropic unidirectional composite....71
Figure 3.18 - GG430T Fabric weave....72
Figure 3.19 - GG245T Fabric weave....73
Figure 4.1 - Operative workflow adopted for VEMs characterization activity....76
Figure 4.2 – Test bench (top) and Oberst beam specimen (bottom)....77
Figure 4.3 - Signal amplifier....78
Figure 4.4 - Microphone power supply (A) and signal analyser (B)....78
Figure 4.5 – Example of dynamo-mechanical plot for VEMs....79

Figure 4.6 – Temperature profile for SAE J1637 79
Figure 4.7 – Humidity (below) and temperature (above) profile for IEC 60068 80
Figure 4.8 – Test apparatus (top) and SLJ specimen (bottom) 81
Figure 4.9 - Test apparatus (top) and DCB specimen (bottom) 82
Figure 4.10 – Test apparatus (top) and ENF specimen (bottom) 83
Figure 4.11 - Output signal vs sampling points 84
Figure 4.12 - Receptance of the system 84
Figure 4.13 - Identification of the modal parameters by the fitting procedure 85
Figure 4.14 - Receptance among specific frequency range: Experimental data (o) and fitting curve (-) 85
Figure 4.15 - HVV Oberst beam 86
Figure 4.16 - HAA Oberst beam 87
Figure 4.17 – Loss factor vs. frequency for HVV and HAA 88
Figure 4.18 – E modulus vs. frequency for HVV and HAA 88
Figure 4.19 - Loss factor and E modulus vs. temperature 89
Figure 4.20 – Twisting effect on one side beam specimen at -20°C 89
Figure 4.21 – Joint strength vs. displacement for HVV and HAA 91
Figure 4.22 - Single Lap Joint coupon tested 91
Figure 4.23 – Mode I toughness comparison at 0 h and 750 h 93
Figure 4.24 – Mode II toughness comparison at 0 h and 750 h 95
Figure 4.25 – Oberst beam FE model 96
Figure 4.26 – Spring placed between beam and constraint 97
Figure 4.27 – DAREA application point (left), sampling point (right) 97
Figure 4.28 – Oberst test sensors configuration 98
Figure 4.29 – Section of structural beam with fiber orientation 99
Figure 4.30 – Receptance vs. frequency for EXP and FEM structural beam 100
Figure 4.31 – One side beam model with HVV (in yellow) 100
Figure 4.32 – HVV receptance vs. frequency for EXP and FEM structural beam 101
Figure 4.33 - HAA receptance vs. frequency for EXP and FEM structural beam 102
Figure 4.34 – Experimental FRF comparison between structural and one side beams 102
Figure 4.35 – FEM FRF comparison between structural and one side beams 103
Figure 5.1 – Mechanical characterization aim and workflow 105

Figure 5.2 - ASTM D3039 dimensions for fabric (top) and UD (bottom)....106
Figure 5.3 - ASTM D3410 apparatus (left) and specimens (right) 107
Figure 5.4 - ATM D790 apparatus (top) and specimen (bottom) 107
Figure 5.5 – ASTM E8 specimen dimension 108
Figure 5.6 - GG245T samples tested.....109
Figure 5.7 - GG430T samples tested.....109
Figure 5.8 - M46J specimen tested.....110
Figure 5.9 - S420MC specimen tested 111
Figure 5.10 – Example OET simulation on UD M46J.....112
Figure 5.11 – Example of specimen simulation on UD M46J 113
Figure 5.12 – Four points bending simulation test.....113
Figure 5.13 - Virtual and experimental comparison on M46J 115
Figure 5.14 - Virtual and experimental comparison on GG245T 116
Figure 5.15 - Virtual and experimental comparison on GG430T 117
Figure 5.16 – Dogbone specimen for steel S420MC 117
Figure 5.17 - Virtual and experimental comparison on S420MC.....118
Figure 6.1 – Chapter 6 aim and workflow 120
Figure 6.2 – FE hybrid model for optimization 123
Figure 6.3 – Element fiber orientation 124
Figure 6.4 – Non design variables on LCA.....124
Figure 6.5 – Element thicknesses after free-size step 126
Figure 6.6 – Thicknesses of plies at 0° and 90° 127
Figure 6.7 - Thicknesses of plies at +45° and -45° 127
Figure 6.8 – UD ply thickness at 0° and 90° 127
Figure 6.9 - GG430T ply thickness at 0° and 45° 128
Figure 6.10 – Ply patches from free-size simulation results 128
Figure 6.11 – Reinforcement patches direction (red lines) 129
Figure 6.12 – Examples of ply drops on lower control arm.....130
Figure 6.13 – Hybrid LCA ply shapes classification 131
Figure 6.14 – Final FE model of the hybrid lower control arm 131
Figure 6.15 – Bending and buckling stiffness results on hybrid LCA.....132
Figure 6.16 – Stress distribution (MPa) on steel part.....132
Figure 6.17 – Stress distribution (MPa) on CFRP structural cover 133
Figure 6.18 – Ply failure index.....133
Figure 6.19 – Strain values (mm/mm) on HVV layer.....134
Figure 6.20 – Von Mises stress (MPa) contour on arm steel part for special events 135

Figure 6.21 – Principal σ_1 stress (MPa) contour on CFRP laminate part for special events 135
Figure 6.22 – Hashin failure index among plies for maximum braking 136
Figure 6.23 – Von Mises stress (MPa) contour on arm steel part for misuse events 136
Figure 6.24 - Principal σ_1 stress (MPa) contour on CFRP laminate for misuse events 137
Figure 6.25 - Hashin failure index among plies for hump obstacle 137
Figure 6.26 – Example of ply flat model (HVV) 138
Figure 6.27 – The hybrid lower control arm CAD model 139
Figure 6.28 - Milling operation on LCA 139
Figure 6.29 – LCA with reduced thickness metal part 140
Figure 6.30 – Surface finishing before lamination 140
Figure 6.31 – Example of ply application 141
Figure 6.32 – First ply of GG245T with interlaminar strain gauges 141
Figure 6.33 – The hybrid lower control arm 142
Figure 6.34 – Mass of hybrid LCA 142
Figure 7.1 - Instruments test scheme for frequency response analysis 144
Figure 7.2 – Accelerometer positions on baseline (left) and hybrid (right) arms 145
Figure 7.3 – Experimental set up for the modal analysis for baseline (left) and hybrid (right) arms 145
Figure 7.4 – Modal parameters extraction and correlation workflow 149
Figure 7.5 - PSD of the input force on baseline LCA 150
Figure 7.6 – Frequency stabilization diagram for baseline LCA 150
Figure 7.7 – Number of extracted poles for baseline LCA 151
Figure 7.8 – Damping stabilization diagram for baseline LCA 151
Figure 7.9 – Coherence plot of accelerometer n°9 of baseline LCA 152
Figure 7.10 - Accelerometer n°9 position on baseline LCA 152
Figure 7.11 - PSD of the input force on hybrid LCA 153
Figure 7.12 - Frequency stabilization diagram for hybrid LCA 153
Figure 7.13 - Number of extracted poles for hybrid LCA 154
Figure 7.14 - Damping stabilization diagram for hybrid LCA 154
Figure 7.15 - Coherence plot of accelerometer n°9 of hybrid LCA 155
Figure 7.16 - Accelerometer n°9 on hybrid LCA 155
Figure 7.17 – FRF comparison between baseline and hybrid LCA 156
Figure 7.18 – Bushing model improvements: FEM (top), real (bottom) 157
Figure 7.19 – Nodes mapping for accelerations output 157

Figure 7.20 – Detail of load cell position on experimental test (left) and FEM (right) 158
Figure 7.21 – Inertance comparison between EXP and FEM of baseline LCA 159
Figure 7.22 – MAC index for baseline LCA 160
Figure 7.23 - Inertance comparison between EXP and FEM for hybrid LCA 161
Figure 7.24 - MAC index for hybrid LCA 161
Figure 7.25 – Bending test analysis apparatus 162
Figure 7.26 – Testing machine for bending strength analysis 163
Figure 7.27 - Strain gauge map on hybrid LCA 163
Figure 7.28 – Test set-up for baseline (left) and hybrid (right) LCA 164
Figure 7.29 – RADIOSS LCA model 164
Figure 7.30 – Details of top and bottom LCA supports 165
Figure 7.31 – Model detail of the mechanical assembly to the testing machine 165
Figure 7.32 – Experimental strength curves for baseline and hybrid LCA 167
Figure 7.33 - Experimental strain curves of baseline LCA 167
Figure 7.34 - Experimental strain curve of hybrid LCA 168
Figure 7.35 – Correlation results for baseline LCA bending test 168
Figure 7.36 - Correlation results for hybrid LCA bending test 169

Nomenclature

Acronyms/Abbreviation

ACSL Advanced Composite Structures Laboratory

ADAS advance driver assistance system;

AEM Ethylene Acrylate monomer

ASF Audi Space Frame

ASTM American Society for Testing and Materials

BIW Body-In-White

CAE Computer Aided Engineering

CFRP Carbon Fiber Reinforced Plastic

CFSMC Carbon Fiber Sheet Molding Compounds

COG Centre Of Gravity

DCB Double Cantilever Beam

DOF Degree Of Freedom

ECC Experimental Compliance Calibration

ENF End-notched flexure test

ENLIGHT ENhanced LIGHTweight Design

EPDM Ethylene-Propylene Diene Monomer

ESL Equivalent Single Layer

EV Electric Vehicle

FE Finite Element

FEA Finite Element Analysis

FEM Finite Element Method

FRA Frequency response analysis

FRF Frequency Response Function

FRP Fiber Reinforced Plastic

FWD Front Wheel Drive

GEMCC Generalized Electromechanical Coupling Coefficient

GFRP Glass Fiber Reinforced Plastic

GHG Green House Gas

GVM Gross Vehicle Mass

IEC International Electrotechnical Commission

IEHV Innovative Electric and Hybrid Vehicles

ISO International Organization for Standardization

IIHS Insurance Institute for Highway Safety

LBJ Lower Ball Joint

LCA Lower Control Arm

LIPEZ Linear Identification by Polynomial Expansion in Z-domain

MBD MultiBoDy

MY Model Year

NCAP New Car Assessment Program

NHTS National Highway Traffic Safety administration

NVH Noise Vibration Harshness

OEM Original Equipment Manufacturer

PA PolyAmide

PCLD Passive Constrained Layer Damping

PSD Power Spectral Density

PZT PieZoelecTric

SAE Society of Automotive Engineer

SEA Specific Energy Absorption

SFRP Short Fiber Reinforced Plastic

SIMO Single Input Multiple Output

SLA Short Long Arm

SLJ Single Lap Joint

UD UniDirectional carbon fiber

UTS Ultimate Tensile Strength

VEM Visco-Elastic Material

Chapter 1

Lightweight lower control arm scenario

1.1. The future of the urban mobility

Since the first vehicle was born, the automobile has always represented a status symbol of power, invincibility and dynamism as defined by Marinetti in its "Manifesto del Futurismo", published in 1909. The automobile became the undisputed icon of modernism and technology progress. This paradigm has characterized mostly the idea of the car during the last century, but today's car vision starts to change radically. Although some aspects will remain almost the same, especially the vehicle performance is concerned, the social function of the car will change in the next years where the new leitmotiv will be clean, safe and smart [1].

As a matter of fact, the European Commission has discussed about the new legislative proposal, setting the CO_2 emission standards for passenger cars and light commercial vehicles in the European Union for the period after 2020. This proposal contemplates a cut of 30% of the average emissions of new cars in 2030, over the values fixed of 95 g CO_2/km for passenger cars of the 2021 [2]. Moreover, the proposed framework aims to support a gradual transition from conventional to electric vehicles, with a technology-neutral incentive mechanism for zero- and low-emission vehicles. The main benefits, obviously, consist in the reduction of fuel consumption to achieve the EU's commitments signed during the Paris Agreement and improvements in the competitiveness of the European automotive industry stimulating employment. The forecast CO_2 reduction is estimated at 170 million tons in the 2020-2030 decade, meaning a sensible air quality improvement in the cities.

In this context, carmakers are currently modifying the architecture and the design of their entire fleet to face the regulatory actions curbing Green House Gas emissions (GHG) and to meet, at the same time, customer demands for substantial

improvements in vehicle efficiency. Future vehicle will be cleaner not only in terms of carbon footprint of their life cycle, but also in terms of noise pollution. Future vehicle will be safer, in order to achieve the ambitious target of zero death on the road [3] enhancing passive and active safety systems, such as the Advanced Driver-Assistance System (ADAS). Future vehicle will be smarter and constantly connected with the passengers, in order to communicate with other vehicles, infrastructure and users.

1.2. Lightweight strategy to tackle CO_2 targets

Despite the trends previously presented, the average weight of automobiles increased by 20% in the last 30 years [4-6]. This is mainly referable to the rising customer's demand for comfort and the passive safety standards defined by NCAP, NHTSA or IIHS. A clear example is provided by the weight variation of the Volkswagen Golf from version I (1975) to version VI (2009) as shown in Figure 1.1.

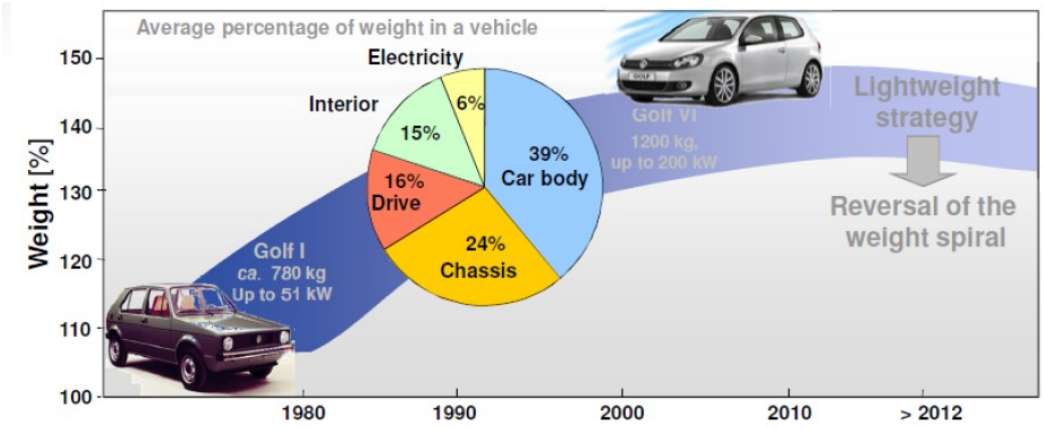

Figure 1.1 - Weight evolution of Volkswagen Golf from 1975 to 2009

However, the need for weight reduction is crucial also in new Electric Vehicles (EV), since additional weight could either reduce driving range or increase battery volume [**7**]. To reverse this trend, the automotive industry identified lightweight design as an important key factor. The driven motto is the right material in the right place with the right amount. Therefore, this design approach is implemented considering mainly three different ways:

- The use of high-strength metal, in particular steel blends;
- The steel substitution for composites or light-alloys;
- The hybridization of dissimilar materials, for instance steel and carbon fibers.

As a matter of fact, carmakers are using a significant amount of resources to face the vehicle weight optimization. For instance, the new Audi A8 chassis is based on a hybrid aluminum and steel frame, taking advantages of their particular construction technique called Audi Space Frame (ASF) [8]. The ASF principle assigns a specific task to each material and each component: the extruded sections bridge spaces, the cast nodes connect the components, the aluminum panels close off the spaces and give stiffness to the framework as shown in Figure 1.2. The body of the new A8 is 35% lighter than the previous model with a torsional stiffness enhanced of 20%.

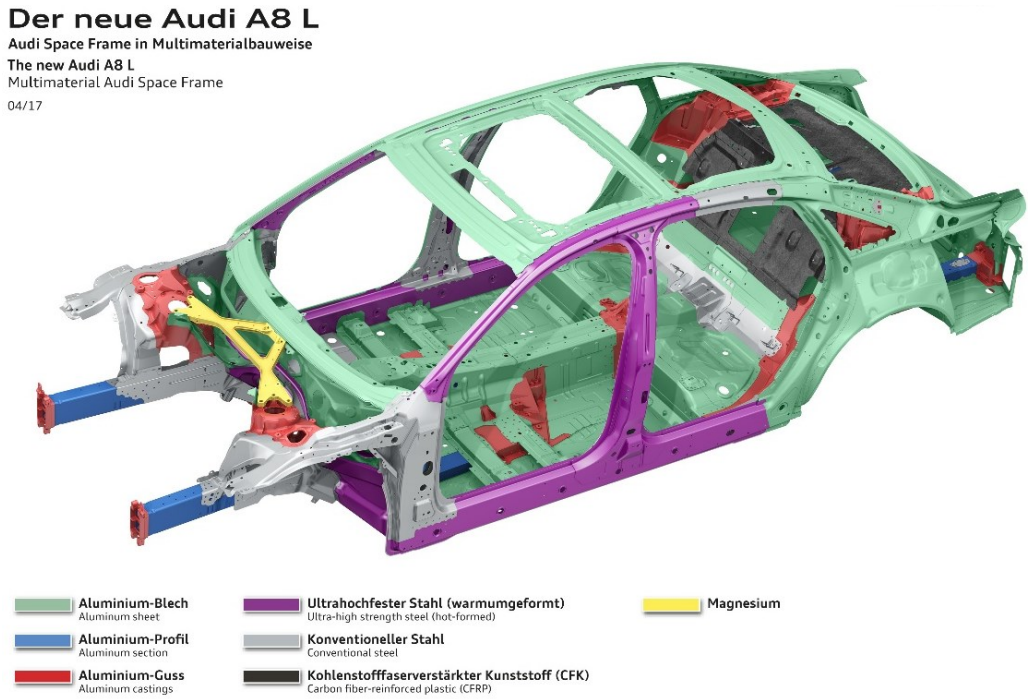

Figure 1.2 - Audi A8 spaceframe material composition

An important example of material substitution is provided by Mercedes-Benz. The Stuttgart's carmaker focus its efforts on an unusually high percentage of aluminum adoption (close to 50%) in their Body-In-White (BIW) [9]. This is the case of the new C-Class, illustrated in Figure 1.3, where its hybrid aluminum body is 70 kg lighter than the previous steel model.

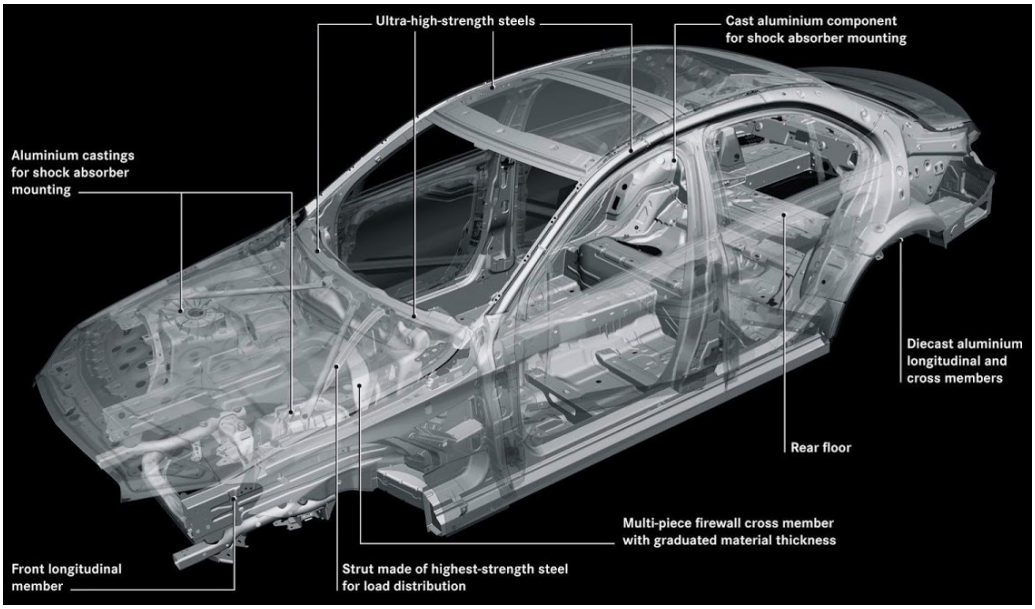

Figure 1.3 - Mercedes-Benz C-Class body

Similar results were obtained with the aluminum bodies of the new SL models (Figure 1.4**)**. Indeed, it is about 110 kg lighter than its predecessor, allowing an improvement of the dynamic performance and a fuel saving of 0,3 L per 100 km.

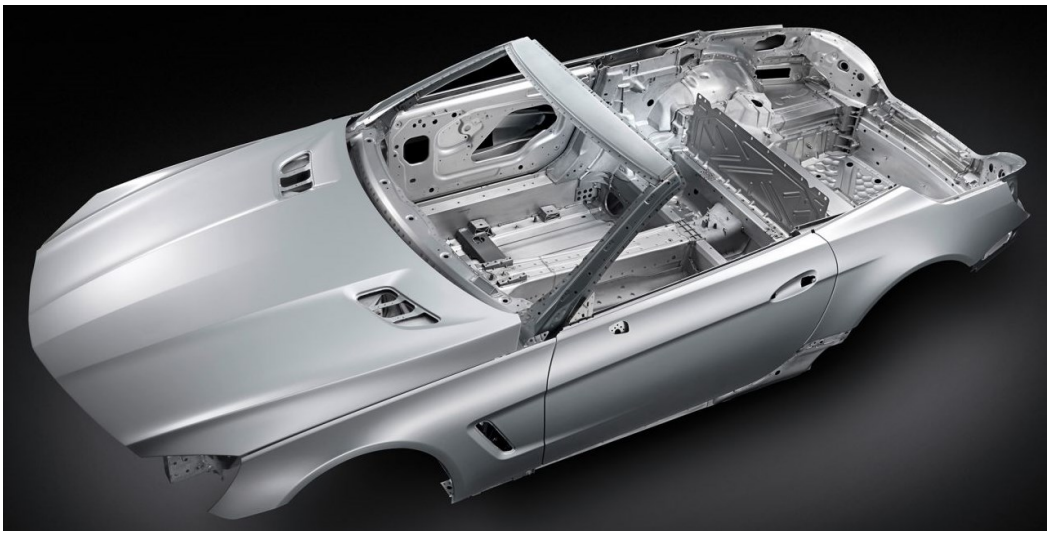

Figure 1.4 - Mercedes-Benz SL body in white

Another interesting example of lightweight design is the i3, the electrically powered vehicle produced by BMW, which represents their vision on sustainable mobility [10]. BMW has developed a novel chassis architecture based on two macro assemblies as depicted in Figure 1.5: the aluminum Drive-module with drive systems, chassis and energy storage; as well as the Life-module of Carbon Fiber Reinforced Plastic (CFRP), which constitutes the passenger compartment. The vehicle curb weight is 1195 kg which allows a 200 km driving range.

Figure 1.5 - BMW i3: Life module (top) and Drive Module (bottom)

The experience, matured with the "*i*" models, has also been transferred to the new BMW 7 Series, a vehicle considered by most as a reference point in lightweight design. The German engineers developed a multi-material body structure – also called Carbon Core – in which CFRP is bonded to the steel by different techniques (clinching, adhesive, etc…) in some specific vehicle parts to increase significantly stiffness and safety. A side view of the vehicle is reported in Figure 1.6.

Figure 1.6 - Side view of BMW 7 Series BIW with CFRP components

The configuration of the sheet metal elements have been adjusted accordingly, allowing body weight to be reduced of about 130 kg, when compared to the outgoing generation of models [11].

1.3. Benefit of lightweight suspension system

Although the body-in-white examples are the most notable industrial applications of weight reduction, all the vehicle sub-systems need to be redesigned

and optimized in order to achieve a full functional integration, especially for EV. Considering a given vehicle, the mass can be subdivided in different macro systems, being the body, the powertrain and the chassis equally important to total vehicle mass [12], as shown in Figure 1.7.

Approximate vehicle mass breakdown[a]	System	Major components in system
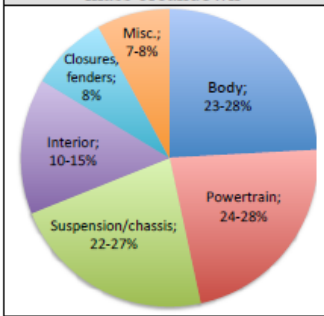	Body-in-white	Passenger compartment frame, cross and side beams, roof structure, front-end structure, underbody floor structure, panels
	Powertrain	Engine, transmission, exhaust system, fuel tank
	Chassis	Chassis, suspension, tires, wheels, steering, brakes
	Interior	Seats, instrument panel, insulation, trim, airbags
	Closures	Front and rear doors, hood, lift gate
	Miscellaneous	Electrical, lighting, thermal, windows, glazing

Figure 1.7 - Mass repartition in a generic vehicle

As a matter of fact, important applications in lightweight suspension system has been developed by carmakers in the last thirty years in which composite materials had played a key role [13-15]. In 1981, GM replaced the front ten-leaf steel spring with a GFRP transverse leaf spring in the Chevrolet Corvette C4, saving 15 kg of unsprung mass and improving handling [16]. This solution has also been adopted on the most recently Corvette C5/C6 (2014), both in front and in rear suspension, as depicted in Figure 1.8.

Figure 1.8 - Corvette C6 rear leaf spring

During the 2013 Frankfurt Motor Show, Peugeot and Total unveiled the 208 Hybrid FE, their technological concept to foster the energy efficiency challenges. The overall vehicle mass is 23% lower than the 208 standard vehicle, due to the intensive use of lightweight materials. In particular, the 208 hybrid FE mounts an

innovative pseudo MacPherson suspension with two GFRP composite transverse blades, as shown in Figure 1.9.

Figure 1.9 - Peugeot 208 Hybrid FE: powertrain and suspension system

Thanks also to the function integration (the blades act as springs, lower control arm and anti-roll bars) Peugeot declares to save 20 kg when compared to the traditional solution [17].

A successful application is the rear transverse composite leaf spring developed by Volvo in partnership with Benteler-SGL and Henkel. This innovative concept is mounted on the SUV XC90, the Sedan S90 and the station wagon V90. The rear suspension of the Volvo XC90 is illustrated in Figure 1.10.

Figure 1.10 - Rear GFRP leaf spring of Volvo XC90

In all three car models, the transverse leaf spring saves significant 4.5 kg compared to steel coil springs, normally used in passenger cars. The high-speed resin transfer molding process, set by Henkel and Benteler-SGL, is able to reach a total amount of 200.000 components per year [18].

Another example is the pseudo MacPherson designed by ZF Friedrichshafen AG, a global supplier of driveline and chassis technology. They developed a

composite wheel-guiding transverse leaf to perform as spring, lower arm and anti-roll bar. This solution, shown in Figure 1.11, is manufactured via heated compression molding, with an epoxy-based resin system and continuous glass fiber reinforcement.

Figure 1.11 - ZF rear suspension layout for small cars

ZF declares that their composite leaf spring suspension is approximately 12% lighter than a conventional MacPherson, approximately 10% lighter than a conventional twist-beam suspension and can be as much as 60% lighter than a steel multi-leaf spring [19].

In this context, Chang [20] carries out a deep analysis on suspension system optimization. He makes a comparison between different front suspensions architecture to evaluate their *potential mass reduction capabilities* due to the components optimization and integration. The analysis involves vehicles from different carmakers, and ranging from A to D segment. Chang mainly focus its studies on the evaluation of two suspension systems: MacPherson and transverse leaf spring. He defines a scoring system (from 0 to 100 points) for different parameters such as potential of market, design advantages and *potential mass reduction*. As concerns the latter, focusing on MacPherson, Chang carries out the following results:

- A-B segment: 87 points;
- C segment: 92 points;
- D segment 89 points.

The high results underline the elevated impacts that the mass optimization on MacPherson suspension could have. These impacts are even greater when considered that it is the most common independent suspension structure. In fact, the 78% of worldwide vehicle are equipped with the MacPherson system and it is mounted on the 90% of the front driven cars [21]. In 2018, the best seller cars in Europe from A to C segment are all equipped with MacPherson on the front axle

[22]. The diffusion of this suspension system is due to the good handling performance, the compact layout and the lower cost than other independent suspensions such as multilink or SLA suspensions.

1.4. MacPherson suspension system

Earle MacPherson, a Ford engineer, developed the homonymous suspension scheme in 1949. This solution has been applied for the first time in the early 50' on the Ford Zephyr and Consul but it spread up since 70' [23]. The MacPherson strut is a simplified version of SLA suspension, in which the upper control arm is removed and its structural function is integrated into a stronger shock absorber. A complete description of the suspension behavior is given by Genta and Morello [24]. MacPherson suspension is usually made of four components: Lower Control Arm (LCA) or lower swinging arm, strut, upright and anti-roll bar as shown in Figure 1.12.

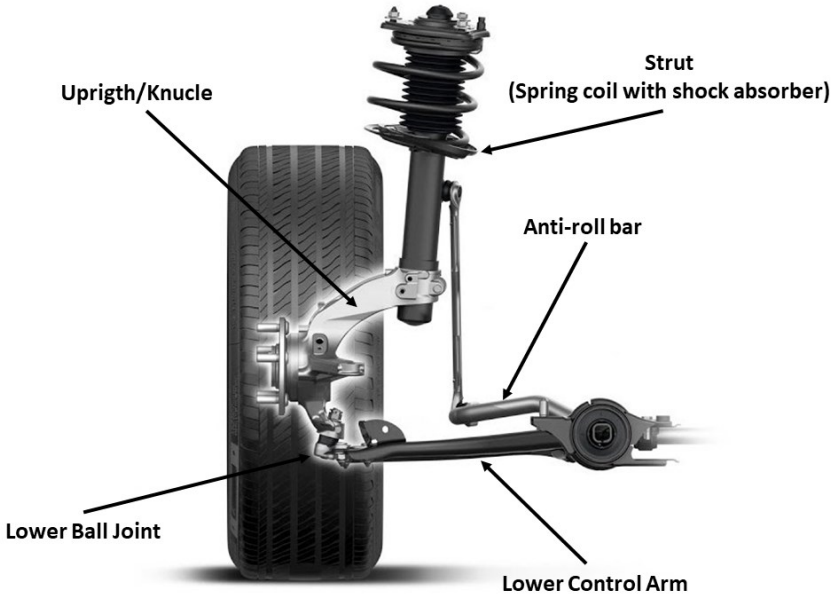

Figure 1.12 - MacPherson suspension scheme

The vertical motion of the wheel is defined by the lower control arm and the shock absorber. The spring is also supported by the shock absorber and it is linked to the car body by an upper pivot. The lower control arm is connected to the chassis through an auxiliary frame, also called subframe, at two different points, through elastic bushings integrated into the arm shape. Finally, the lower control arm is also linked to the upright and through a spherical joint, also called Lower Ball Joint (LBJ). For this reasons, the LCA plays an important role on the suspension, in fact, the relevant sign off capabilities of a swinging arm are:

- Buckle loads in lateral (Y Axis) and longitudinal (X Axis) direction;
- Resist to fatigue loads;

- Resist to special events conditions;
- Resist to misuse conditions;
- Prevent to liability issues;
- Resist to environmental conditions (corrosion, dust, abrasion, thermal cycles, etc…);
- Present repeatable behavior in frontal crashes, especially misaligned crashes.

The designing process of a lower control arm needs the help of different computer-aided software and numerical simulation, both for structural and for vehicle dynamic analysis. As consequence, the choice of the shape of the lower arm is a fundamental part of the design of the front suspension and must be compatible with handling, comfort and packaging targets as well. Moreover, the LCA absorbs a relevant portion of the forces coming from the wheel during braking or cornering maneuvers. As a result, car manufacturers are used to design the lower arms in a banana-like shape as shown in Figure 1.13.

Figure 1.13 - The banana-like shape of a lower control arm

The manufacturing technologies used to the lower control arms production are different and the mechanical properties and costs can vary according to the process. In particular:

- Cast iron technology achieves minimum cost, but reduced mechanical characteristics especially in terms of rupture percentage elongation. An example is presented in Figure 1.14;

Figure 1.14 - Example of cast iron LCA

- Stamped steel sheet LCA are built by welding two semi-shells together as in Figure 1.15. The lower ball joint housing has to be riveted, while bushing housings show local reinforcements. This solution is characterized by reduced weight, better rupture elongation but slightly increased cost;

Figure 1.15 - Example of welded clamshell LCA

- Hot stamped steel arm presents a notable size reduction in cross-section, as shown in Figure 1.16. With this technology excellent mechanical properties can be obtained at a higher cost. But aluminum adoption allows a relevant weight reduction.

Figure 1.16 - Example of single stamped shell LCA

The optimization of the suspension system covers multiple fields that are fundamental for the global behavior of the car. The benefits of suspension mass reduction does not concern only the fuel consumption, but also the improvement of handling and comfort. As a matter of fact, the reduction of the unsprung mass represents a key factor in handling: the lower the unsprung mass, the lower the inertia withstand by the shock absorber, and consequently the work required to keep the tire in contact with the ground in an uneven road surface. Therefore, in the case of a MacPherson suspension, a study of a lightweight lower control arm assumes a significant relevance.

1.5. The lower control arm case study

The hybridization and electrification of vehicle powertrain pushing carmakers on reducing the weight of vehicles to extend as much as possible the vehicle range. Thus, the application of advanced materials, like carbon fiber, to reduce suspension mass is becoming a common practice. The design of a lightweight lower control arm is a feasible solution, but some important aspects must be analyzed carefully in order to guarantee the component functionality and preserve the life during its duty cycles.

1.5.1. Noise Vibration and Harshness

Lightweight material can significantly change the Noise Vibration and Harshness NVH behavior of a component [25]. Noise and vibration are an increasingly important issue in the automobile industry, for implications on both environmental noise pollution and comfort perceived by driver and passengers. Moreover, the continuous improvement of NVH performance increase the customers' expectations concerning the global quality of the car. Hence, every feature and noise generation point must be analyzed, especially in an electric vehicle, in which part of noise is not covered by the strong presence of the thermal

engine. In order to improve the overall NVH performance of a vehicle, the knowledge of the main noise sources and the transmission paths represents a fundamental aspect, especially because lightweight structure are susceptible to vibration problems.

The investigation of noise and vibration in a vehicle is a complex task due to the presence of hundreds of sources to identify and analyze. In a vehicle, it is possible to distinguish noise according to the speed or the frequency range [26]. As shown in Figure 1.17**,** at low speed the main source is the thermal engine. Then, at middle range speed, strong influence is given by the tire/road noise while, at high speed, the major influence is given by the wind noise. In the case of an electric car at low speeds, the powertrain noise tends to have lower influence and it will be overlapped by some other noise generation source.

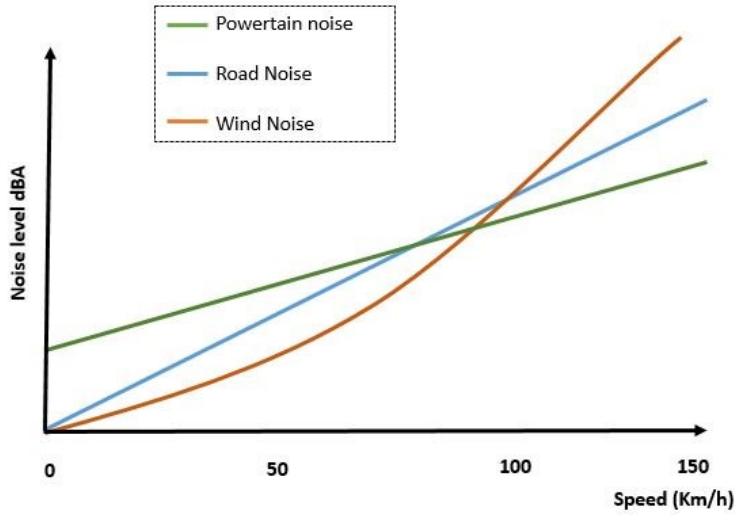

Figure 1.17 - Noise level trend vs. speed

As concerns the noise transmission path according to frequency range, there are two different categories: structure-borne and air-borne paths. Usually, the structure-borne noise transmission path dominates at low frequency (<200 Hz) while the air-borne noise transmission path dominates above 500 Hz [27]. The noise contribution of the main sources are reported in Figure 1.18. At low and middle frequencies, the major noise sources are the engine and the noise caused by road excitation. Instead, the wind noise usually covers the high frequency range. In a case of EV, the electric motor and the gearbox cover a range from middle to high frequencies.

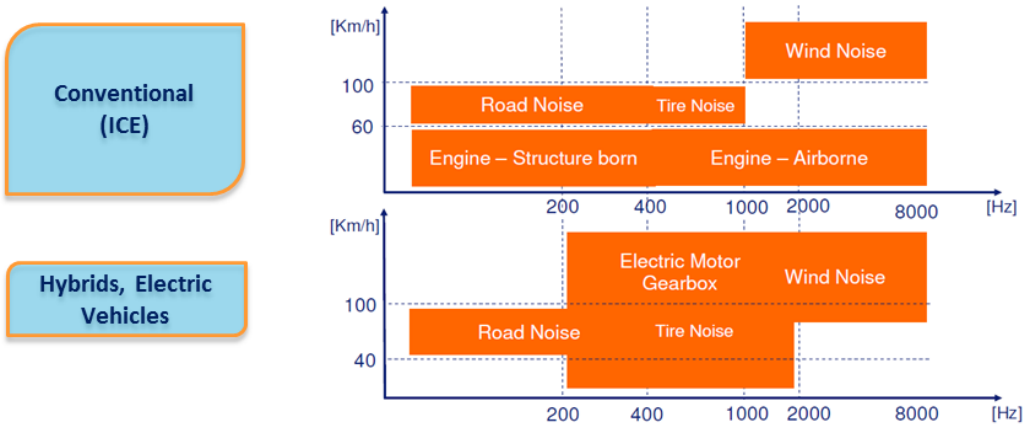

Figure 1.18 - Noise sources accordingly to the frequencies

The vehicle suspension system plays a crucial role in vibration transmission and its excitations are located in the structure-borne transmission path, between the road–tire interaction and the vehicle body [28]. In particular, the lower control arm is one the main transfer paths for vibrations coming from the wheels into the chassis [25]. The reduction of these vibrations is considered by carmakers a design objective because they can influence the comfort of passengers, for example when driving through a train crossbeam or running over small obstacles. Only small part of the road vibrations is damped by the two elastomeric bushings of the swing arm [29]. In fact, whereas soft bushing improve the comfort and increase vibration insulation, they drastically degrade vehicle drivability and handling. However, the high axial and radial stiffness of the bushings transfer the vibration directly to the subframe.

1.5.2. Mechanical coupling

Besides the NVH issues, in a lower control arm it is fundamental to preserve the main mechanical connection between the subframe and the upright, especially if the LCA is made of FRP materials. In this case, three main aspects must be considered:

- *Bushing fittings*: bushings transfer the loads from lower control arm to the chassis, so it is mandatory to guarantee the precise mechanical interference to fit correctly the bushings into the holes. In composite laminate, drilling operations are critical because they can trig delamination and decrease fibers strength [30]. The structural integrity of the area around the holes is a safe requirement. Moreover, the elastomeric mountings need to be replaced during the LCA life and the maintenance operation may damage the bushing seats.

- *Lower Ball Joint connection*: the LBJ is bolted or riveted on the swing arm. Composite material are usually more brittle than metallic alloys so the loads are not uniformly distributed around a stress concentration such as a bolt

holes [31]. Moreover, the maximum bearing strength in a composite laminate is governed by several factors such as joint geometry, laminate thickness and stacking sequence, clamping load and bolt-hole clearance [32].

- *Galvanic corrosion*: when carbon fiber are inappropriately joined with metals, corrosion issues may arise and the metal is susceptible to suffer galvanic corrosion. In presence of a fastener, bolt, or nut, the situation worsens, because a large surface area of CFRP is coupled to small metallic parts. In these circumstances, the rate of galvanic corrosion may be accelerated due the high cathode to anode surface area ratio [33] [34].

1.5.3. Suspension safety standards

Lower control arms play a significant safety role in a vehicle because they hold the wheels in position and absorb the greater part of the energy in case of obstacle impacts and crashes. The stiffness, deformation and failure mode of the LCA are critical factors in crash safety because they can affect the frame rail's ability to buckle and absorb the energy [35-37]. To better understand a possible frontal crash kinematic, Figure 1.19**,** from [35], shows a typical suspension configuration: the bushings (pt.3 and pt.4) have a significant role on the deformation and rupture of the swinging arm because they allow the arm to rotate at the two joints where the LCAs connect to the frame. The LCA failure allows the portion of the frame rail between the LCAs two connection joints to buckle and absorb additional energy from the crash.

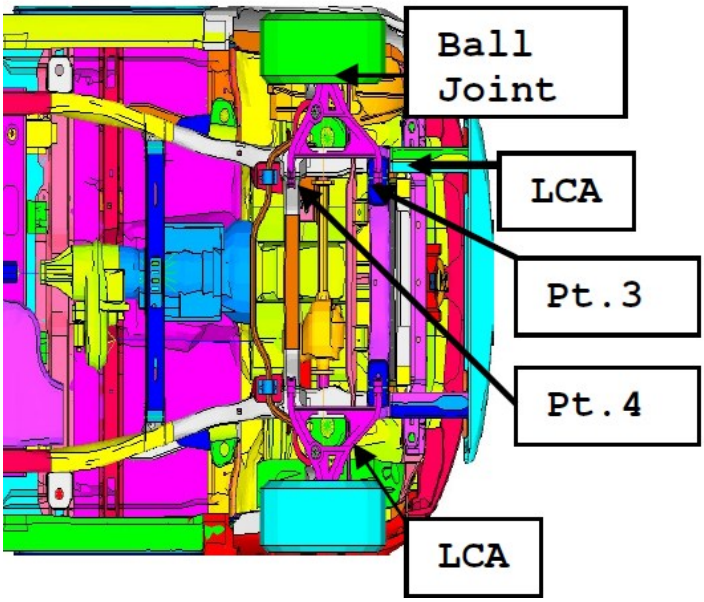

Figure 1.19 - Bottom view of a vehicle [35]

Moreover, in case of misaligned collision, such as in moderate overlap test or small overlap frontal crash, the impact involves the entire suspension component. The deformation and rupture modes of LCAs can affect load path and crush distance in vehicle crashes, which could affect the severity of occupants' injuries [38]. Composite materials usually have brittle failures, so their behavior until rupture does not present any plastic deformation. Therefore, failure mechanism in a composite structure is not always progressive, but could be catastrophic [39]. In addition, the lower control arm working conditions include several events at various speed and loads, which could compromise the component health, such as: driving/braking over a pot hole, curb impact while skidding in transversal direction and so on. This events could damage the structure and, in the case of composite material, generate the growth of a crack inside the laminate that is hard to detect.

1.6. Lightweight lower control arm state of art

The richness of research literature on lightweight lower control arms highlights the great interest of the automotive industry on this suspension component [7, 25, 29, 40-49].

The studies analyzed in this section underline the complexity of the optimization process for a LCA, mainly due to its design requirements. Until now, no unified procedure has been developed to design a lower control arm, because the identification of its precise working condition is hard. Indeed, every carmaker define its own load cases procedure from a cluster of possible maneuvers or events. As consequence, researchers take advantage of several advanced CAE tools and experimental tests to match all the targets, especially in case of composite structures. It is possible to identify different research approaches that can be summarized as follow:

- Lightweight metallic LCA as a function of costs reduction;
- Lightweight composite LCA as a function of material substitution and component re-design;
- Hybrid lightweight LCA (CFRP and metal) in which mass reduction is combined with NVH performance enhancing.

From the industrial point of view, cost reduction is a key factor. In fact, Calli et al. [40] proposed a topology optimization of a lower control arm for a commercial vehicle to meet the requirements of energy absorption, durability and fatigue, but also reducing production costs. Different load cases were considered: steering loads, vertical acceleration, braking and longitudinal acceleration loads. The authors define a design space volume according to the packaging of the vehicle, while the bushings and the LBJ have been considered as non-design areas. The result of the topology optimization is a major amount of material close to the front

bush case and to the LBJ. Moreover, the maximum stresses due to critical loads is concentrated close to the connection points of the LCA with the vehicle subframe. They, finally, carried out an optimized shape, obtained by stamped steel shell and forged bushing case as depicted in Figure 1.20.

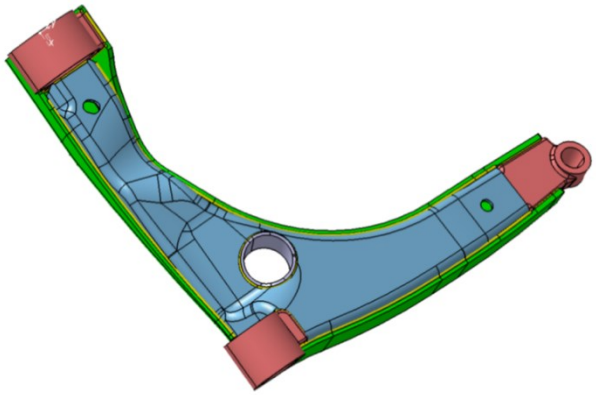

Figure 1.20 - LCA shape from [40]

Similar approach has also been used by Fuchs and Salmon [41]. They studied a lightweight steel lower control arm concept, to achieve equivalent performance and function at a reduced cost, when compared to the baseline in aluminum, defining the following design targets:

- Equal structural performance;
- Cost reduction of 30%;
- Lower or equal mass;
- Meet available packaging constraints;
- Meet OEM corrosion requirements.

Several load cases were consider for the comparison: lateral and longitudinal stiffness; longitudinal buckling strength; three extreme and durability loads. An iterative optimization strategy was used to minimize the mass of each design, while meeting the specified structural requirements. In particular the design path adopted was:

- Size-Shape optimization;
- Stiffness optimization with material selection;
- Fine tuning to achieve durability and strength;
- Manufacturing and cost assessment.

Finally, three design concepts were carried out: clamshell, I-beam and forged. Different steel quality were adopted on the three arms to meet the targets. The results of the study support the following conclusions for a volume production of 250.000 vehicles per year:

- The Clamshell Design, in Figure 1.21, has equivalent mass to the baseline, with up to a 34% cost reduction potential. The weakness of this solution is represented by limited lateral stiffness and durability;

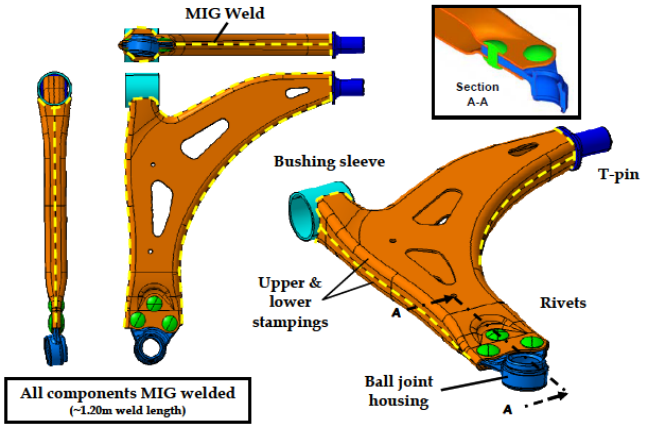

Figure 1.21 - Clamshell design

- The I-beam Design, in Figure 1.22, is predicted to have the highest buckling resistance and high stiffness, with a 2% (0.05 kg) higher mass than the baseline assembly and up to a 21% cost reduction potential. The design is only limited in durability;

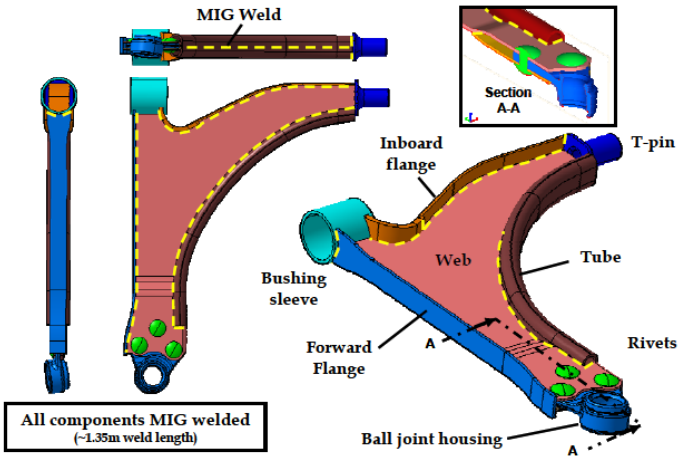

Figure 1.22 - The I-Beam design

- The Forged Design, in Figure 1.23, is predicted to have the highest stiffness and durability performance (no welds) of all designs, with a 4% (0,13 kg) higher mass than the baseline assembly, but the authors does not provide any cost reduction prevision due to the lack of some manufacturing data.

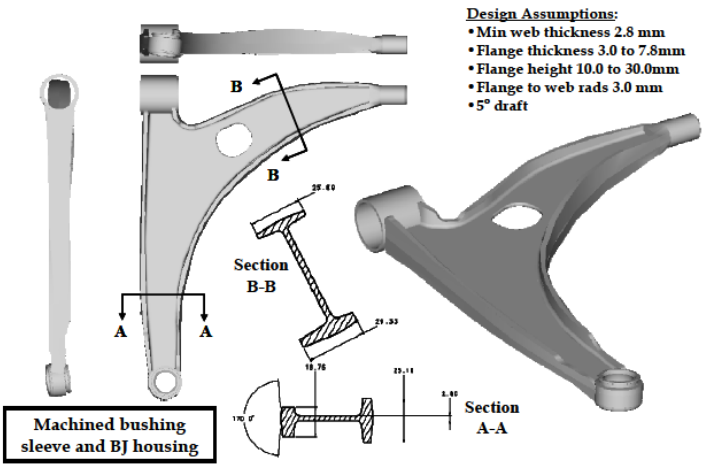

Figure 1.23 - Forged Design

During the 2011 JEC the "Innovation Award" has been given to a thermoplastic composite arm developed by PSA group (Peugeot-Citroen), in partnership with Onera, Compose and Cetim [42] [43]. Starting from the original metallic design, the authors made a shape optimization and a stacking sequence tailoring, maintaining the same connection points and the overall performance. The innovation of this component consists in the material used and the process manufacturing. In fact, the lower control arm is made of two single Carbon-PA organosheet thermoformed simultaneously and welded together using a novel tool installed on an automated press. Moreover, bushings are directly overmoulded inside the holes, in order to increase the lifetime of the joints and assure good mechanical performance. The final design, shown in Figure 1.24, presents a hollow body structure with mass of 1.2 kg, which means a 40% reduction respect to the conventional arm.

Figure 1.24 - Thermoplastic CFRP lower control arm by PSA group

Since 2008 the Automobili Lamborghini Advanced Composite Structures Laboratory (ACSL) in Seattle, is developing an advanced composite material technology called "Forged Composite". Forged Composite technology is not

exactly a material, but represents an evolution of Carbon Fiber Sheet Molding Compounds (CFSMC), that improve fibers orientations and molding process to obtain enhanced strength performance and reproducibility. Lamborghini firstly introduces this technology in the *Sesto Elemento*, especially on the wishbone suspension arms. In particular, Feraboli et al [44] worked on the development of the Forged Composite suspension arm, whose target was to reduce the mass by 30% from the baseline aluminum design. In this case, the authors defined 9 different operational load cases, such as curb strike, braking and cornering. The material is supplied by Quantum Composites and consists of 25,4 mm long carbon fiber tows (fiber content 53% by weight), randomly distributed into a mat, sandwiched between two layers of vinylester resin. A comparison between mechanical properties is reported in Table 1.1.

Average Properties	Tensile Strength [MPa]	Tensile Modulus [GPa]
6xxx Aluminum	260	70
Prepreg 2x2 twill	754	40
RTM stiched NCF	634	34
Forged Composite	246	33

Table 1.1 - General properties of aluminium and composite materials [44]

In order to meet the control arm requirements and save mass, the wishbone geometry has been locally reinforced and optimized to make up for the lack of material stiffness, as shown in Figure 1.25.

Figure 1.25 - Lamborghini LCA with thinned flange to increase stiffness

The holes for the bushing have been obtained during the molding process while the LBJ seat has been machined after using waterjet cutting. The final mass obtained, including bushings and lower ball joint, is equal to 2,1 kg compared to the 2,9 kg of the aluminum solution.

In 2012, Prof. Thilo Bein from Fraunhofer LBF coordinated two significative lower control arm case studies inside the European Enhanced Lightweight Design

(ENLIGHT) project, which involved many companies and universities for 4 years. The aim of this project was to study advance highly innovative lightweight material technologies for application in structural parts of Electric Vehicles (EVs) [45] [46]. In this contest, inside the FP7 framework, Magneti Marelli Sistemi Sospensivi and Fraunhofer LBF developed two different solution of lightweight suspension arm.

Magneti Marelli studied a suspension arm by using innovative SFRP composite [47] following the example of Lamborghini. This material, commercially named Quantum AMC 8592 ESC, is a compound with chopped carbon fibers (50 mm long) impregnated between two layers of vinylester resin. The pre-impregnated sheets are cut and put inside the mould with the aluminum inserts. When the mould closes, a cycle of pressure, temperature and curing starts. Finally, the arm is extracted for cooling. The main results carried out highlight that:

- Fibers keep their original length during the manufacturing process;
- Fiber orientation after the molding is random so the mechanical properties can be considered as quasi-isotropic;
- Metallic inserts co-molding guarantee a strong cohesion between composite and metal due to the high forming pressure applied;
- Fatigue limit tested and longitudinal load collapse obtained overcome the targets;
- Final mass is equal to 1.79 kg, with a reduction of 54% compared with the reference steel component. The LCA developed is shown in Figure 1.26

Figure 1.26 - Magneti Marelli Sistemi Sospensivi LCA

At the same time, researchers from Fraunhofer in Darmstadt developed an interesting hybrid LCA concept combining CFRP sheets with steel reinforcement strips wrapped of UD carbon fibers [**7**]. This solution can be considered “hybrid”, although the metal structural contribution is limited to certain function. Nevertheless, besides the traditional structural optimization, Salloum et al [25] [29] present a new methodology for a full design of a smart structure by using piezoceramics semi-active damping. In fact, the core activities of their works consist in the study of a piezoelectric shunt damper device to reduce structural vibration in lightweight applications. The method involves coupling a piezoceramic

transducer to a mechanical structure and then connecting it to a shunt circuit, as shown in Figure 1.27.

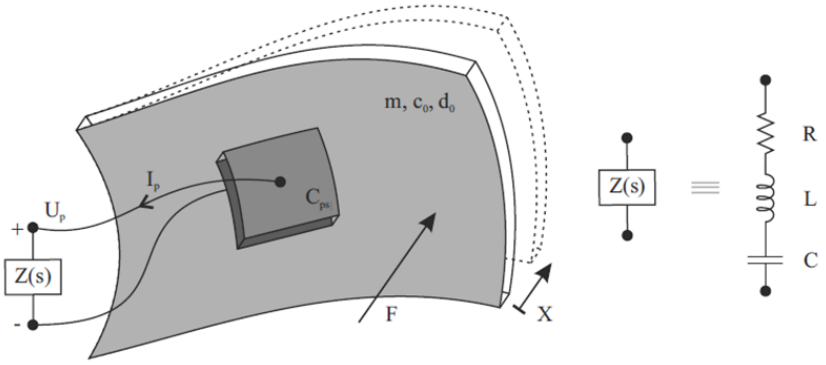

Figure 1.27 - Shunt circuit model

To increase the damping of a structure, a possible strategy is to dissipate the electrical energy converted by the piezoceramics. Hence, to improve the system efficiency in shunt damping, is important to evaluate the Generalized Electro-Mechanical Coupling Coefficient (GEMCC) K_{31}. The square of the GEMCC physically describes how much mechanical energy is converted into electrical energy, and vice versa, at a given eigenfrequency of the system.

The lower control arm laminate is composed of 22 layers of T300 woven carbon fiber fabric, while unidirectional fibers have been placed in strategic areas in order to improve the static strength of the points connecting the load inputs. In Figure 1.28 is illustrated the LCA laminate.

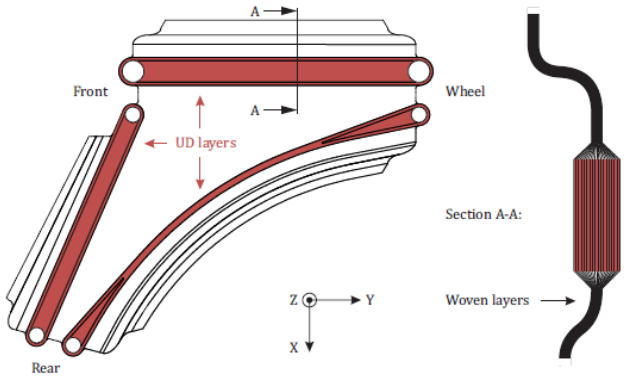

Figure 1.28 - Fraunhofer LCA laminate

A modal analysis has been performed to identify the mode shape of the two most important transmission modes. In particular, the mode shapes extracted happen at 63 Hz (the 1st mode) and at 260 Hz (the 2nd mode). Moreover, the modal analysis also allowed the identification of the areas for the application of a piezoelectric module, analyzing the strain distribution. Since the 1st mode is a bending vibration, the highest strain is located in the curved area of the arm as shown in Figure 1.29.

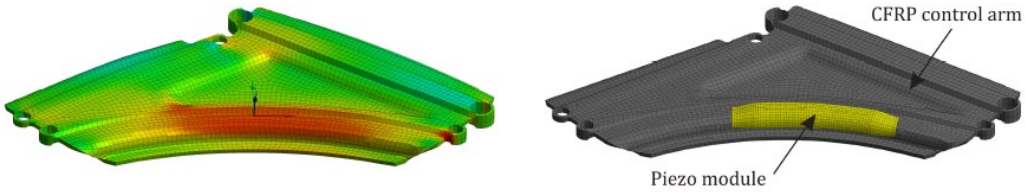

Figure 1.29 - Modal analysis results and piezo positioning

The results obtained show that:

- The application of a PZT module allowed mass reduction, because 4 layers has been removed from the original laminate. In fact, the module has a mass of 0.05 kg against the 0.1 kg of the 4 layers.

- An optimized stacking sequence is needed to enhance the value of K_{31}^2. The complete optimization process of the shunt damped device is described in [48] [49].

- Simulations shows that when an optimal tuned mass damper is used, the maximum vibration reduction is equal to -19.9 dB, with a mass ratio of 0,1. The RLC-shunt, instead, is able to reduce the vibrations of -17.7 dB without excessive mass addition, similarly to the tuned mass damper. However, experimental modal analysis shows a peak reduction of 6 dB at 1st resonance frequency instead of the predictive results of simulations.

1.7. Research aim and workflow

Despite the notably application explained in Section 1.6, it has been highlighted none of them are able to integrate simultaneously features of lightweight, damping and safety.

This thesis is focused on the design, analysis and testing of a multi-material lightweight suspension arm made of steel and carbon fiber. The novelty of this research is represented by the application of an innovative low density viscoelastic interface that works simultaneously as damper and adhesive. Moreover, the complete research activity has been conducted on an off-the-shelf component actually installed on a real vehicle. This is a constraint that will allow to integrate the hybrid LCA on a realistic car permitting a "ready-to-run" approach. Therefore, starting from an existing component (made of steel), the LCA mass has been reduced by using a hybrid technology, diminishing the steel thickness and adding a carbon fiber tailored cover without compromising the mechanical performance in terms of stiffness. In so doing, it has been possible to evaluate the potential and the capabilities of the hybridization without re-designing the component totally. Hence,

the original shape is kept almost unmodified, with the exception of the areas reinforced by carbon fiber (fabrics and unidirectional).

This approach allows satisfying the requirements related to mechanical coupling and safety standards. Moreover, particular attention is paid on the investigation of the dynamic response in terms of vibration reduction in the range of structure-borne frequencies of 0-600 Hz.

The research workflow followed is reported in Figure 1.30. A complete methodology path, consisting in five macro steps, has been developed that combine both virtual and experimental activities to face the hybridization challenges of mechanical coupling, damping and lightweight.

At the beginning, it has been accomplished both FEM patterns and multi-body to define the load cases and the performance of the original component in order to identify the hybrid LCA target values. Then, the hybrid LCA concept has been developed analysing the design constraints and screening the suitable materials to meet the research aim of mechanical coupling, damping and lightweight.

An intensive testing activities have been done to investigate, firstly, damping and adhesive properties on this innovative viscoelastic material by comparing two different compounds, secondly, carbon fiber and steel used in the hybrid arm accordingly to the international testing standards. The experimental characterization has been completed by a virtual correlation analysis in order to carry out the material card for RADIOSS and Optistruct solver for FEM simulation.

A structural optimization has been also performed favoring mass minimization in order to investigate the potential mass reduction obtainable guarantying the same performance of the conventional arm. Then, the same simulation set of the baseline component have been performed on the hybrid LCA to compare the performance and to validate the design phase virtually before manufacturing.

Finally, a correlation activity has been conducting both on baseline and hybrid component to validate the entire design process and evaluate the real structural and damping performance.

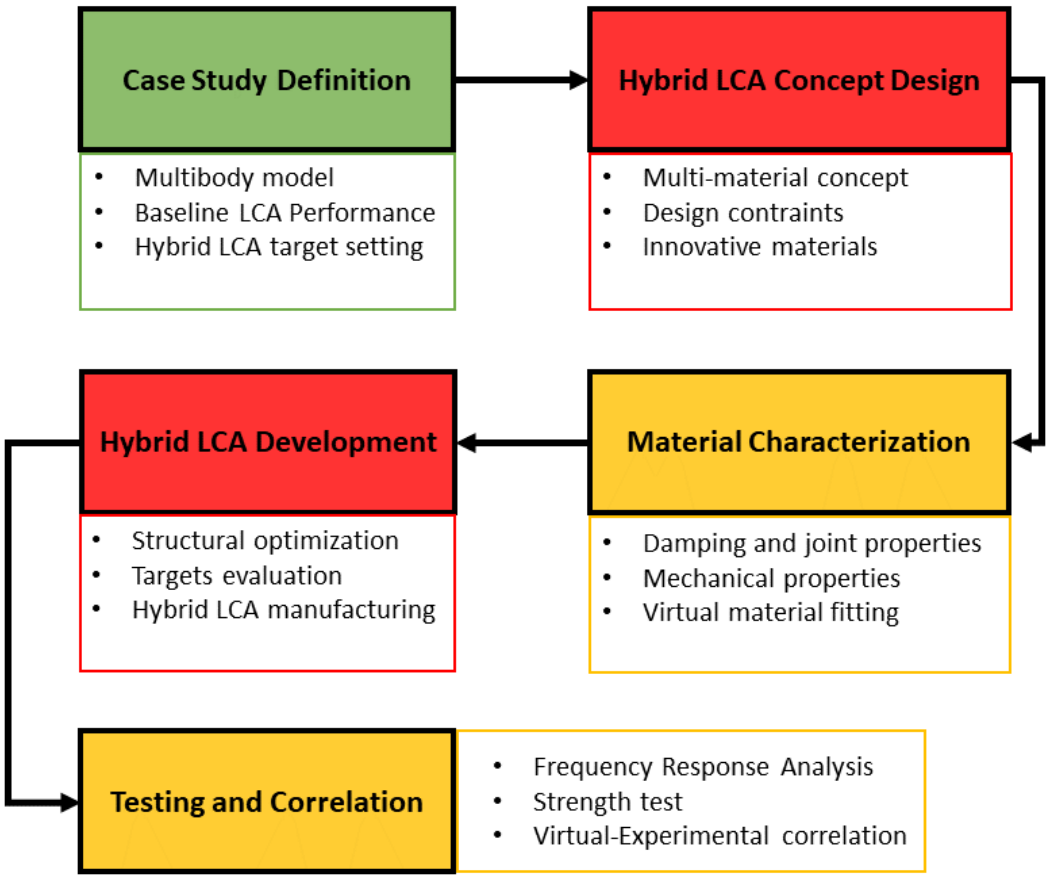

Figure 1.30 - Research workflow

Chapter 2

LCA case study definition

This chapter is composed by two main parts. The first one describes the approach used to create the multi body model to investigate the force acting on the LCA according to different load cases (Figure 2.1). At the beginning, the reference vehicle information have been presented together with the baseline lower control arm characteristics. Hence, a set of vehicle working condition has been defined in order to carry out the forces acting on the LCAs. In particular, two different maneuvers set have been chosen which include special and misuse events cases. Then, the procedure used to create the multibody model has been presented, explaining the different steps from the suspension assembly to the full vehicle.

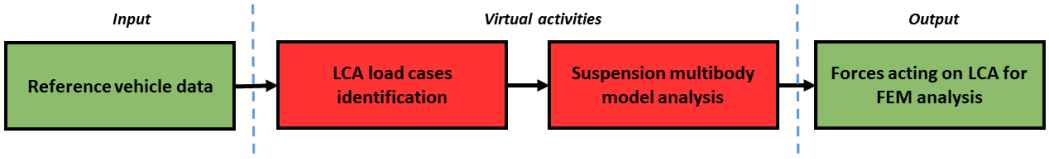

Figure 2.1 - LCA load case definition workflow

The second part describes the process to create the whole virtual model in order to evaluate the mechanical performance of the baseline arm. Due to the component nature to re-create a reliable CAD model, a reverse engineering activity has been performed. In Figure 2.2 the complete workflow is clarified.

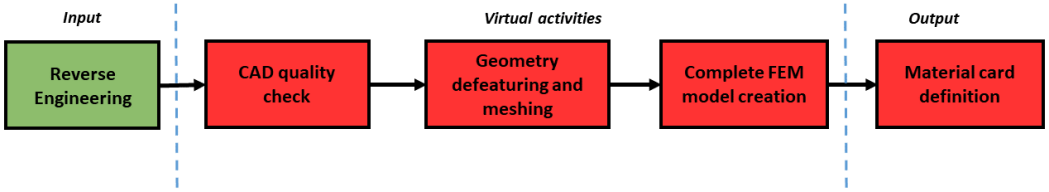

Figure 2.2 - FEM virtual model workflow

Firstly, the lower control arm CAD model has been created by a reverse engineering activity on the real component. Then, a detailed procedure on the FE model creation has been described, especially for stiffness, special and misuse events simulations on the baseline arm. Finally, the results obtained in terms of stiffness and stress distribution have been discussed in order to define the mechanical target for the hybrid lower control arm.

2.1. Reference vehicle

The analysis of the vehicle sales data has revealed the constant growth of the C-segment cars since 2014 [22]. In 2017, the 30% of the car in Italy belong to the C-segment that includes hatchbacks, sedans small SUV/crossover. As results, for the purpose of this thesis, the vehicle reference chosen is the Fiat 500X (MY 2014), which is the bestseller crossover in Italy [50]. This car model has a Front Wheel Drive (FWD) powertrain system and is equipped on the front with MacPherson suspensions. In Figure 2.3 is illustrated a Fiat 500X model.

Figure 2.3 – Fiat 500X

As concerns the 500X lower control arm, in Figure 2.4 are depicted a couple of front left original LCA (also defined *baseline*) that have been used for this research activity.

Figure 2.4 – Fiat 500X lower control arms

The LCA is manufactured with a single sheet metal stamped of about 4 mm, made of micro-alloyed steel S420MC (FEE 420). The mass of the complete assembly is about 3,45 kg which becomes 2,16 kg without lower ball joint and bushing as illustrates in Figure 2.5. In Figure 2.6, are reported the overall dimension of the baseline swinging arm.

Figure 2.5 – LCA total mass (left) and without bushings and lower ball joint (right)

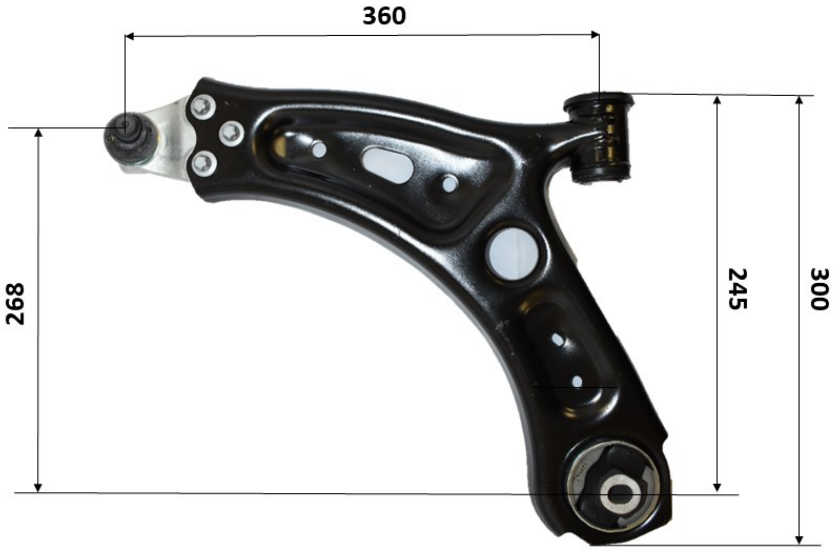

Figure 2.6 – LCA dimensions [mm]

The main information of the reference model vehicle studied have been obtained from official FCA website [51] and they are described in Table 2.1.

Specification	Unit	Value
Standard-A mass (Kerb weight + 75 kg driver + 10 kg luggage)	[kg]	1405
Kerb mass	[kg]	1320
Gross Vehicle Mass (GVM)	[kg]	2430
Misuse mass (70% of GVM)	[kg]	1870
Maximum velocity	[km/h]	190
Wheel base	[mm]	2570
Track	[mm]	1545
Wheel size	[-]	215/60 R16
Steering Diameter	[m]	11
Transmission system	[-]	MT
1st gear	[-]	4.154
2nd gear	[-]	2.118
3rd gear	[-]	1.361
4th gear	[-]	0.978
5th gear	[-]	0.756
6th gear	[-]	0.622
Final drive	[-]	3.833
Weight distribution ratio	[front/rear]	60/40
Driveline	[-]	Front Wheel Drive
Front/rear suspensions system	[-]	MacPherson
Engine	[-]	1600 cm^3, Diesel, 120 Hp

Table 2.1 – Fiat 500X technical data

2.2. Vehicle load case configurations

As discussed in Chapter 1, the definition of the load conditions on a lower control arm is a complex task. The forces acting on a LCA have various intensities and directions and are difficult to estimate only by analytical equations. Several variables have to be consider to get an assessment of load applied, such as the wheel travel, the vehicle speed or the tire contact patch.

The first step consists in the definition of a maneuvers set to define the load cases for the structural performance evaluation. Several papers [41, 52-55] have considered many different load conditions that can be summarized in three main categories:

- *Permanent deformation* cases that are all those situation in which the control arm could overcome yield condition, such as pothole, front bumper impact;
- *Lateral and longitudinal load*, mainly used to define stiffness arm characteristics;
- *Durability* load cases that are the standard working LCA condition such as braking, cornering and acceleration.

Therefore, considering the purpose of this thesis, two macro load cases configuration have been defined in order to cover the above-mentioned working condition. In particular, it has been identified three maneuvers called as “special events” and other three maneuvers called “misuse events” with the intent to satisfy as much as possible the real conditions.

Special events are those situations in which the arm has to assure its working in the elastic range. In this category has been included a part of the durability load cases:

1. Curve with a constant radius to the grip limit (also called skid-pad);
2. Maximum acceleration;
3. Maximum braking.

On the contrary, *misuse events* are those situations where the arm can exceed the material elastic limit without breaking showing a permanent deformation. They consist of:

1. Driving on a crossbeam;
2. Driving on a hump;
3. Driving on a drain.

2.3. Multibody model on ADAMS/Car

As mentioned before, the MBD model has been created in MSC ADAMS/Car using a customized template specially developed for this application. Different

phases have been studied to define firstly the behavior of the front and the rear suspension, secondly the global vehicle dynamics response of the car. These steps are:

1. Definition of the suspensions hard points;
2. Suspension system components modeling;
3. Full vehicle assembly;
4. Load cases modeling and forces estimation.

The most of the information necessary to define the multibody model of the Fiat 500X are obviously covered by industrial secrecy. Due to the lack of certain technical information, some assumption have been considered according to the background and knowledge of the IEHV research group in vehicle dynamics. In particular:

1. *Hard points*: has been obtained from a reverse engineering activity on the vehicle;
2. *Elasto-Kinematic components*: values from benchmark database [56];
3. *Center of gravity (COG)*: extracted from mass repartition, and assumed to be 530 mm from the ground at 1028 mm from front wheel center;
4. *Unsprung mass*: assumed 40 kg for each wheel;
5. *Tire properties*: normal performance city car tire (Pacejka model).

2.3.1. Front McPherson suspension modelling

At the beginning, the front suspension model has been created modifying a standard McPherson suspension template to adapt the front wheel drive (FWD) powertrain as shown in Figure 2.7. The front suspension model includes the main assembly components such as knuckle bracket, McPherson strut, mounting points on the body, braking caliper mounts and lower control arm. The lower control arm is mounted on the sub-frame with its two bushings on the front and on the rear. In this case, the sub-frame has been modelled as rigid frame with mounting point to car body. The LCA is also connected with the knuckle bracket with a rigid lower ball joint to ensure the free rotational movement during suspension travel and steering maneuver.

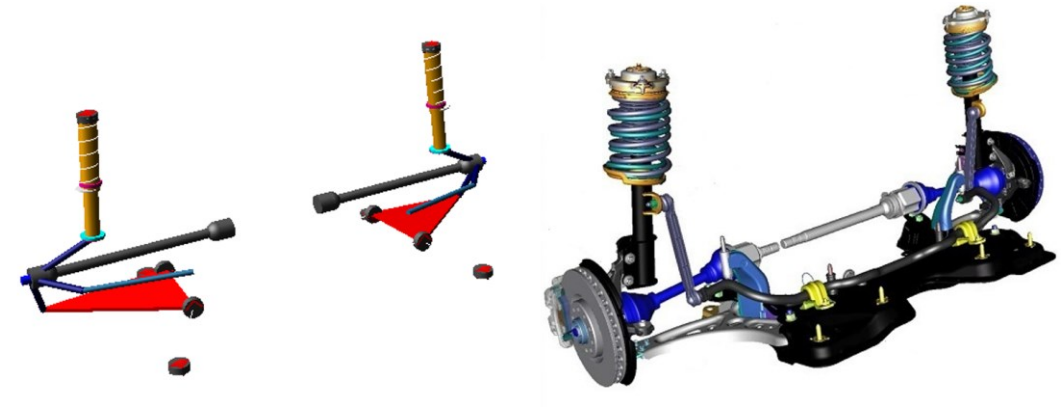

Figure 2.7 Front McPherson suspension with powertrain modification

The stiffness of the bushing represent a key factor in vehicle dynamics because they change completely the lateral stiffness and the dynamic performance. Hence, to make the model closer to reality, it has been taken into account database values [56] carried out from similar vehicle and reported in Table 2.2.

Bushing	Direction	Stiffness [N/mm]
LCA front bushing	X	8020
	Y	8020
LCA rear bushing	X	983
	Y	329

Table 2.2 – Front bushing stiffness values

The coil spring has been created starting from database values of similar vehicle [56] and modified with respect to suitable natural frequency around 1,4-1,5 Hz, according to the common practice for passenger's comfort [24]. The spring stiffness is calculated with the formula [57]:

$$K_s = 4\pi^2 f_r^2 m_{sqm} MR^2 \tag{2.1}$$

Where:

- K_s is the spring rate in N/m;
- f_r is the ride frequency (1,4-1,5Hz);
- m_{sqm} is the quarter sprung mass of the suspension;

MR is the motion ratio of the coil spring, that is wheel travel on spring travel: for MacPherson suspension, this value is normally bigger than 1. In this case MR is equal to 1,05. In the end, the front spring stiffness is equal to 45 N/m.

Damper characteristic curves are very hard to get since a long and intensive experiment should be performed. The damper curves have been created respecting database values [56], as shown in Figure 2.8.

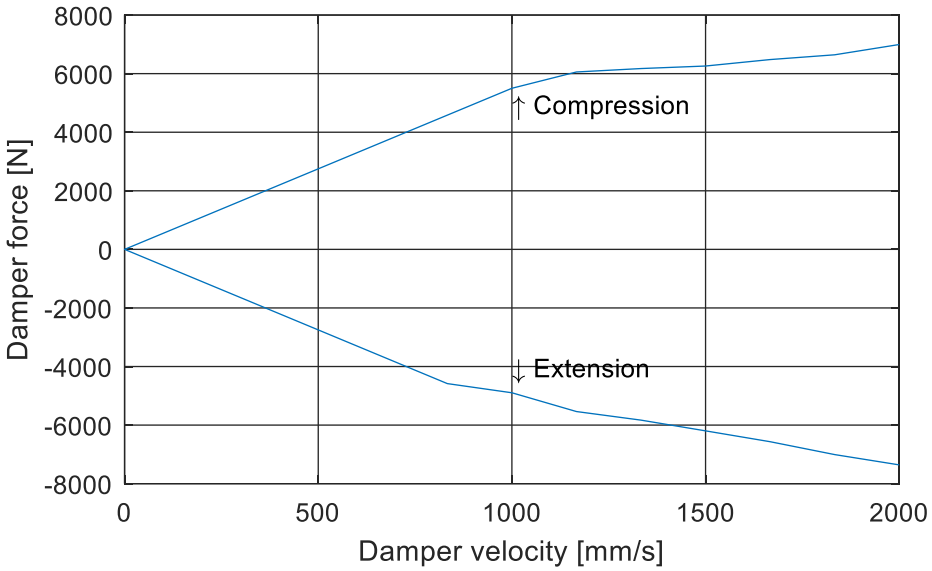

Figure 2.8 – Dampers characteristic curves

2.3.2. Rear McPherson suspension modelling

The rear suspension of Fiat 500X is not the conventional MacPherson suspension. It has the McPherson strut, which constrains the lateral movement of the wheel but with two separated transversal links control the toe and the camber variation, and another longitudinal link constrains the longitudinal movement of the wheel. This kind of suspension and it is illustrated in Figure 2.9. Because the lower control arm is mounted just on the front, the influence of the rear suspension system on the force estimation is considered negligible. Therefore, the value concerning the bushings and the dampers are used by default with the exception of the springs stiffness that have been fixed at 35 N/m due to the vehicle mass repartition.

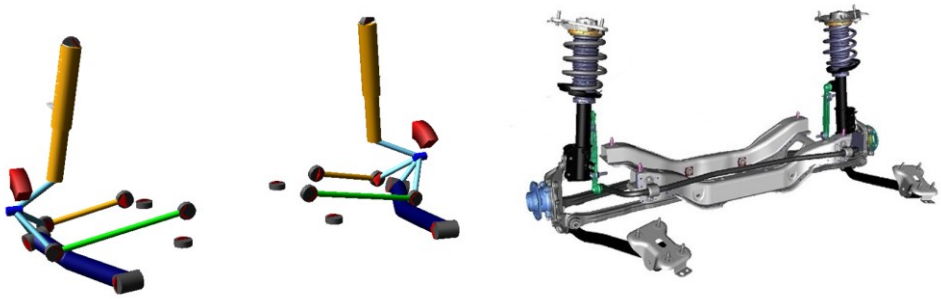

Figure 2.9 - Rear McPherson suspension with powertrain modification

2.4. Full vehicle assembly and simulation

As shown in Figure 2.10, the full vehicle assembly has equipped with front and rear antiroll bar, the front-wheel-drive semi-axis and steering system. The engine graphical presentation is hidden to have a clear view of the suspension system.

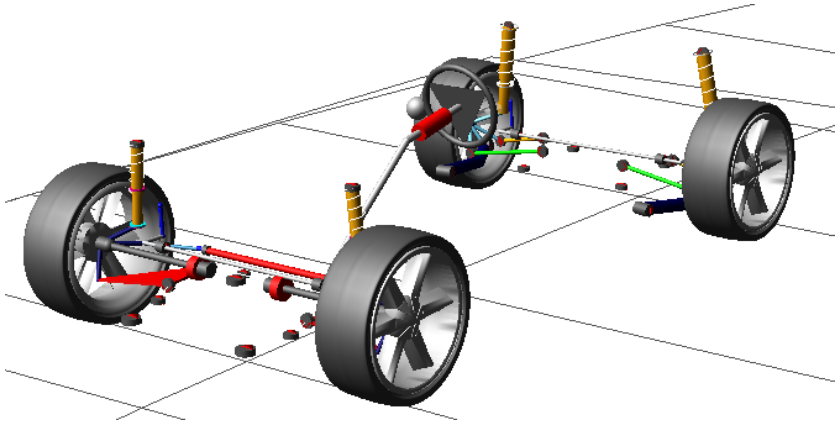

Figure 2.10 - Full vehicle assembly in ADAMS/Car

To understand the most critical working condition of the LCA, the set of simulations reported in Table 2.3 has been performed:

Maneuver	Aim	Model Input	Typology	Vehicle configuration
Skid-pad test	Lateral Force	Constant radius cornering 40 m	Quasi-steady state simulation	Standard A (1405 kg)
Maximum acceleration test	Longitudinal Force	Full throttle	Dynamic simulation	Standard A (1405 kg)
Maximum braking test	Longitudinal Force	Full braking	Dynamic simulation	Standard A (1405 kg)
Crossbeam test	Lateral Force + Longitudinal Force	70 km/h constant speed	Dynamic simulation	70% of GVM (1870 kg)
Hump test	Lateral Force + Longitudinal Force	70 km/h constant speed	Dynamic simulation	70% of GVM (1870 kg)
Drain test	Lateral Force + Longitudinal Force	70 km/h constant speed	Dynamic simulation	70% of GVM (1870 kg)

Table 2.3 – Set of multibody simulations for LCA forces estimation

Therefore, the output forces carried out from the multibody model simulations set have been used as input for respective FEM simulations. In order to define a common reference system between the MBD and the FE model, the output forces carried out from the ADAMS/Car simulation have been calculated according to the lower ball joint system (in green) as shown in Figure 2.11. In this way, the longitudinal force is parallel to the virtual axis connecting the front/rear bushing, while the lateral force lays on the LCA surface and it is perpendicular to the front/rear bushing axis. As consequence, the vertical force is perpendicular to the LCA surface.

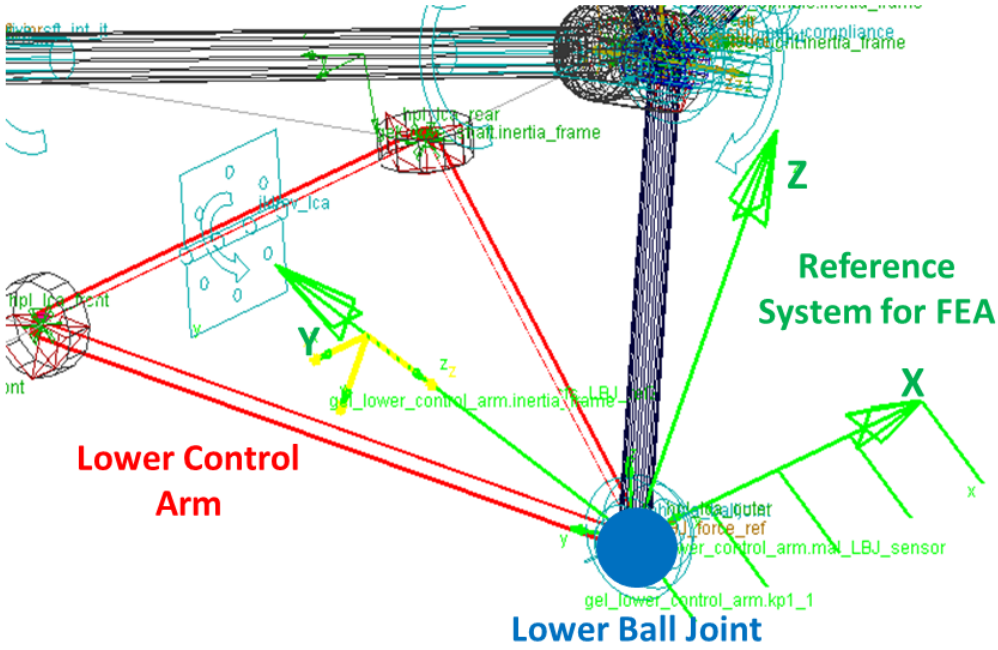

Figure 2.11 - LBJ force orientation for FE calculations

Because the lower control arm in a MacPherson suspension works mainly in XY plane, only lateral and longitudinal forces have been taken into account for all the maneuvers because the structural shock absorber opposes on the vertical loads.

2.4.1. Skid-pad test

The skid-pad test is a quasi-steady-state test with closed-loop controlled steering event. The acceleration should be slow enough to avoid dynamic behavior. The simulation has been performed with a given acceleration range from 0.1g to 1g on lateral direction and the steering radius is 40 m (Figure 2.12).

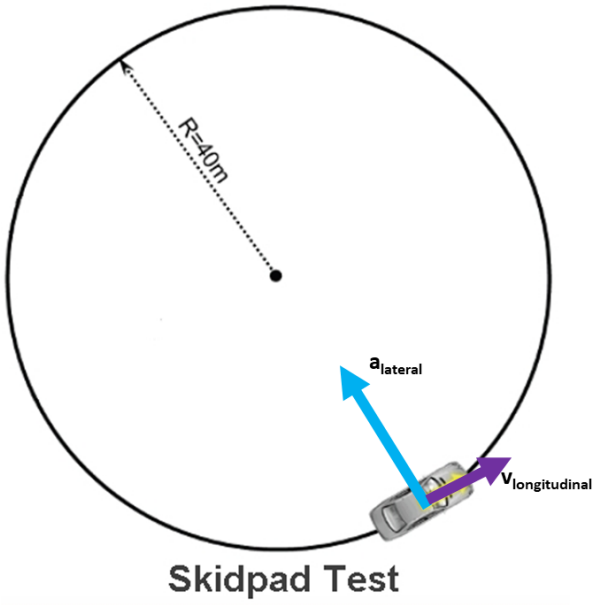

Figure 2.12 – Skid-pad test configuration

Figure 2.13 illustrates the evolution along the time of the LBJ forces and acceleration. In particular, the lateral acceleration is referred to the CG of the vehicle. The car can reach as high as 0,95g lateral acceleration before sliding, so the output forces have been calculated in that moment (vertical dashed line). In Table 2.4 are reported the output values sampled on the lower control arm that has been used as input forces for the FEM model simulation.

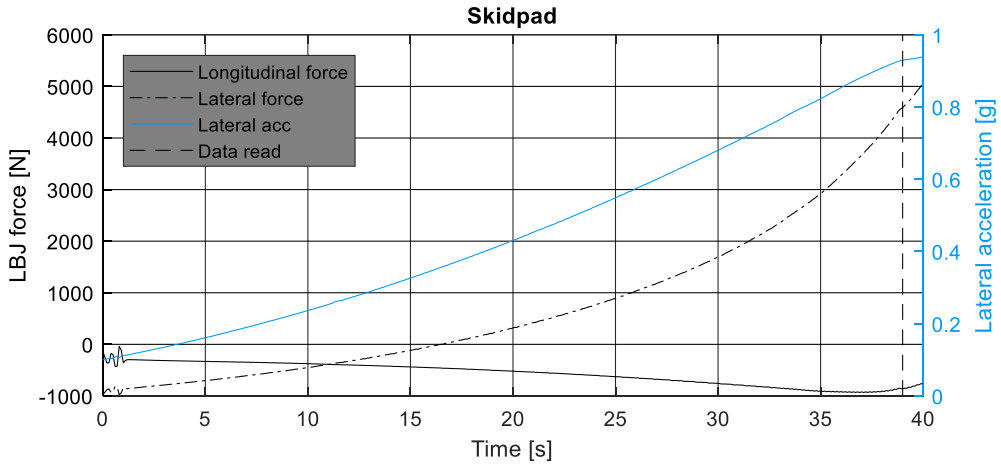

Figure 2.13 - Skid-pad test simulation results

Longitudinal force [kN]	Lateral force [kN]
-0,76	5,05

Table 2.4 – Input force for skid-pad FEM simulation

2.4.2. Maximum acceleration test

The maximum acceleration test means to determine the maximum force along longitudinal direction. When a car is accelerating, the mass tends to shift to the rear axis and this cause a vertical load reduction on the front axis.

For a front-wheel-drive car such as the Fiat 500X studied, the maximum acceleration is lower than the all-wheel-drive (AWD) version, since only the two front wheel are working to accelerate the car.

Therefore, the maximum value of longitudinal acceleration the car can reach is about 0,5g (referred to the CG of the vehicle) as shown in Figure 2.14. From the force/acceleration diagram of the lower ball joint, the outputs have been sampled at the peak of the longitudinal force (vertical dashed line). The subsequent oscillations represent the gear shifting. In Table 2.5 are reported the output values sampled on the lower control arm that has been used as input forces for the FEM model simulation.

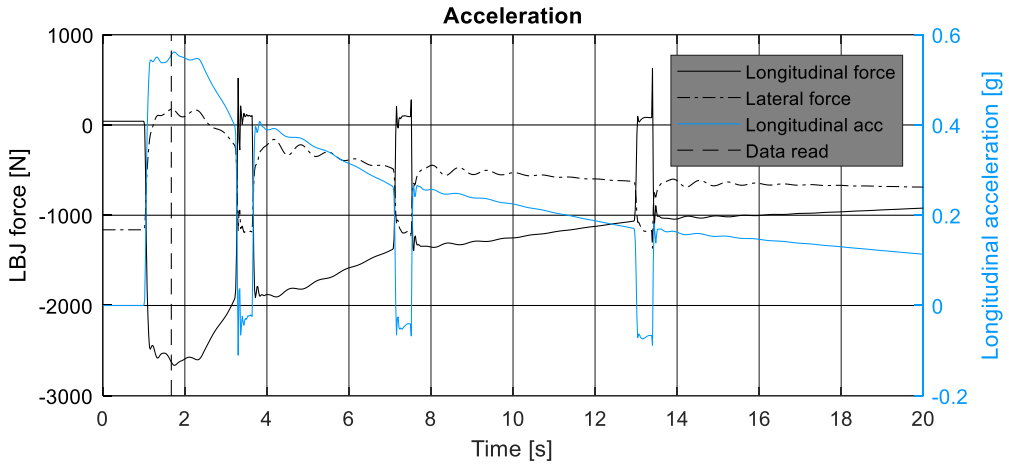

Figure 2.14 – Maximum acceleration simulation results

Longitudinal force [kN]	Lateral force [kN]
-2,66	0,17

Table 2.5 – Input force for maximum acceleration FEM simulation

2.4.3. Maximum braking test

The full braking deceleration can be as high as 1,1g to 1,2g according to the ground condition. Not like accelerating, the braking force is applied to all four wheels through the brake caliper pressure.

When a car is very heavy and it has a relative high CG, the weight will shift to the front axis and, even in some case, to lift the rear axis. This situation can be very dangerous because the car can loss control.

A more reasonable way to test the braking load is to consider a closed-loop constant deceleration. For these reasons, the lateral and longitudinal loads have been found out after the first gear shifting as highlighted in Figure 2.15 by the vertical dashed line.

The maximum deceleration value of 0,7g reached by the car can be consider a very good trade-off as the ground is never ideal and normal tires performance are usually compromised for non-perfect surface contact. Even in this case, the longitudinal acceleration is referred to the vehicle CG. In Table 2.6 are reported the output values sampled on the lower control arm that has been used as input forces for the FEM model simulation.

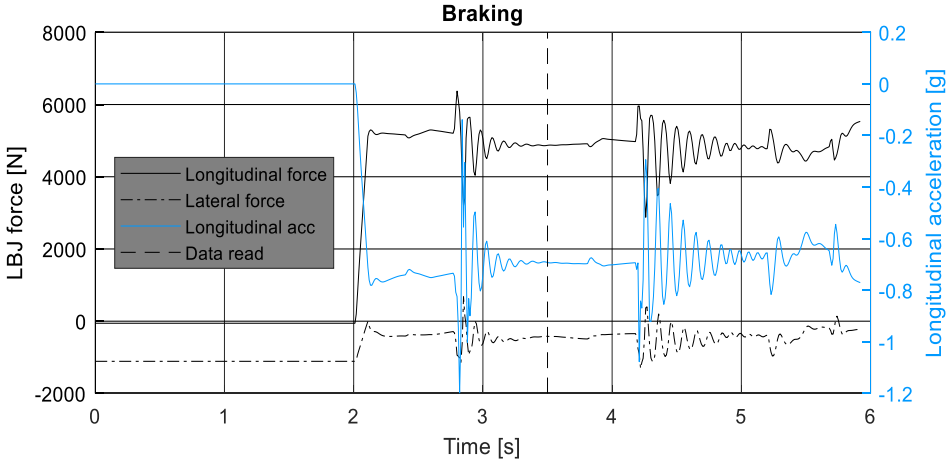

Figure 2.15 - Maximum braking simulation results

Longitudinal force [kN]	Lateral force [kN]
4,87	-0,42

Table 2.6 – Input force for maximum braking FEM simulation

2.4.4. Obstacle misuse test: Crossbeam

Misuse tests give loads under extreme conditions: in fact, the damage of the LCA is considered possible. The misuse is set-up with 70% of the gross vehicle mass (GVM) that is about 1870 kg with a velocity of 70 km/h. The obstacle is designed with the dimension of 70x100 mm as shown in Figure 2.16.

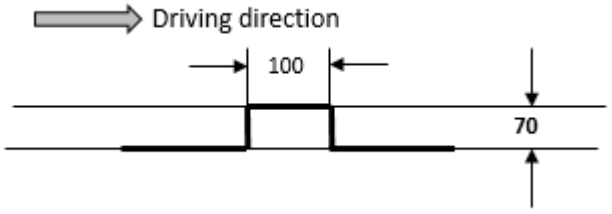

Figure 2.16 - Crossbeam obstacle design

Then the output requests sampled on the front LCA in terms of maximum force and acceleration on the LCA are reported in Figure 2.17. The maximum longitudinal and lateral forces have been carried out when the wheels are impacting the obstacle (vertical dashed line). The vertical acceleration is referred to the vehicle CG. Table 2.7 are reported the output values sampled on the lower control arm that has been used as input forces for the FEM model simulation.

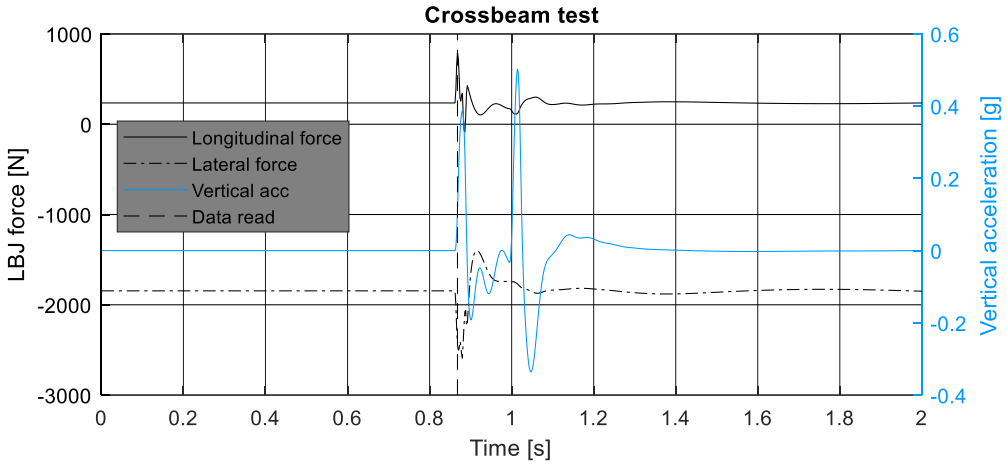

Figure 2.17 – Crossbeam simulation results

Longitudinal force [kN]	Lateral force [kN]
0,80	-2,60

Table 2.7 – Input values for FEM crossbeam simulation

2.4.5. Obstacle misuse test: Hump

The hump obstacle is designed with the dimension of 100 mm and the detail of dimensions are reported in Figure 2.18. This misuse test is performed with 70% of the gross vehicle mass (GVM) with a velocity of 70 km/h.

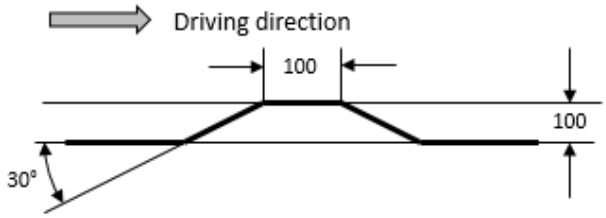

Figure 2.18 - Hump obstacle design

The output requests on the LCA in terms of maximum force and acceleration on the LCA are reported in Figure 2.19. As for the crossbeam test, the maximum

longitudinal and lateral forces have been carried out when the wheel is impacting the obstacle (vertical dashed line). The vertical acceleration is referred to the vehicle CG. In Table 2.8 are reported the output values sampled on the lower control arm that has been used as input forces for the FEM model simulation.

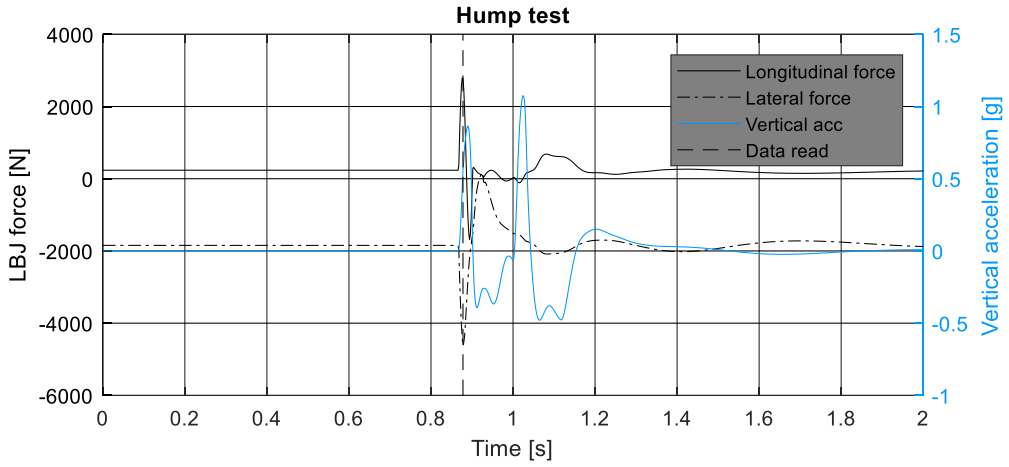

Figure 2.19 - Hump test simulation results

Longitudinal force [kN]	Lateral force [kN]
2,79	-4,62

Table 2.8 - Input values for FEM hump simulation

2.4.6. Obstacle misuse test: Drain

The drain obstacle begins with a negative slop of 10% of 1000 mm long, follows with 120 mm flat surface and end with 100 mm high at 30° inclination positive slop (Figure 2.20). This misuse test is performed with 70% of the gross vehicle mass (GVM) with a velocity of 70 km/h.

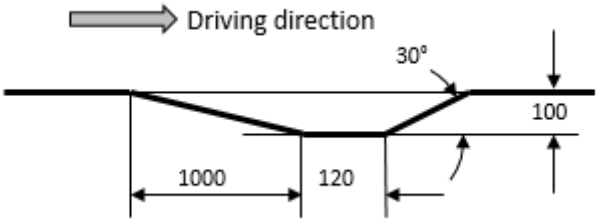

Figure 2.20 – Drain obstacle design

The output requests on the LCA in terms of maximum force and acceleration on the LCA are reported in Figure 2.21. In this case, the maximum longitudinal and lateral forces have been found out when the wheel is overcoming the obstacle, between the flat surface and the positive slope (vertical dashed line). The vertical acceleration is referred to the vehicle CG. In Table 2.9 are reported the output values

sampled on the lower control arm that has been used as input forces for the FEM model simulation.

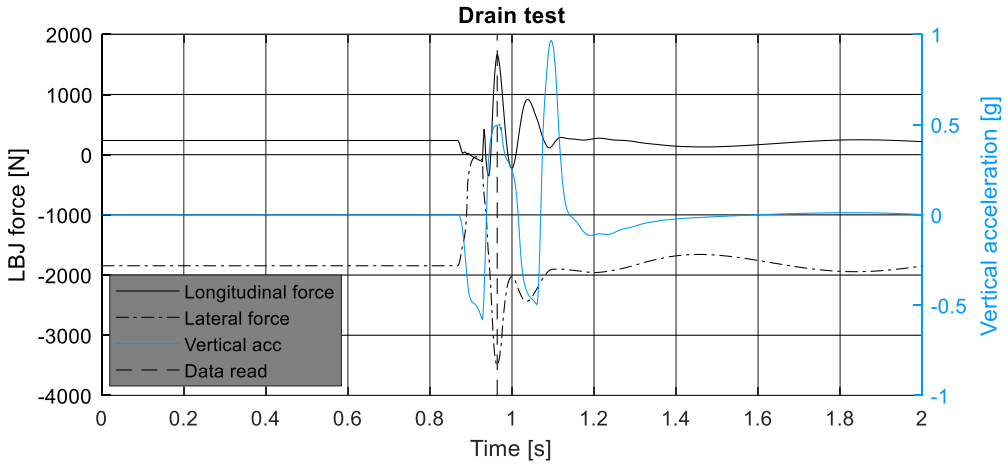

Figure 2.21 - Drain test simulation results

Longitudinal force [kN]	Lateral force [kN]
1,67	-3,5

Table 2.9 - Input values for FEM drain simulation

2.5. Final consideration on MBD simulations

In Table 2.10, the MDB test results are summarized considering the force acting in XY plane and their resultant defined according to the following relationship:

$$F_{tot} = \sqrt{F_x^2 + F_y^2} \tag{2.2}$$

Load Conditions	F_x [kN]	F_y [kN]	F_{tot} [kN]
SPECIAL EVENT SIMULATION FORCES			
Skid-Pad	-0,77	5,1	5,11
Max Acceleration	-2,66	0,17	2,66
Max Braking	4,87	-0,42	4,88
MISUSE EVENT SIMULATION FORCES			
Crossbeam	0,8	-2,6	2,72
Hump	2,79	-4,62	5,40
Drain	1,67	-3,5	3,87

Table 2.10 – Multibody simulation results summary

As shown the results, for special events, the lateral force F_y is greater than the longitudinal force F_x only when doing the skid-pad test, as the lateral acceleration

caused by cornering force. The longitudinal force are always greater for accelerating and braking test because the lateral force is only caused by the rotation of the LCA when weight is shifting on the longitudinal direction.

During the misuse event tests, the longitudinal force is always lower because impact force is not perfect on the longitudinal direction but point to the wheel center: the force is diverted to the vertical direction and sustained by the shock absorber and spring as shown in Figure 2.22. The vertical force (green arrow) tends to rotate the knuckle bracket counter-clock wisely, so the reaction force generated by the LBJ (light blue arrow) pointing to center of vehicle holds the knuckle bracket in position. Because action force on LCA has the same magnitude but opposite direction of the reaction force, the LBJ moves the LCA outward, which gives a negative force reading.

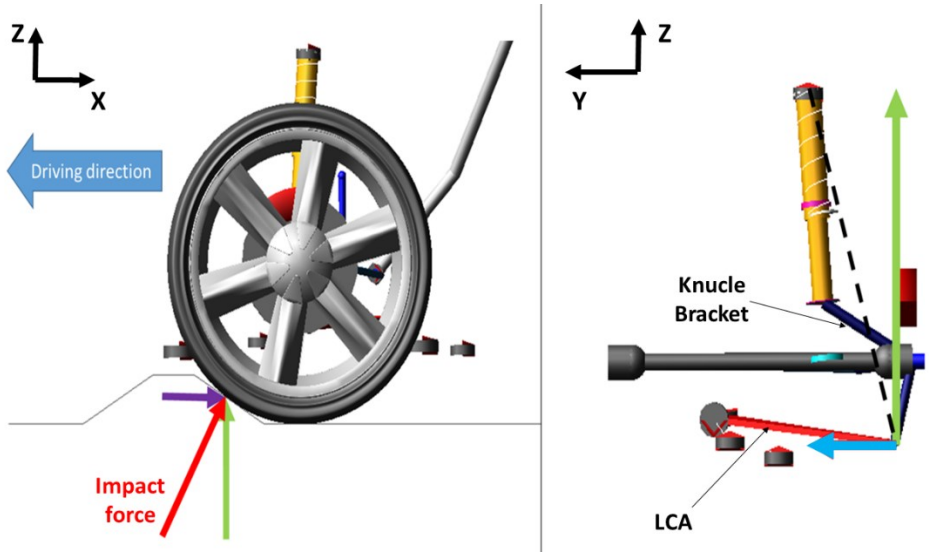

Figure 2.22 - Impact force for obstacle (left) and impact force on LBJ (right)

2.6. Lower control arm CAD file creation

In order to perform the CAD and the CAE activities, especially for FE analysis, it has been necessary to obtain a well-defined virtual geometry of the lower control arm. This represented a crucial step because the results of the analysis are affected by the quality of the component surfaces, as highlighted in [58]. Moreover, if the virtual surfaces are mismatched from the real one, several problem could happen during the manufacturing process. Unfortunately, for this thesis activity it was not possible to get the original CAD file of the LCA because it has been classified by the company as confidential. Therefore, a reverse engineering activity has been set in order to build the virtual geometry from a 3D scansion.

First of all, the original lower control arm has been scanned by using an anthropomorphous laser arm to digitize its surfaces as shown in Figure 2.23.

Figure 2.23 - Anthropomorphous laser arm

The scan output is a *.stl* file made of thousands triangles that are not connect each other. Thus, the respective surfaces are open and the file dimension is too huge to be affordable by standard workstation. As matter of fact, the geometry scanned has been used as reference model to build a lighter CAD file in which all the surfaces are closed and linked together as shown in Figure 2.24.

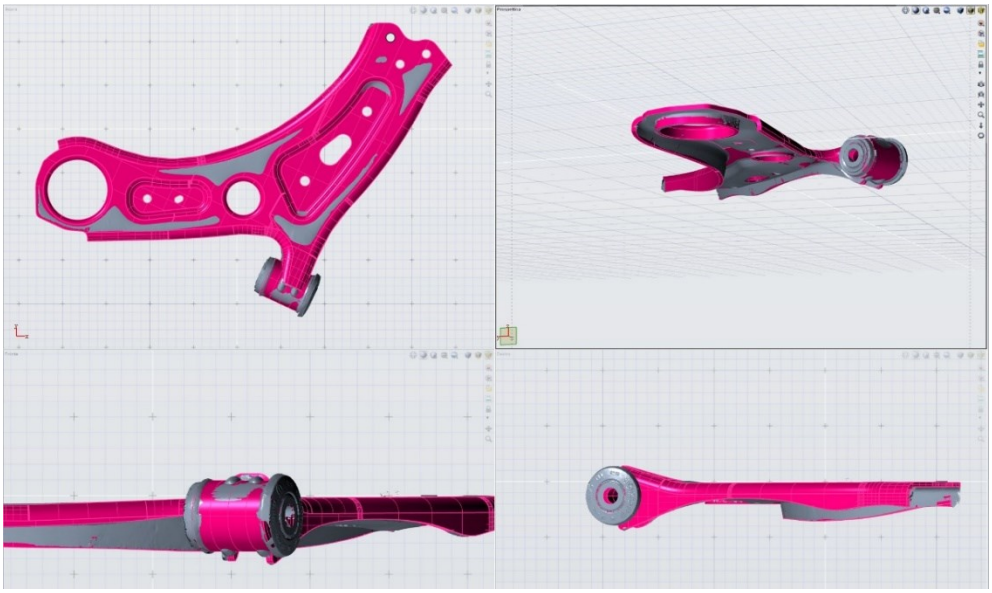

Figure 2.24 – Surfaces generation from *.stl* scan

The final format file obtained is a *PARASOLID* model part that is also fully compatible with the most popular post-processor softwares. In Figure 2.25 is illustrated the final render correspondent to the final CAD including the lower ball joint assembly.

Figure 2.25 – Render of final lower control arm CAD model

2.7. Finite element simulation set

The set of FE simulation has been carried out not only to complete the comparison analysis between the baseline and the hybrid LCA but also to individuate the tests that can be carried out for the experimental results correlation. By doing so, it's possible to validate a design procedure that could predict the structural and vibrational behavior of multi-material structure especially in terms of vibration reduction. Therefore, three specific analysis have been added to the special and the misuse event simulations:

- Stiffness analysis;
- Frequency Response Analysis (FRA);
- Strength analysis.

The stiffness analysis consists in the application of a unit force on the lower ball joint along the X and the Y axis of the vehicle to reproduce a condition of bending (X axis) and buckling (Y axis) load. In this way, it has been able to evaluate respectively the longitudinal and the lateral stiffness of the component. This simulation represents the starting point for the hybrid LCA optimization analysis. In fact, the results carried out from the baseline simulation have been used to define the stiffness target value for the hybrid component. Instead, as concerns the special and misuse simulations, they have been used to estimate the stress distribution during the defined working conditions.

The frequency response analysis and the strength analysis are the two simulations cases that have been correlated with the respective experimental tests. The frequency response analysis is necessary to evaluate the vibrational

characteristics in terms of resonance frequencies, damping and mode shapes. While the strength test is necessary to identify and compare the structural performance of the two types of lower control arms and to carry out their characteristic curves until a certain load value (further description have been reported in Chapter 7 as concerns the frequency response analysis and the strength analysis).

Although loads, mesh and boundary conditions remain the same for both baseline and hybrid model for all the comparison, two different solvers have been used for finite element analysis: Altair Optistruct for implicit linear simulation and Altair RADIOSS for non-linear explicit simulation. In Table 2.11 are summarized the simulation subdivision according to the solvers used.

Simulation	Type	Solver
Stiffness Analysis	Linear Implicit	Optistruct
Special/Misuse Events	Linear Implicit	Optistruct
Frequency Response Analysis	Linear Implicit	Optistruct
Optimization Analysis	Linear Implicit	Optistruct
Strength Analysis	Non-Linear Explicit	RADIOSS

Table 2.11 – Finite element simulation set

2.8. Optistruct FE model

At the beginning, the *PARASOLID* model of the lower control arm has been imported into the Altair Hypermesh environment. The CAD assembly is composed by the sheet metal of the swing arm, the front bushing and the lower ball joint as shown in Figure 2.26.

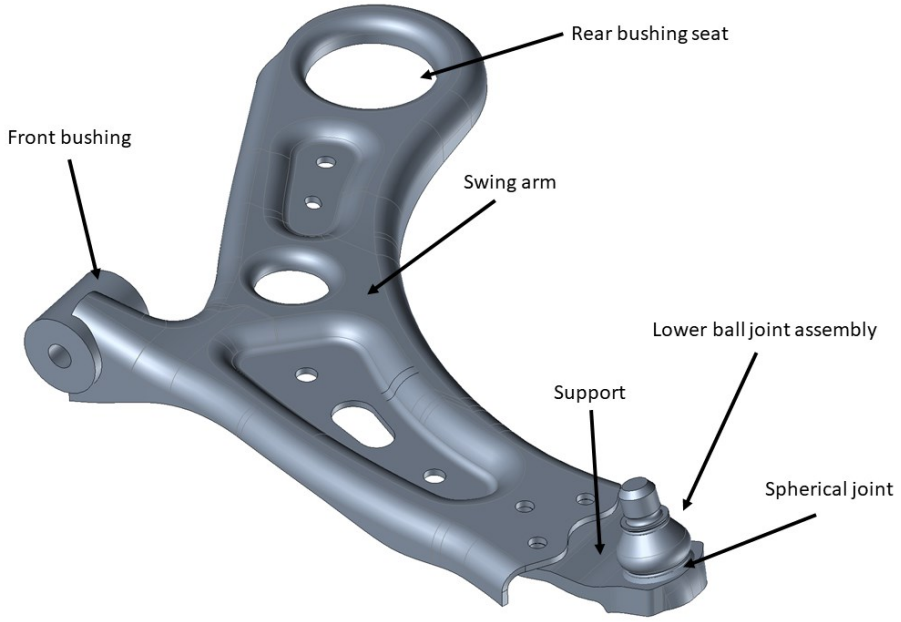

Figure 2.26 – CAD model assembly

The meshing strategy adopted consists in model with three-dimensional solid elements of the LBJ and the bushing housing, while the swing arm with bi-

dimensional shell elements. First of all, the mid-surface has been extracted from the solid geometry of the swing arm by using the *midsurface* tool. The extraction options have been optimized to get the best off-set geometry quality along planes and sweeps. Then, the surface obtained has been subdivided into different small patches, in order to guide and homogenize the mesh as shown in Figure 2.27.

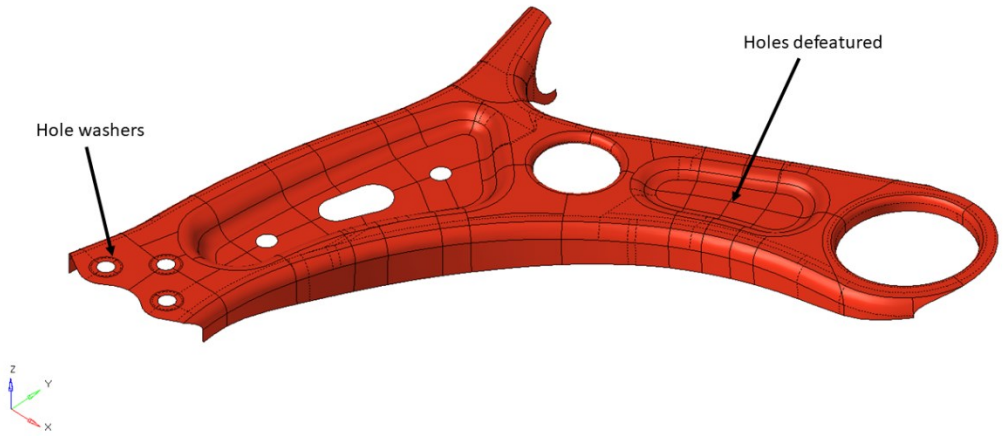

Figure 2.27 – Surface subdivision and defeaturing

Moreover the swing arm mid-surface has been edited to enhance more the quality of the mesh. In particular, two holes from the rear emboss has been defeatured because their diameters were under the nominal mesh size, avoiding possible discontinuity. Instead, on the front holes it has been created three washers to improve the final detail stress level and avoid unphysical spikes.

Thus, for the swing arm has been chosen CQUAD4 formulation for quadrangular shell elements and TRIA3 for triangular shell elements with an average size mesh of 4 mm. The element property chosen is the PHSELL with a constant thickness of 4 mm. In Figure 2.28 are illustrated the final meshed model.

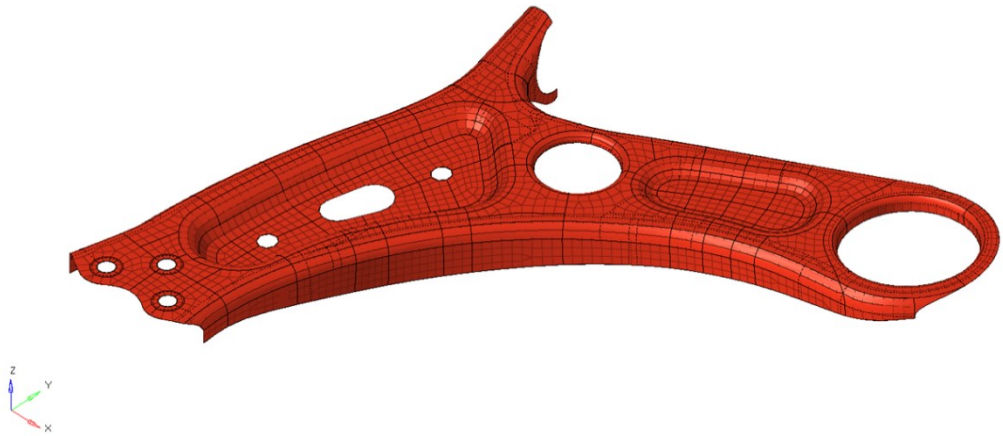

Figure 2.28 – Meshed model

As concerns the bushing housing, the solid geometry has been edited in order to distinguish the steel part from the rubber one, because in the CAD were not divided. Then, a 3D mesh has been created by using CHEXA elements according

to dimension of component as illustrated in Figure 2.29. In this case, it has been used a PSOLID card as element property.

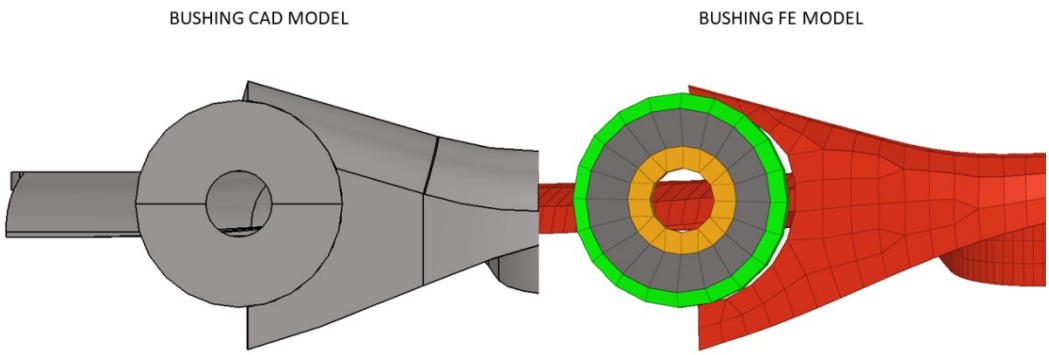

Figure 2.29 – Front bushing modellization

Finally, the bushing has been connected to the swing arm through four shell element strips to reproduce the welding lines, as shown in Figure 2.30. This solution avoids stiffness raising between the boundaries elements that can cause nonphysical stress peak, as could happen with the RBE2 links. The thickness given to the respective PSHELL card is equal to 6 mm.

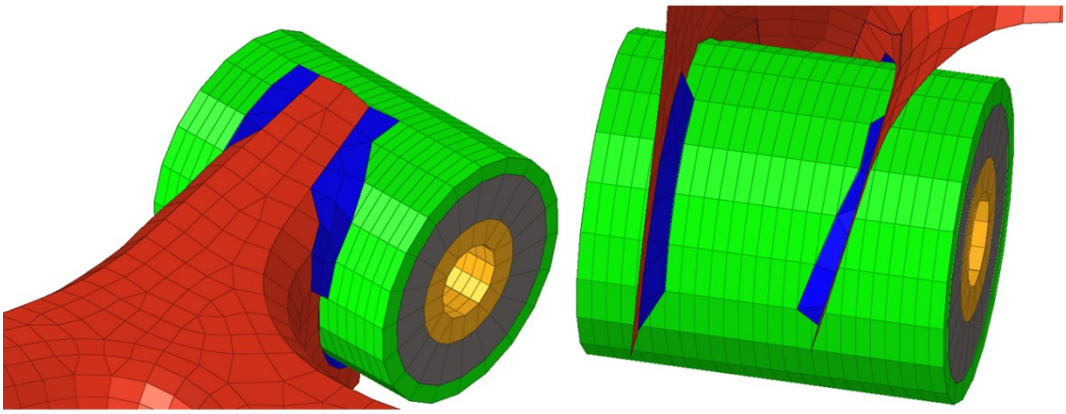

Figure 2.30 – Particular of welding lines on FE model

As regards the lower ball joint assembly, the spherical joint has been removed from the model because force passing through that are transmitted by a spider of rigid link (RBE2). In this case, due to the complex shape of the support, it has been meshed with a combination of pyramidal (CPYRA) and tetrahedral (CTETRA) elements as shown in Figure 2.31.

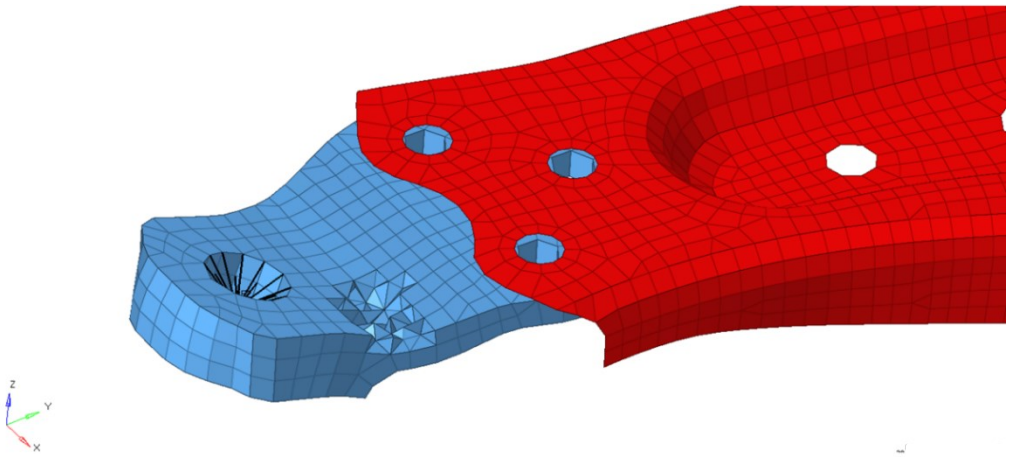

Figure 2.31 – Section of tetrahedral elements on LBJ support

The connection between the lower ball joint assembly and the swing arm has been guaranteed by a kinematic condition defined through a surface to surface contact (FREEZE) as highlighted in Figure 2.32.

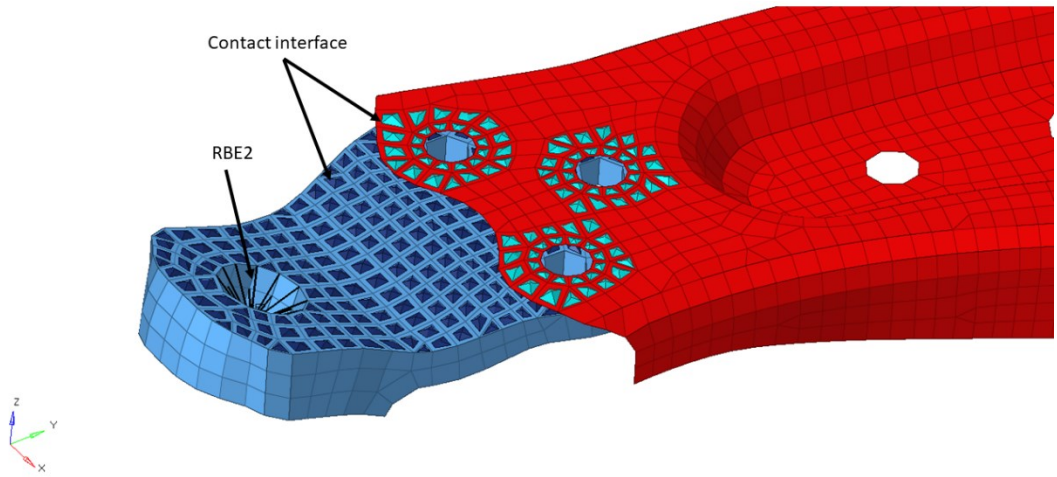

Figure 2.32 – Contact area between LBJ and LCA

As regards the material property, it has been used the MAT1 card that is an isotropic elastic material law. This card need only the value of the Young modulus E, the density ρ and the Poisson ratio ν defined. At the beginning, it has been used the nominal values of the S420MC [59] for all the steel components modelled. The material property values are reported in Table 2.12.

S420MC	Value
Density [kg/m^3]	7890
Young Modulus [GPa]	210
Poisson's Ratio	0,3
Yield Stress [MPa]	420
UTS [MPa]	550

Table 2.12 – Datasheet values for S420MC

2.9. Stiffness simulation on Baseline LCA

As explained in Section 2.7, the simulation for the stiffness analysis include two load steps that consist in the application of a unit load of 10 kN in longitudinal and lateral direction. These two cases are also called bending (longitudinal case) and buckling (lateral case) simulation due to the deformed shape caused by loads. In Figure 2.33 is reported the configuration adopted for the analysis. The numbers reported under the constraint icons represent the Degree Of Freedom (DOF) locked. In particular, translational DOF are numbered from 1 to 3 where 1 stands for X, 2 for Y and 3 for Z. Same situation is for the rotational DOF numbered from 4 to 6.

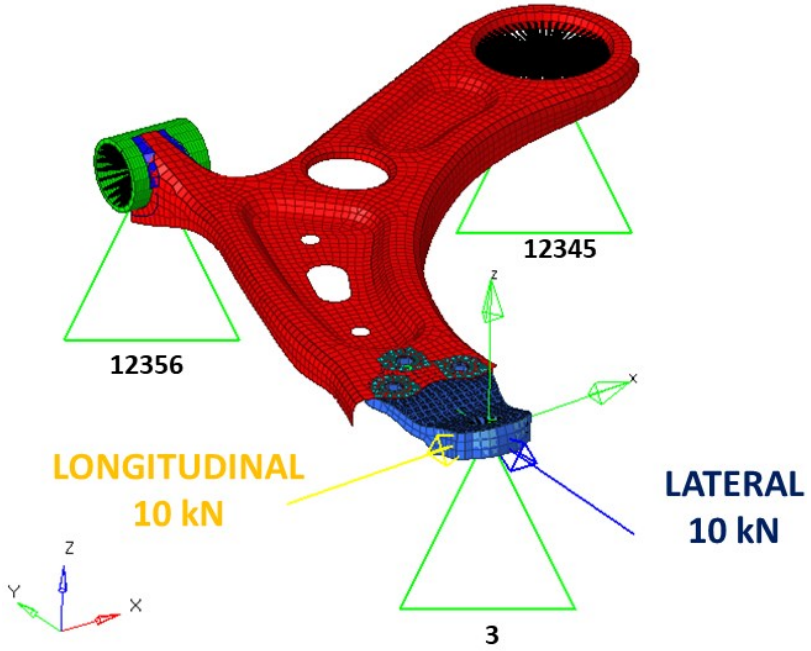

Figure 2.33 – Stiffness model configuration

The simulation has been set to maintain as much as possible the same vehicle configuration: however, some assumption have been done. In Figure 2.34 is shown the front bushing, where the inner rubber part has been substituted with a spider of RBE2 rigid elements.

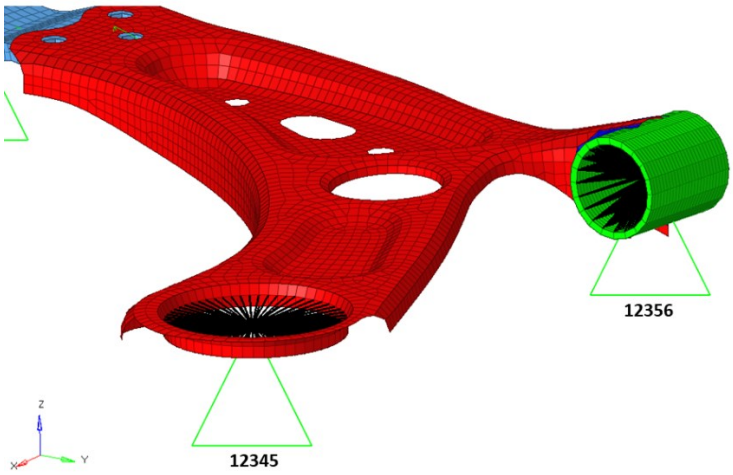

Figure 2.34 – Bushing constraints: numbers represent the DOF fixed

On this RBE2 master node has been applied a constraint that allow only the rotation in X axis. The same condition has been replicated on the rear bushing, where only the rotation in Z axis has been left free. By doing so, it has been avoided the bushing deformation that would had affected the stiffness of the swing arm. As concerns the lower ball joint, the RBE2 master node has been constrained in the Z translation in order to guarantee the displacement of the arm only on the XY plane and simulate the effect of the wheel. Moreover, the lower control arm has been inclined in the same manner as in the vehicle in order to be aligned to MBD model previously developed. In fact as shown in Figure 2.35, a reference system has been created with the origin on the LBJ master node and it is placed as the same as in the multi-body model: all the forces applied to the FE models are oriented according to that system.

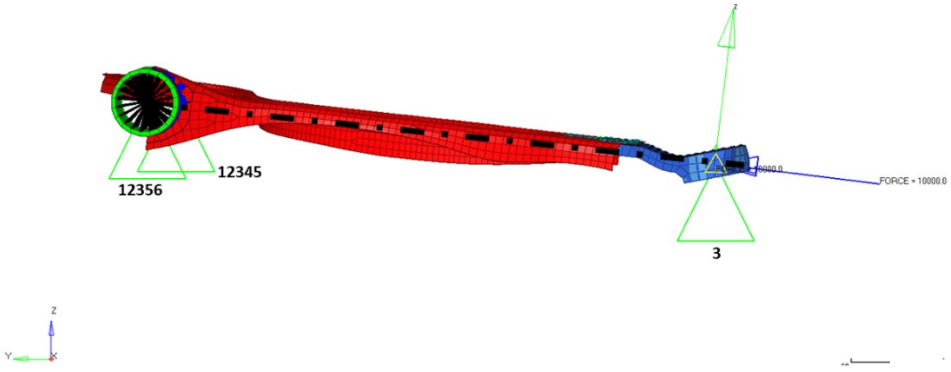

Figure 2.35 – LBJ reference system (green) oriented as in MBD model

2.10. Special and misuse event simulations on Baseline LCA

The model configuration of the stiffness analysis has been adopted also for the multibody load cases for what concerns constraints and arm position. The load conditions are still referred to the common reference system between FEM simulations and MDB. For the sake of clarity, in Table 2.13 are reported the resultant forces carried out from the multibody analysis in section 2.5.

Load Cases	F_{tot} [kN]
Skid Pad	5,11
Maximum Acceleration	2,66
Maximum Braking	4,88
Crossbeam	2,72
Drain	3,87
Hump	5,4

Table 2.13 - Resultant forces due to special and misuse events

In particular, for the special events the resultant forces are placed as displayed in Figure 2.36**,** where the skid-pad load is represented in blue, the braking in light blue and the acceleration in ocher.

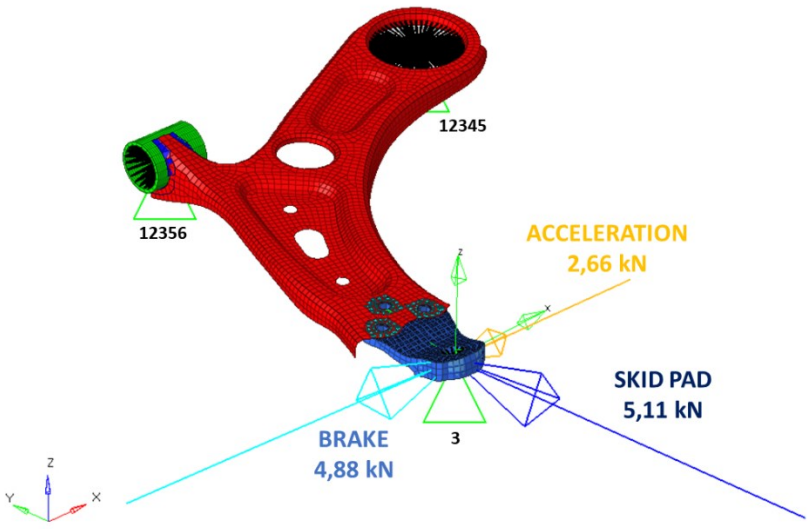

Figure 2.36 – Special events configuration

On the other hand, for the misuse events the resultant forces are placed as in Figure 2.37, where the crossbeam load is reported in magenta, the hump in bright red and the drain in dark red.

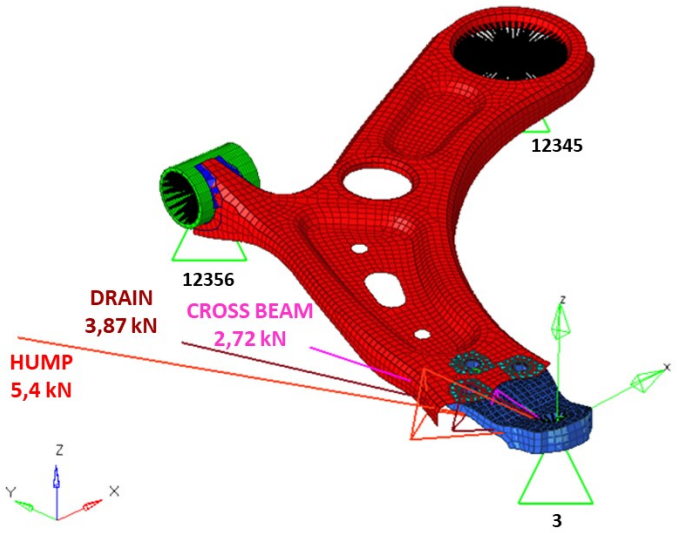

Figure 2.37 – Misuse events configuration

2.11. Simulation results on Baseline LCA

The post-processing analysis has been conducted on Altair Hyperview, in which is possible to carry out all the information necessary to evaluate stress and displacement. In the case of the stiffness analysis, the displacement has been sampled on the RBE2 master node of the lower ball joint. Hence, the lateral stiffness K_x has been calculated as:

$$K_x = \frac{F_x}{\Delta_x} \tag{2.3}$$

Where: F_x is the unit force applied on the X axis and Δ_x is the displacement of the master node.
While longitudinal stiffness K_y is:

$$K_y = \frac{F_y}{\Delta_y} \tag{2.4}$$

Where: F_y is the unit force applied on the Y axis and Δ_y is the displacement of the master node. The result obtained for the bending load step is show in Figure 2.38.

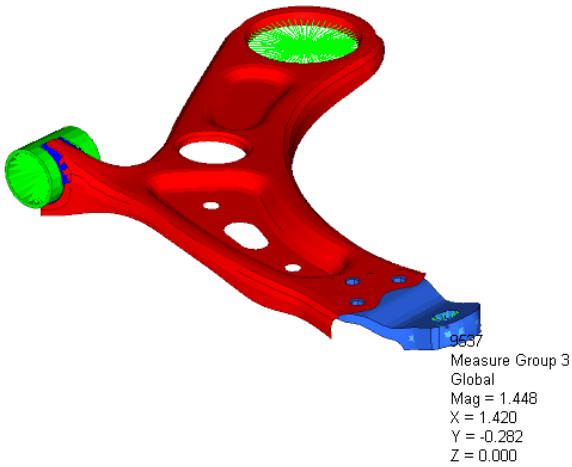

Figure 2.38 – Displacement for bending case

As displacement, it has been considered the resultant value between X and Y direction although the Y contribution could be consider negligible. Therefore, the final displacement is equal to 1,44 mm that means a longitudinal stiffness of 6,94 kN/mm.

The same consideration has been applied to the buckling load step, where the final displacement is equal to 0,37 mm that means a lateral stiffness of 27,2 kN/mm. In Figure 2.39 is shown the results.

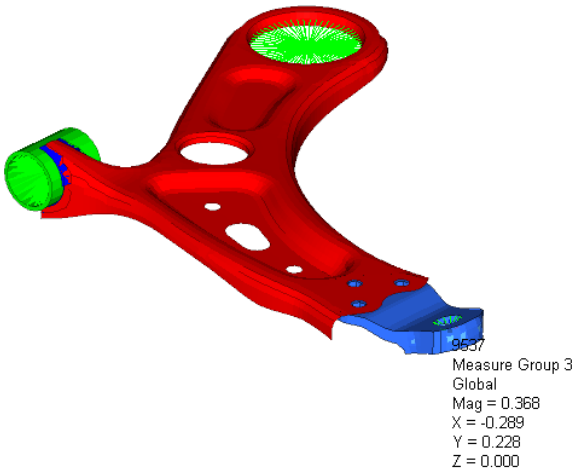

Figure 2.39 – Displacement for buckling case

Finally, in order to verify the condition of linearity that is fundamental to validate the simulation, a stress analysis has been done. Considering that all the material modelled are isotropic metals, the Von Mises criterion has been used to evaluate the equivalent stress values. In fact, as shown in Figure 2.40, the maximum value registered between the two simulations is about 354 MPa that is lower than 420 MPa that is the yield limit of the S420MC, so the linear behavior is guaranteed.

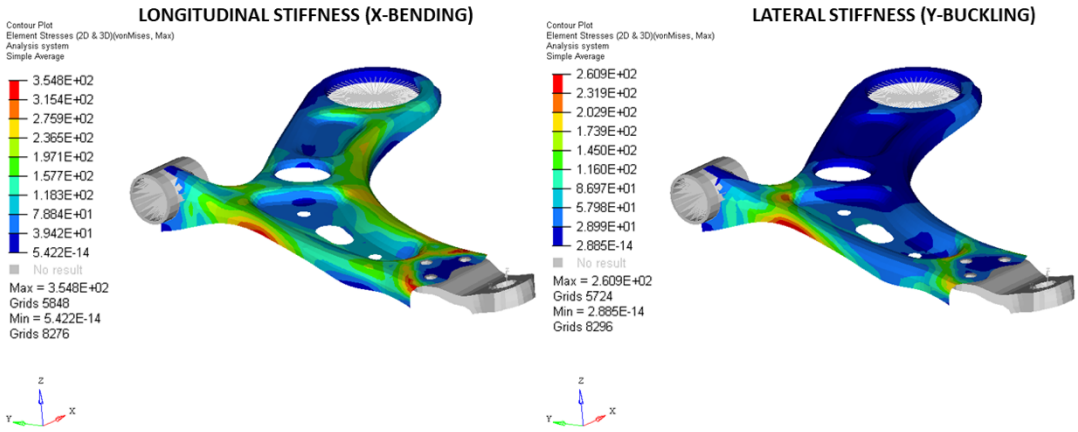

Figure 2.40 – Stress distributions (MPa) on stiffness simulations

As concerns the special events, in Figure 2.41 are reported the stress distribution for the relative load steps.

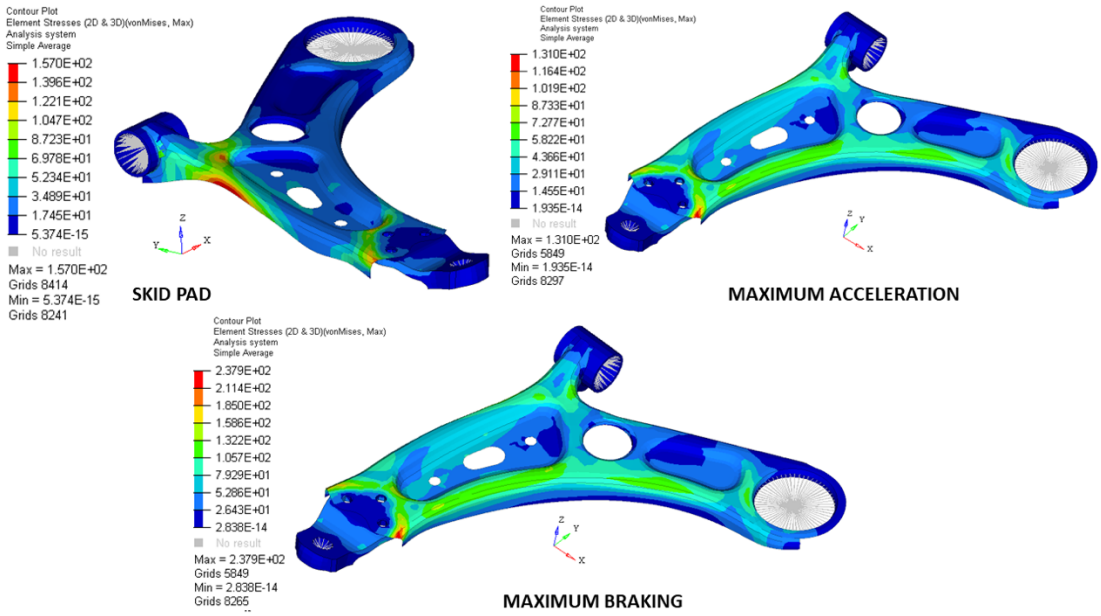

Figure 2.41 – Stress distribution (MPa) for special events simulations

The most critical cases are the two condition of acceleration and braking at grip limit, although the resultants loads applied are less than the skid pad one. This situation is due to the notably stiffness difference in longitudinal and lateral direction. In fact, the maximum Von Mises stress is reported for the braking case, which is about 238 MPa. The peak is located close to the lower ball joint support and it is due to the twisting condition caused by direction of the force and the inclination of the LBJ as shown in Figure 2.42: the red meshed geometry on the left represents the undeformed shape.

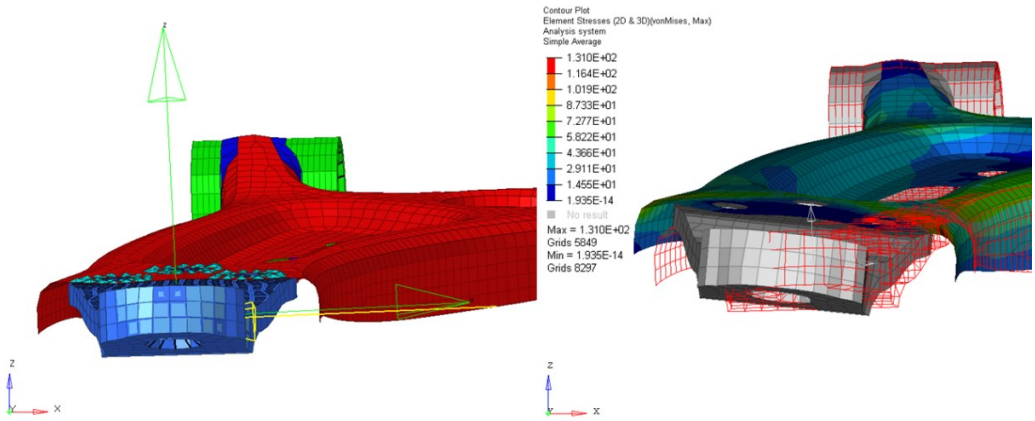

Figure 2.42 – Deformed shape caused by braking load

The same situation is reproduced in the condition of maximum acceleration as highlighted on Figure 2.43.

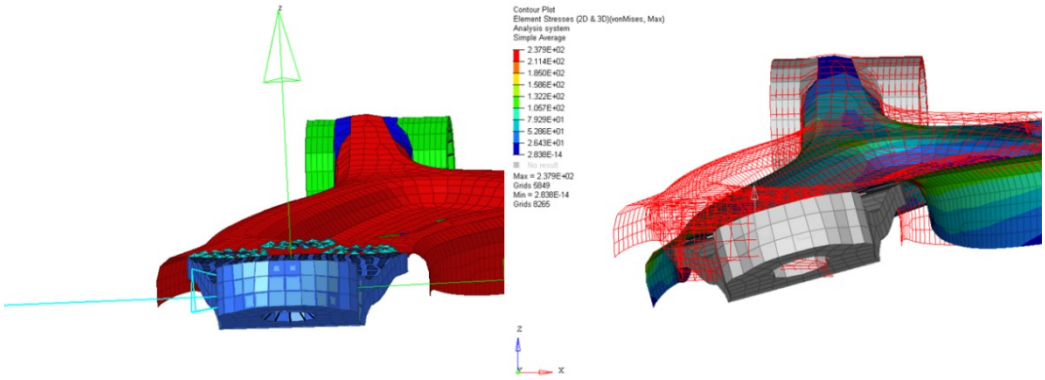

Figure 2.43 – Deformed shape caused by acceleration load

As regards the misuse simulation results, in Figure 2.44 is reported a general overview. The most critical case is the hump one in which the Von Mises stress is about 214 MPa. Even in this case, the stiffness plays an important role: the more is the load inclination from Y axis, the more is the stress level on the arm.

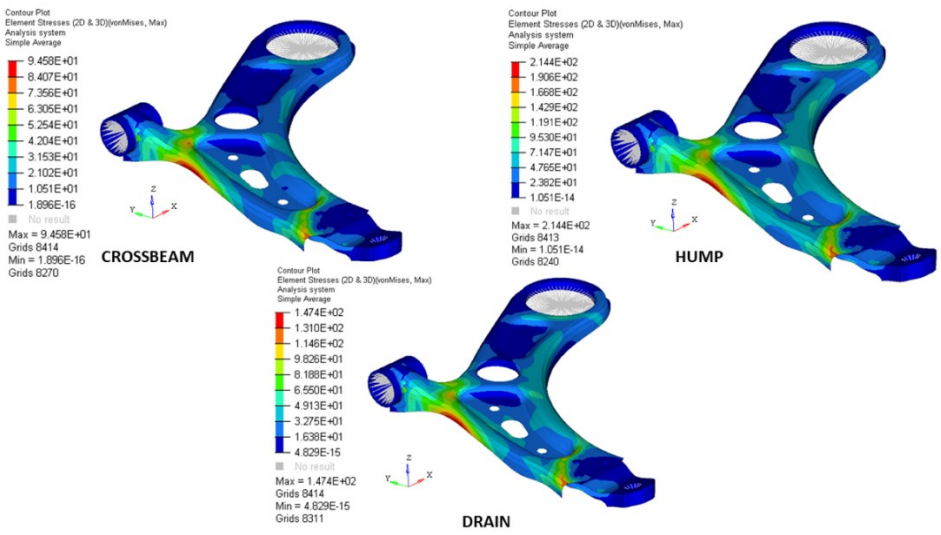

Figure 2.44 - Stress distribution for misuse events case

In conclusion, it has been verified that the baseline lower control arm remains always in elastic condition for all of the special and misuse simulation cases.

2.12. Target definition for Hybrid lower control arm

From the baseline results it has been carried out the reference performance for the hybrid lower control arm design. In Table 2.14 are reported a result summary of the baseline LCA.

	Mass [kg]	**K_x [kN/mm]**	**K_y [kN/mm]**	**Stress in special events [MPa] (Rp_{02}=420 MPa)**	**Stress in misuse events [MPa] (Rp_{02}=420 MPa)**
FEM BASELINE	2,16	6,94	27,2	238	214

Table 2.14 – Results summary for Baseline lower control arm

According to the research aim defined in section 1.7, from the mechanical point of view the scope of this thesis is to design a first prototype of a hybrid lower control arm whose main tasks are:

- Obtaining the minimum mass as possible guarantying the same longitudinal and lateral stiffness with a maximum difference of 10%;
- Satisfying the special and misuse events requirements in terms of stress distribution both for metal and composite materials;
- Improving the global damping effect than the conventional component to reduce vibration transmission to the chassis.

Chapter 3

Multi-material LCA concept

This chapter describes the steps followed to design the multi-material (or hybrid) lower control arm. Although the arm has been perceived as a unique prototype, a set of design constraints has been defined concerning the LCA geometry and mechanical coupling in order to be replaceable on the vehicle and compliant to standard manufacturing process.

An innovative technology to couple carbon fiber and steel has been used to face the problem of joining dissimilar materials and match the design targets. These particular viscoelastic materials consist in a calibrated rubber foil that works as passive constrained layer damper (PCLD) and adhesive simultaneously.

Hence, a hybrid design solution has been developed to satisfy the requirements of lightweight, vibration damping and safety. Moreover, the suspension packaging has been analysed and a maximum arm envelop has been identified as also the design volume for the structural optimization analysis. Finally, a description of the approach used to design the CFRP cover has been reported and the composite material screening has been discussed.

3.1. Design constraints and solutions

The ambitious target defined in Section 2.12, need to be treated carefully in order to match the best trade-off solution. Mass reduction objective is achievable by combining the right quantity of carbon fiber and steel. A clear issue of these composites is the bonding agents conventionally used that can cause a weakening of the component. Moreover, the lower control arm interfaces with three different mechanical components, which transfer high load from the tire to the chassis. Although the prototype has been though for a research activity, this thesis work has been conducted to develop a concept whose content is potentially industrialized. Therefore, the design constraints take into account the following points:

- Component geometry;

- Mechanical coupling to the chassis;
- Manufacturing technology feasible for prototype;
- Vehicle Packaging.

However, these constraints must also be compliant to the safety requirements of the swinging arm. The hybridization gives its advantages not only in terms of lightweight but also in terms of mechanical performance. In this context, it is possible to distinguish two main approaches. The first one is the so-called "Erlanger Beam", in which the high stiffness is achieved by reinforcing a thin-walled steel structure with short fiber reinforced plastic ribs by means of form closure. The second one constitutes a combination of steels and continuous FRP bonded tightly across a large area, to increase the overall strength of the components. This design allow manufacturers to produce safety-relevant vehicle components, such as body pillars, at lower costs compared to a mere CFRP design [6].

The presence of the steel makes up for the lack of ductility of the carbon fiber, avoiding unstable and catastrophic failures in case of impacts and increase the Specific Energy Absorption (SEA) [60] [61]. One of the main aspect of this project is to evaluate the structural contribution of carbon fiber maintaining the existing steel original shape.

The approach adopted is to reduce the thickness of the arm in order to overlay a carbon fiber laminate precisely tailored. The LCA bottom surface is connected to the LBJ, so the machined operation has to be conducted on the upper surface to avoid possible interference between laminate and LBJ. Therefore, the entire surface has been milled except for the areas in which are located the two bushings and the bolts, as shown in Figure 3.1**,** where the thickness has been left at 4 mm. As result, the local stiffness of the connected parts remains, at least, the same of the baseline configuration.

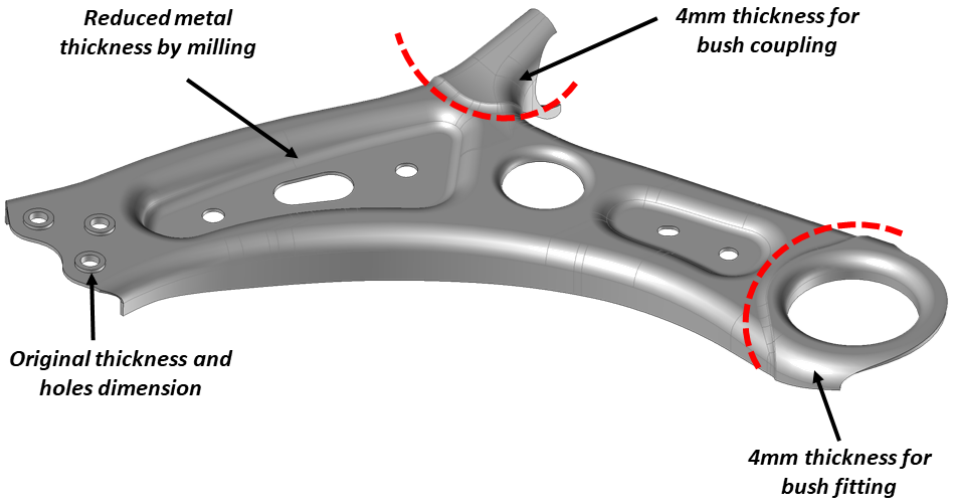

Figure 3.1 – Main modification on metal shape

Moreover, this condition allows the right mechanical coupling between the lower control arm and the bushings that is crucial to guarantee the connection with

the suspension sub-frame. In this way, the bushings fit perfectly in their original housing and the structure is not affected by any kind of damage during the maintenance operation. The thickness has been reduced from 4 mm to 2 mm in the remaining areas. This choice is due to a manufacturing limit avoiding possible distortion of the metal shape during the machining. By doing so, the thickness has been reduced of the 50% for more than the 80% of the LCA surface.

In the area close to the bushing seats, the thickness variation has been design to be progressive and smooth in order to reduce as much as possible stress concentration, as shown in Figure 3.2. In this way, wide fillet has been done to make a small overlap on the original metal thickness to gradually transfer stress and forces between CFRP structure and metal one.

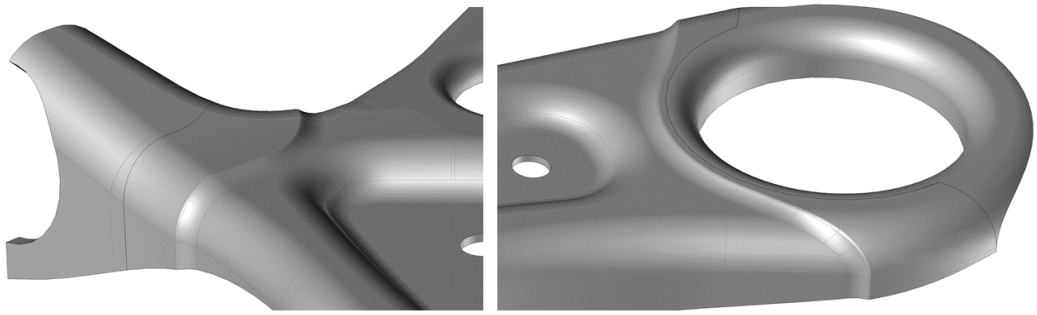

Figure 3.2 - Fillet details on bushings seats

As concerns the bolt connection between the arm and the lower ball joint, the holes have been left with their original dimensions in terms of diameters and thicknesses. Therefore, the direct contact between CFRP and bolts is avoided, as shown in Figure 3.3. The head of the screw and nuts lay on the metal surfaces and a calibrated spacer will fill the difference in thickness created by the CFRP cover.

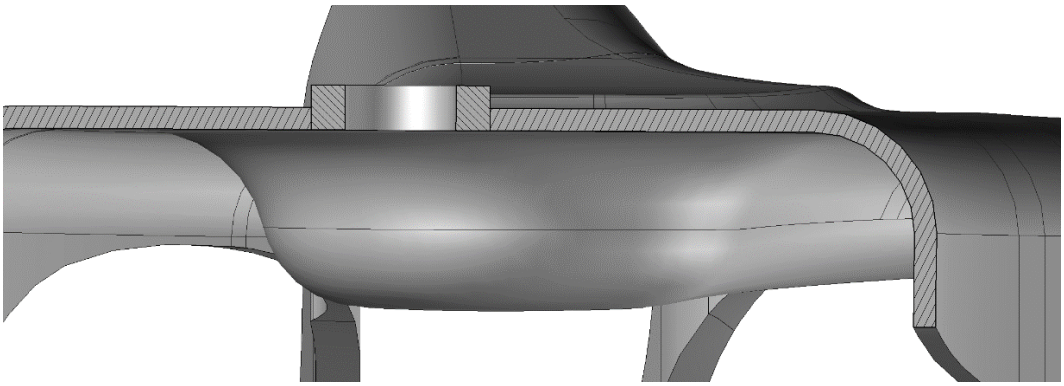

Figure 3.3 - Section detail on bolt connection

3.2. Innovative application

The major challenge in multi-material design consists in the joining of dissimilar material. Traditional technique such as clinching or riveting are not suitable for the lower control arm applications. Neither standard liquid adhesive are a viable solution for the following reasons:

- Complex geometry shape that make difficult glue distribution;
- Difficulty in control glue thickness variation, especially inside the embosses;
- Difficulty to find adhesive types that are compliant to pre-pregs autoclave curing cycles.

On the other hand, the direct contact between CFRP and steel represents the best solution from the mechanical performance point of view. Nevertheless, the NVH properties of the laminate could not improve considerably due to the very low damping properties of these two materials.

In this context, an innovative solution is given by Kraibon® viscoelastic materials, manufactured by Kraiburg GmbH. Kraibon® is a thin calibrate film made of non-cross-linked rubber that hardens within the component laminate in the same curing process. The important advantages are the direct integration of the elastomers in the normal manufacturing process and the direct connection without additional bonding agents. Moreover, the viscoelastic properties are set to improve NVH, impact and splintering behavior. In fact, as shown in Figure 3.4, the manufacturer declares that, even at low layer thicknesses, Kraibon® has a higher damping capacity than traditional aluminum-butyl, weighing 80% less.

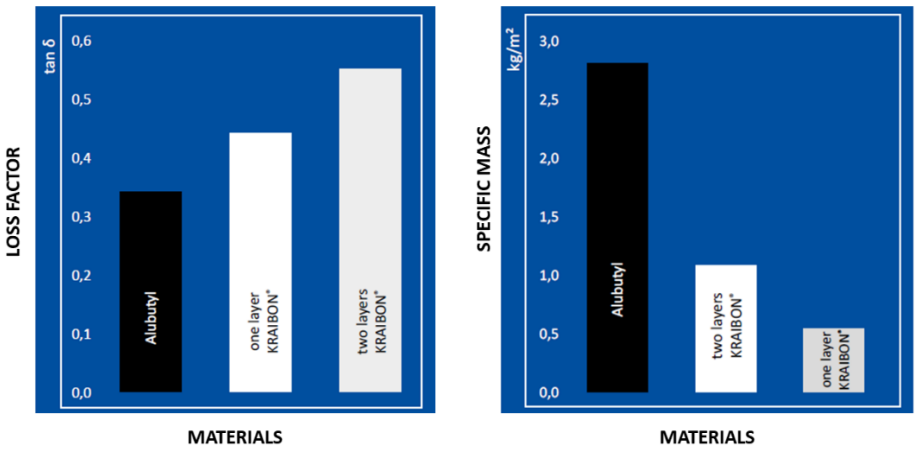

Figure 3.4 - Kraibon damping properties (left) and specific mass (right)

Several scientific works [62-64] confirmed the excellent vibro-acoustic properties of these VEMs especially applied on automotive component such as a CFRP car door and hybrid laminate [65].

The integration of Kraibon® enhances the damage tolerance capabilities of the laminate. During an impact, the first layer of CFRP absorbs the majority of the impact load and is consequently destroyed. Kraibon® elastomer are able to accommodate the occurring loads with relative independence for individual layers. Thus, multiple load-bearing layers exist, which in the event of impact simultaneously absorb the maximum occurring load. In addition, the elastomers

enter into an outstanding bond with the fiber composite material and prevents the shattered fragments from detaching as shown in the example reported in Figure 3.5.

Figure 3.5 – Formula student front nose CFRP crash

These results have also been validated in [66] [67], where Kraibon® materials have been used to improve energy absorption and reduce delamination.

As discussed in Section 3.1, in hybrid structure metal is combined directly with carbon using a bonding agent: so contact corrosion can occur. Kraibon® works also as an insulating layer between the two materials, which prevents corrosion and considerably extends the service life of the component. This characteristic is confirmed by [68].

From the manufacturing point of view, the main advantages are represented by the high draping capability and the perfect compatibility with pre-pregs curing cycles. Moreover, the substrates do not need surface pre-treatments before film application.

For the sake of clarity, the benefits of Kraibon® solution are illustrated in Figure 3.6 and summarized:

- Calibrated thin film;
- Constrained Layer Damping (PCLD) properties;
- Direct bonding and adhesion between metal and CFRP;
- Thermal and Electrochemical decoupling;
- High draping capabilities;
- Total composite curing cycles compliance.

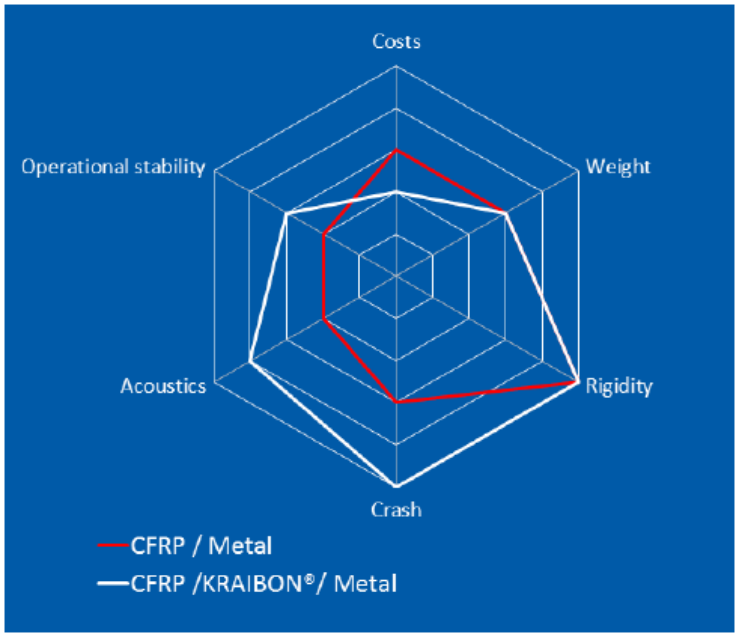

Figure 3.6 - Advantages on application of Kraibon in hybrid material

For the purpose of this thesis, Kraibon® supplies two different compounds (Figure 3.7): the HAA 9275/45 and the HVV 9632/59.

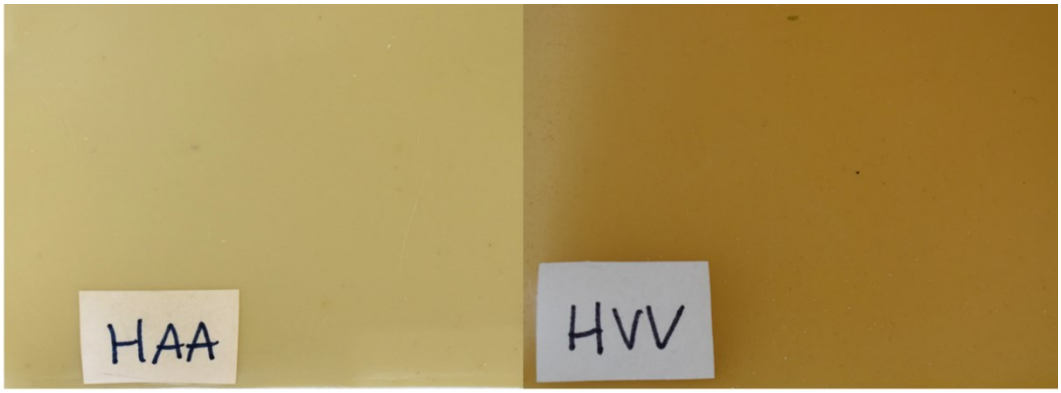

Figure 3.7 - Kraibon® compound: HAA (left) and HVV (right)

These two materials has been characterized in Chapter 4 in order to compare their performance in terms of damping and adhesive properties and to carry out the necessary data for FEM analysis.

In conclusion, the design proposal for the multi-material lower control arm has been drawn as illustrated in Figure 3.8. Laminate thickness, fiber orientation and ply stacking sequence have been defined through a CAE structural optimization. As concerns manufacturing technology, a standard hand lay-up process has been considered feasible for one prototype building.

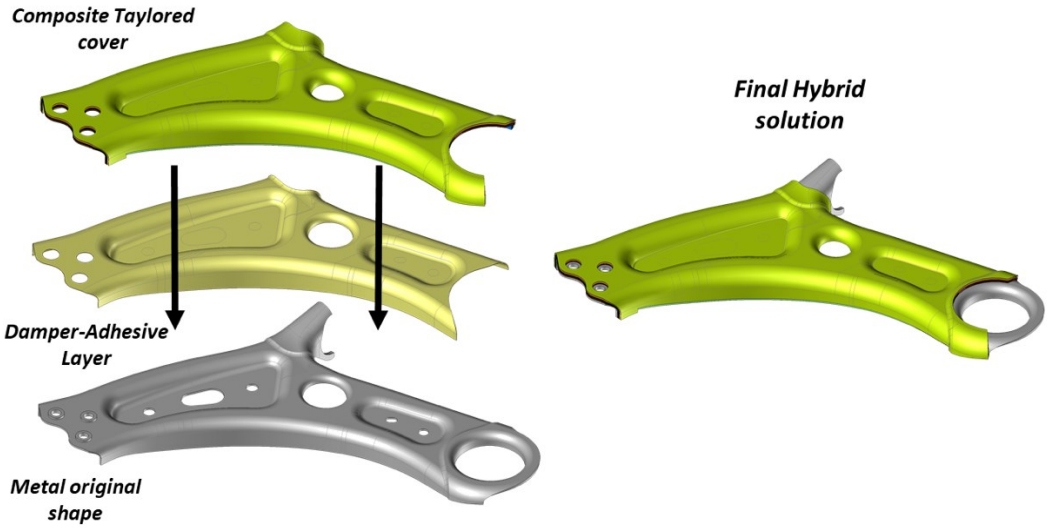

Figure 3.8 – Hybrid LCA design proposal

3.3. Suspension Packaging

Once the suspension scheme has been decided, the envelope of the external shape of the tire can be designed, factoring in steering motion and suspension stroke. The lower arm shape must obviously be outside this envelope and must take into account assembly and disassembly conditions. That is the practice used during a suspension car design [24].

In this case, the front suspension of the Fiat 500X has been reproduced on CAD (Figure 3.9**)** starting from the hard points used for the multibody model. The CAD suspension assembly is composed by the strut, the upright, the brake disk, the steering tie rod and the wheel assembly. The packaging analysis is fundamental to avoid any interference between the arm and the other part of the assembly in order to design the hybrid LCA replaceable with the original component.

Figure 3.9 – Wheel assembly (left) and its simplified CAD model (right)

Three parameters are fundamental during the packaging evaluation: wheel travel, steering angle and wheel dimension. These values are reported in Table 3.1.

Data	Value
Wheel travel	±100 mm
Steering angle	Inner= 22° Outer= 27°
Wheel size	215/60 R16

Table 3.1 – Vehicle data for packaging analysis

Firstly, an enlarged lower control arm has been drawn to evaluate the maximum volume available (Figure 3.10). Therefore, an off-set of 15 mm from the original outer surface has been made in order to create a fictitious component defining the maximum envelope of the arm.

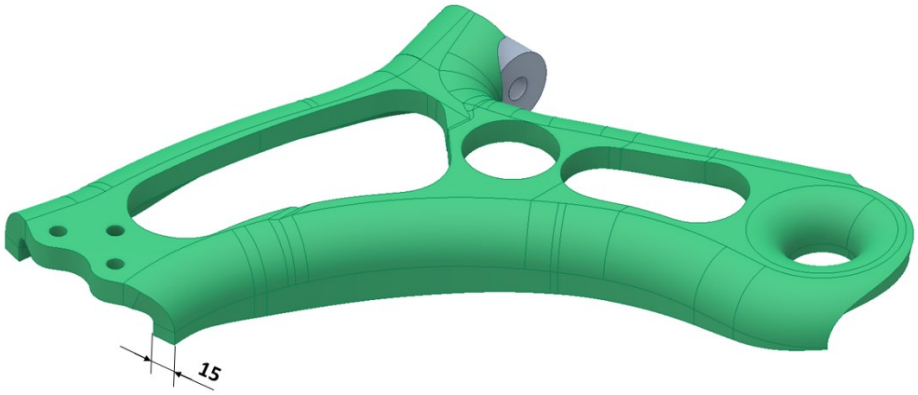

Figure 3.10 - Enlarged lower control arm

Secondly, six configurations have been checked according to travel and steering angle values as reported in Figure 3.11.

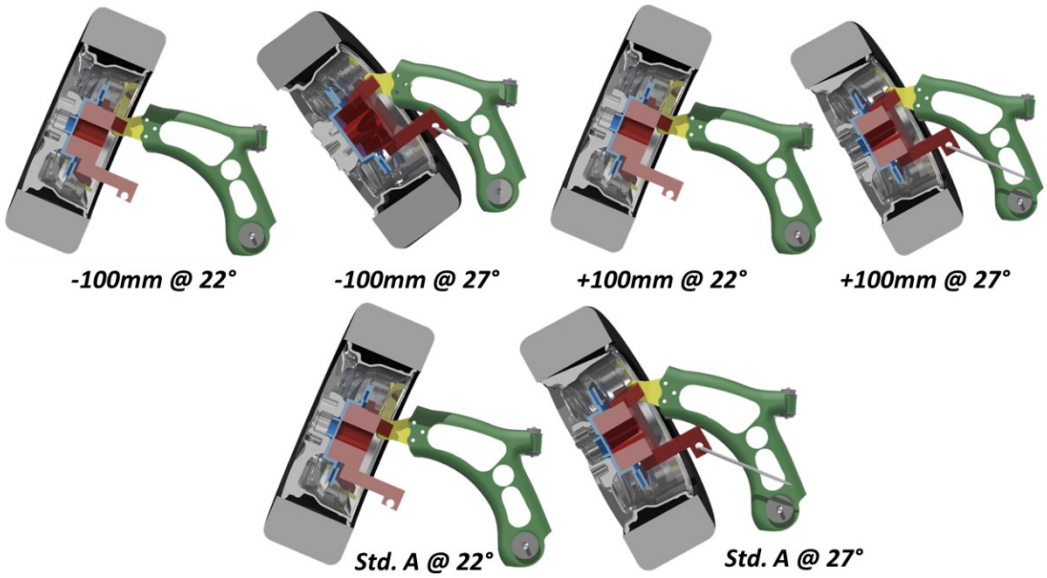

Figure 3.11 – Packaging analysis at different configuration

From the packaging CAD analysis, all the configurations are free of component interferences. Hence, the maximum design volume for the hybrid LCA has been defined. In so doing, it has been possible to face the lack of information about the original suspension assembly layout and guarantee a possible replacement with the new hybrid LCA.

3.4. Carbon fiber material cover

Although the benefits of composites, in particular of the carbon fibers, are well recognized by the industry, so far their use has been hampered by especially the lack of design experience and knowledge of their behavior, which is very different from the one of conventional metal.

A key factor to foster the spread of composites is the use of advanced computational tools to model and predict the performance of components. Robust and reliable predictive modelling tools are indeed critical for proving the quality and performance of polymer composite, especially to simulate accurately the behavior of a suspension component.

A useful design guideline is provided by the *building block approach* [69] reported in Figure 3.12 and schematically summarized as follow:

1. Block group A: Material screening and testing taking into account the manufacturing process suitable for the final application;
2. Block group B: sub-components characterization also assisted by virtual simulation;
3. Block group C: final component test and correlation.

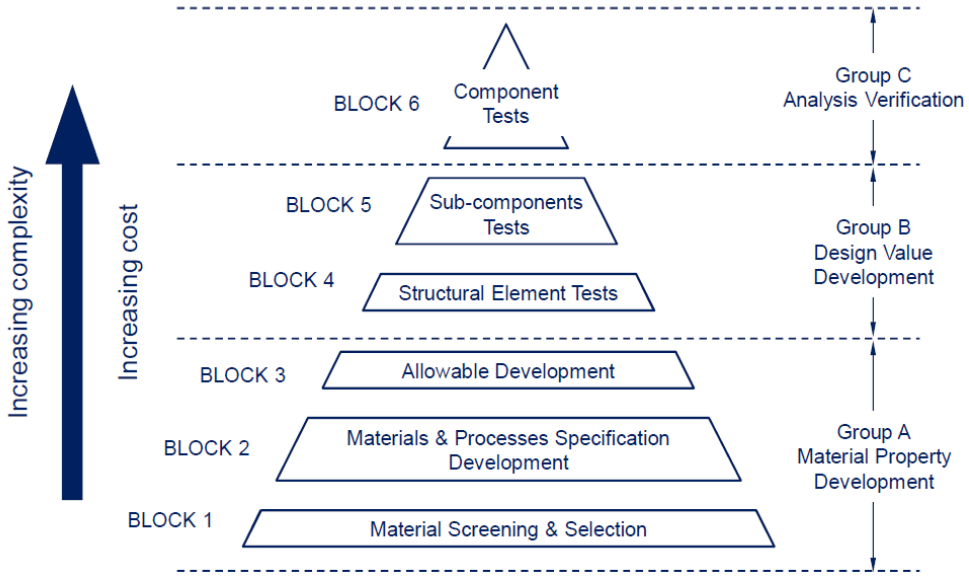

Figure 3.12 – Building block approach

The design of the composite cover has the main task to meet the structural target of stiffness and strength. Therefore, the material selection is a key factor because

external volume and mass are two optimized parameters to match lightweight and packaging layout. The complex shape of the arm does not allow an easy tailoring in terms of fiber orientation, hence the local properties could be vary sensibly.

In this context, carbon fibers represent the best trade off in terms of stiffness and strength than glass or aramid fibers, as depicted in Figure 3.13.

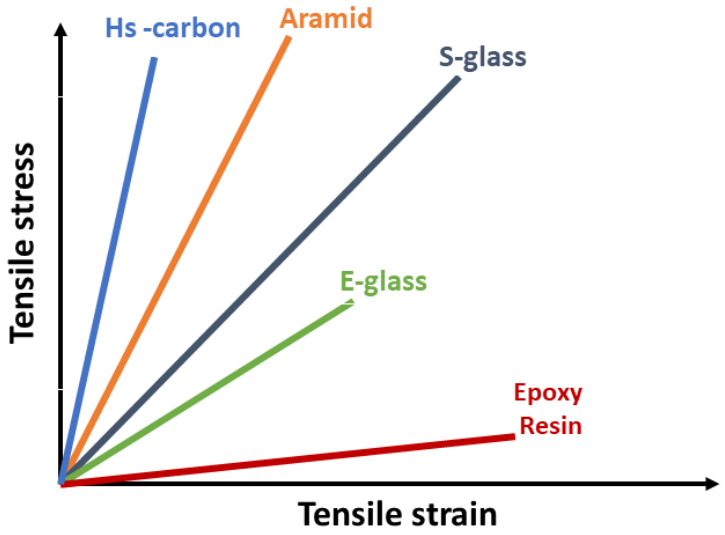

Figure 3.13 – Stress vs. strain for different fiber types

Moreover, carbon fibers are available in different typology according to their predisposition to be stiff or strength as shown in Figure 3.14.

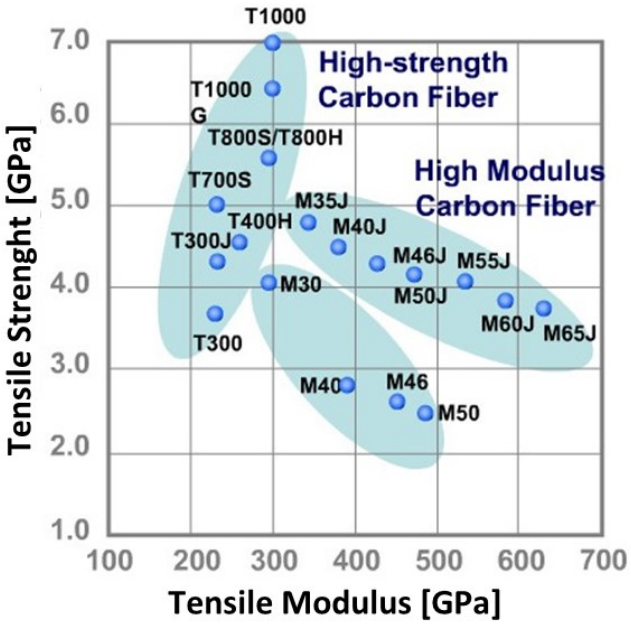

Figure 3.14 – Strength vs. modulus for fibers classification

Focusing on the multi-material LCA, two different kind of fiber reinforcements have been selected: unidirectional and fabric. The unidirectional (UD) composite chosen is the M46J carbon fiber produced by Torayca and provided in pre-preg

laminate by Deltatech. The M46J (Figure 3.15) is an advanced high modulus composite material, frequently used in aerospace application thanks to its high mechanical performances. This material has a mass per area ratio of 150 g/m^2 and it is impregnated by an epoxy resin.

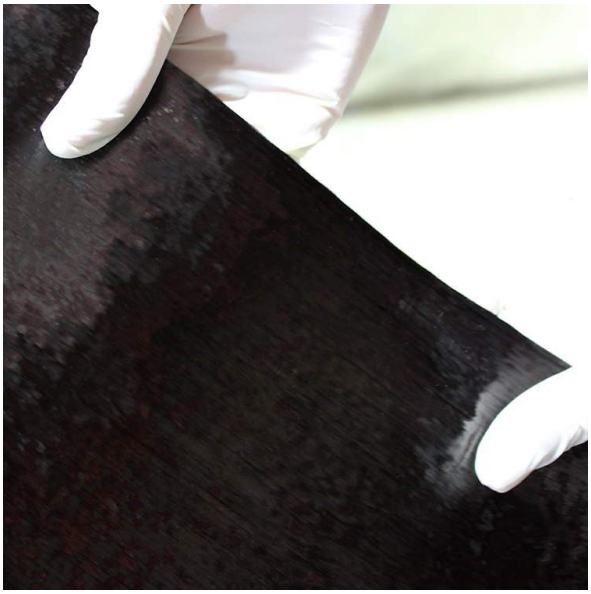

Figure 3.15 - M46J Unidirectional carbon fiber

In this kind of material, mechanical properties are strongly dependent from fiber orientation especially the Young's modulus, as illustrated in Figure 3.16.

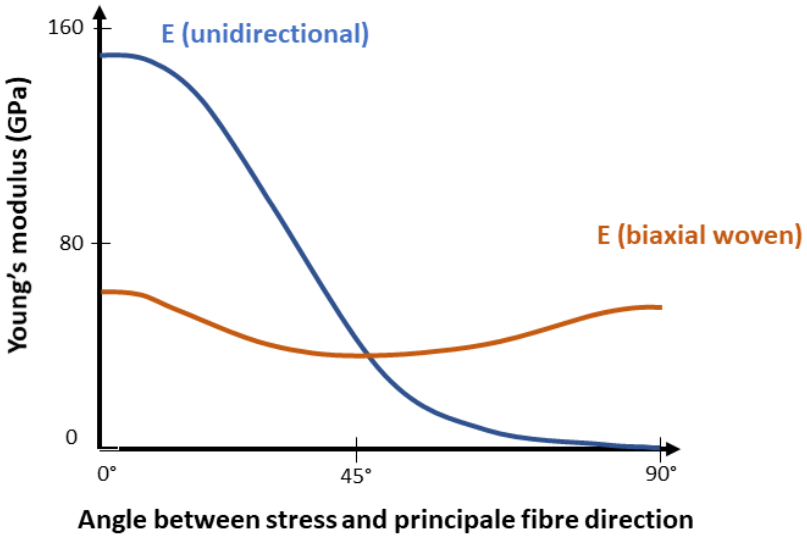

Figure 3.16 – Example of Young modulus variation along fiber orientation

This behavior is due to the intrinsic properties of the unidirectional composites because they are orthotropic materials and totally different from metals. In fact, metal alloys are considered isotropic material, which means they have an infinite number of planes of material property symmetry. Thus, material properties are the same in all directions at a point within a body. Isotropic linear elastic materials have

two independent engineering constants, any two of Young's modulus E, shear modulus G, or Poisson's ratio ν that are related by equation:

$$G = \frac{E}{2(1+\upsilon)} \tag{3.1}$$

Hence, the Stress-Strain relationship can be written as:

$$\begin{Bmatrix} \varepsilon_1 \\ \varepsilon_2 \\ \varepsilon_3 \\ \gamma_{12} \\ \gamma_{23} \\ \gamma_{13} \end{Bmatrix} = \begin{bmatrix} \frac{1}{E} & \frac{-\nu}{E} & \frac{-\nu}{E} & 0 & 0 & 0 \\ \frac{-\nu}{E} & \frac{1}{E} & \frac{-\nu}{E} & 0 & 0 & 0 \\ \frac{-\nu}{E} & \frac{-\nu}{E} & \frac{1}{E} & 0 & 0 & 0 \\ 0 & 0 & 0 & \frac{1}{G} & 0 & 0 \\ 0 & 0 & 0 & 0 & \frac{1}{G} & 0 \\ 0 & 0 & 0 & 0 & 0 & \frac{1}{G} \end{bmatrix} \begin{Bmatrix} \sigma_1 \\ \sigma_2 \\ \sigma_3 \\ \tau_{12} \\ \tau_{23} \\ \tau_{13} \end{Bmatrix} \tag{3.2}$$

Where:

- ε_i and σ_i with $i = 1,2,3$ are respectively the normal strains and stress
- γ_{ij} and τ_{ij} with $i, j = 1,2,3$ are respectively the tangential strains and stress

Instead, composites are usually orthotropic materials with 3 orthogonal planes of material property symmetry in which properties are the same along these orthogonal planes at a point within a body. Orthotropic materials have 9 independent engineering constants, E_1, E_2, E_3, ν_{12}, ν_{23} and ν_{13}, G_{12}, G_{23}, and G_{13}. Then, the orthotropic compliance matrix is defined as:

$$\begin{Bmatrix} \varepsilon_1 \\ \varepsilon_2 \\ \varepsilon_3 \\ \gamma_{12} \\ \gamma_{23} \\ \gamma_{13} \end{Bmatrix} = \begin{bmatrix} \frac{1}{E_1} & \frac{-\nu_{12}}{E_2} & \frac{-\nu_{31}}{E_3} & 0 & 0 & 0 \\ \frac{-\nu_{12}}{E_2} & \frac{1}{E_2} & \frac{-\nu_{32}}{E_3} & 0 & 0 & 0 \\ \frac{-\nu_{13}}{E_1} & \frac{-\nu_{23}}{E_2} & \frac{1}{E_3} & 0 & 0 & 0 \\ 0 & 0 & 0 & \frac{1}{G_{12}} & 0 & 0 \\ 0 & 0 & 0 & 0 & \frac{1}{G_{23}} & 0 \\ 0 & 0 & 0 & 0 & 0 & \frac{1}{G_{13}} \end{bmatrix} \begin{Bmatrix} \sigma_1 \\ \sigma_2 \\ \sigma_3 \\ \tau_{12} \\ \tau_{23} \\ \tau_{13} \end{Bmatrix} \tag{3.3}$$

In particular, unidirectional CFRP are considered a special case of orthotropic material called transverse isotropic. In fact, transversely isotropic materials have one plane of material property symmetry in which the material properties are the same that is the 23-plane as shown in Figure 3.17.

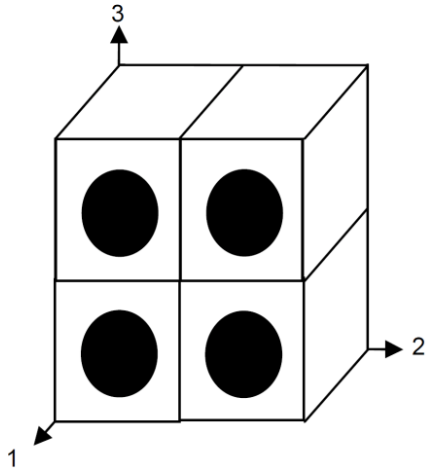

Figure 3.17 - Transversely isotropic unidirectional composite

Due to the symmetric nature of the transversely isotropic compliance matrix, equation (3.4) can be defined.

$$\frac{\nu_{ij}}{E_i} = \frac{\nu_{ji}}{E_j} \tag{3.4}$$

These materials have five independent engineering constants, E_1, E_2, ν_{12}, ν_{23} and G_{12}. Then, the Strain-Stress relation is:

$$\begin{Bmatrix} \varepsilon_1 \\ \varepsilon_2 \\ \varepsilon_3 \\ \gamma_{12} \\ \gamma_{23} \\ \gamma_{13} \end{Bmatrix} = \begin{bmatrix} \frac{1}{E_1} & \frac{-\nu_{21}}{E_2} & \frac{-\nu_{21}}{E_2} & 0 & 0 & 0 \\ \frac{-\nu_{12}}{E_1} & \frac{1}{E_2} & \frac{-\nu_{23}}{E_2} & 0 & 0 & 0 \\ \frac{-\nu_{12}}{E_1} & \frac{-\nu_{23}}{E_2} & \frac{1}{E_2} & 0 & 0 & 0 \\ 0 & 0 & 0 & \frac{1}{G_{12}} & 0 & 0 \\ 0 & 0 & 0 & 0 & \frac{2(1+\nu_{23})}{E_2} & 0 \\ 0 & 0 & 0 & 0 & 0 & \frac{1}{G_{12}} \end{bmatrix} \begin{Bmatrix} \sigma_1 \\ \sigma_2 \\ \sigma_3 \\ \tau_{12} \\ \tau_{23} \\ \tau_{13} \end{Bmatrix} \tag{3.5}$$

As a matter of fact, unidirectional composites are usually applied as reinforcement strips, especially in laminate with complex geometry, to locally increase stiffness and strength performance.

For this reason, a T700 carbon fiber weaved in 2x2 twill scheme has been chosen as structural fabric. The fabric selected is the GG430T epoxy pre-preg (Figure 3.18), with a mass per area ratio of 430 g/m^2, produced by Torayca and supplied by Deltatech.

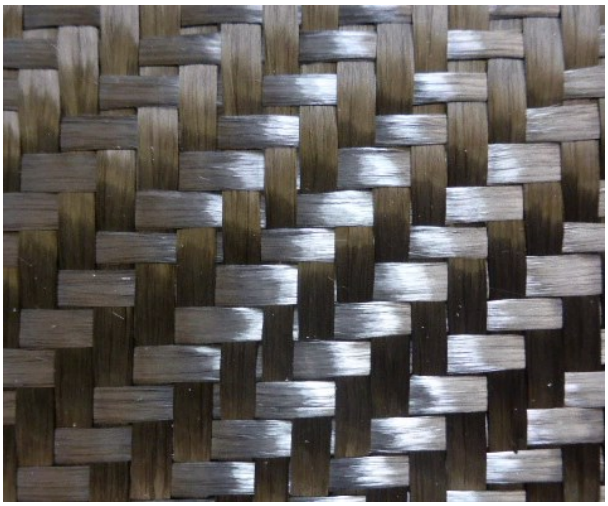

Figure 3.18 - GG430T Fabric weave

The GG430T is a balanced fabric: due to its weave, the in-plane longitudinal and transverse properties can be consider the same because $E_1 \approx E_2$ as well as strength characteristics at 0 and 90 degrees. In this case, the Strain-Stress relationship becomes:

$$\begin{Bmatrix} \varepsilon_1 \\ \varepsilon_2 \\ \varepsilon_3 \\ \gamma_{12} \\ \gamma_{23} \\ \gamma_{13} \end{Bmatrix} = \begin{bmatrix} \frac{1}{E_1} & \frac{-\nu_{12}}{E_1} & \frac{-\nu_{31}}{E_3} & 0 & 0 & 0 \\ \frac{-\nu_{12}}{E_1} & \frac{1}{E_1} & \frac{-\nu_{31}}{E_3} & 0 & 0 & 0 \\ \frac{-\nu_{13}}{E_1} & \frac{-\nu_{13}}{E_1} & \frac{1}{E_3} & 0 & 0 & 0 \\ 0 & 0 & 0 & \frac{2(1+\nu_{12})}{E_1} & 0 & 0 \\ 0 & 0 & 0 & 0 & \frac{1}{G_{13}} & 0 \\ 0 & 0 & 0 & 0 & 0 & \frac{1}{G_{13}} \end{bmatrix} \begin{Bmatrix} \sigma_1 \\ \sigma_2 \\ \sigma_3 \\ \tau_{12} \\ \tau_{23} \\ \tau_{13} \end{Bmatrix} \tag{3.6}$$

At the interface with Kraibon®, a different fabric material has been applied: the T300 2x2 twill epoxy pre-preg called GG245T supplied by Deltatech (Figure 3.19). This material has a mass per area ratio of 240 g/m^2 and higher draping capabilities that make it suitable as first layer. Because the GG245T is a balanced fabric too, the in-plane longitudinal and transverse properties can be consider the same $E_1 \approx E_2$ as well as strength characteristics at 0 and 90 degrees. In addition, the GG245T will be placed also in the last layer as aesthetic skin for its typical carbon look woven.

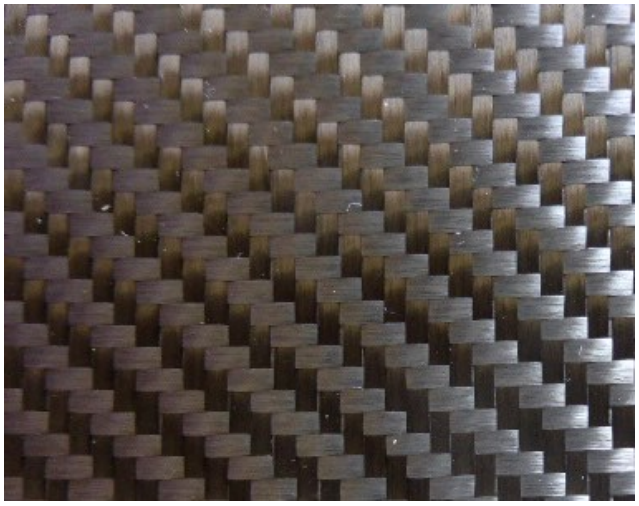

Figure 3.19 - GG245T Fabric weave

In conclusion, the proposed solution for the hybrid lower control arm consists in coupling a carbon fiber cover on the reduced thickness metal shape of the original arm, by using an innovative VEM that works at the same time as damper and adhesive. Therefore, the design iter requires different analysis levels that follow precise workflow, as for example the building block approach, in order to carry out the best performance solution.

In addition, composite material design need the use of cutting-edge computational tools and methodology to model and predict the performance of the component and obtain reliable simulation. Under those circumstances, materials testing assume a fundamental importance for the following reasons:

- The characterization of the VEMs are crucial to define the best damping material and to evaluate the joint properties between steel and GG245T.

- The mechanical characterization of steel and carbon fibers is fundamental to obtain a complete overview on the material properties, necessary to set the design phase and the optimization analysis.

The elaboration of the experimental data are also necessary to define a specific methodology to fit the virtual material card in order to obtain robust and reliable virtual model for the final correlation on RADIOSS and Optistruct solvers.

Chapter 4

Viscoelastic material testing and correlation

Elastomeric material as Kraibon® are generally included inside viscoelastic category. In particular, the HAA 9275/45 is an Ethylene Propylene Diene monomer (EPDM) which exhibits excellent electrical insulation, good resistance to aging but low temperature properties [59]. Instead, the HVV 9632/59 is an Ethylene Acrylate Monomer (AEM) that has good resistance to heat, weathering, and many chemicals. Besides these properties, AEMs have outstanding vibration dampening and good dynamic and abrasion performances over a wide temperature range [59].

As consequence, the aim of the elastomers characterization is to evaluate, firstly, the damping properties between the two viscoelastic and, secondly, to estimate the adhesive characteristics in terms of joint strength and toughness. The substrates used for joining are the CFRP GG245T and the steel S420MC as they are interfaced in the hybrid lower control arm configuration. Then, a detailed testing plan has been developed as reported in Table 4.1.

Material	Test	Specimen ID number	Aim
GG245T+KRAIBON	Oberst - One-side (No treatment)	From o1 to o4	KRAIBON Young modulus E and loss factor ζ
GG245T+KRAIBON	Oberst - One-side (Aging 750h)	From o1 to o4	
GG245T+KRAIBON	Oberst - One-side (Thermal test)	From o5 to o8	
S420MC+KRAIBON+GG245T	Single lap joint (No treatment)	From s9 to s13	Joint strength comparison
S420MC+KRAIBON+GG245T	Single lap joint (Aging 750h)	From s14 to s18	
S420MC+KRAIBON+GG245T	Double cantilever beam (No treatment)	From d19 to d23	Joint toughness G_{Ic} and G_{IIc}
S420MC+KRAIBON+GG245T	Double cantilever beam (Aging 750h)	From d24 to d28	
S420MC+KRAIBON+GG245T	End-Notched flexure (No treatment)	From e29 to e33	
S420MC+KRAIBON+GG245T	End-Notched flexure (No treatment)	From e34 to e38	

Table 4.1 – Experimental test set-up on VEMs

Finally, a virtual correlation activity has been conducted only on the experimental Oberst beam test in order to tune the elastomer material card to predict damping on the FEM lower control arm model. In Figure 4.1 a schematic workflow of this activity is reported.

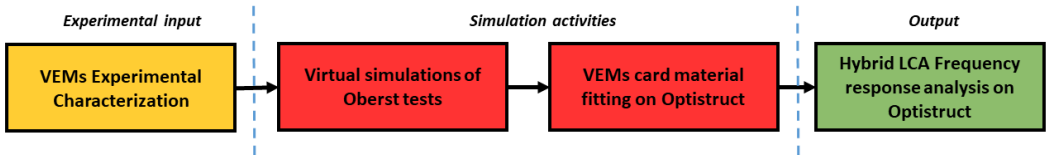

Figure 4.1 - Operative workflow adopted for VEMs characterization activity

4.1. Oberst test method

As concerns the vibrational behavior, the Oberst test method has been chosen because it permits to define both the structural material and the damping layer characteristics without depending on the geometry of the sample: once found the elastic modulus and the loss factor, it is possible to use these values for a virtual simulation of the component. The reference standard test used to evaluate the damping characteristics is, the ASTM E756-05 [70]. The aim of this test is the

characterization of the “structural” material and the evaluation of the influence of type and thickness of damping material.

The test is performed firstly with only the structural material (carbon fiber), then with one layer of damping material. From the experimental data, the Young modulus and loss factor are estimated for each material and each sample considered. Oberst test consists in a beam, fully constrained on one side and free on the other, that is excited by a contactless electromagnetic transducer. The experiment is performed in a climatic cell, to maintain constant and controlled the test temperature. The exciting force is applied near the constraint point, while the response is recorded at the free end of the beam by a capacitive transducer.

The vibrational frequencies are function of the free length “L”, the height “h”, the Young modulus “E” and the density “ρ” of the specimen. Therefore, it is possible to compute the Young’s modulus of the material of the tested beam, knowing the natural frequencies and applying the Euler-Bernoulli formula. This can be done for each natural frequency, but usually the value computed from the first mode is discarded, because it is highly influenced by the transient initial response. Oberst test is performed measuring the Frequency Response Function (FRF) on both the base and the damped beam: the first measure is done to determine the natural frequencies within the range of interest and the second one to determine the natural frequencies and the corresponding modal loss factor of composite beam. It is important to guarantee the repeatability of the test, because at least two FRF measurements (one for the bare beam and the other for damped beam) are needed for the determination of material properties. This procedure is precisely described in [70] and a particular case is provided by [71], which gives a reference case to be used as guideline. Figure 4.2 shows the test apparatus and the specimen dimensions.

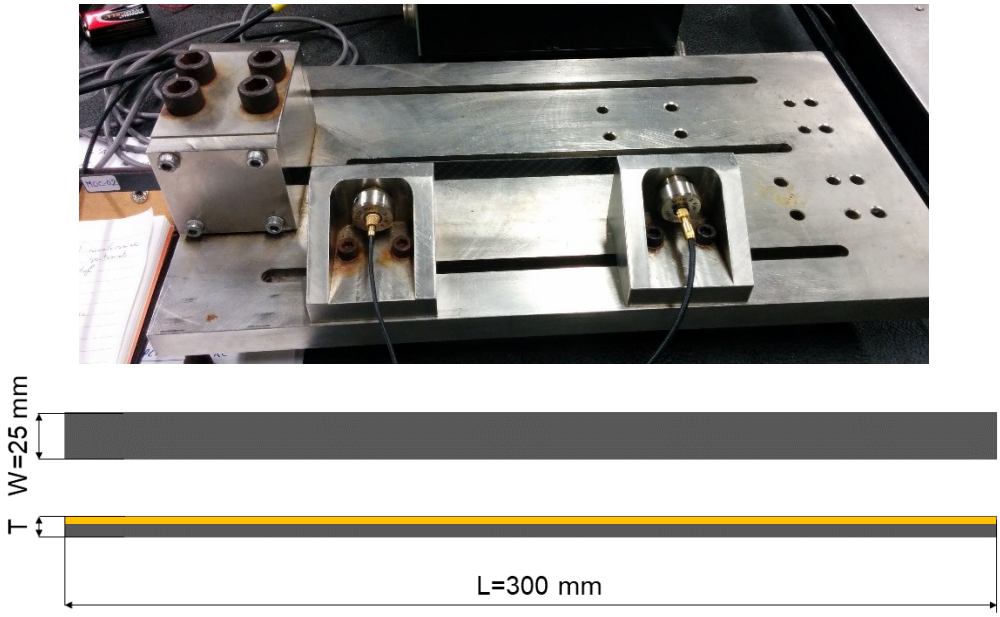

Figure 4.2 – Test bench (top) and Oberst beam specimen (bottom)

A calculator generates the exciting force, whose shape is a sine sweep: its amplitude is constant in time, while the frequency increases linearly. The excitation

signal, after being amplified, is transmitted to the sample through an electromagnetic transducer (Brüel & Kjær MM-0002). This is a non-contacting transducer and it is chosen because it does not influence the test results, adding its mass to the one of the sample. Because the beams are constituted of nonferrous material, a small patch of magnetic materials has been put on the beam to achieve specimen excitation and measurable response. Figure 4.3 shows the signal amplifier used in this test.

Figure 4.3 - Signal amplifier

On the free end of the beam, a capacitive transducer (Brüel & Kjær MM-0004) measures the displacement of the sample and this position is chosen because there are not vibrating nodes in this point and the displacements have the higher modulus. This transducer measures the variation of the quantity of air between its extremity and the sample and relates this quantity with the displacement. At the end, the output signal is recorded by a microphone and sent to the signal analyser that converts the analogue signal into a digital one, which can be post-processed by a calculator. Figure 4.4 show the microphone power supply and the signal analyser.

Figure 4.4 - Microphone power supply (A) and signal analyser (B)

4.2. Thermal test SAE J1637

The properties of Young modulus E and loss factor are highly dependent on temperature and frequency [72]. As depicted in Figure 4.5, at a constant frequency, the storage modulus E decreases with the increasing temperature from glassy to rubberlike region, while the loss factor has its maximum peak value in the transition region, where E drastically decrease.

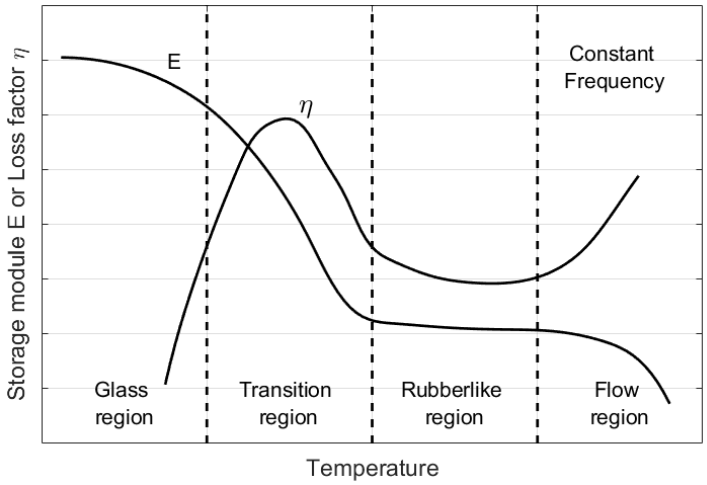

Figure 4.5 – Example of dynamo-mechanical plot for VEMs

Hence, the Oberst test is performed at different temperature integrating the test bench inside a climatic chamber. The test temperature range chosen for this analysis is inspired to the SAE J1637 [71] but with some modification, in order to enlarge the range of interest obtaining the material characteristics in a temperature range in which vehicles will work for majority of its life. Therefore, thermal tests are performed from -20°C up to 60°C with steps of 10°C. To avoid problem of thermal gradient of the components, samples are maintained at target temperature for at least one hour and half as shown in Figure 4.6 before starting the data logging.

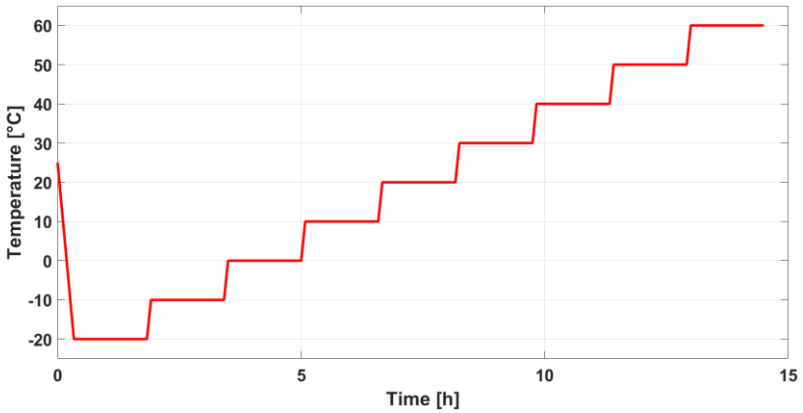

Figure 4.6 – Temperature profile for SAE J1637

4.3. Aging test IEC 60068

To understand the behavior of the damping materials after an ageing cycle, the IEC 60068 [73] standard has been followed. For statistical purpose and to obtain reliable data each sample is tested and output results are the average of three specimens. The cycle used for the aging is defined in Figure 4.7, it has a duration of about 24 h, so each aging step of 750 h lasts for about 33 days, which correspond approximately to 3 year of life in the natural environment. Specimens are exposed to different temperatures (-20◦ +80◦ C) at different stages of humidity. The Oberst test has been performed at the end of the aging step.

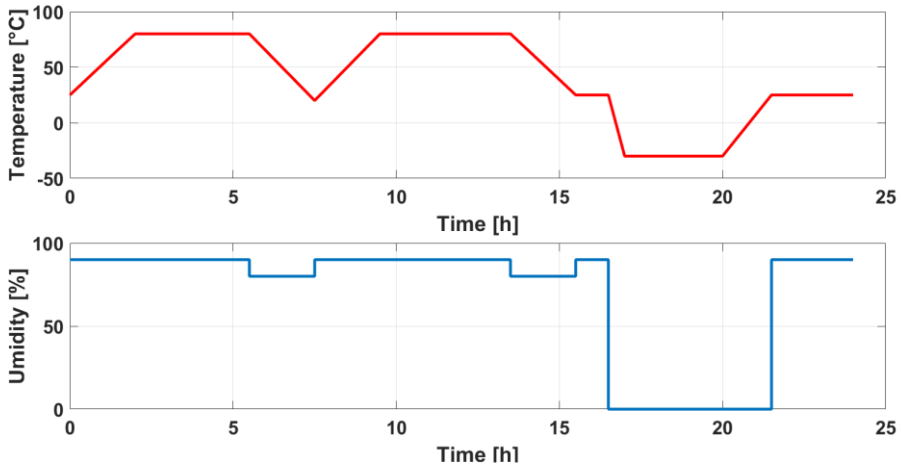

Figure 4.7 – Humidity (below) and temperature (above) profile for IEC 60068

4.4. Single Lap Joint Test (SLJ)

As concerns the joint strength, the reference standard used is the ASTM D5868-01 [74] that describes a lap shear test for use in measuring the bonding characteristics of adhesives for joining fiber reinforced plastics to metals. This test method is intended to complement test method D1002 [75] and it is useful for generating comparative apparent shear strength data between different joints. For this reason, it is important to remark that the test method is primarily comparative. The measure of strength values obtained from this test method as design-allowable stress values for structural joints could lead to product unexpected failure. In fact, the apparent shear strength of an adhesive obtained from a given small single-lap specimen may differ from that obtained from a joint made with different adherends or by a different bonding process. Hence, single-lap test has been used only for comparing and selecting adhesives between the two elastomeric compounds available. Specimen and apparatus are illustrated in Figure 4.8.

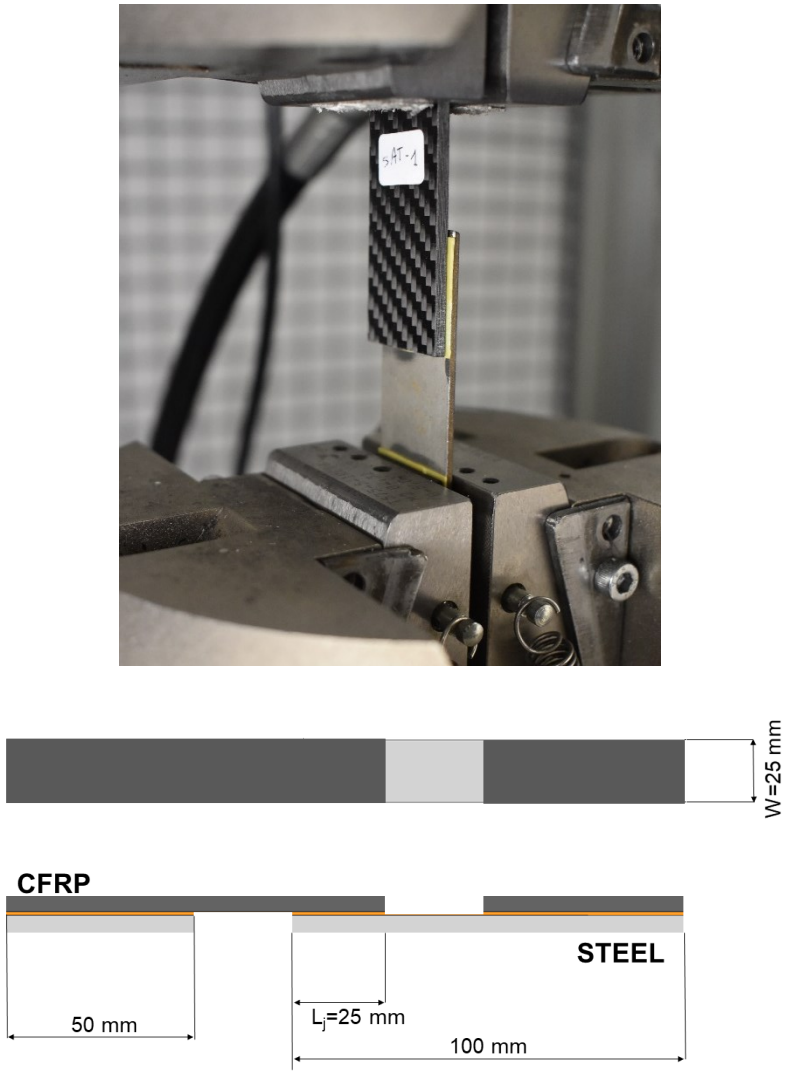

Figure 4.8 – Test apparatus (top) and SLJ specimen (bottom)

4.5. Double Cantilever Beam test (DCB)

The double cantilever beam test has been chosen to estimate the fracture toughness G_{Ic} of the adhesive mode I (opening). The reference test method is the ASTM 5528 [76], although is limited to use with composites consisting of unidirectional carbon fiber. Unfortunately, no established standardized test methods have been defined yet for hybrid laminates for any kind of delamination modes (included mode II opening). Therefore, the adaptation of the standardized method has become a common practice [77]. The specimen has been made in accordance with the DCB test method standard, and in Figure 4.9 are reported the coupon layout adopted. On the specimen side, several markers have been drawn every 5 mm to investigate the Crack Opening Displacement (COD) by camera recording.

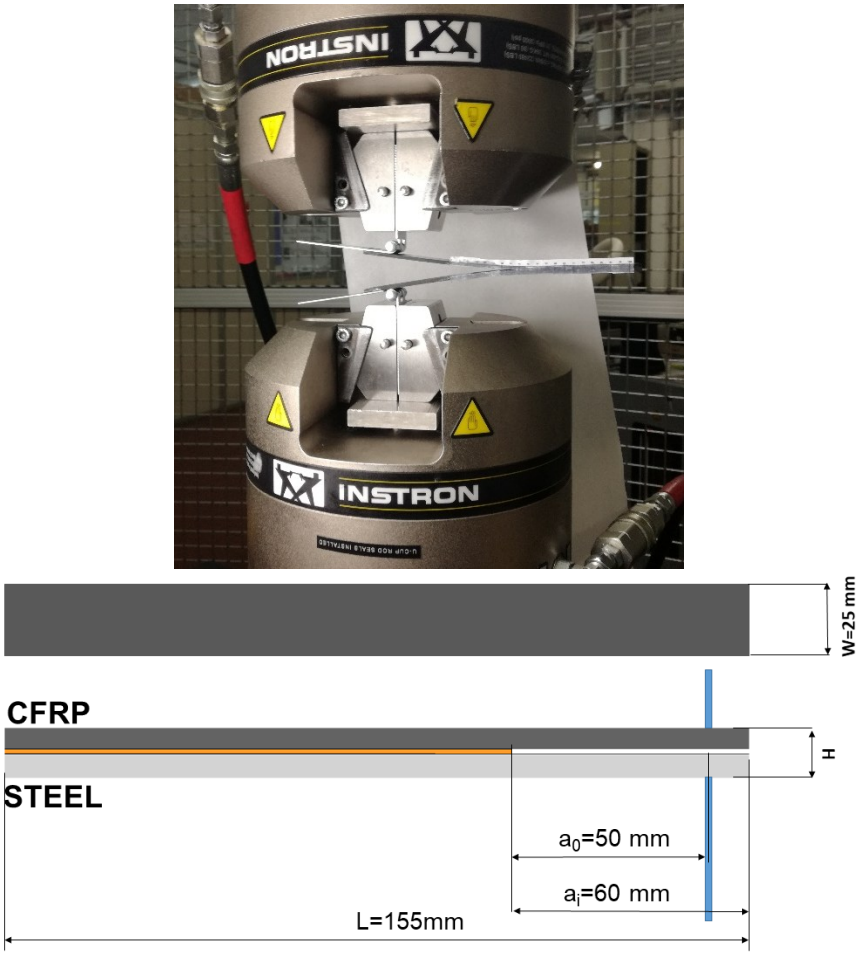

Figure 4.9 - Test apparatus (top) and DCB specimen (bottom)

4.6. End-Notched Flexure test (ENF)

The End-Notched Flexure test has been chosen to estimate the fracture toughness G_{IIc} of the adhesive mode II (shearing). The reference test method is the ASTM D7905M - 14 [78] and, even in this case, the ASTM standard has been adapted for hybrid laminates [77]. The specimen used, made in accordance with the standard, is the same of the DCB test and in Figure 4.10 are reported the coupon dimension and test apparatus. Crack opening displacement is investigated by camera recording.

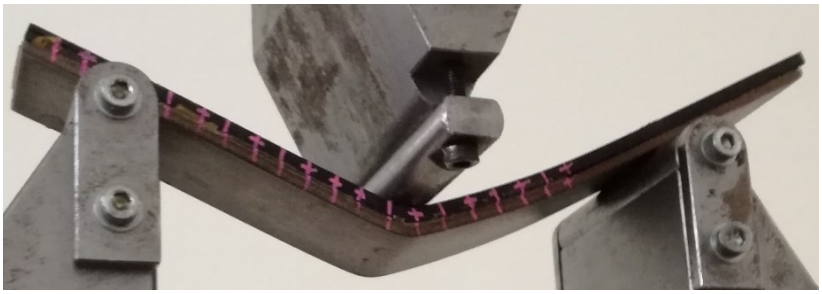

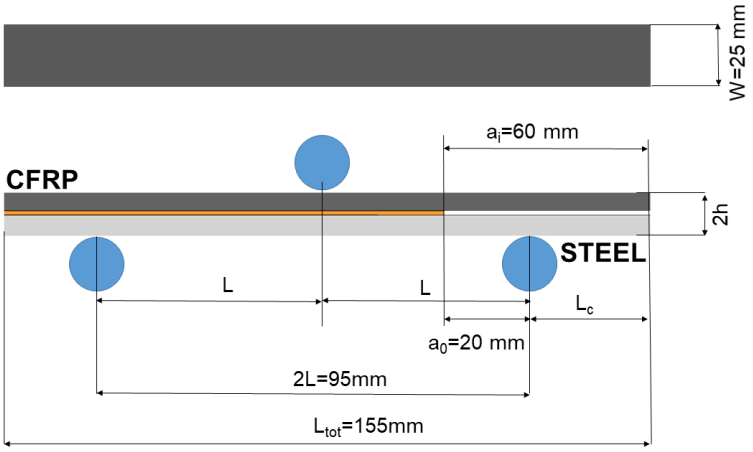

Figure 4.10 – Test apparatus (top) and ENF specimen (bottom)

4.7. Experimental results: damping behavior

In this section are presented the results obtained from the Oberst test on the two elastomeric materials called, for simplicity, HAA and HVV. The fitting procedure to find out the natural frequencies and the damping ratios for each mode has been set up by Ausano [79] in Matlab environment. This fitting method permits the identification of the modal factors by the interpolation of the function of the eigenspectrum, calculated for the displacements recorded in the experiments. The method used is not exactly the half power bandwidth method, described by the standard, but it tries to improve the criticalities of this method for very high or very low damping of the material. In the following, a brief description is reported.

The MATLAB program starts its work loading the displacement of the extremity point of the sample measured by the capacitive transducer and processed by the signal analyser. At this proposal it is important to underline that the input signal is an analog function of time, which must be converted in digital form. The analog digital converter uses a sampling period that is not related with the period of the analysed function and the values recorded by this instrument are only the ones corresponding to the sampling instants, all other points are lost.

For this reason, the sampling frequency must be chosen in a correct way, for example following Shannon (Nyquist) theorem, for which the maximum frequency of the system must be lower than half the sampling frequency. If this requirement is satisfied, no information is lost and there is not the risk to have an aliasing error. The tests performed use the sampling frequency of 6400 Hz and Figure 4.11 shows an example of the signal as a function of the sampling points.

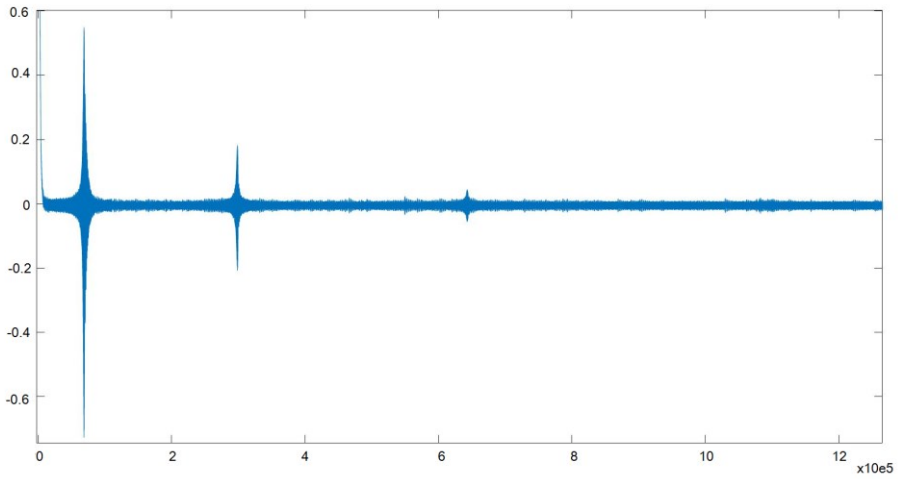

Figure 4.11 - Output signal vs sampling points

Then, the measured signal is cleaned, trying to cut the noise from the recorded signal, and the negative displacement values are discarded. Moreover, to improve the quality of the analysed data, the Hanning windowing function is applied, in order to correct potential periodicity errors of measured signal. To this data, the fast Fourier Transform is applied and the resulting data are the displacements of the specimen in function of frequency. At this point, the receptance of the system is plotted as function of frequency and the natural frequencies of the system can be qualitatively identified (Figure 4.12).

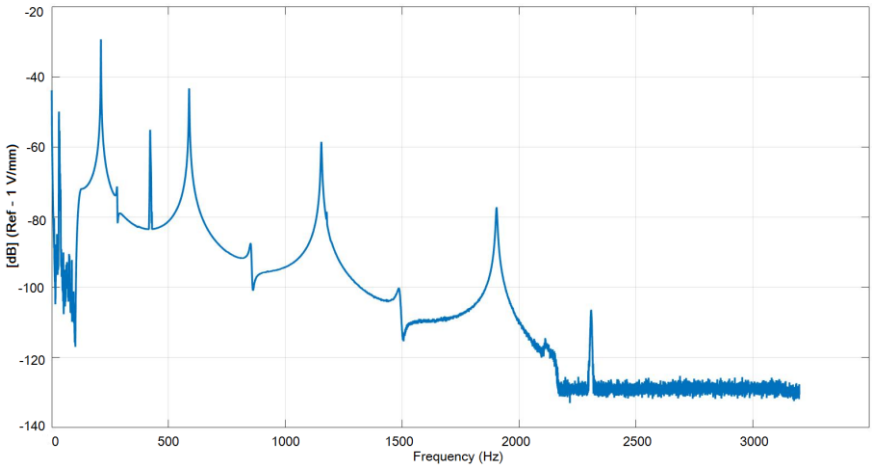

Figure 4.12 - Receptance of the system

The aim of this program is to compute the values of the natural frequencies and the equivalent damping factor. The procedure starts with the definition of the frequency range to analyse: with two subprograms it is possible to move two cursors and chose the frequency interval around a natural frequency. The function "*Calcola*" is recalled in this moment to compute the approximated curve. Figure 4.13 shows the two cursors and the push button to run the approximation.

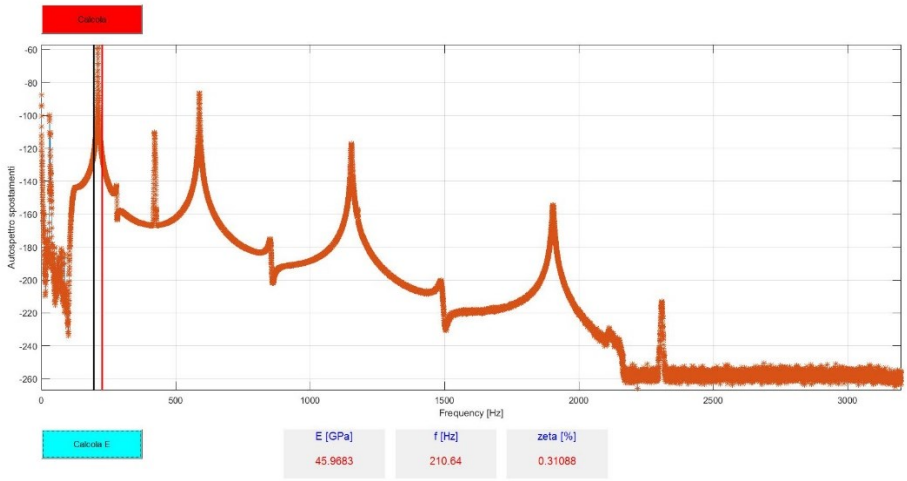

Figure 4.13 - Modal parameters identification by the fitting procedure

The fitting method used in this thesis permits the identification of the modal factors by the interpolation or fitting of the function of the eigenspectrum, calculated for the displacements recorded in the experiment. Once determined the unknown parameters, it permits to plot the original function, to verify the correctness of the results.

The approach followed in this method considers a multi degrees of freedom system with viscous proportional damping, excited by a sine sweep signal in one point, whose response is measured in another point. In order to evaluate the modal parameters of the system, the eigenspectrum of the displacement is computed and it can be considered constant for varying frequencies, because it is assumed that, the exciting function has the same amplitude at all frequencies. With the previous assumption, it is verified the identity between the displacement eigenspectrum and the square of the receptance. From this consideration and applying several calculations, it is possible, for each degree of freedom, to compute the natural frequency and the corresponding damping value. Figure 4.14 shows an example of the approximated curve.

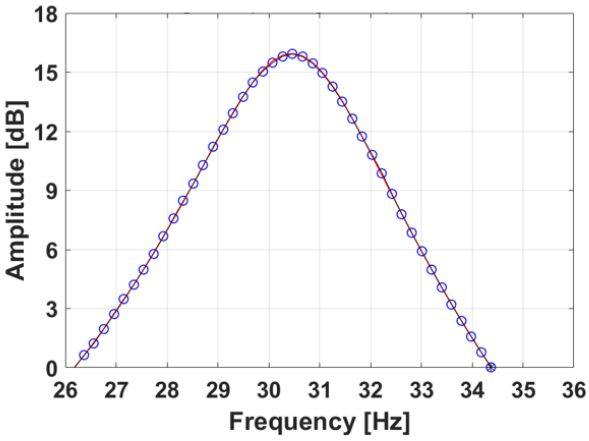

Figure 4.14 - Receptance among specific frequency range: Experimental data (o) and fitting curve (-)

At the end, the values computed with this software are used to compute the Young's modulus of the material, by applying the formula, provided by the legislation.

In Table 4.2 and Table 4.3 are reported the specimen specification used for the Oberst test. The IDs from "o1" to "o4" have been tested firstly no treated and subsequently after 750 h aging. While, IDs from "o5" to "o8" have been tested only in compliance of the SAE J1637.

Oberst tests have also been done on the structural beam made of GG245T carbon fiber, but no tests on aged structural beam have been performed because it has been demonstrated T300 epoxy carbon fibers performances are almost constant in temperature after treatment [58]. In Figure 4.15 and Figure 4.16 are reported the one side beams tested for HVV and HAA.

ID	Fiber orientation	T [mm]	W [mm]	L [mm]	Mass [g]	Density [g/mm^3]
HVV-o1	0°	1,43	12,42	299,84	7,56	0,001416
HVV-o2	0°	1,42	12,58	299,95	7,63	0,001427
HVV-o3	0°	1,39	12,43	300,19	7,44	0,001431
HVV-o4	0°	1,41	12,46	300,47	7,55	0,001430
HVV-o5	0°	1,41	12,66	300,51	7,65	0,001429
HVV-o6	0°	1,42	12,48	300,46	7,59	0,001425
HVV-o7	0°	1,42	12,28	299,65	7,39	0,001415
HVV-o8	0°	1,38	12,47	300,43	7,68	0,001482
AVG		**1,41**	**12,48**	**300,17**	**7,55**	**0,001431**

Table 4.2 – HVV specimen tested

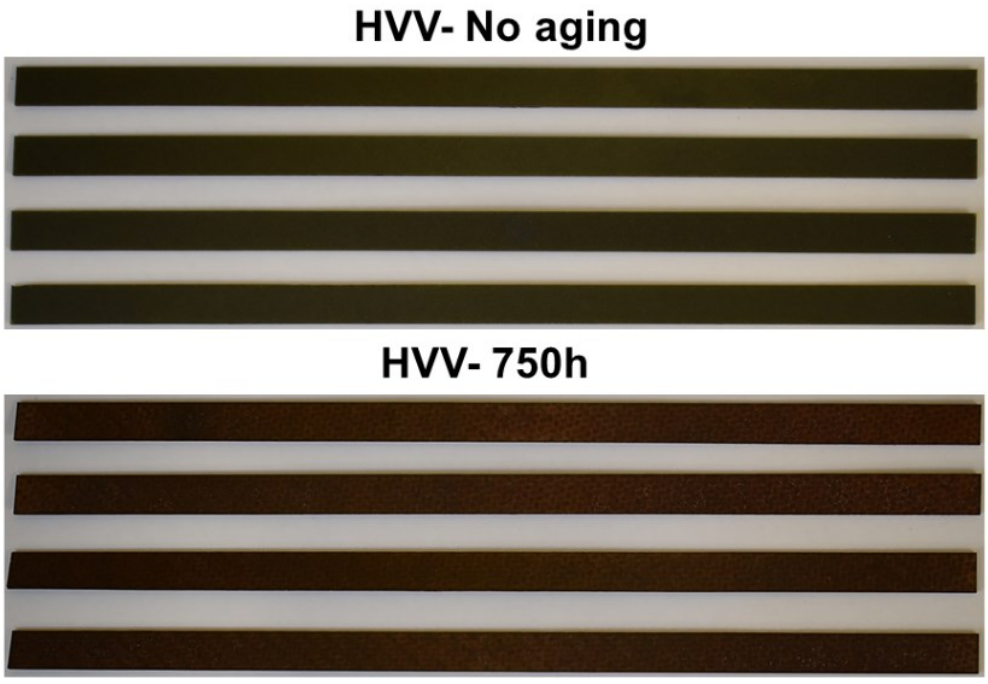

Figure 4.15 - HVV Oberst beam

ID	Fiber orientation	T [mm]	W [mm]	L [mm]	Mass [g]	Density [g/mm³]
HAA-o1	0°	1,31	12,60	299,10	6,88	0,001320
HAA-o2	0°	1,31	12,53	299,22	6,90	0,001340
HAA-o3	0°	1,30	12,58	299,14	6,87	0,001370
HAA-o4	0°	1,34	12,53	299,26	6,99	0,001304
HAA-o5	0°	1,34	12,61	300,41	7,05	0,001336
HAA-o6	0°	1,32	12,41	288,59	6,83	0,001324
HAA-o7	0°	1,34	12,70	300,55	7,10	0,001366
HAA-o8	0°	1,33	12,43	300,53	6,99	0,001360
AVG		**1,32**	**12,55**	**298,35**	**6,95**	**0,001402**

Table 4.3 – HAA specimen tested

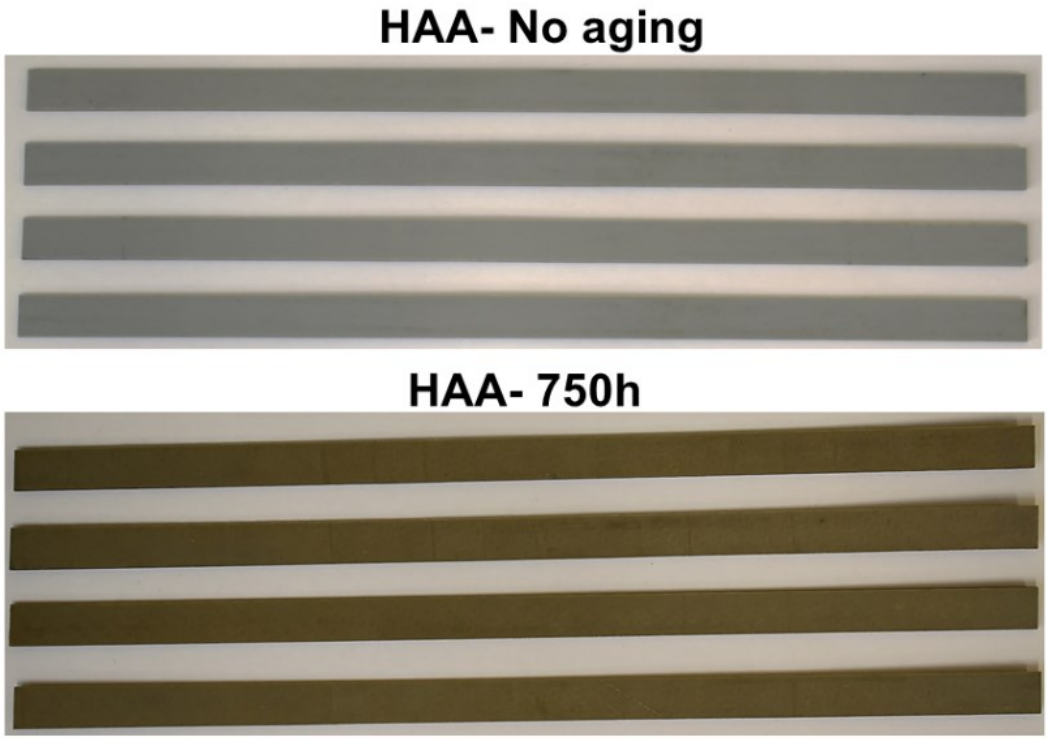

Figure 4.16 - HAA Oberst beam

As suggested by the standard, values from the first natural frequency can be discarded from the results analysis because they are affected by boundary condition. Figure 4.17 shows that both materials have a quite constant trend along frequency. In particular, HVV has the best performance in terms of loss factor before and after the climatic chamber treatment. The aging has increased the loss factor value at the second natural frequency while it has decreased in the last frequency. Aging in HAA materials has globally increased the loss factor curve maintaining also its peak at the third frequency.

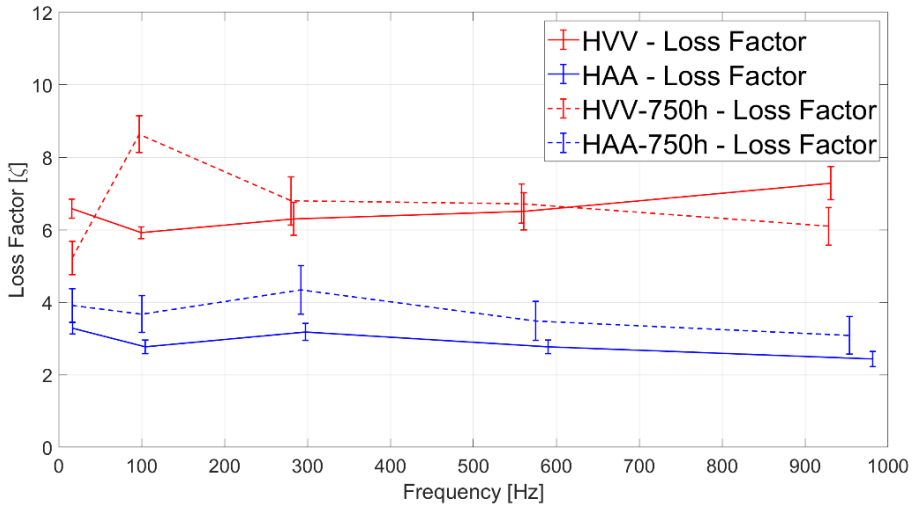

Figure 4.17 – Loss factor vs. frequency for HVV and HAA

As concerns the E modulus, the situation is reversed than loss factor ζ and it is reported in Figure 4.18. HAA material has always the highest values of E modulus before and after 750 h even though the aging caused a sensible drop of performance in all the frequency range. Nevertheless, HVV is not affected by the aging maintaining the same constant trend along the frequency.

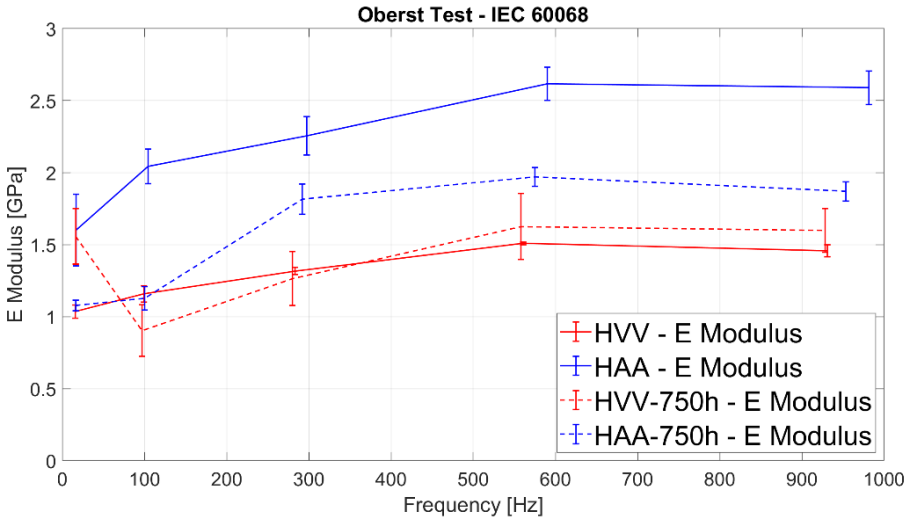

Figure 4.18 – E modulus vs. frequency for HVV and HAA

As concern the properties variation by temperature, reported in Figure 4.19, it can be observed that HVV loss factor is always higher than HAA in the range of frequency tested. The maximum peak is reached at -10°C by the HVV whose maintain very good value until 30°C. After that, the loss factor tends to remain quite constant. On the other hand, HAA increases its Young modulus with the temperature, while the loss factor diminishing from -20°C to 20°. High data scattering is reported at low temperatures due to shrink effect of the damping material that twist the extremity of the specimens and moves them out from the

sensor (Figure 4.20). This situation affects measurements making the test not reliable at -20°C.

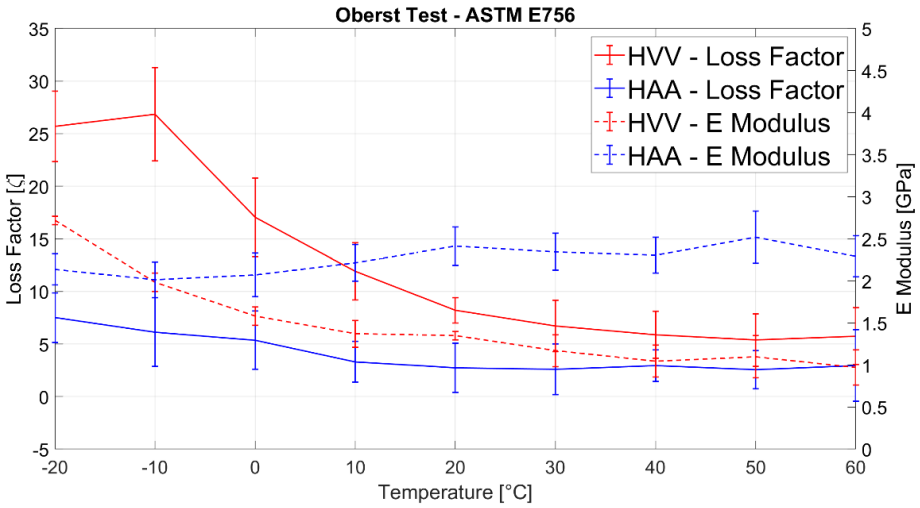

Figure 4.19 - Loss factor and E modulus vs. temperature

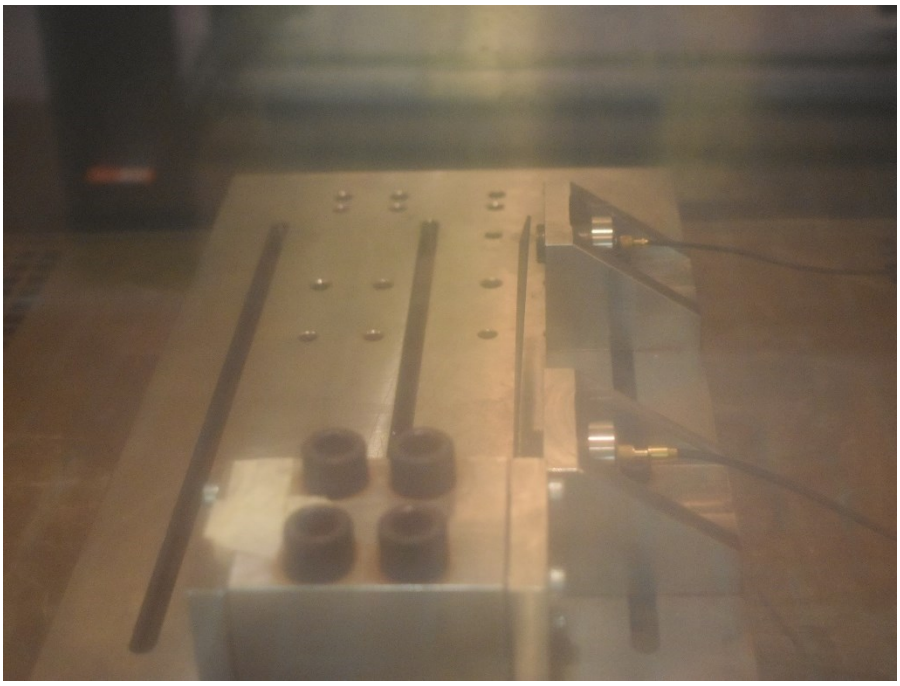

Figure 4.20 – Twisting effect on one side beam specimen at -20°C

4.8. Experimental results: joint properties

In this section are presented the results from the SLJ, DCB and ENF tests conducted on the two elastomeric materials, in order to give a complete overview on the VEMs properties. Tests have been done in two different configurations: non-treated and after 750 h aging in climatic chamber according to IEC 60068. A total number of ten coupons have been used for each test: five as non-treated and other five after 750 h treatment.

4.8.1. Single lap joint results

In Table 4.4, Table 4.5 are reported the specimen specifications used for the single lap joint. The IDs from "s9" to "s13" are the no treated specimens, while IDs from "s14" to "s18" are the aged coupon.

ID	Adhesive Thickness [mm]	Adhesive Width [mm]	Adhesive Length [mm]	Adhesive Area [mm^2]
HVV-s9	0,50	24,67	24,52	604,9
HVV-s10	0,48	24,68	24,08	594,3
HVV-s11	0,47	24,43	24,97	610,0
HVV-s12	0,46	24,67	24,79	611,4
HVV-s13	0,48	24,51	24,28	595,0
HVV-s14	0,47	24,23	24,88	602,8
HVV-s15	0,47	24,72	24,71	610,8
HVV-s16	0,48	24,55	24,82	609,3
HVV-s17	0,48	24,63	24,57	605,2
HVV-s18	0,46	24,28	24,67	599,0
Avg.	**0,48**	**24,53**	**24,62**	**604,27**

Table 4.4 – HVV specimens tested

ID	Adhesive Thickness [mm]	Adhesive Width [mm]	Adhesive Length [mm]	Adhesive Area [mm^2]
HAA-s9	0,46	25,23	25,48	642,9
HAA-s10	0,41	25,53	25,09	640,5
HAA-s11	0,46	25,35	25,89	656,3
HAA-s12	0,47	25,46	25,72	654,9
HAA-s13	0,43	25,27	25,26	638,2
HAA-s14	0,45	24,60	25,01	615,2
HAA-s15	0,49	24,57	24,40	599,4
HAA-s16	0,47	23,90	24,21	578,6
HAA-s17	0,42	23,22	23,42	543,7
HAA-s18	0,46	23,83	24,05	573,1
Avg.	**0,45**	**24,69**	**24,85**	**614,28**

Table 4.5 – HAA specimens tested

As highlighted in Figure 4.21, HVV reaches a force maximum until breaking of 40% more than HAA, although the initial stiffness is slightly less. Despite this, the effect of the aging determines a drop of the performance on HVV especially after 5000 N, while HAA remains more stable even though its data scattering is quite higher in both conditions. Nevertheless, HVV maintains the force peak of about 3000 N over the HAA.

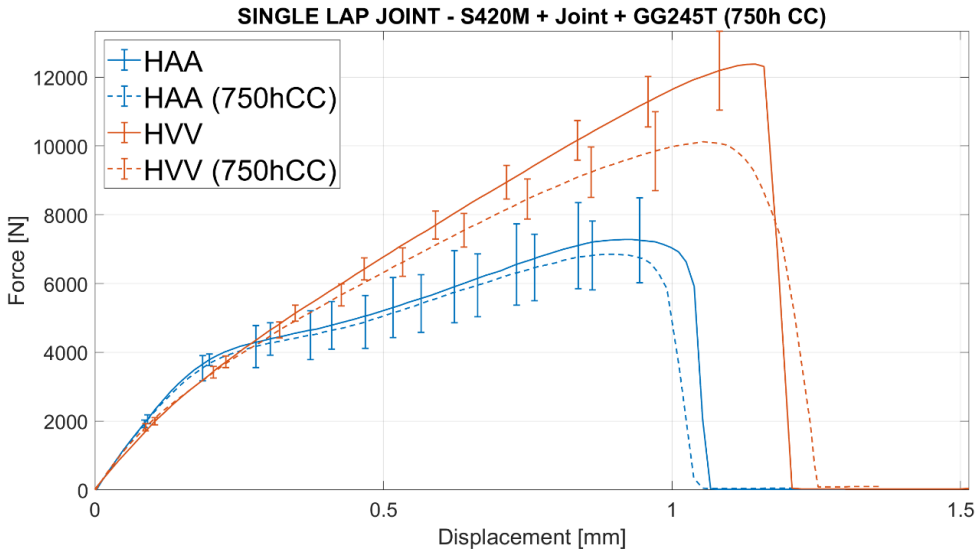

Figure 4.21 – Joint strength vs. displacement for HVV and HAA

In Figure 4.22 are reported the SLJ samples tested. The visual inspection shows that, in both cases of HVV and HAA, failure modes are adhesive or caused by the delamination of the carbon fiber substrate. This trend is also confirmed for the specimen treated in climatic chamber although in two HVV specimen a thin layer of adhesive is left on the CFRP substrate.

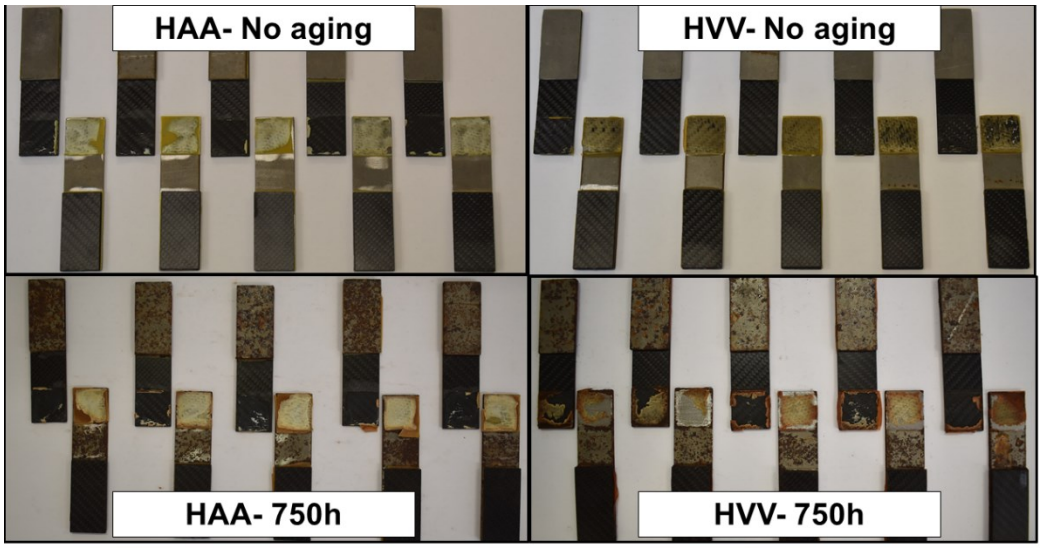

Figure 4.22 - Single Lap Joint coupon tested

4.8.2. Double cantilever beam results

In Table 4.6, Table 4.7 are reported the specimen specifications used for the double cantilever beam test. The IDs from “d19” to “d23” are the no treated specimens, while IDs from “d24 to “d28” are the aged coupon.

ID	Adhesive Thickness [mm]	Adhesive Width [mm]	Adhesive Length [mm]	Adhesive Area [mm²]
HVV-d19	0,50	24,67	97,25	2431,25
HVV-d20	0,48	24,86	96,54	2413,50
HVV-d21	0,49	24,53	94,15	2353,75
HVV-d22	0,48	24,76	97,22	2430,50
HVV-d23	0,48	24,51	98,36	2459,00
HVV-d24	0,47	25,23	97,43	2435,75
HVV-d25	0,50	24,72	97,42	2435,50
HVV-d26	0,48	24,55	95,19	2379,75
HVV-d27	0,48	24,63	94,90	2372,50
HVV-d28	0,47	25,28	97,43	2435,75
Avg.	**0,48**	**24,77**	**95,58**	**2414,72**

Table 4.6 – DCB specimen tested for HVV

ID	Adhesive Thickness [mm]	Adhesive Width [mm]	Adhesive Length [mm]	Adhesive Area [mm²]
HAA-d19	0,45	25,25	95,97	2399,25
HAA-d20	0,43	24,53	96,06	2401,50
HAA-d21	0,46	25,35	95,52	2388,00
HAA-d22	0,47	25,46	94,87	2371,75
HAA-d23	0,43	25,27	97,20	2430,00
HAA-d24	0,45	24,60	95,97	2399,25
HAA-d25	0,44	24,57	96,06	2401,50
HAA-d26	0,45	23,90	95,52	2388,00
HAA-d27	0,42	24,22	94,87	2371,75
HAA-d28	0,46	23,83	97,20	2430,00
Avg.	**0,44**	**24,69**	**95,92**	**2398,1**

Table 4.7 - DCB specimen tested for HAA

The evaluation of the fracture energy in mode I begins when the crack is opening, which occurs at the peak of force, but it is find out considering only the crack opening displacement. Then, according to the Experimental Compliance Calibration (ECC) method, the critical energy release rate G_{Ic} is calculated as:

$$G_I^{ECC} = \frac{nP\delta}{2Ba} \tag{4.1}$$

Where:

- n is the "$\log a - \log C$" plot slope
- P is the force sampled
- δ is the displacement at the hinge
- B is the specimen width

- a is the crack opening length

The G_{Ic} trends is shown in Figure 4.23. The highest peak is reached by HAA in both the configuration and its values of G_{Ic} at 0h is about 63% more than HVV. Nevertheless, after aging the G_{Ic} of HAA drops down after 10 mm while HVV shows a slightly improvement in terms of energy peak.

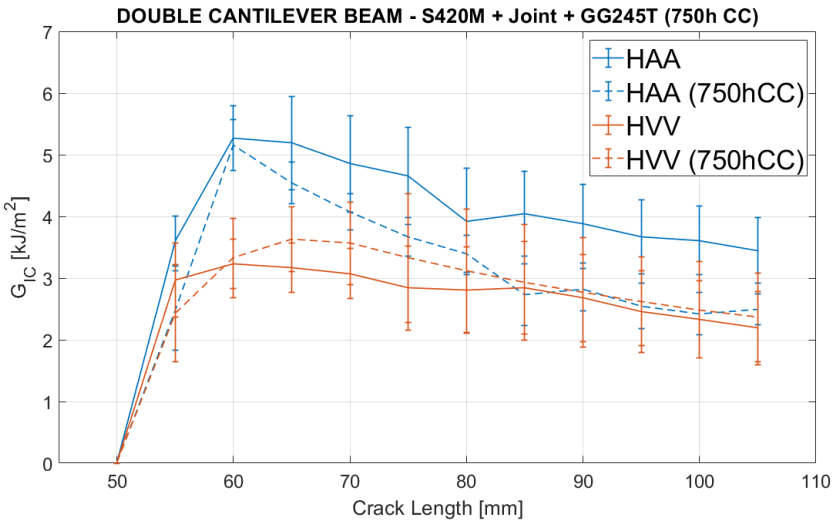

Figure 4.23 – Mode I toughness comparison at 0 h and 750 h

4.8.3. End-notched flexure results

In Table 4.8, Table 4.9 are reported the specimen specifications used for the end-notched flexure test. The IDs from "e29" to "e33" are the no treated specimens, while IDs from "e34" to "e38" are the aged coupon.

ID	Adhesive Thickness [mm]	Adhesive Width [mm]	Adhesive Length [mm]	Adhesive Area [mm²]
HVV-e29	0,50	24,67	97,12	2450,34
HVV-e30	0,48	24,68	95,08	2427,39
HVV-e31	0,49	24,53	95,15	2412,05
HVV-e32	0,46	24,76	95,95	2442,89
HVV-e33	0,48	24,51	95,46	2412,27
HVV-e34	0,47	25,23	96,00	2400,00
HVV-e35	0,50	24,72	95,15	2378,75
HVV-e36	0,48	25,34	95,10	2377,50
HVV-e37	0,49	24,63	97,29	2432,25
HVV-e38	0,47	25,28	96,00	2400,00
Avg.	**0,48**	**24,83**	**95,83**	**2413,34**

Table 4.8 - ENF specimen tested for HVV

ID	Adhesive Thickness [mm]	Adhesive Width [mm]	Adhesive Length [mm]	Adhesive Area [mm^2]
HAA-e29	0,46	25,25	92,97	2324,25
HAA-e30	0,42	24,53	96,02	2400,50
HAA-e31	0,45	25,35	95,84	2396,00
HAA-e32	0,47	25,46	96,80	2420,00
HAA-e33	0,43	25,27	94,86	2371,50
HAA-e34	0,47	24,60	97,85	2446,25
HAA-e35	0,44	24,57	97,35	2433,75
HAA-e36	0,45	23,90	95,96	2399,00
HAA-e37	0,43	24,22	97,19	2429,75
HAA-e38	0,46	23,83	97,85	2446,25
Avg.	**0,44**	**24,69**	**96,26**	**2406,75**

Table 4.9 – ENF specimen tested for HAA

Even in this case, the evaluation of the fracture energy in mode II begins when the crack is opening, which occurs at the peak of force. The Experimental Compliance Calibration (ECC) method has been used to evaluate the critical energy release rate G_{IIc}:

$$G_{II}^{ECC} = \frac{3ma^2p^2}{2B} \tag{4.2}$$

Where:

- m is the "$a^3 - C$" plot slope
- P is the force sampled
- B is the specimen width
- a is the crack opening length

As shown in Figure 4.24, the maximum values of G_{IIc} belong to the HVV that is the 30% higher than the HAA while after 750 h of aging, the HVV performance decreases more than HAA and both maintain the same trend.

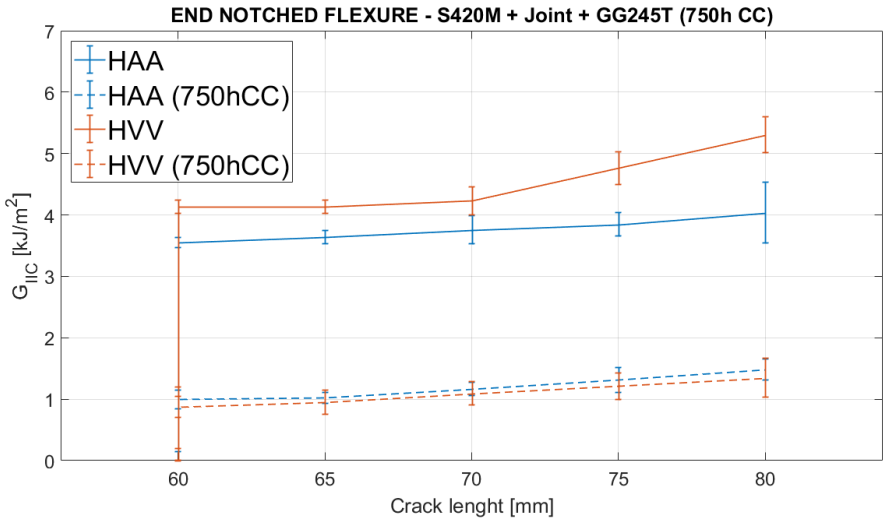

Figure 4.24 – Mode II toughness comparison at 0 h and 750 h

4.9. Synthesis of the experimental results on viscoelastic materials

To sum up the comparison between the two elastomeric compounds, in the following are reported the main characteristics of HVV and HAA:

- HVV loss factor is always higher than HAA before and after the climatic chamber treatment and its trend is almost constant. Moreover, this behavior is confirmed in the range of temperature between -20° C and 60° C. On the other hand, HAA Young's modulus has always higher values than HVV even though it drops of 25% after 750 h aging. In addition, the HAA E modulus increases according to the temperature.

- HVV presents a higher shear joint strength than HAA and this behavior is maintained also after aging. On the contrary, HAA shows the best peeling toughness (mode I) with no climatic chamber treatment while it decrease at similar values of HVV after 750 h, vice versa for the shearing toughness (mode II) in which HVV has the highest value at 0h while after 750h the HAA is slightly over the HVV.

4.10. Virtual-Experimental correlation on Oberst beam test

The aim of this activity is to define the virtual material card that is able to predict the correct damping behavior of the viscoelastic material on the hybrid lower control arm model. In particular, to evaluate the goodness of the virtual fitting, the natural frequency values and the shape of the frequency response functions have been compared. Therefore, the experimental Oberst test has been

simulated in Optistruct by setting a Frequency Response Analysis (FRA). Two different specimen typologies have been modelled and correlated:

1. Structural beam (CFRP T300 GG245T $[0]_3$, 240 g/m^2);
2. One side beam (CFRP T300 GG245T $[0]_3$, 240 g/m^2 + HVV or HAA).

The approach used to model the carbon fiber laminate (with or without VEMs) is the Equivalent Single Layer (ESL) method, where the stacking sequence is modelled on a single mid-surface mesh as shown Figure 4.25. Because the coupon thicknesses are negligible compared to length and width, the shell requirements are satisfied. This modelling technique has been chosen because it will be also adopted on the complete model of the hybrid lower control arm in order to reduce any possible discrepancies between the samples model and the LCA one.

Element properties PCOMPP, PLY and LAMINATE define thickness, orientation and shape of each layer and the mesh size used is equal to 4 mm. For this simulation, a novel Altair feature introduced in version 17 has been adopted: it is the GE USEMAT flag that gives the possibility to define the loss factor for every single material stacked in a laminate. In fact, until version 14, the loss factor was defined only as a global system property with the TABDAMP card. That approach was limitative especially in presence of different material loss factor, as in the case of the hybrid LCA, because it reduced the predictive capabilities of the simulation.

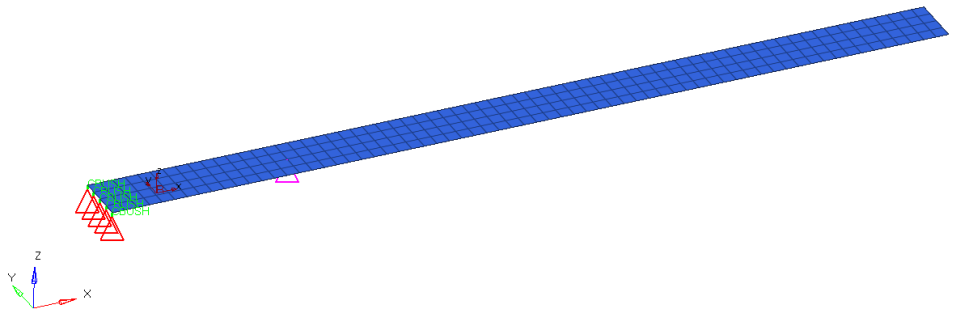

Figure 4.25 – Oberst beam FE model

The material property for CFRP has been defined by MAT 8 material card whose constitutive law are suitable for orthotropic material and, as consequence, for transverse isotropic. Instead, as concerns the damping materials, it has been chosen an isotropic material card with pure elastic behavior (MAT 1 card).This assumption is based on the hypothesis that the simulation is performed in linear field and, as consequence, the material is subjected to small deformations. Moreover, this approach has also been used and validated by Ferraris in its PhD thesis [58].

The structural damping values has been taken into account by activating the material card flag MATF, that permits the definition of material characteristic as function of frequency, including loss factor. In this case, through a TABLED1 load collector, the loss factor values have been set for both CFRP and VEMs.

To simulate the experimental boundary conditions, the sample was constrained at one end, as shown in Figure 4.26. Then, the total length of the meshed specimen corresponds to the free length of the experimental one. A series of springs have been set between the coupon boundary and the fixed support to model the constraint compliance. The springs have been considered deformable only in Z axis (the direction of the motion) with a stiffness of 25 N/mm, while the other translations and rotations have been kept as rigid.

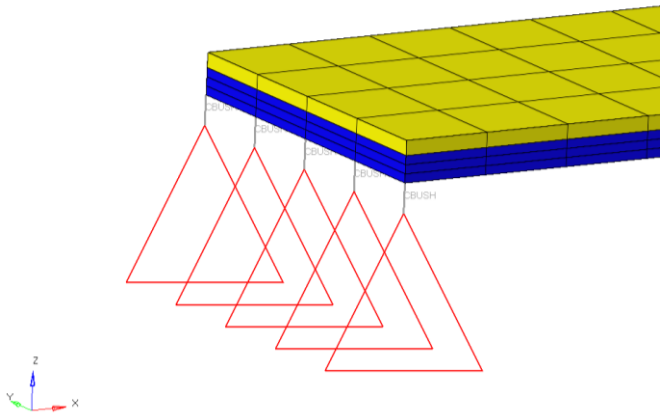

Figure 4.26 – Spring placed between beam and constraint

The definition of the input location is done with the Load Collector "DAREA". It defines the location of the input signal and its direction, as shown in Figure 4.27. In this case, the DAREA constraint has been located exactly in the point in which the magnetic input is positioned in the experimental test bench, as shown Figure 4.28.

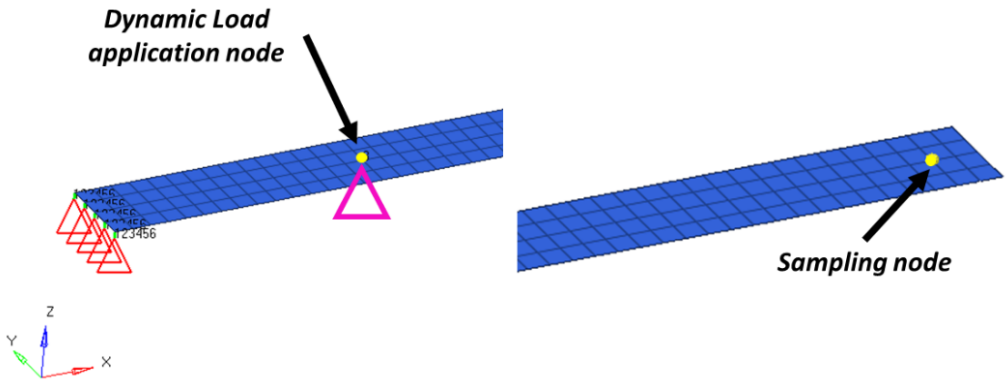

Figure 4.27 – DAREA application point (left), sampling point (right)

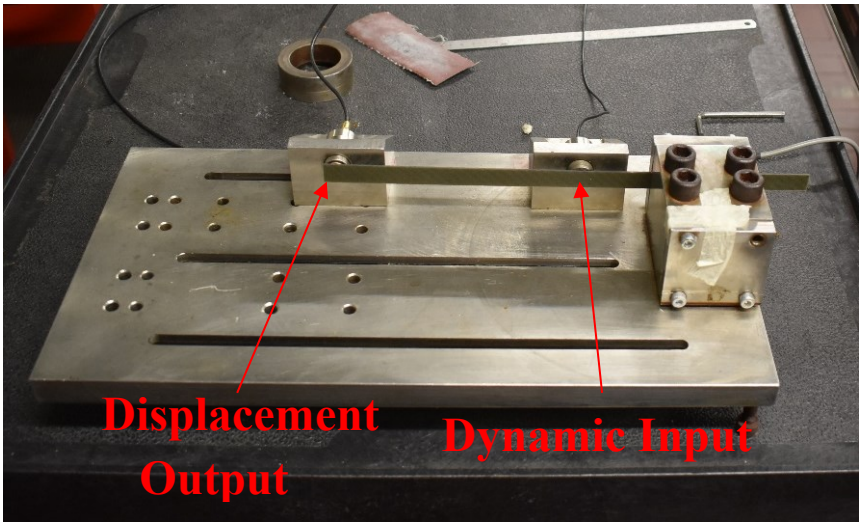

Figure 4.28 – Oberst test sensors configuration

At this point, one problem of the experiment test bench must be considered. Test bench input function at sample is not exactly known. In fact, the input is defined up to the magnetic exciter, but considering the varying distance between transducer and metal plate on the sample, the amplification factor remains unknown. To define the exciting load, another load Collector called "RLOAD" has been set. This load collector permits to define the load applied, in a zone defined by DAREA Card, with the input amplification factor $C(f)$, following the relation of the dynamic load $\{P(f)\}$ defined by the equation [80]:

$$\{P(f)\} = \left\{A\left[C(f) + iD(f)\right]e^{i(\vartheta - 2\pi ft)}\right\} \tag{4.3}$$

To define the $C(f)$ function, a Load Collector is created, which uses the card TABLED1, in which it is possible to define the amplitude of the input function (the Sine–Sweep function is used in the test). In the performed test, the amplitude is kept constant and equal to one, in the frequency range from 0 Hz to 1100 Hz.

As output, it has been chosen the node corresponds to the point in which the output is registered in the ASTM 756-05 test bench, in order to obtain data comparable with the experimental ones.

4.10.1. Structural beam correlation results

The tested structural material is the T300 carbon fiber GG245T twill 2x2 with a mass per area ratio of 240 g/m^2. The stacking sequence is composed by 3 layers oriented at 0°. The FE specimen is shown in Figure 4.29.

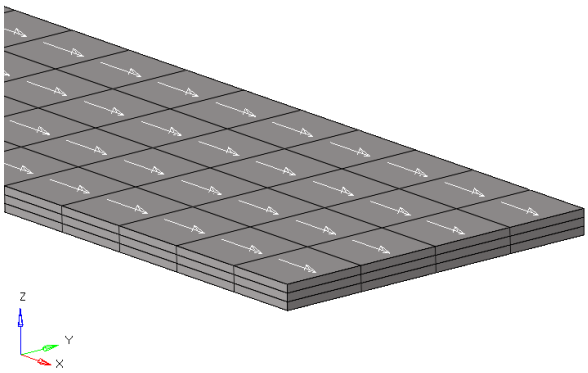

Figure 4.29 – Section of structural beam with fiber orientation

Sample average dimension and characteristics are reported in Table 4.10.

ID	Material	Damping	T [mm]	W [mm]	L [mm]	Mass [g]	Density [g/mm³]
GG245T	T300 CFRP	None	0,9	12,25	299,69	4,8	0,00146

Table 4.10 – Structural beam model dimension

Therefore, to evaluate the consistency of the simulation, the natural frequencies, computed with the simulation method and with the experimental one, are compared in Table 4.11.

Mode	Experimental frequency [Hz]	FEM frequency [Hz]	Difference [%]
Fn 1	18,56	18,77	+1,13
Fn 2	114,75	117,47	+2,37
Fn 3	325,825	328,11	+0,70
Fn 4	639,275	640,52	+0,19
Fn 5	1065,3	1053,2	-1,13

Table 4.11 – CFRP frequency correlation

The experimental values of frequency have been obtained as the average of the tested structural beam. From the frequency comparison, the maximum difference observed is slightly over the 2% on the second natural frequency, while the other variation can be consider negligible. Moreover, in Figure 4.30 is reported the comparison between the FEM and the experimental (EXP) receptance. The trend of the FEM frequency response is very close to experimental, hence, the virtual model can be consider very good correlated with the experimental data.

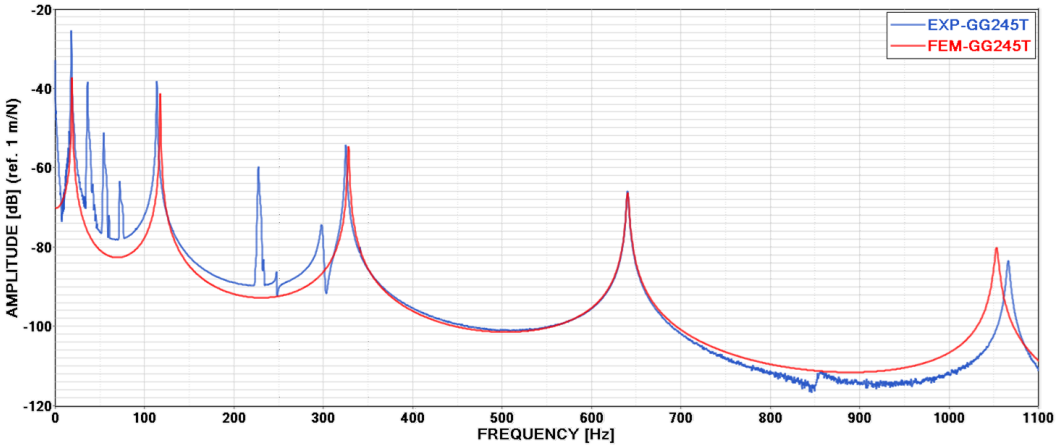

Figure 4.30 – Receptance vs. frequency for EXP and FEM structural beam

4.10.2. One side beam correlation results

Once the structural beam has been correlated, the one side FE models have been created. The damped beams are made of T300 carbon fiber GG245T twill 2x2 co-cured with HVV or HAA. The stacking sequence is composed by 3 layers of CFRP oriented at 0° with one layer of damped material on top. An example of the FE one side specimen is shown in Figure 4.31.

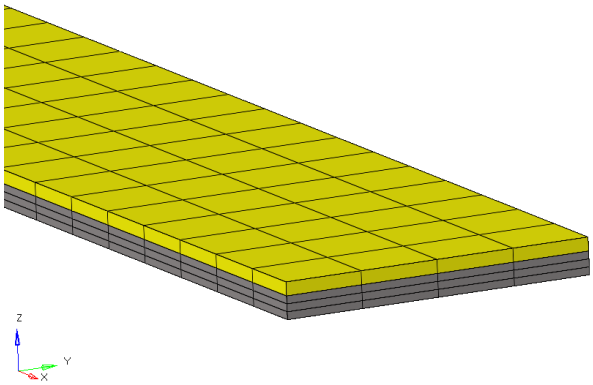

Figure 4.31 – One side beam model with HVV (in yellow)

Samples dimension and characteristics are reported in Table 4.12.

ID	Material	Damping	T [mm]	W [mm]	L [mm]	Mass [g]	Density [g/mm³]
HVV	GG245T+HVV	HVV	1,41	12,48	300,17	7,55	0,001431
HAA	GG245T+HAA	HAA	1,32	12,55	298,35	6,95	0,001402

Table 4.12 – One side beam models data

In the following, the HVV model has been reported. As concerns the frequency comparison, the major difference is observed in the first natural frequency that is usually discarded from the evaluation, consisting in a forward shifting of 2%, as reported in Table 4.13. Finally, the difference between experimental and FEM is

very low and this is also confirmed by the shape of the FEM frequency response, illustrated in Figure 4.32, that is close to the experimental trend, especially in terms of damping.

Mode	Experimental frequency [Hz]	FEM frequency [Hz]	Difference [%]
Fn 1	15,98	16,36	+2,37
Fn 2	99,23	101,36	+2,14
Fn 3	283,32	285,79	+0,87
Fn 4	560,64	557,51	-0,55
Fn 5	930,78	915,68	-1,62

Table 4.13 – HVV frequency correlation

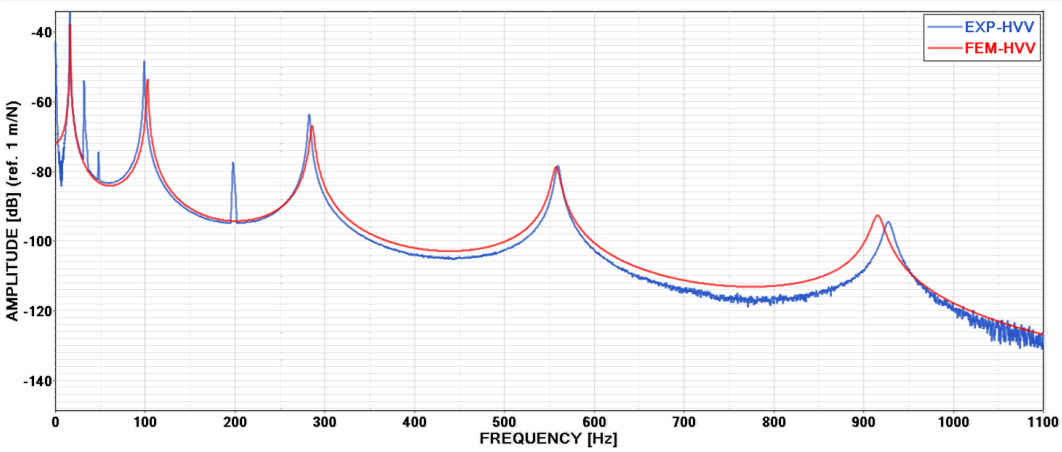

Figure 4.32 – HVV receptance vs. frequency for EXP and FEM structural beam

As concerns the HAA simulation, in Table 4.14 are reported the natural frequencies comparison. As for the HVV, the major difference is observed in the first natural frequency that is usually discarded from the evaluation, consisting in a forward shifting of 3%. Even in this case, the final correlation obtained is very good especially in terms of damping behaviour as shown in Figure 4.33.

Mode	Experimental frequency [Hz]	FEM frequency [Hz]	Difference [%]
Fn 1	16,66	17,2	+3,27
Fn 2	104,19	106,63	+2,33
Fn 3	297,55	300,47	+0,98
Fn 4	590,09	586,1	-0,67
Fn 5	981,38	962,47	-1,92

Table 4.14 – HAA frequency correlation

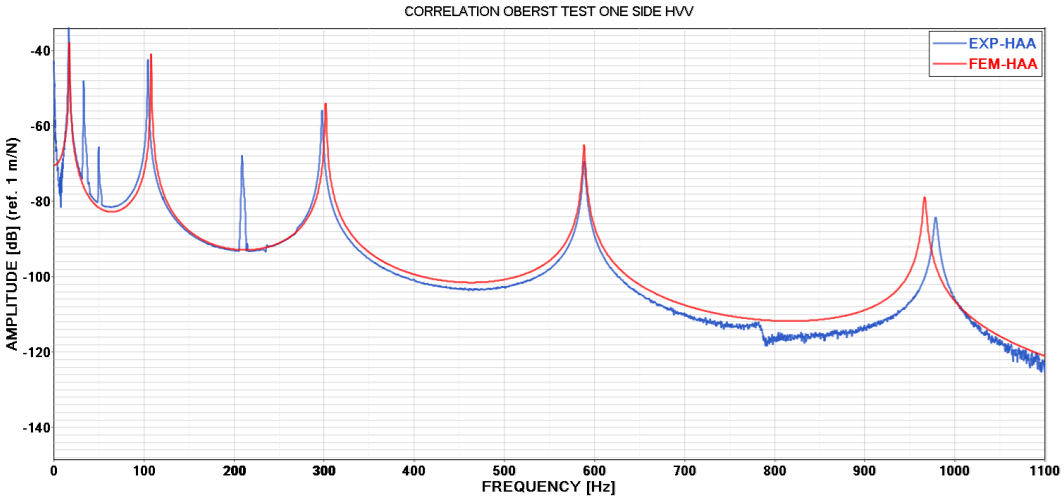

Figure 4.33 - HAA receptance vs. frequency for EXP and FEM structural beam

Adding the damping material on one side of structural beam, the response changes sensibly as shown in Figure 4.34. Firstly, all the peaks are smoothed down thanks to the damping characteristics of the two materials and, as a side effect, the natural frequencies are shifted backward because of the mass added to the sample and the variation of the overall stiffness. Therefore, the response function of the one side layout beam is a superposition of the structural response and the two effects of damping material. Secondly, from the experimental FRFs it's clear that the damping properties of the HVV are predominant in comparison with the HAA material.

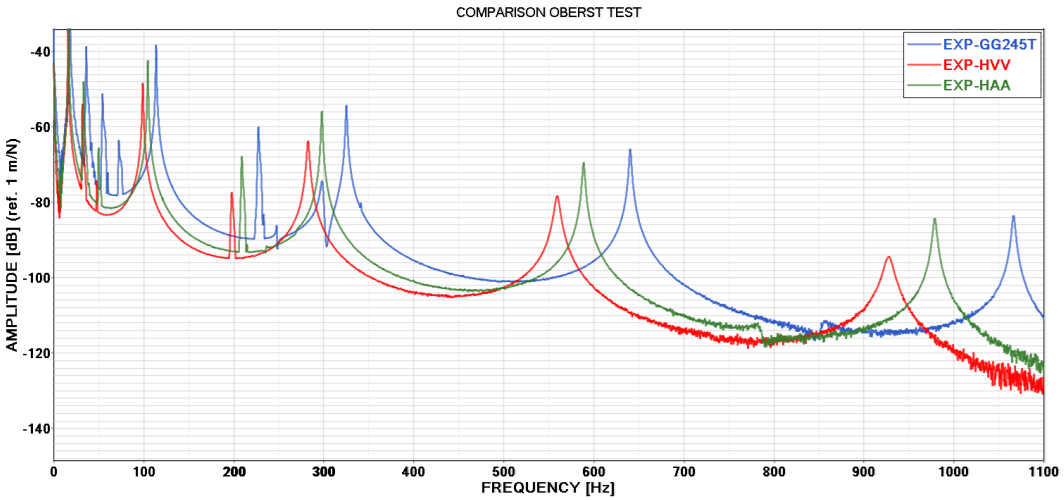

Figure 4.34 – Experimental FRF comparison between structural and one side beams

In addition, FEM simulations on Oberst tests are able to catch the experimental difference between these three kinds of specimens as well as the FRFs trend as highlighted in Figure 4.35.

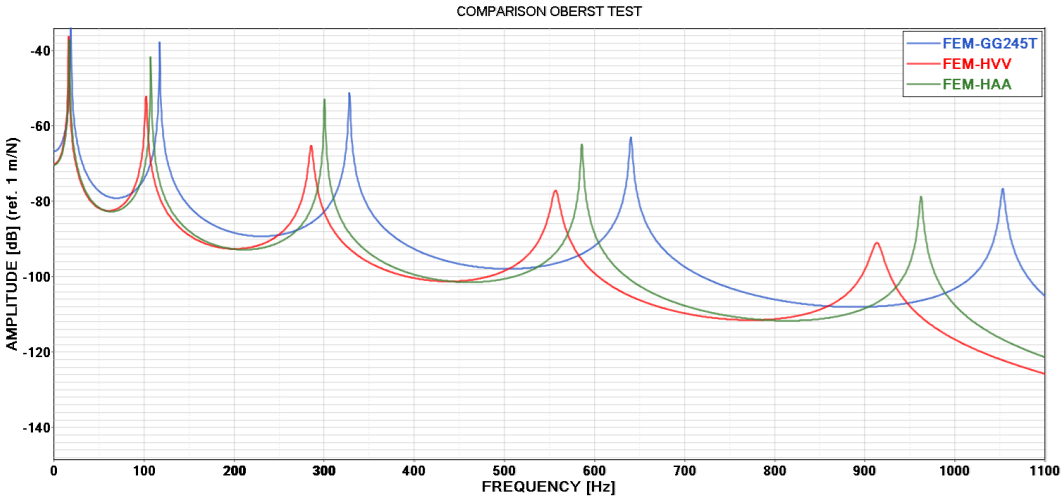

Figure 4.35 – FEM FRF comparison between structural and one side beams

Therefore, in order to obtain a very good correlation level, it is important to remark some important recommendations:

- FEM specimens have to reproduce the same characteristics of the experimental coupons in terms of geometric dimensions and mass values
- Free length, exciting and acquisition point on the virtual specimen have to be as much as possible close to the real coupon value
- FEM modelling technique adopted on specimen level have to be the same on component level in terms of element properties and material cards to contain further correlation errors
- Loss factor values have to be implemented in function of frequency especially for the damping material. Optistruct GE USEMAT represents a useful tool to consider loss factor for each material stacked in a laminate contemporaneously.

On the other hand, the use of a pure elastic material card (MAT1) to model the VEMs could be consider a limitation in the Oberst fitting procedure. Nevertheless, because the behaviour of the real sample and the simulation type are linear, this approximation has not affected the accuracy of the fitting results and, as consequence, has been considered valid for dynamic simulation. However a further validation is needed in case of structural application in order to assure the elastic condition respected.

4.11. Final considerations on VEMs characterization

In conclusion, two viscoelastic compound have been tested in order to evaluate their damping and adhesive properties. Experimental tests have shown that the HVV compound presents the best damping performance especially for its capability to maintain a high constant loss factor even after 750 h of climatic chamber.

In addition, because HVV has the highest shear toughness and also the highest shear strength, it represents the best material in terms of adhesive properties.

In the end, in order to achieve the NVH performance in terms of vibration reduction as defined in the research targets, the HVV compound has been chosen as interlaminar material between steel and carbon fiber.

As regards the virtual correlation analysis on the Oberst test, the results obtained have been allowed to define a specific Optistruct card material that is able to reproduce virtually the damping effect of the HVV in a very good way. As consequence, this card material developed has been used for hybrid LCA model for the frequency response analysis.

Chapter 5

Mechanical characterization on hybrid LCA materials

The material characterization activity has been conducted to investigate the experimental values necessary to define the FEA card materials in RADIOSS (Figure 5.1). This step is crucial to obtain a robust design process and predictable simulations especially in case of multi-material components. Hence, in this chapter is presented the mechanical characterization of carbon fibers and steel materials whose the hybrid lower control arm is made of. Finally, for each materials is presented the fitting process adopted and the results of the virtual correlation.

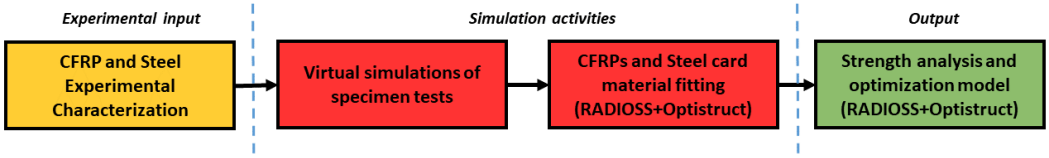

Figure 5.1 – Mechanical characterization aim and workflow

In Table 5.1 are summarized the set of tests conducted on carbon fibers and steel.

Material	Test	Aim
T300-GG245T	Tensile, compression, bending	Young moduli and maximum stress for each direction
T700-GG430T	Tensile, compression, bending	
M46J-UD	Tensile, compression, bending	
STEEL S420MC	Tensile	Young moduli, yield and maximum tensile stress

Table 5.1 – Experimental test set-up on CFRP and steel

All the experiments were done using an Instron Model 8801 machine with a maximum load capacity of 100 kN. A biaxial extensometer, capable of recording longitudinal deformation up to 25 mm and transverse up to 1 mm per side, or a strain gauge (HBM LY-48-3/350 Ohm) were attached to each specimen to sample the strain measurements. For each specimen, the force-displacement curves and stress-strain were calculated along with elastic modulus, maximum stress, strain at break and maximum load using the data obtained directly. A dedicated Matlab code has been developed and used to obtain mean value curves and the standard deviation.

5.1. Tensile test ASTM D3039

The ASTM D3039 [81] is used to determine the longitudinal and transverse elasticity modules, the Poisson module and the tensile strength in the longitudinal and transverse directions. This standard is applied both for fabric and for unidirectional fiber reinforced plastic materials. The composite material is usually made of laminates, therefore, rectangular section specimens are recommended to avoid possible fiber discontinuity. The specimens layout prescribed is illustrated in Figure 5.2.

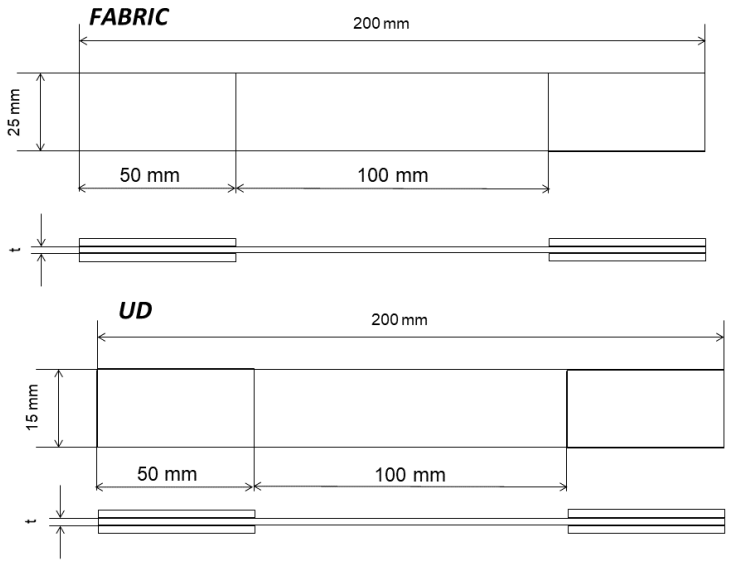

Figure 5.2 - ASTM D3039 dimensions for fabric (top) and UD (bottom)

5.2. Compression test ASTM D3410

Compression tests have been performed in compliance of the ASTM D3410 standard [82]. Usually, these tests present important criticality due to the buckling condition that can affect the real compression behaviour of the material, especially in terms of failure stresses. For this reason, the IITRI anti-buckling device has been used during the test to assure the longitudinal alignment between the specimen and the direction of load. This improvement needs to increase the quality of the

experimental results and to delay as much as possible the buckling collapse. In Figure 5.3 are shown the apparatus and the specimens layout used.

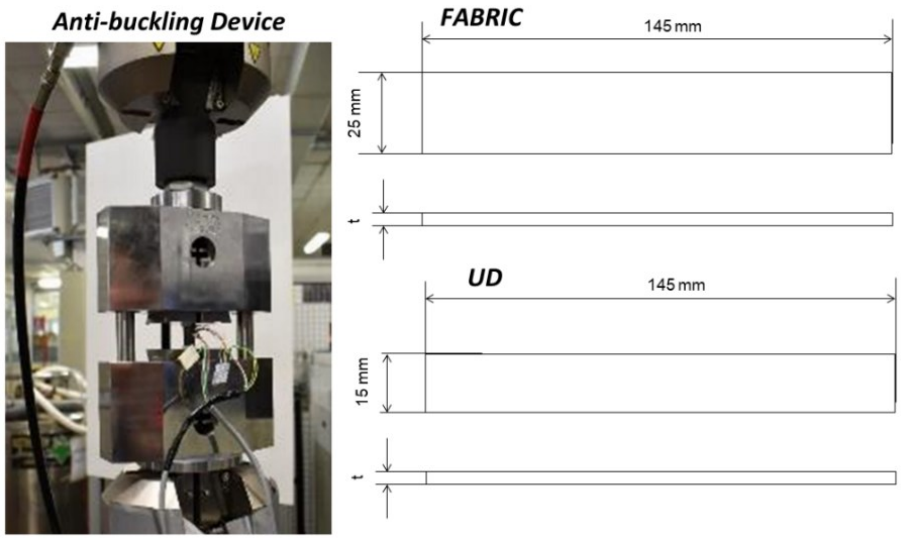

Figure 5.3 - ASTM D3410 apparatus (left) and specimens (right)

5.3. Bending test ASTM D790

The flexural test has been done following the ASTM D790 [83] prescriptions. The four point bending configuration has been chosen in order to obtain a constant bending moment in the localized area between the two upper cylinders. Specimens dimension and apparatus are depicted in Figure 5.4.

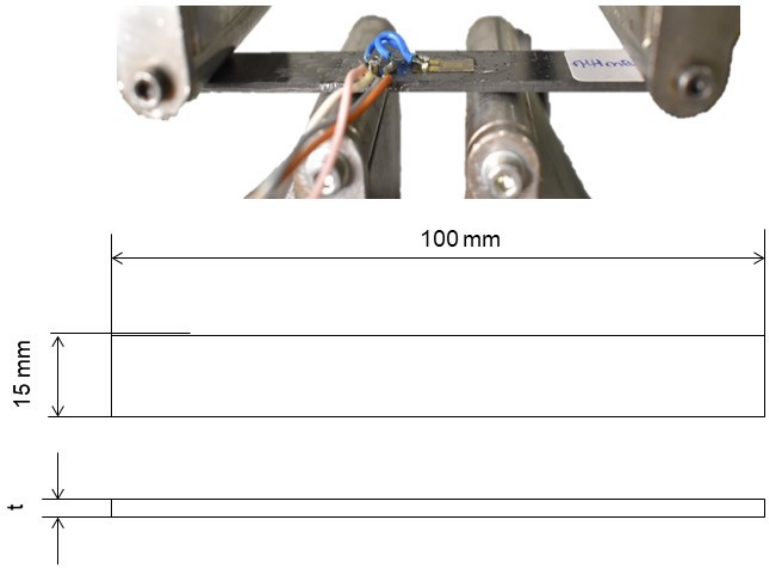

Figure 5.4 - ATM D790 apparatus (top) and specimen (bottom)

5.4. Tensile test ASTM E8/E8M-16A

The ASTM E8 [84] is the standard reference for tensile tests on metals to investigate Young modulus, Poisson's ratio, yield stress and ultimate tensile stress. The dogbone specimen layout are reported in Figure 5.5.

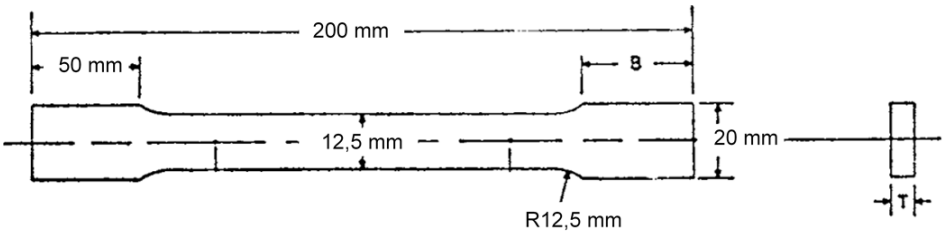

Figure 5.5 – ASTM E8 specimen dimension

5.5. Experimental results

In this paragraph are presented the results obtained from the mechanical tests on carbon fibers and steel, where five specimens have been tested for each proof. In the following tables, material properties are summarized according to the mean values elaborated from experimental test.

In Table 5.2 are presented the experimental mean values for T300 GG245T. As the material is balanced, the properties are assumed to be the same for both 0° and 90°. In Figure 5.6 are shown the specimen tested.

	TENSILE 0°	COMPRESSION 0°	TENSILE 45°	BENDING 0°
Elastic Modulus [GPa]	57	58	3,2	59
Poisson's Ratio	0,04	-	-	-
Maximum Stress [MPa]	564	529	123	824
Deformation at breaking [mm/mm]	0,013	0,009	0,32	0,014

Table 5.2 - Mechanical properties of T300 epoxy GG245T

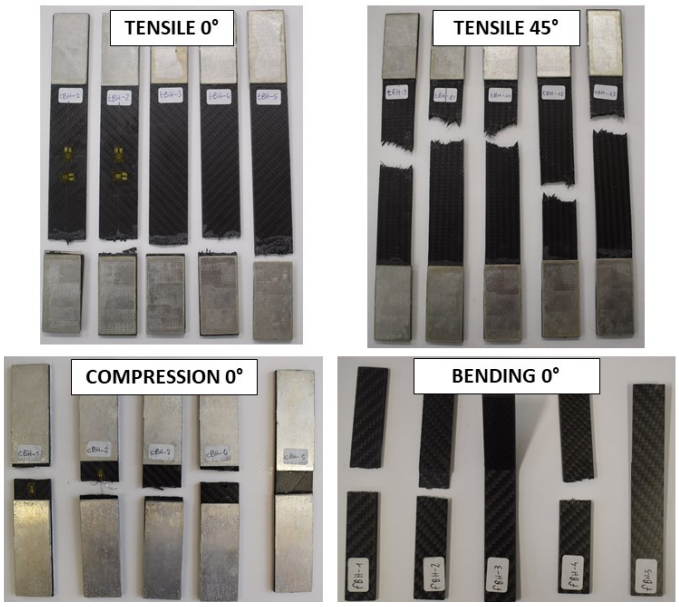

Figure 5.6 - GG245T samples tested

In Table 5.3 are shown the experimental mean values for T700 GG430T. Even in this case, because the material is balanced, the properties are assumed to be the same for both 0° and 90°. In Figure 5.7 are presented the set of specimens tested.

	TENSILE 0°	COMPRESSION 0°	TENSILE 45°	BENDING 0°
Elastic Modulus [GPa]	59	60	3,6	65
Poisson's Ratio	0,05	-	-	-
Maximum Stress [MPa]	988	605	104	818
Deformation at breaking [mm/mm]	0,028	0,010	0,32	0,014

Table 5.3 - Mechanical properties of T700 epoxy GG430T

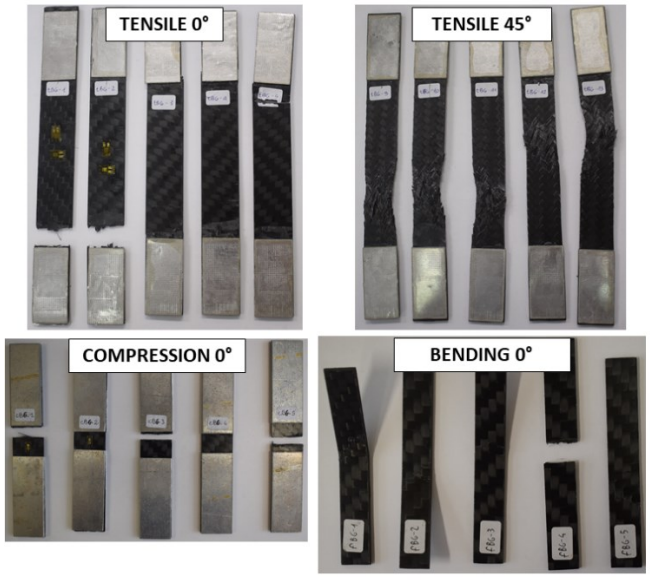

Figure 5.7 - GG430T samples tested

Finally, in Table 5.4 are summarized the experimental mean values for UD M46J. In Figure 5.8 are reported the UD coupons tested.

	TENS. 0°	COMP. 0°	TENS. 45°	TENS. 90°	COMP. 90°	BEND. 0°	BEND. 90°
Elastic Modulus [GPa]	221	210	2,6	6,2	6,9	217	6,6
Poisson's Ratio	0,17	-	-	-	-	-	-
Maximum Stress [MPa]	1821	903	36	17	72	1096	39
Deformation at breaking [mm/mm]	0,014	0,0042	0,0036	0,003	0,01	0,005	0,006

Table 5.4 - Mechanical properties of UD M46J epoxy

Figure 5.8 - M46J specimen tested

As concerns steel tensile tests on the S420MC, in Table 5.5 are reported the average values for Young modulus, Poisson's ratio, and maximum stress and strain. Specimen tested are reported in Figure 5.9.

	TENSILE TEST
Elastic Modulus [GPa]	208
Poisson's Ratio	0,3
Yield Stress (Rp02) [MPa]	422
Maximum Stress [MPa]	506
Deformation at breaking [mm/mm]	0,26

Table 5.5 – Mechanical properties of steel S420MC

Figure 5.9 - S420MC specimen tested

5.6. Virtual-Experimental correlation on carbon fibers and steel

In this section is presented the correlation activity between simulation and experimental tests on the lower control arm structural materials. For each material, a virtual card material has been set accordingly to the solver and the modelling adopted. The following simulation has been performed and correlated on RADIOSS because its card material can be also defined in the non-linear field. For this reason, it is possible to evaluate and correlate the complete stress-strain curve as opposed to Optistruct. As concerns the tests, they are:

1. Tensile, compression and flexural tests on UD and fabrics carbon fibers.
2. Tensile test on steel.

The card material obtained will be used in the model presented in Chapter 7 and chapter 8 for the complete correlation on the lower control arm. Nevertheless, the elastic value fitted in RADIOSS material card has been used inside the Optistruct model in order to be aligned to the experimental values.

5.6.1. Correlation on CFRP mechanical tests

The experimental tests of tensile, compression and bending allow the investigation of the main material parameters in terms of elasticity, non-linearity and failure. The definition of a fitting procedure is crucial to increase the reliability of the virtual results and to limit the errors inside certain values. Moreover, the accuracy of the correlation are also influenced by the mesh size and the quality of

the elements, especially as concern failures. Therefore, the fitting models have to respect as much as possible the same parameters of the final component model.

In RADIOSS, the law material used for composite is the LAW25 (COMPSH) with CRASURV formulation, developed for orthotropic shells. The CRASURV is an advanced option allows taking into account work plasticity hardening separately for each orthotropic direction [85]. All yield stresses are expressed as a function of plastic work, and, as result, plasticity hardening is anisotropic. For this reason, it represents an improvement of the standard Tsai-Wu formulation. A detailed explanation of the law material is reported on [86-88].

Simulations have been performed with QBAT element formulation, a fully-integrated shell element based on Batoz theory [89] with four Gauss points used to evaluate the nodal forces. The mesh size chosen is the same of the average value on the lower control arm model is 4 mm.

In order to find the correct fitting values, a specific procedure has been set which consist of three main simulation steps:

1. One Element Test (OET).
2. Specimen Test (ST).
3. Bending test (FLEX).

This procedure permits the validation of a single material card that fit simultaneously all the experimental curves.

The One Element Test consists in a simulation of several separated single element oriented at 0°, 90° and 45° both for tensile and compression. This test is necessary to investigate the pure element behaviour accordingly to the parameters set. Each element is modelled with four dummy layers oriented at a given inclination with a fictitious thickness of 1 mm. The element numbers depend on the typology of material to fit. In the specific case of this thesis, for unidirectional the model is composed by five elements, as shown in Figure 5.10, in order to define:

1. Elastic moduli on plane (E_1, E_2, G_{12});
2. Tensile and compression properties at 0° and 90°;
3. Tensile properties at 45°.

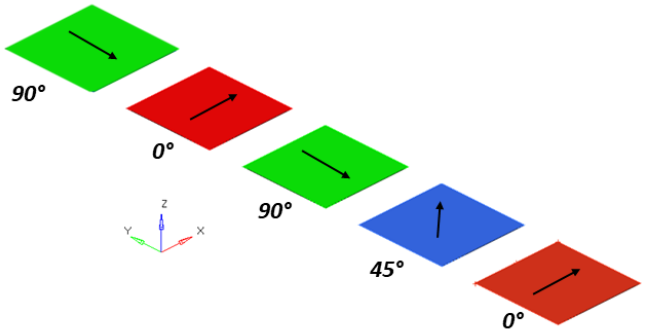

Figure 5.10 – Example OET simulation on UD M46J

On the other hand, for the two fabric, four elements are sufficient to define the complete behavior. The constraints are set in each nodes in order to allow only the in-plane deformation without over-constraint the elements. An imposed displacement has been applied on the two nodes free to move in X direction. The simulation outputs are the elemental stress\strain values.

In the specimen test simulation, the gauge length of the coupons are reproduced. In this case, the global response of the material is tested as results of the interaction between different elements and more real boundary conditions. The number of specimen simulated is the same of the relative OET but each coupon is modelled with the experimental thicknesses and dimensions. Moreover, the constraints configuration is different from OET simulation, as shown in Figure 5.11.

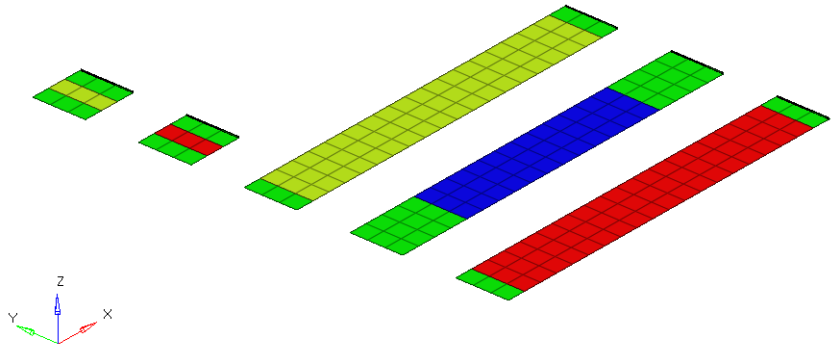

Figure 5.11 – Example of specimen simulation on UD M46J

Two spiders of rigid elements are applied in both the end: on one side, the master node is fully constrained while in the other an imposed displacement is applied in X direction. The simulation outputs consist in force/displacement values subsequently converted in stress\strain as prescribed by the standard.

Finally, the flexural test simulation is performed, in particular a four point bending test. This analysis needs to validate simultaneously the traction and compression behavior of the material card and allows a tuning operation for failure parameters. The specimen is placed between two couple of rigid cylinders whose span is defined from the experimental set-up, as illustrated in Figure 5.12.

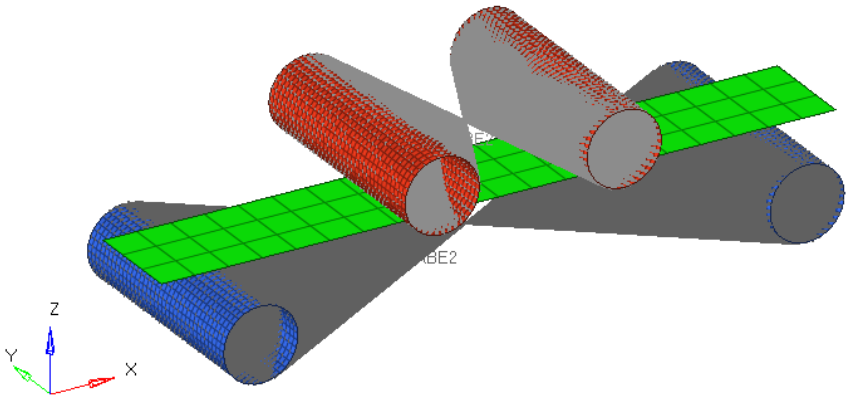

Figure 5.12 – Four points bending simulation test

The top two rolls are free to move against the coupon while the bottom two are fixed. A general auto-contact nodes-to-surfaces (TYPE 7) is created between all the simulation components in order to transmit forces from specimen to cylinders. Even in this case, the output is represented by a force-displacement plot converted in stress-strain as prescribed by standards.

For the sake of simplicity, the correlation results on the three carbon fibers material has only been reported for the ST and for the FLEX simulations.

5.6.2. Fitting results on CFRP UD M46J

The UD specimens are made of M46J carbon fiber composed by 8 layers oriented accordingly to the test. Sample dimensions and characteristics are reported in Table 5.6.

ID	T [mm]	W [mm]	L [mm]	Upper span [mm]	Lower span [mm]
TENSILE 0°	1,19	15,11	99,40		
TENSILE 90°	1,22	14,85	99,07		
TENSILE 45°	1,21	15,03	99,40		
COMPRESSION 0°	1,23	15,35	15,01		
COMPRESSION 90°	1,23	14,95	15,10		
BENDING 0°	1,21	15,24	100,20	27	81
BENDING 90°	1,21	15,13	100,10	27	81

Table 5.6 – UD specimens dimensions and set up for FE analysis

Comparison between experimental and virtual results are presented in Figure 5.13, where they have been overlaid and the experimental standard deviation has been also taking into account.

The global correlation result is very good and all the virtual curves lay inside the experimental standard deviations. However, the main differences regard strains at breaking: the most critical simulations are those at 90° where the maximum difference is 8% both in bending and in tensile. Nevertheless, the other difference are considered negligible.

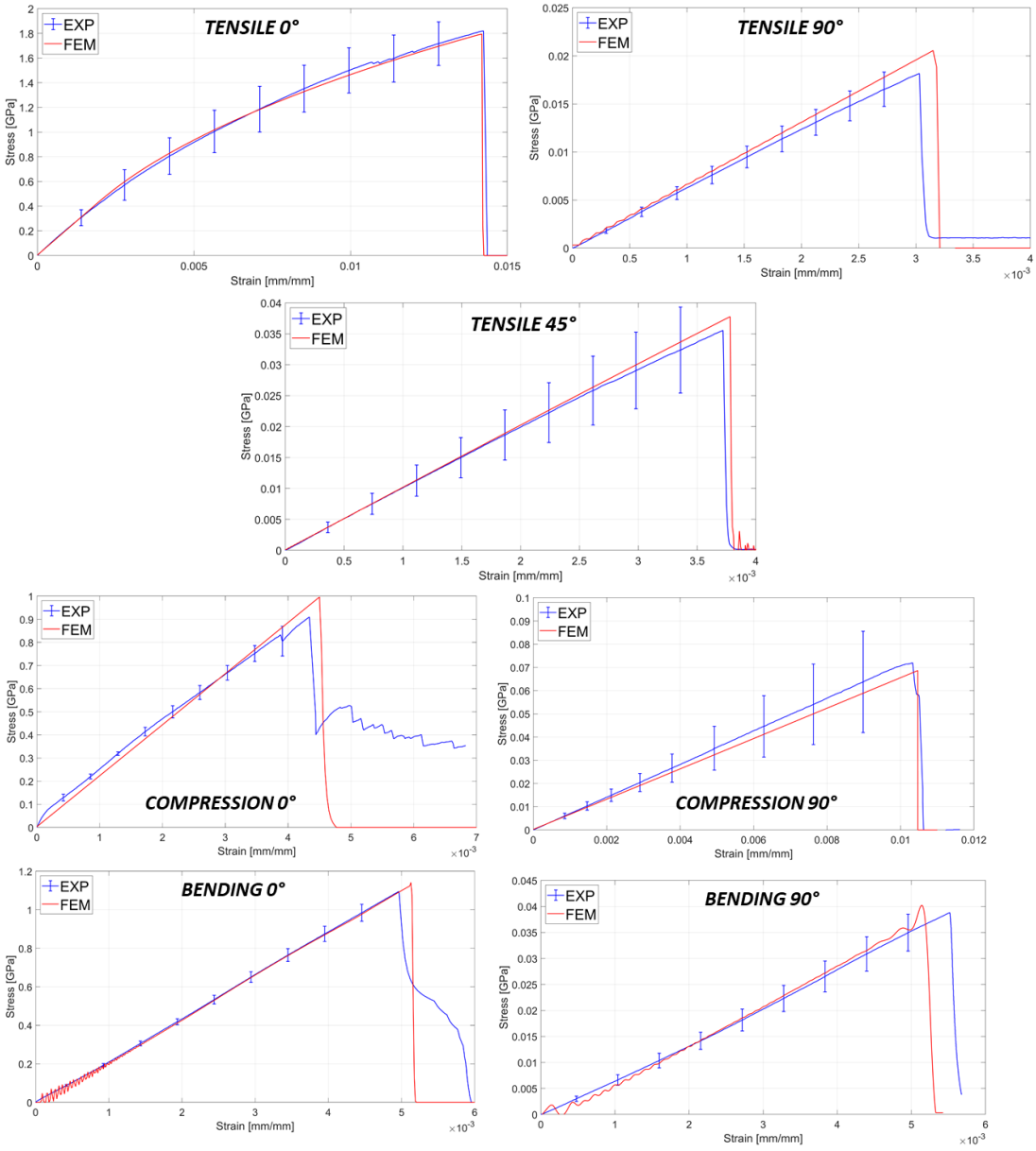

Figure 5.13 - Virtual and experimental comparison on M46J

5.6.3. Fitting results on CFRP T300-GG245T

The GG245T specimens are made of T300 carbon fiber composed by 8 layers oriented accordingly to the test. In this case, the simulation performed are only five because for twill fabric the properties at 90° have been assumed as the same of 0°. Sample dimension and characteristics are reported in Table 5.7.

ID	T [mm]	W [mm]	L [mm]	Upper span [mm]	Lower span [mm]
TENSILE 0°	2,22	24,88	100,04		
TENSILE 45°	2,23	24,87	100,03		
COMPRESSION 0°	2,21	24,87	14,98		
BENDING 0°	2,23	14,82	100,01	27	81

Table 5.7 – GG245T specimens dimensions and set up for FE analysis

In this case, it has been necessary to increase the maximum tensile strain at 0° of 5% to fit in a very good way the bending test, as illustrated in Figure 5.14. As regards tensile test at 45°, the trend carried out from FEM is defined by the parameters used to fit contemporaneously tensile, compression and bending at 0°. Moreover, the strong non-linearity of the tensile test at 45° makes difficult the fitting by the analytical formulation of the LAW 25 power law. Although the FEM curve does not lay always inside the experimental standard deviations, the global trend is considered acceptable.

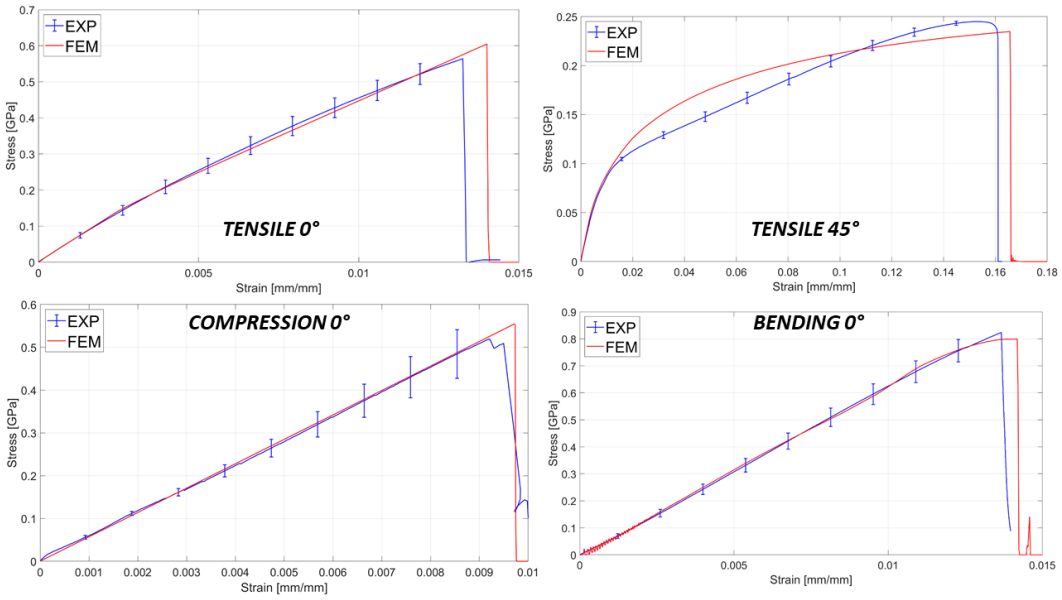

Figure 5.14 - Virtual and experimental comparison on GG245T

5.6.4. Fitting results on CFRP T700-GG430T

The GG430T specimens are made of T700 carbon fiber composed by 4 layers oriented accordingly to the test. Sample dimension and characteristics are reported in Table 5.8.

ID	T [mm]	W [mm]	L [mm]	Upper span [mm]	Lower span [mm]
TENSILE 0°	1,81	24,77	100,28		
TENSILE 45°	1,80	24,75	100,14		
COMPRESSION 0°	1,85	24,77	14,98		
BENDING 0°	1,85	14,78	100,10	27	81

Table 5.8 – GG430T specimens dimensions and set up for FE analysis

Correlation results has been reported in Figure 5.15, where virtual curves have been overlaid on the experimental ones together with their standard deviation.

For the GG430T, compression test presents the major deviation from experimental results. The difference is highlighted especially in the last part of the curve, where buckling effects affect the material behavior before rupture. However, the parameters set for tensile and compression at 0° have been permitted a precise fitting of the bending test.

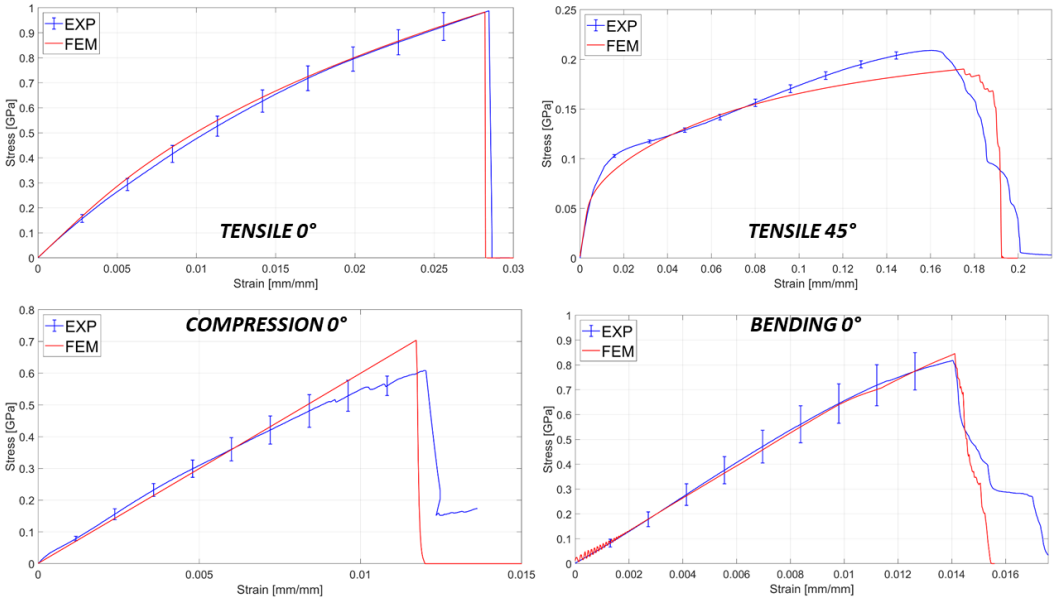

Figure 5.15 - Virtual and experimental comparison on GG430T

5.6.5. Correlation on steel mechanical tests

Many constitutive law are listed in RADIOSS to model isotropic materials such as steel or aluminium. In particular, for the hybrid lower control arm application, it has been chosen LAW36 (PLASTAB). This law models an isotropic elastic-plastic material using user-defined curve for the work-hardening portion of the stress-strain curve as for instance plastic strain vs stress. Moreover, LAW36 is compatible with the most used element properties for hybrid composite laminate.

In this case, a single specimen simulation has been set to find out the fitting parameter. Therefore, the dogbone coupon has been created in Hypermesh as shown in Figure 5.16.

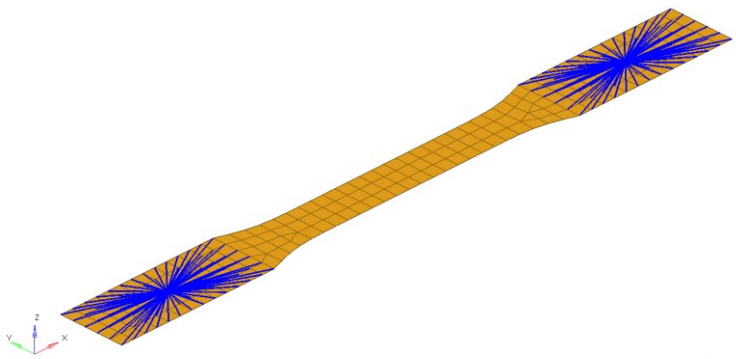

Figure 5.16 – Dogbone specimen for steel S420MC

A mesh size of 4 mm has been adopted and PSHELL element property with QEPH formulation has been selected for shell elements. Two spider of rigids have been created on the tab areas in order to fix one specimen end and pull the other. As output, FEM plots force and displacement that are converted in engineering stress and strain.

5.6.6. Fitting results on steel S420MC

The S420MC sample dimension are reported in Table 5.9, where L_0 is the gage length considered to calculate the strain.

ID	T [mm]	W [mm]	L_0 [mm]
TENSILE TEST	1,91	12,49	60

Table 5.9 - Steel specimen dimensions and set up for FE analysis

As highlighted in Figure 5.17, the correlation between virtual simulation and experimental test has successfully obtained.

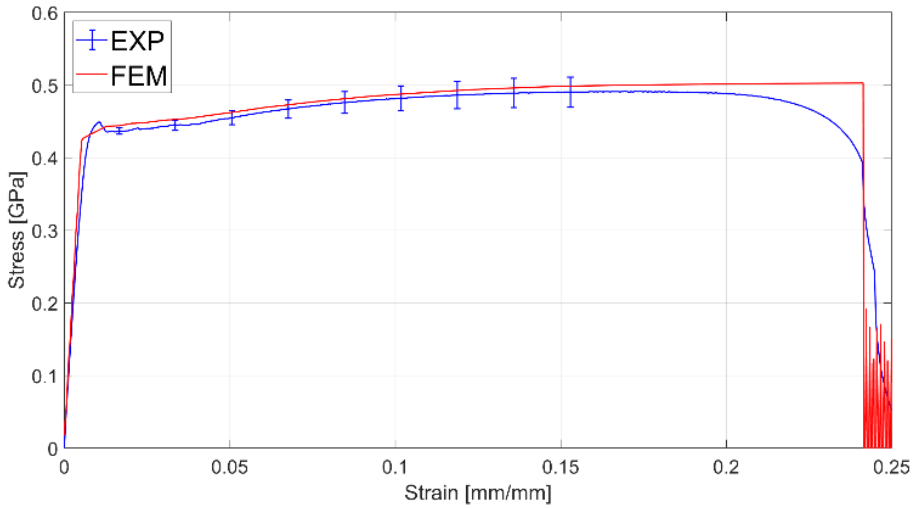

Figure 5.17 - Virtual and experimental comparison on S420MC

5.7. Final considerations on materials characterization

In conclusion, CFRP materials composing the structural cover of the hybrid LCA has been characterized according to the ASTM standards for tensile, compression and bending tests.

A very good correlated material card has been created for RADIOSS solver, editing LAW 25 (CRASURV) parameters. In addition, the steel alloy of the baseline LCA has been characterized according to the ASTM for metal tensile tests. Even in this case, the experimental results have been successfully fitted in RADIOSS by using LAW36 (PLASTAB) isotropic elastic-plastic material card.

The elastic values fitted and validated in RADIOSS have also been used for the respective linear elastic material card in Optistruct, in particular MAT8 for

CFRP and MAT1 for steel. These data obtained have been used inside the optimization analysis and, subsequently, in the frequency response model and in the longitudinal strength simulation.

Finally, in Table 5.10 have been summarized the main mechanical properties of the materials tested compiled inside the FEM material card.

	UD M46J	**T300 GG245T**	**T700 GG430T**	**S420MC**
E_1 [GPa]	220	57	59	208
E_2 [GPa]	6,2	57	59	-
ν	0,17	0,04	0,05	0,3
G_{12} [GPa]	2,6	3,2	3,6	-
σ^t_{1max}[MPa] - σ_{Rp02}[MPa]	1830	564	988	422
σ^t_{2max}[MPa] - σ^t_{max}[MPa]	17	564	988	506
σ^c_{1max}[MPa]	903	529	605	-
σ^c_{2max}[MPa]	71	529	605	-
τ^t_{12max}[MPa]	35	123	104	-

Table 5.10 - Experimental mechanical properties of arms CFRP and steel

Chapter 6

Hybrid LCA optimization and manufacturing

In this chapter, the development of the hybrid LCA is discussed. First of all, the optimization process implemented in Optistruct is explained in detail by describing the three main phases of concept, sizing and shuffling as well as the FE model created. The optimization analysis has been addressed to minimize the mass of the LCA while maintaining the same longitudinal and lateral stiffness. Once the optimized model has been refined to face the composite manufacturing issues, it has been compared virtually to the baseline one to evaluate the performance in terms of special and misuse events strength. After the targets achievement validation, the manufacturing process has been reported through the complete description of the milling operation on the steel shape and the subsequent hand lay-up lamination. In Figure 6.1 is summarized the process workflow.

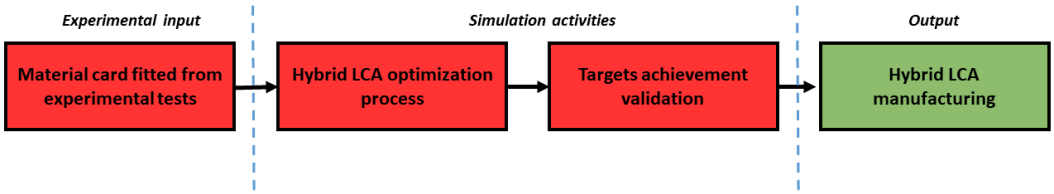

Figure 6.1 – Chapter 6 aim and workflow

6.1. Composite optimization in Optistruct

Composite material structures offer higher design freedom and flexibility thanks to the material properties locally tailored. Composite optimization is usually a big challenge and in the case of the lower control arm represents a necessary step

due to the design complexity of the component. Moreover, composite behaviour is strongly influenced by stacking sequence adopted and ply orientation. Considering, for example, a simple composite plate complying the Classical Laminate Theory (CLT) [90] requirements, it is possible to define the constitutive relationship:

$$\begin{Bmatrix} N_x \\ N_y \\ N_{xy} \\ M_x \\ M_y \\ M_{xy} \end{Bmatrix} = \begin{bmatrix} A_{11} & A_{12} & A_{14} & B_{11} & B_{12} & B_{14} \\ A_{12} & A_{22} & A_{24} & B_{12} & B_{22} & B_{24} \\ A_{14} & A_{24} & A_{44} & B_{14} & B_{24} & B_{44} \\ B_{11} & B_{12} & B_{14} & D_{11} & D_{12} & D_{14} \\ B_{12} & B_{22} & B_{24} & D_{12} & D_{22} & D_{24} \\ B_{14} & B_{24} & B_{44} & D_{14} & D_{24} & D_{44} \end{bmatrix} \begin{Bmatrix} \varepsilon_x \\ \varepsilon_y \\ \gamma_{xy} \\ \kappa_x \\ \kappa_y \\ \kappa_{xy} \end{Bmatrix} - \begin{Bmatrix} N_x^T \\ N_y^T \\ N_{xy}^T \\ M_x^T \\ M_y^T \\ M_{xy}^T \end{Bmatrix} \tag{6.1}$$

Where:

- N_x, N_y, N_{xy} are the resultant forces of the plate;
- M_x, M_y, M_{xy} are the resultant moments of the plate;
- ε and κ are the strains and the curvature of the middle plane plate;
- N_x^T, N_y^T, N_{xy}^T are the equivalent thermal plate resultant forces;
- M_x^T, M_y^T, M_{xy}^T are the equivalent thermal plate resultant forces.

In particular:

- *Matrix [A]* is stacking sequence independent. It includes the interaction between mid-plane forces and mid-plane extension (tension and compression). Moreover A_{14} and A_{24} terms represent extensional – shear coupling between the mid-plane forces and mid-plane shear strain;
- *Matrix [B]* include the interaction between mid-plane forces and plate curvature strain (bending and twist), mid-plane moments with mid-plane extension (traction and compression);
- *Matrix [D]* include the interaction between mid-plane forces and plate curvature strain (bending and twist). Moreover D_{14} and D_{24} terms represent bending - twist coupling between the mid-plane moments and plate curvatures.

As matter of fact, the optimization analysis on carbon fiber cover is also addressed to find the optimum combination of ply shape, orientation and stacking to avoid any undesired coupling effects. The design process of the hybrid lower control arm does not include only the optimization phase but also stress evaluation on special and misuse events.

Optimization on CAE can be described as the automatic search process for a minimum or a maximum of a response. The general optimization problem [90] can be mathematically defines as:

$$Minimize \quad f(X) = f(X_1, X_2, X_3, ..., X_N) \tag{6.2}$$

Subject to

$$g_j(X) \leq 0 \qquad j = 1,...,m \tag{6.3}$$

$$X_i^L \leq X_i \leq X_i^U \qquad i = 1,...,n \tag{6.4}$$

Where $f(X)$ is the objective function to be minimized and $g_j(X)$ are the constraint function which must be satisfied to obtain a feasible design. Both $f(X)$ and $g_j(X)$ are function of the design variables X_i that can have lower and upper bound limits.

Hence, the optimization set up is defined by the following key factors known with the acronym DRCO:

1. Design variables are values which can be changed in a model;
2. Responses are values which are measured from a model;
3. Constraints are limits on the responses of the model which must be satisfied for a feasible design;
4. Objective is a single response of the model which is to be minimized.

The objective function $f(X)$ and the constraint functions $g_j(X)$ are structural responses obtained from a finite element analysis. On Optistruct the selection of the design variables x define the type of optimization. Optistruct optimization solves for the optimum value of an objective function based upon the response of the model to its load cases by changing model geometry and properties.

The approach adopted in the lower control arm optimization consisted mainly in three different phases:

- *Phase I – Concept*: Free-sizing optimization is used to generate design concepts, while only considering global responses and optional manufacturing constraints;
- *Phase II – Dimension*: Sizing optimization – with ply-based modelling – is performed to control the thickness of each ply bundle, while considering all design responses and optional manufacturing constraints;
- *Phase III – Sequence*: Ply-stacking optimization (shuffling) is applied to determine the detailed stacking sequence, again while considering all behaviour responses and manufacturing constraints.

Even though these techniques can be used independently, it is strongly recommended to use them together as a three-phase integrated process guiding the design from concept to finish. This is particularly important when manufacturing constraints are involved. Although the simulation process follows a sort of automatic and precise sequence, interpretation of optimization results are not straightforward as they could appear and they require an important engineering effort and skill.

6.2. FE Optimization model

The optimization analysis is based on a sequence of linear static simulations reproducing the stiffness load cases, so the hybrid LCA model shares the same mesh and components of the baseline. In this case, the LCA steel part and the composite one have been modelled as unique laminate in which every single ply has its specific shape and material. Accordingly with the multi-material LCA targets, the optimization has been carried out considering the stiffness load cases of bending and buckling load as depicted in Figure 6.2.

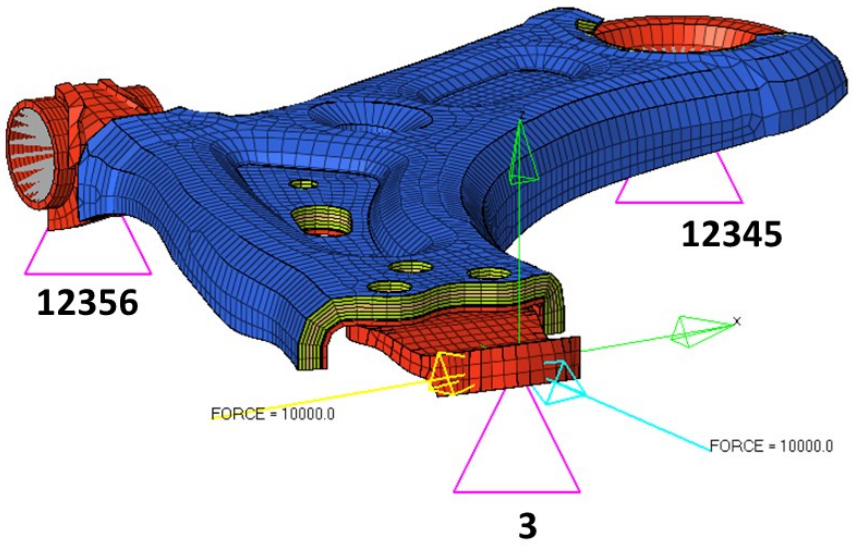

Figure 6.2 – FE hybrid model for optimization

The maximum envelope of the lower control arm defined by packaging analysis has been used as starting design volume. At the beginning, composite plies has been distributed uniformly on the arm, considering Y direction has the reference manufacturing direction for 0 degree orientation. This means that fiber oriented at 0° are parallel to Y axis, as shown in Figure 6.3 by the white arrows.

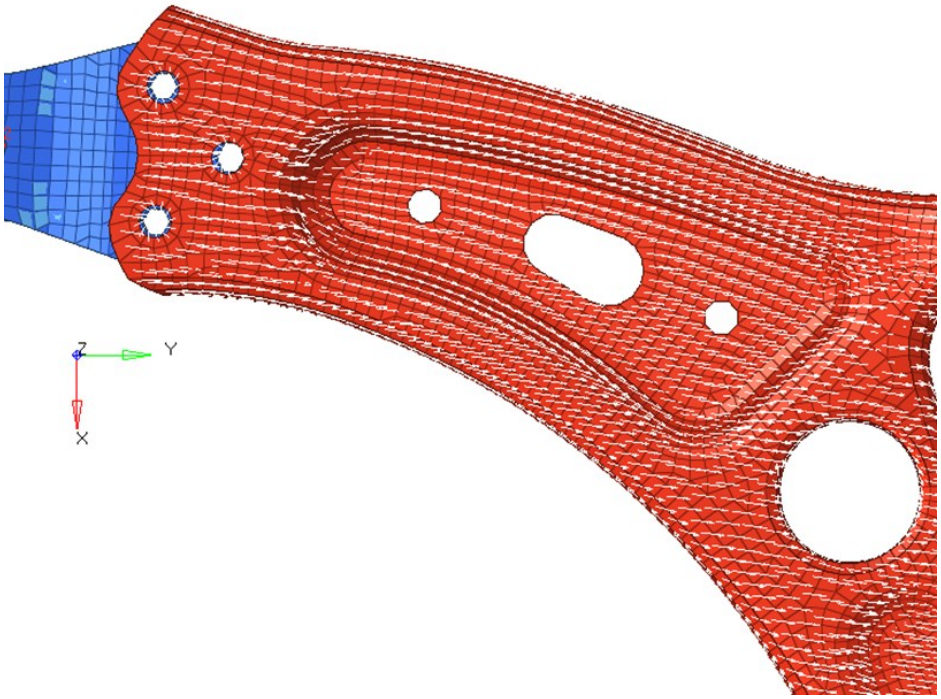

Figure 6.3 – Element fiber orientation

As concerns the non-design space, Figure 6.4 illustrates the LCA area and components that are excluded from the optimization process. They are: bushings seats, welding lines, LBJ, HVV ply and the original metallic shape (in red) whit its differentiated thicknesses imposed as constraints.

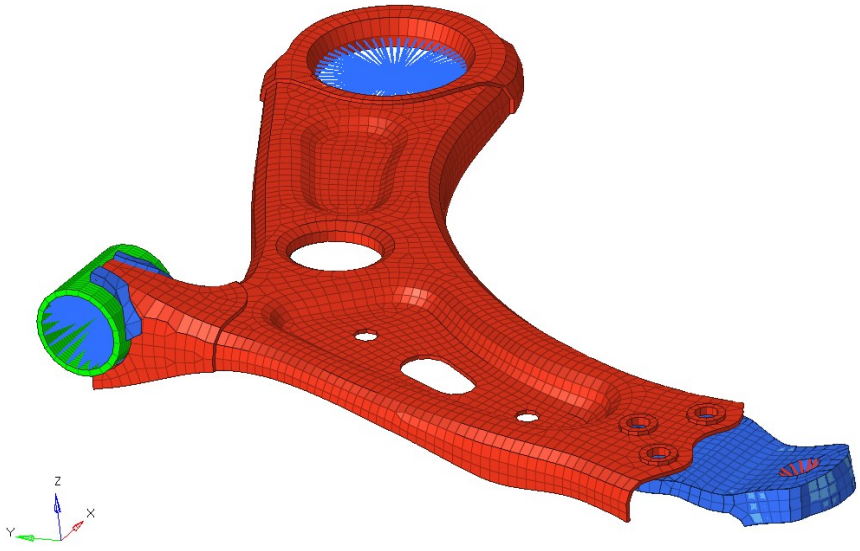

Figure 6.4 – Non design variables on LCA

At this stage, material data used in the model are those correlated with experimental tests where only the linear part has been consider. The material laws chosen according to Optistruct library were:

- *S420MC*: isotropic elastic material law (MAT1) for arms metal parts;

- *Carbon fiber materials (GG245T, GG430T an M46J)*: orthotropic material law (MAT8);
- *HVV*: isotropic elastic material law (MAT1).

For the sake of clarity, in Table 6.1 are summarized the input values edited inside the material cards carried out from the correlation activity performed in Chapter 5 and 6 according to Optistruct material card.

	Material Card	E_1 [GPa]	E_2 [GPa]	G_{12} [GPa]	ν	ρ [kg/m^3]
S420MC	MAT1	208	-	-	0,3	7890
GG245T	MAT8	57	57	3,2	0,04	1450
GG430T	MAT8	59	59	3,7	0,05	1500
UD M46J	MAT8	220	6,2	2,6	0,17	1560
HVV	MAT1	1,36	-	-	0,45	1300

Table 6.1 – Material data used in hybrid LCA FEM model

Then, the targets and the constraints defined (in Chapter 3 and Chapter 4) for the design concept have been set into the optimization model. The minimization of the mass has been imposed as objective function by using DESOBJ(MIN) load collector. The relative displacements in X and Y of the baseline LCA has been set as constraint functions in order to impose the stiffness requirements on the hybrid LCA. Nevertheless, the maximum constraint violation percentage has been set equal to 10% in order to investigate the maximum weight reduction possible in multi-material structures without compromising the overall stiffness. As consequence, three optimization responses has been created concerning the mass and the relative displacement on the bending and buckling load cases.

6.3. Phase I: Free-Size

The purpose of composite free-sizing optimization is to create design concepts that utilize all the potentials of a composite structure where both structure and material can be designed simultaneously. By varying the thickness of each ply with a particular fiber orientation for every element, the total laminate thickness can change 'continuously' throughout the structure, and at the same time, the optimal composition of the composite laminate at every element is achieved simultaneously. At this stage, a super-ply concept has been adopted, in which each available fiber orientation is assigned a super-ply whose thickness is free-sized between specific limits.

In addition, because stacking sequence is initially indeterminate, the SMEAR option [80, 90] has been adopted. This technology is a powerful tool that combine ABD matrix in order to make the concept design optimization process stacking sequence independent.

As concerns the free size design variables, different parameters have been defined to perform the simulation and obtain the output for the size phase. In particular:

- *Laminate thickness*: minimum value of 2,5 mm and maximum of 15 mm; Minimum value corresponds to the sum of metal thickness and HVV ply;
- *Ply orientation and thickness*: prescribes the set of angle to be used for each materials and the element thickness range;
- *Constant ply thickness*: defined for metal parts and HVV ply;
- *Ply balancing*: in order to balance unidirectional plies orientation at ±45°;
- *GG245T plies*: only two plies have been defined (one at the interface with the HVV and one in the external LCA surface). For this reason they have been excluded from the sizing steps.

As regards the laminate thickness bounds, the initial upper value represents the physical limit defined by packaging analysis. Therefore several attempts have been run to evaluate the minimum upper bound in order to equally distribute the material on the component, avoiding thick concentrated areas. A feasible design has been obtained with an upper limit of 10 mm. In Figure 6.5 has been presented the carbon fiber thickness distribution on the lower control arm.

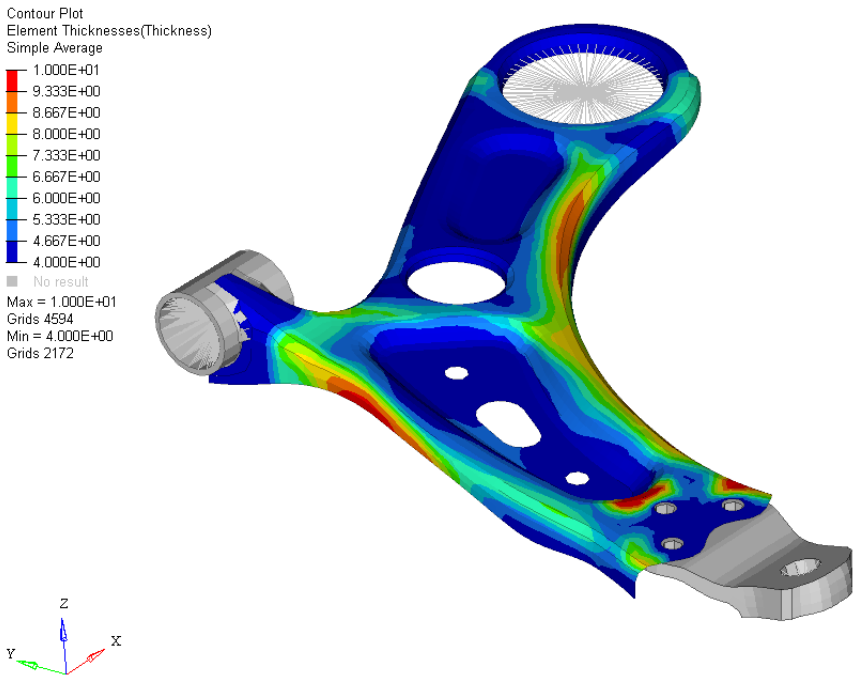

Figure 6.5 – Element thicknesses after free-size step

First of all, a minimum uniform thickness of 4 mm is required on the entire shape of the lower control arm. The thickness is mostly concentrated on the inner part of the swinging arm to oppose on bending load and in the outer to face the buckling behaviour. Moreover, the analysis highlight the thickness in function of the orientation, as illustrated in Figure 6.6 and Figure 6.7.

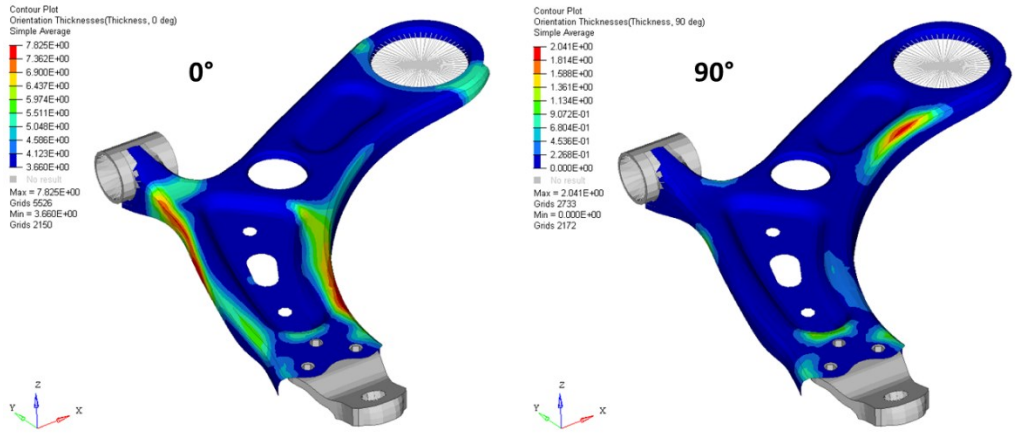

Figure 6.6 – Thicknesses of plies at 0° and 90°

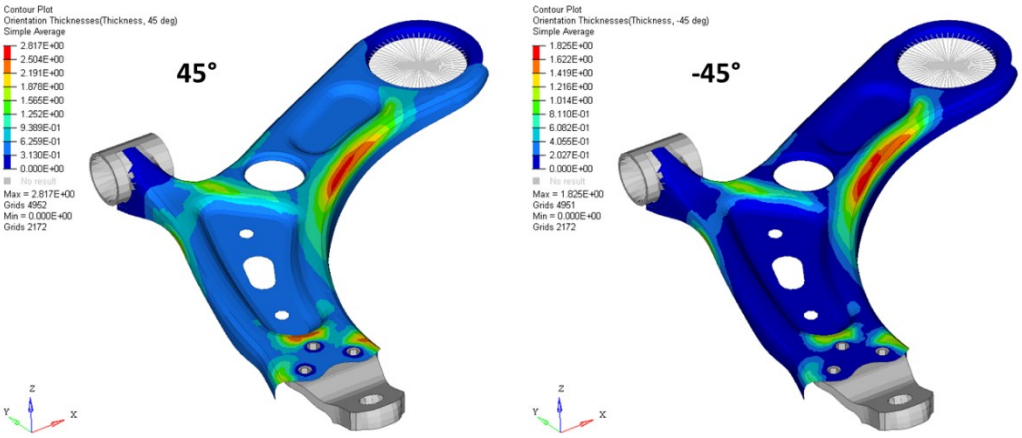

Figure 6.7 - Thicknesses of plies at +45° and -45°

These information are extremely useful to define the correct orientations of the tailored reinforcements, especially as a function of the material. For instance, in Figure 6.8 are presented the ply thickness distribution of the M46J at 0° and 90°. Thanks to this evaluation, it has been decided to apply only a uniform layer at 90° without any kind of localized reinforcement as for the 0°.

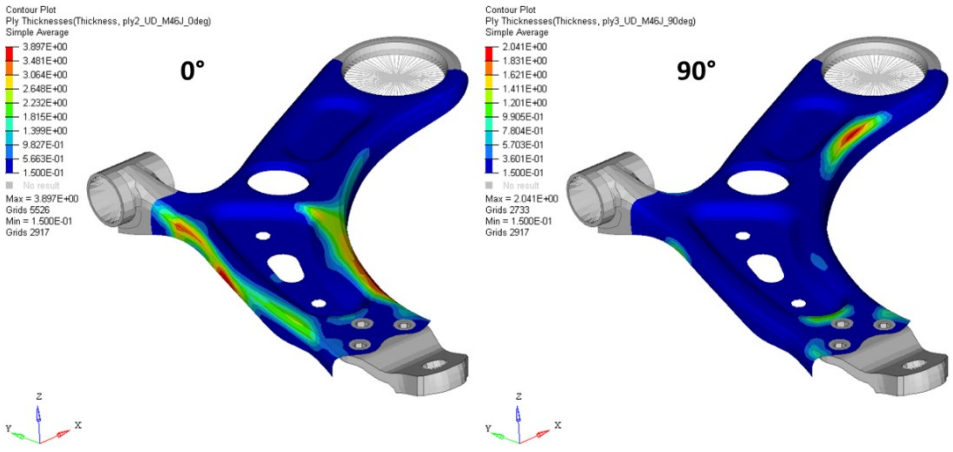

Figure 6.8 – UD ply thickness at 0° and 90°

As concerns the fabric CFRP, in Figure 6.9 are reported the ply distribution of the twill GG430T. Although the results suggest to limit the application of the GG430T to one total layer and very few localized reinforcement, in this case it has been chosen to put two total plies for each direction in order to homogenized the stress distribution along the LCA surface thanks to its strength properties that are the same at 0/90° (and, obviously, at ±45°).

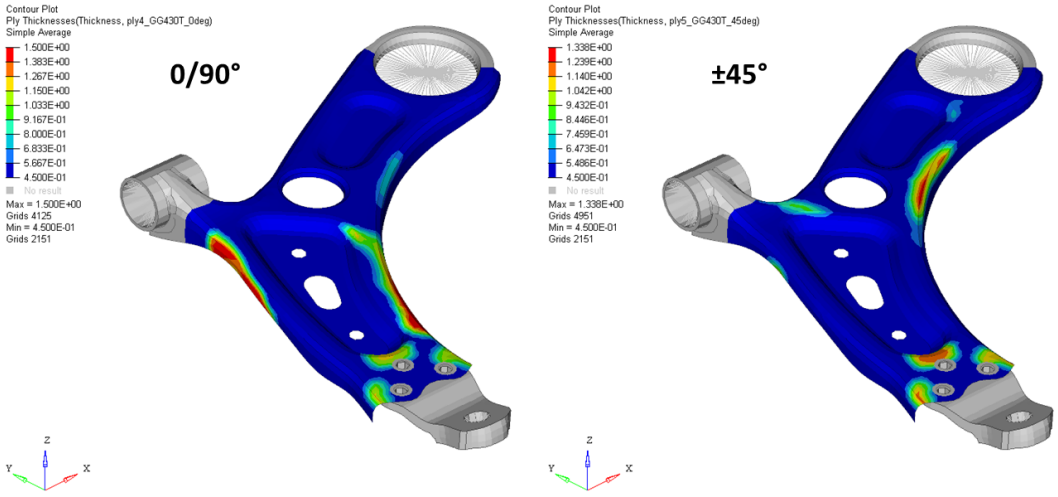

Figure 6.9 - GG430T ply thickness at 0° and 45°

6.4. Phase II: Size

Size is a crucial stage of the entire optimization process. In fact, composite size is detailed design optimization as opposed to composite free-size which is concept design optimization [90]. As matter of fact, in this phase the number of plies and their shapes are defined. One of the most apparent challenges of interpreting free size optimization with composite materials is in constructing the ply shapes after optimization is completed. The *fem* file output of the free-size simulation is the starting point for the size analysis. The thickness variation displayed on the contour plot of the post-processor is discretized in mesh, as shown in Figure 6.10.

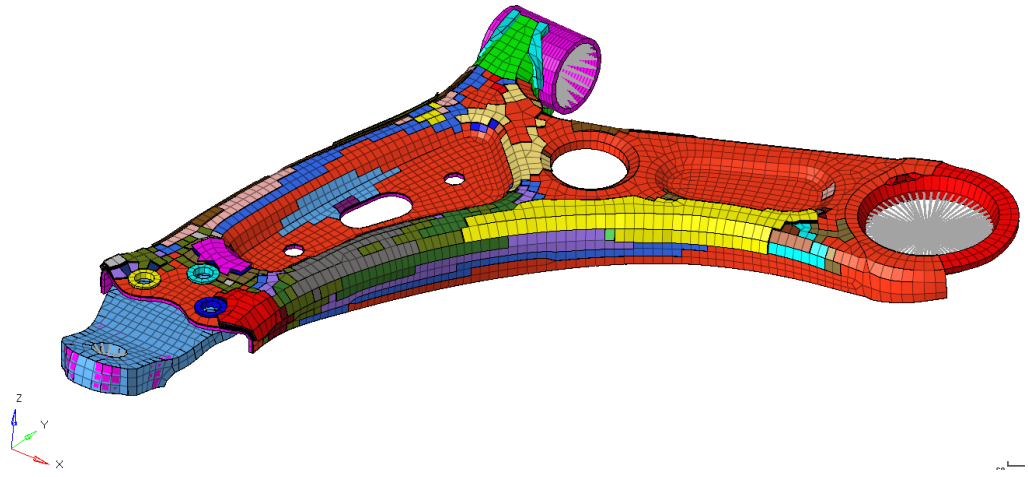

Figure 6.10 – Ply patches from free-size simulation results

The coloured patches are the local reinforcements defined by the solver. The total number of plies generated by the optimization was about 130, where most of them had a 0,01 mm thickness while others were coupled together. Moreover, if carefully analysed, the laminate obtained from free-size simulation in Figure 6.10 are not completely suitable for manufacturing process. Important issues are not taken into account both structural and manufacturing. For instance, in some areas are located very small patches of two or three elements that in the reality could break the fiber continuity and weaken to structure. On the other hand, some reinforcements have been added to increase strength performance according to the special and misuse event load cases. In addition, overlaps between plies are not been considered by the solver in free-size step. Hence, in this stage it has been combined the structural requirements with the manufacturing process.

At first, all the ply which were lower manufacturing thickness have been deleted by using TMAUNF flag and imposing the experimental layer thickness. Subsequently, coupled plies with the same orientation have been split into multiple of the real layer thickness. Then, layers shape have been modified in order to be compliant with manufacturing process and free-size thickness distributions: reinforcements have been located mainly in the yellow area, in particular along the red lines highlighted in Figure 6.11.

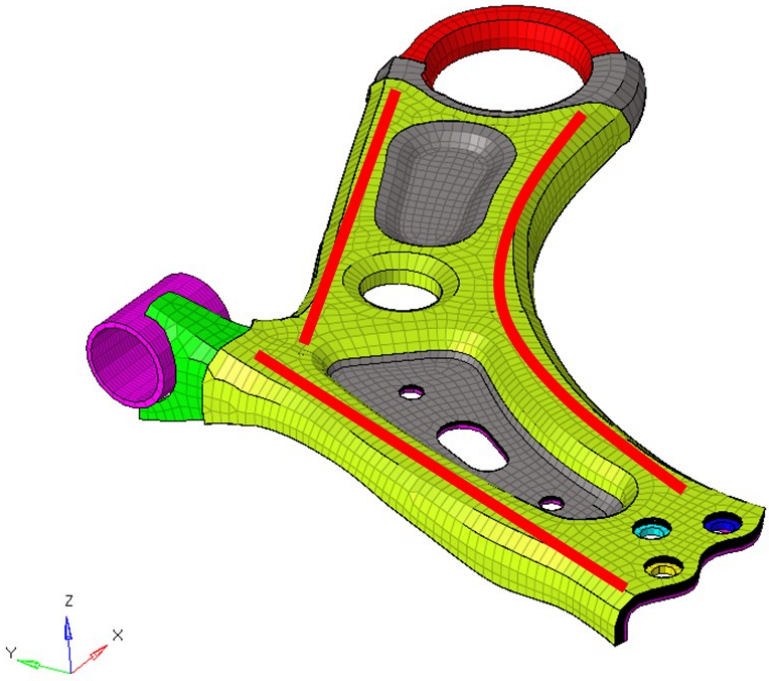

Figure 6.11 – Reinforcement patches direction (red lines)

After 8 iterations, the simulation has converged in a feasible solution and the output has been imported in Hypermesh to prepare the last optimization phase.

6.5. Phase III: Shuffling

Composite plies are shuffled to determine the optimal *ply-book*, satisfying additional manufacturing constraints with the DSHUFFLE card. In fact, as a

composite laminate is typically manufactured through a stacking and curing process, certain manufacturing requirements are necessary in order to limit undesired side effects emerging during this curing process.

One typical such constraint for carbon fiber reinforced composite is that plies of a given orientation cannot be stacked successively for more than 3 or 4 plies to avoid possible delamination effects. This condition has been imposed defining MAXSUCC load collector orientations to break the succession of plies of the same orientation. In addition, by setting the pairing constraint it has been balanced +45° and -45° unidirectional plies to eliminate twisting of a plate bended along the 0 axis. Finally, by using COVER card, it has been imposed the application of GG245T as first and last layer of the laminate.

6.6. Hybrid lower control arm performance

Once the shuffling process was finished, ply drops have been designed between layers in order to smoothing as much as possible the section variation as illustrated in Figure 6.12.

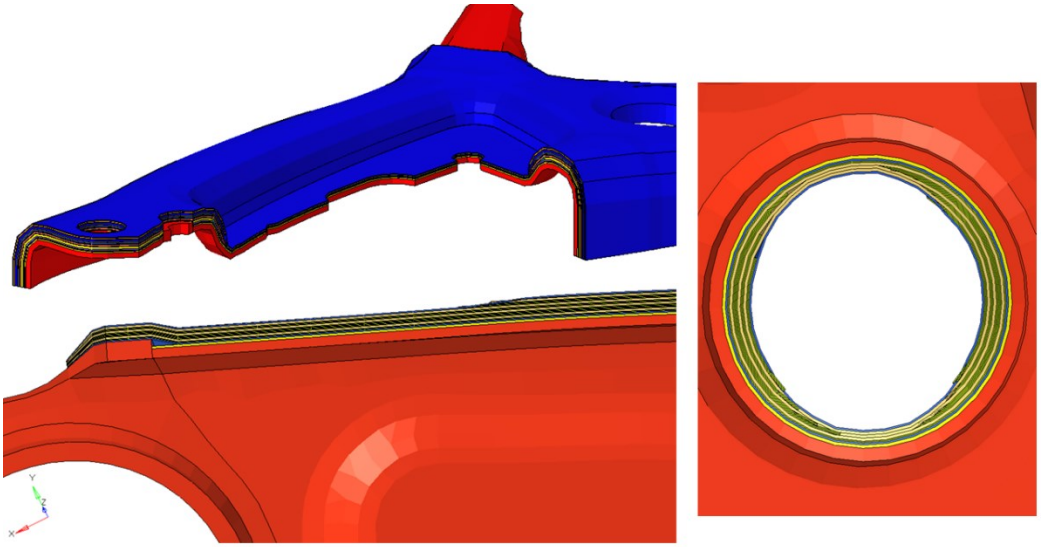

Figure 6.12 – Examples of ply drops on lower control arm

Moreover, carbon fiber layers have been subdivided in 8 configuration based on the shape of the patch (Figure 6.13). The structural core of the laminate is made by plies with shape “A” that cover the totality of the arm surface. Then, plies from shape “B” to “D” are those considered as global reinforcements while layers from shape “E” to “H” are the local reinforcement especially made of M46J. Because the geometry of each patch has been obtained as off-set of the previous, the cutting operation of the pre-pregs has been also optimized.

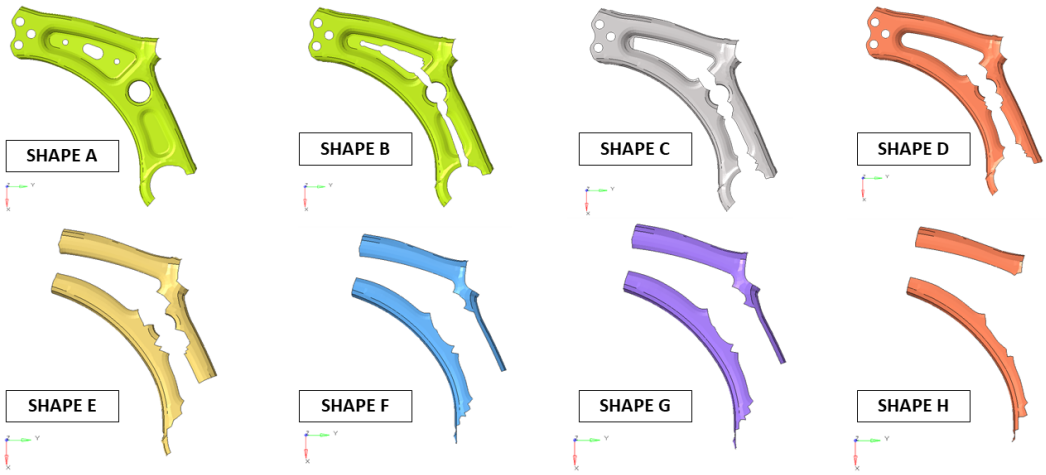

Figure 6.13 – Hybrid LCA ply shapes classification

Finally, the optimized hybrid LCA model has been carried out as illustrated in Figure 6.14.

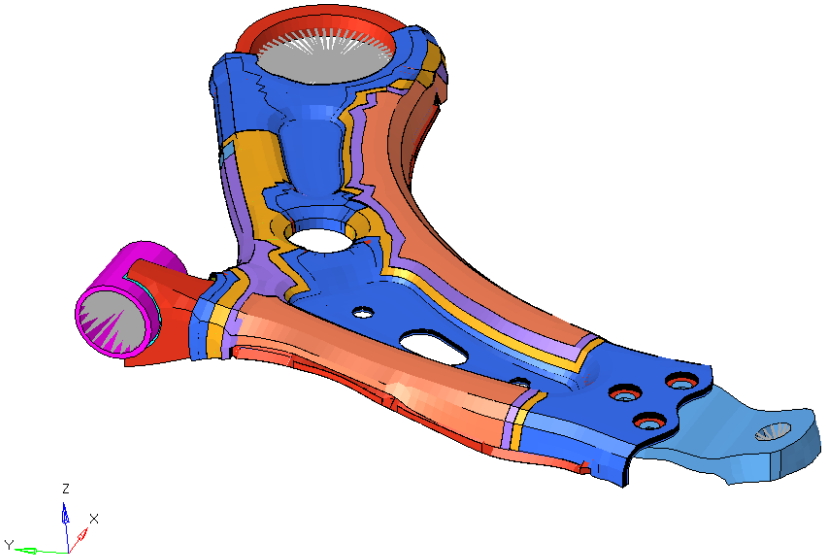

Figure 6.14 – Final FE model of the hybrid lower control arm

The virtual final mass of the hybrid arm is about 1,68 kg that is 23% less than the baseline as previously reported in Table 2.14. This mass takes into account the arm with only the front bushing case welded. The total number of plies is 23 and the composite mass added is 130 g in the face of 620 g of steel saved from the conventional arm.

As concerns performance, first of all the stiffness simulations have been carried out. In Figure 6.15 are reported the stiffness simulation results with their relative displacement on the hybrid lower control arm. Considering the application of 10 kN in lateral and longitudinal direction, the bending stiffness K_x obtained is equal to 6,3 kN/mm while the buckling K_y is 25,3 kN/mm that are respectively 9% and 7% less than the original arm.

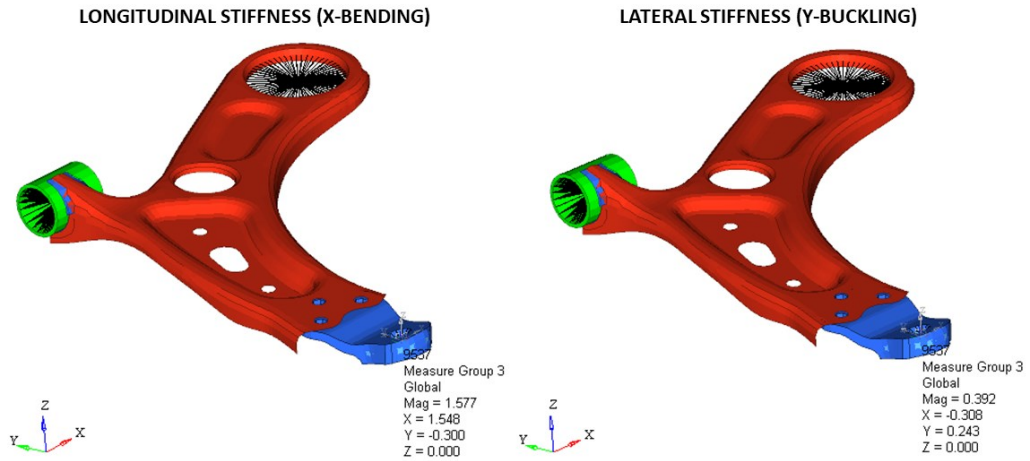

Figure 6.15 – Bending and buckling stiffness results on hybrid LCA

The stiffness values have respected the maximum violation percentage of 10% imposed during the optimization analysis. In particular, the constraint imposed by the arm metal shape has strongly limited the possibility to improve stiffness by using specific geometric reinforcements. For this reason, the results obtained have been considered compliant with the structural target defined.

Therefore, the hybrid LCA has been tested according to the simulation set defined for the baseline arm to verify the stress distribution. Hybrid lower control arm is, of course, made of steel and carbon fibers, then the results analysis has been subdivided considering the peculiarity of this two materials.

In particular, for the metallic part has been used Von Mises criterion while for composite has been evaluated the maximum stress in the principal direction σ_1 and Hashin criterion [91] has been adopted to estimate the failure index, which must be lower than 1 to avoid ruptures.

At the beginning, the elastic condition has been verified for the stiffness simulation as in the baseline case. The maximum stress reported is for the bending configuration, in which the value is 356 MPa for the steel arm part (Figure 6.16) that is lower than the yield limit of 420 MPa of the material.

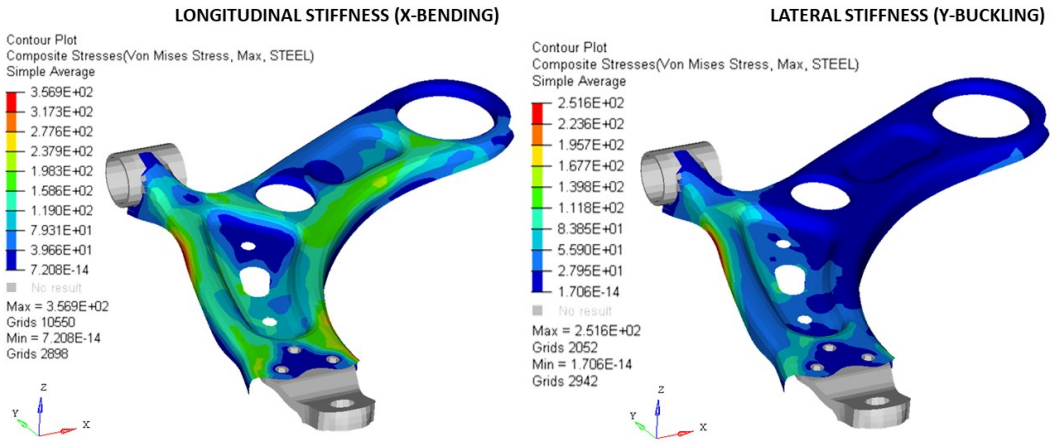

Figure 6.16 – Stress distribution (MPa) on steel part

In the carbon fiber cover, the maximum principal stress σ_1 is 239 MPa (Figure 6.17) that is far from the failure limits of the CFRP materials and the maximum Hashin value registered is 0,18 as shown in Figure 6.18.

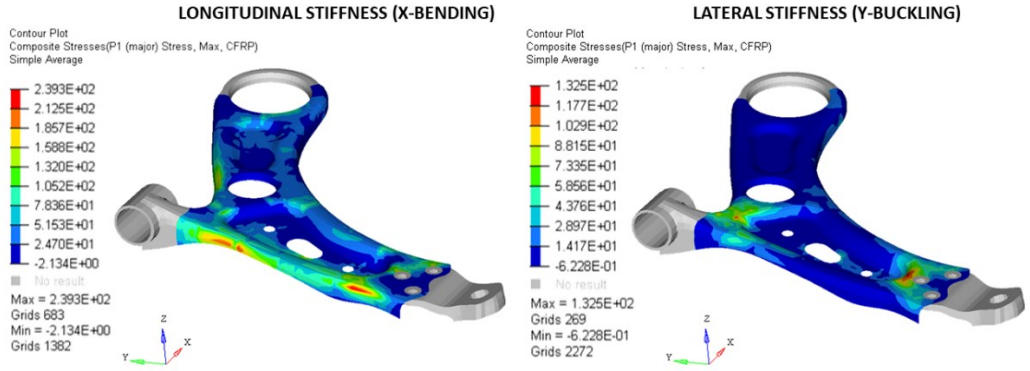

Figure 6.17 – Stress distribution (MPa) on CFRP structural cover

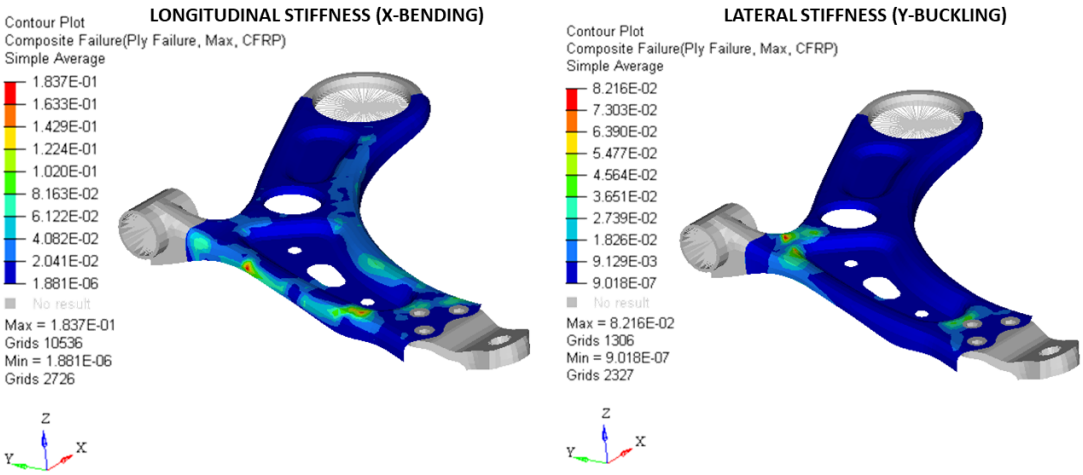

Figure 6.18 – Ply failure index

Moreover, the HVV strain distribution has been evaluated in the worst case represented by the bending simulation. As shown in Figure 6.19, the values of ε_x (A) ε_y (B) and γ_{xy} (C) can be considered sufficiently small to validate the use of an isotropic elastic law to model a viscoelastic material.

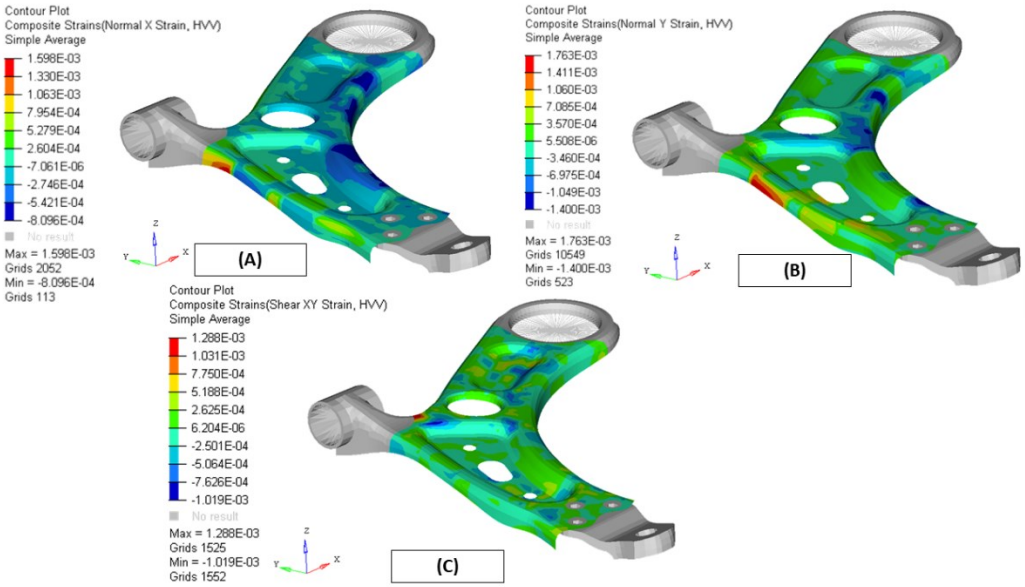

Figure 6.19 – Strain values (mm/mm) on HVV layer

For these reasons, the stiffness simulation have been considered in linear elastic field and the results obtained valid. In Table 6.2 are compared the stiffness and the mass values of the two lower control arms.

	Mass [kg]	**Δ Mass [%]**	**K_x [kN/mm]**	**Δ K_x [%]**	**K_y [kN/mm]**	**Δ K_y [%]**
FEM BASELINE	2,16	-	6,9	-	27,2	-
FEM HYBRID	1,67	-23%	6,3	-9%	25,3	-7%

Table 6.2 - Baseline and Hybrid LCA mass and stiffness comparison

Therefore, the hybrid LCA has been tested according to the simulation set defined for the baseline arm to verify the stress distribution. Among the special events, the most critical case is again the maximum braking. In this case, the steel part has a maximum stress of 184 MPa as described in Figure 6.20, while composite cover has a maximum principal stress σ_1 of 117 MPa as shown in Figure 6.21 reported on a layer of UD M46J.

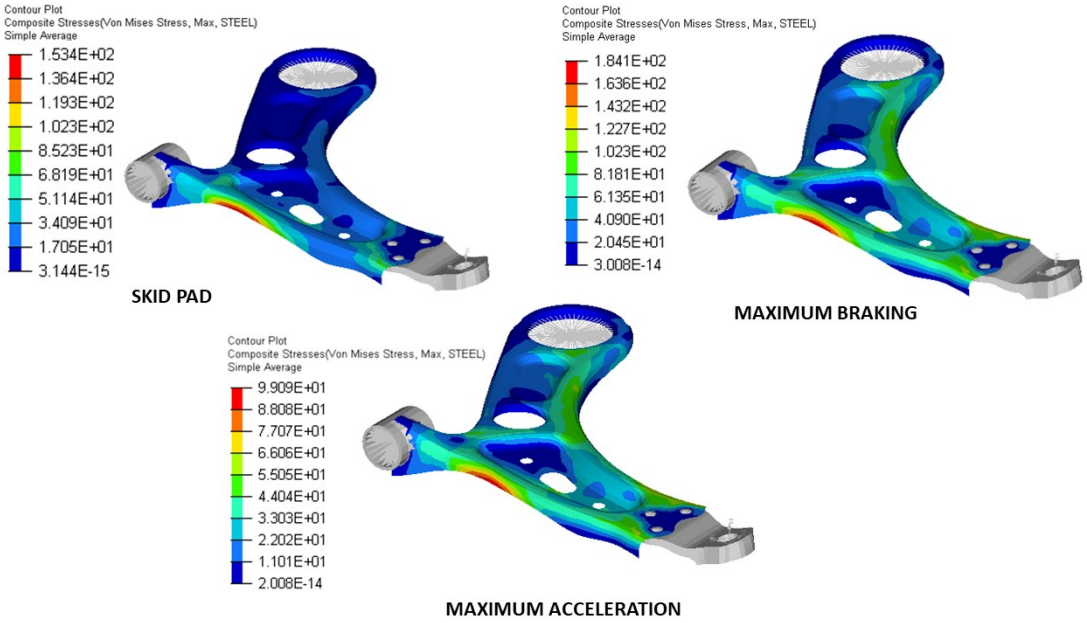

Figure 6.20 – Von Mises stress (MPa) contour on arm steel part for special events

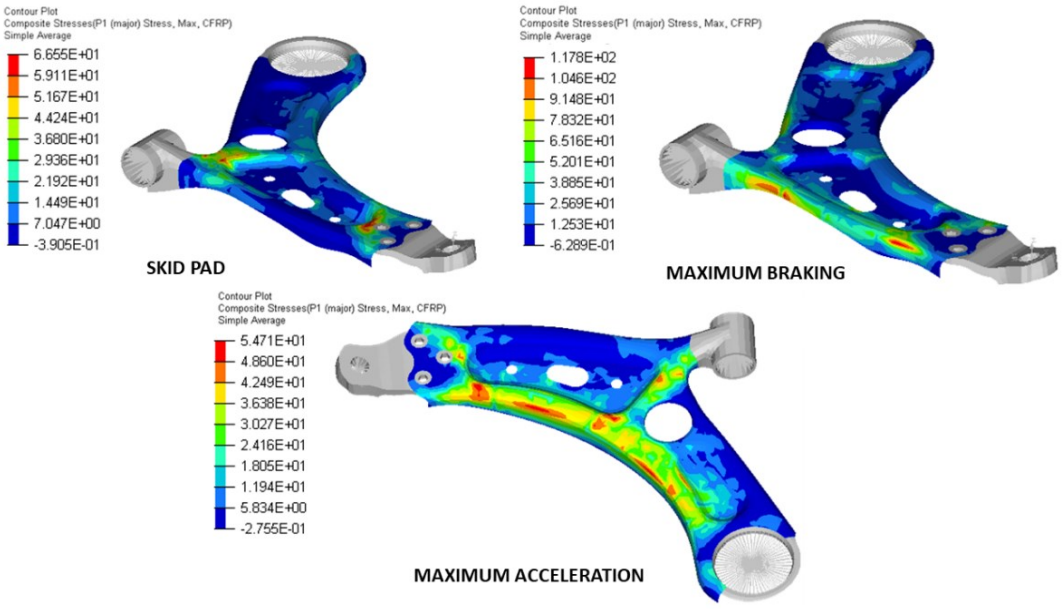

Figure 6.21 – Principal σ_1 stress (MPa) contour on CFRP laminate part for special events

Then, the global stress state of the metallic shape is far from the yield and the failure index given by Hashin on the composite cover is 0,052 for the braking case, as shown in Figure 6.22.

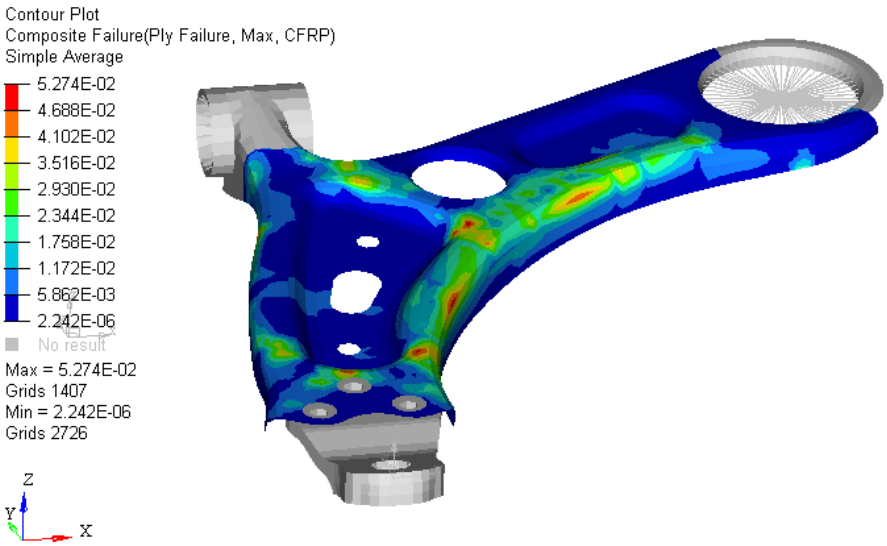

Figure 6.22 – Hashin failure index among plies for maximum braking

As concerns the misuse events, the most critical is the hump. In this case, the steel part has a maximum stress of 214 MPa as described in Figure 6.23, while composite cover has a maximum principal stress σ_1 of 110 MPa as shown Figure 6.24 on a ply of UD M46J.

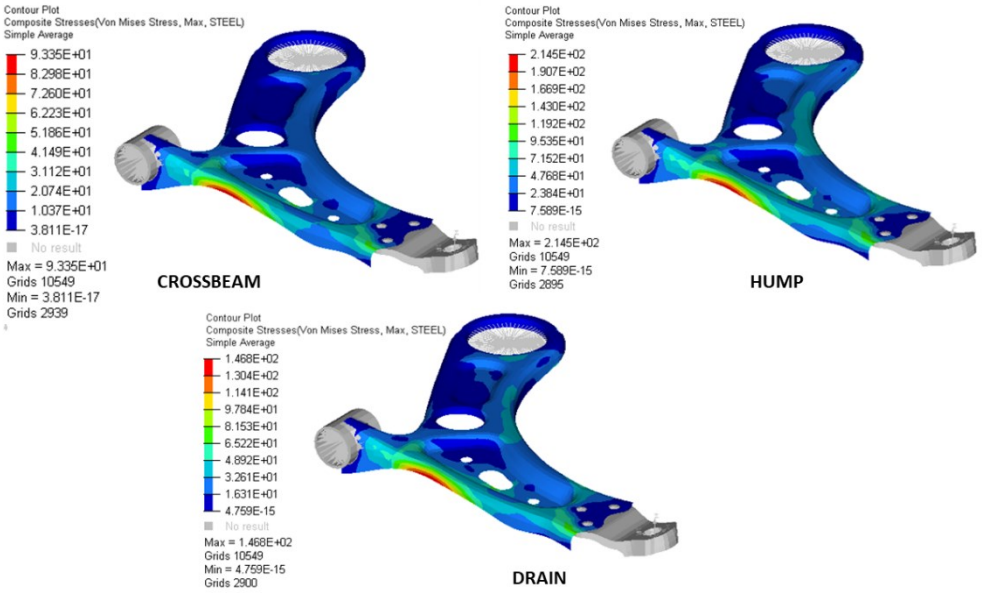

Figure 6.23 – Von Mises stress (MPa) contour on arm steel part for misuse events

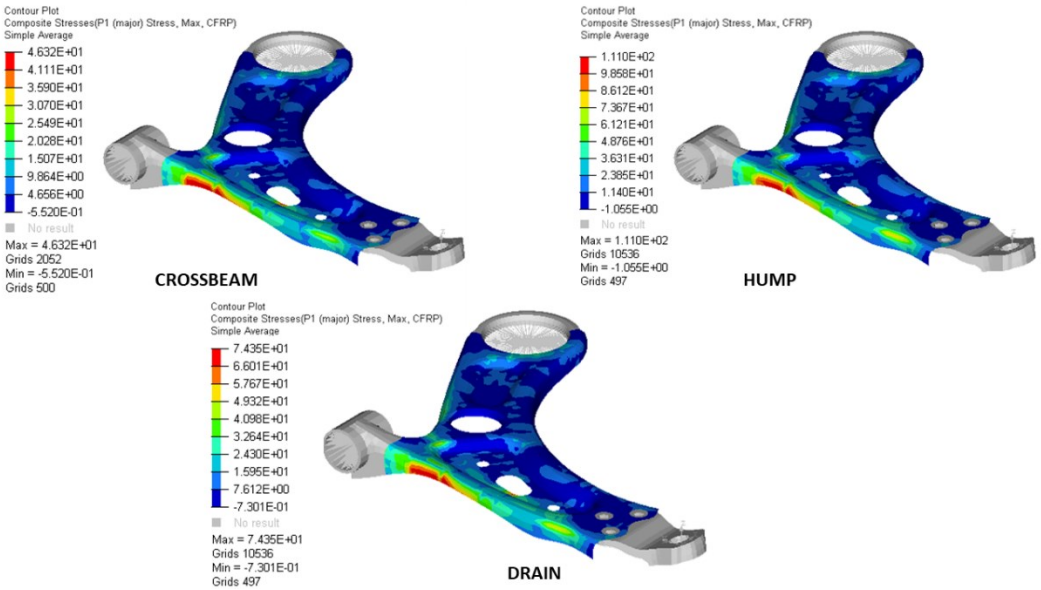

Figure 6.24 - Principal σ_1 stress (MPa) contour on CFRP laminate for misuse events

Even in this case, stresses are abundantly below the threshold limit of the materials. The failure index given by Hashin among composite plies is 0,044 for the hump case, as shown in Figure 6.25.

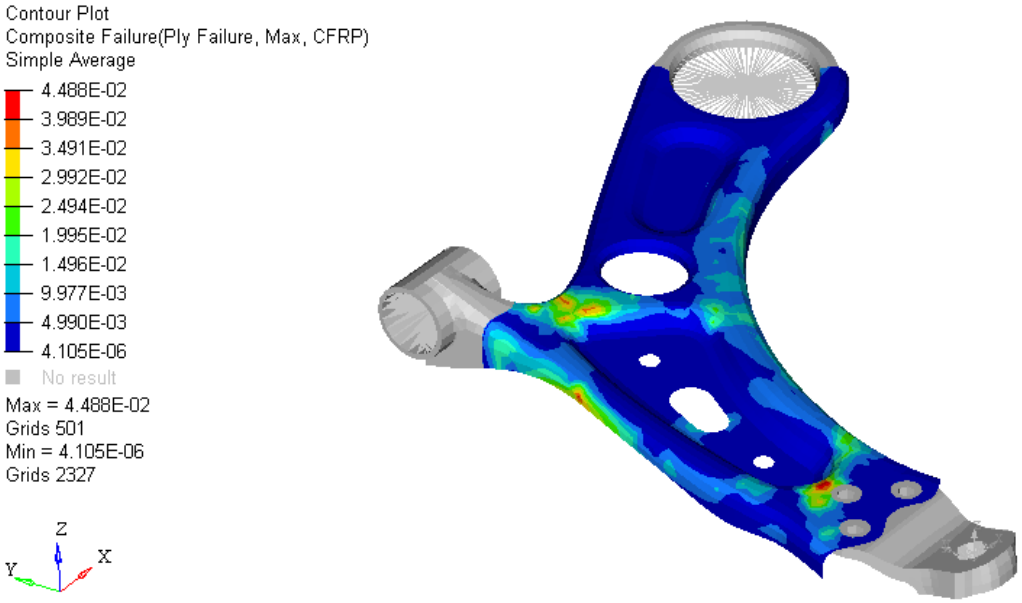

Figure 6.25 - Hashin failure index among plies for hump obstacle

Finally, in Table 6.3 has been shown the virtual results achieved by the hybrid lower control arm compared with the baseline.

	Special event stress on STEEL [MPa] (Rp_{02}=422 MPa)	Special event stress on CFRP [MPa]	Misuse event stress on STEEL [MPa] (Rp_{02}=422 MPa)	Misuse event stress on CFRP [MPa]
FEM BASELINE	238	-	214	-
FEM HYBRID	184	117 (on M46J layer with σ_{max}=1830 MPa)	214	110 (on M46J layer with σ_{max}=1830 MPa)

Table 6.3 – Baseline and Hybrid LCA stress comparison

6.7. Manufacturing process

Once the simulation path has been concluded, the FE model information regarding ply shapes have been reproduced in CAD environment. Each ply has been drawn and stacked in the arm as single solid sheet in order to carry out the flat model (Figure 6.26) for the cutting operation on plotter.

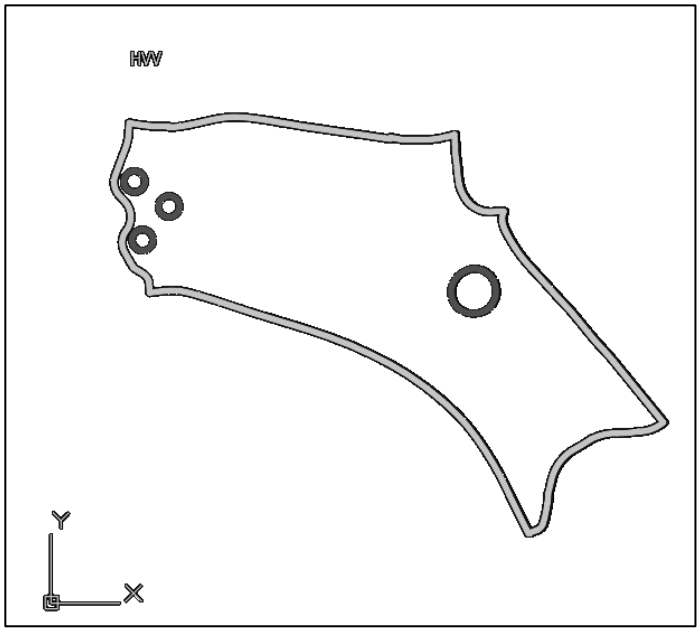

Figure 6.26 – Example of ply flat model (HVV)

A render of the final CAD model is illustrated in Figure 6.27. Because the maximum laminate thickness is no more than 10 mm, the hybrid arm meets the packaging constraints.

Figure 6.27 – The hybrid lower control arm CAD model

Subsequently, a standard lower control has been milled by using a five axis CNC machine. The arm has been fit into a resin mould obtained as male of the inner arm shape, as shown in Figure 6.28. In order to avoid excessive thermal distortions, the machining operation has been last for three days because the tool was set to remove steel by step of 0,8 mm in thickness and 0,3mm in lateral and longitudinal direction.

Figure 6.28 - Milling operation on LCA

Once the milling operation was finished, the thickness measured on the component was ranged between 1,98 and 2,02 mm. The final metallic shape is illustrated in Figure 6.29.

Figure 6.29 – LCA with reduced thickness metal part

Thus, the arm has been sandblasted and prepared to the hand lay-up lamination as shown in Figure 6.30.

Figure 6.30 – Surface finishing before lamination

Therefore, all the ply shape have been cut, classified and numbered according to their shape category and stacking position. By doing so, the lamination process has been monitored in order to have a direct comparison with the virtual stacking sequence. As a matter of fact, in Figure 6.31 are reported three different steps of the

lay-up operation, in particular the HVV foil (A), the first carbon fiber ply (B) and one of the last unidirectional reinforcements (C) compared with their virtual counterparts.

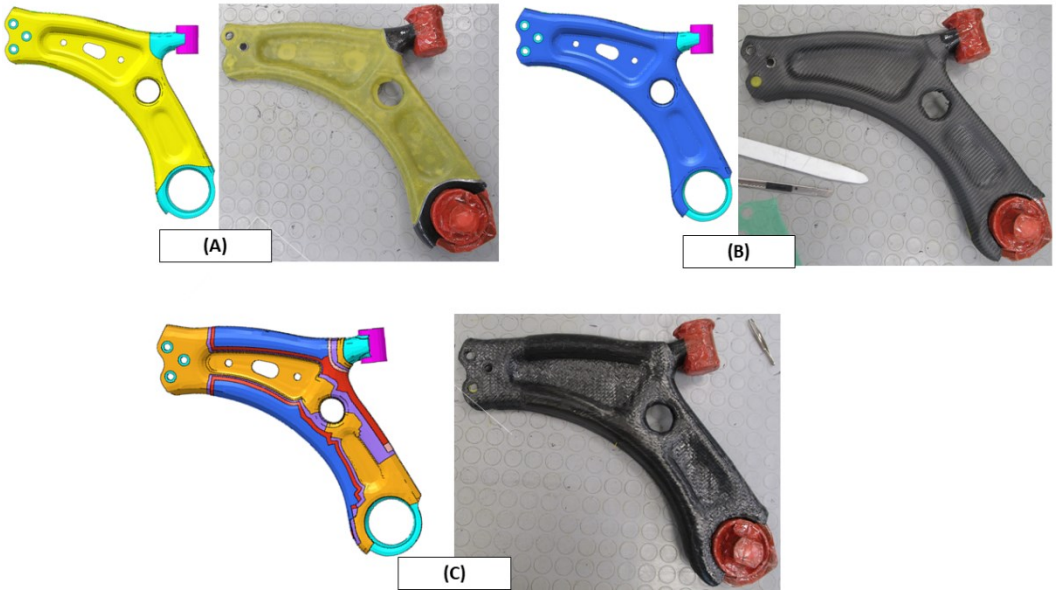

Figure 6.31 – Example of ply application

Moreover, two embedded strain gauges (HBM LI66-10/350 Ohm) has been placed between the 1st and the 2nd layer to estimate deformation close to the interface in two different areas: one has been located in the inner curved shape (A), while the other inside the main emboss (B) as shown in Figure 6.32

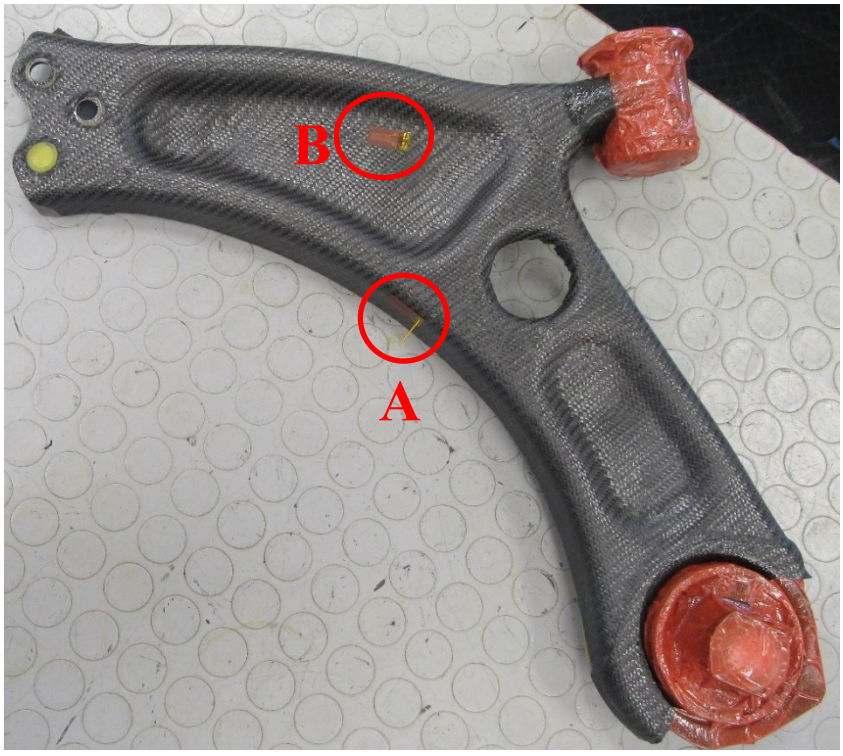

Figure 6.32 – First ply of GG245T with interlaminar strain gauges

Finally, the hybrid lower control arm has been cured in autoclave following a cycle of 90 minutes at 130°C with a pressure of 5,5 bar. In Figure 6.33 is reported the final component after the finishing surface treatment.

Figure 6.33 – The hybrid lower control arm

The mass measured of the hybrid lower control arm is 1,67 kg that is perfectly aligned with FEM estimation, as shown in Figure 6.34. Finally, the hybrid LCA has been prepared firstly for the frequency response analysis and secondly for the strength test together the baseline one.

Figure 6.34 – Mass of hybrid LCA

Chapter 7

Virtual experimental correlation on lower control arms

7.1. Experimental modal analysis set up

The purpose of the test is to evaluate the dynamic performance of the two LCAs and compare their capability to damp vibrations, in particular computing the modal response of the system, by measuring the frequency response function. The results provided are: the inertance of the system, the ratio between the acceleration, measured in several points, and the force applied on the system in a different point. The frequency range of the tests is between 100 and 1500 Hz.

The experiment scheme is shown in Figure 7.1. The setup to produce the excitation signal is composed by the exciter, a power amplifier and an exciter control. An electromagnetic exciter (also known as shaker) has been used to produce the input vibration of the system and it has been suspended and fixed on a seismic block to limit the environmental vibrations. This instrument converts the input electrical signal, coming from the input generator, into a controlled mechanical movement. The signal generator sends a predefined input signal to the amplifier then to the exciter, which produces a mechanical input to the component that is directly correlated to the one given by the user.

The input signal, imposed by the signal generator, is a random input, which has a flat spectrum, within a specified frequency range 100-1500 Hz for both the lower control arms. This system has some advantage with respect to the sine sweep signal: for instance, the time needed for the test is shorter, because it acts on all resonances at the same time.

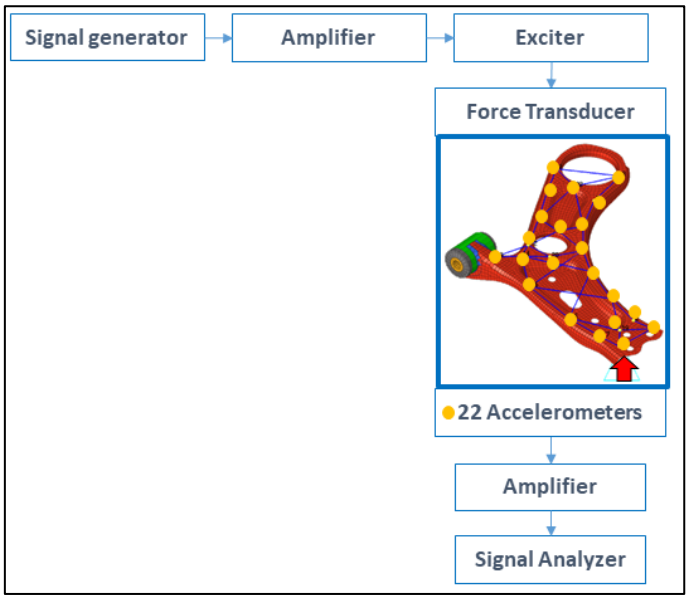

Figure 7.1 - Instruments test scheme for frequency response analysis

The exact value of the input signal on the component can be controlled and measured with a force transducer having the characteristics as reported in Table 7.1.

Model	Manufacturer	Mass [g]	Measurement Range [N]	Sensitivity [mV/kN]
208C02	PCB piezotronic	22,7	±444,8	11241

Table 7.1 – Load cell characteristics

Therefore the input function is known and can be used to compute the inertance and the receptance of the system. The response of the system to the excitation input is measured through 22 piezoelectric accelerometers, positioned in different points on all the surface of the component, and the signals are required thanks to a signal analyser. The accelerometers output are proportional to the force and, consequently, to the acceleration: their characteristics are illustrated in Table 7.2.

Model	Manufacturer	Typology	Mass [g]	Measurement Range [m/s^2]	Sensitivity [mV/(m/s^2]
DeltaTron 4397	Brüel &Kjær	Monoaxial	2,37	±700	91
DeltaTron 4507	Brüel &Kjær	Triaxial	4,62	±500	91
8763A500	Kistler	Triaxial	3,27	±500	1
356A16	PCB piezotronic	Triaxial	7,16	±490	10,2
333B30	PCB piezotronic	Monoaxial	3,98	±490	10,2

Table 7.2 – Accelerometers characteristics

The choice of the points in which the accelerometers have been fixed are very important and must be done with care: if a point is put in correspondence of a vibrating node, this accelerometer does not register any movement. Then, the positioning of the accelerometers is chosen in order to equally distribute them, in order to have results on all the surface of the components. Figure 7.2 shows the grid points chosen for each arms. Moreover, due to the high stiffness of the component and the low mass of whole accelerometers set (about 80 g), the measurements done are not affected by the presence of the accelerometers in both cases.

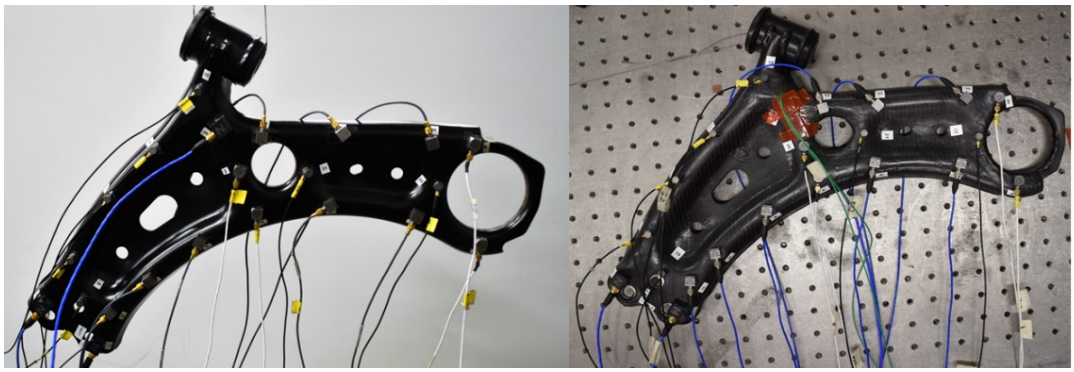

Figure 7.2 – Accelerometer positions on baseline (left) and hybrid (right) arms

Finally, the positioning of the tested components have been chosen carefully to simulate a free-free constraint condition: the samples were attached to the ceiling and suspended with a cable, which it does not influence the experimental measurements. Once the components have reached a stable condition, the shaker can be positioned and excite them only in one direction. Figure 7.3 shows the baseline (on the left) and the hybrid (on the right) LCA prepared for the experiment with accelerometers and shaker.

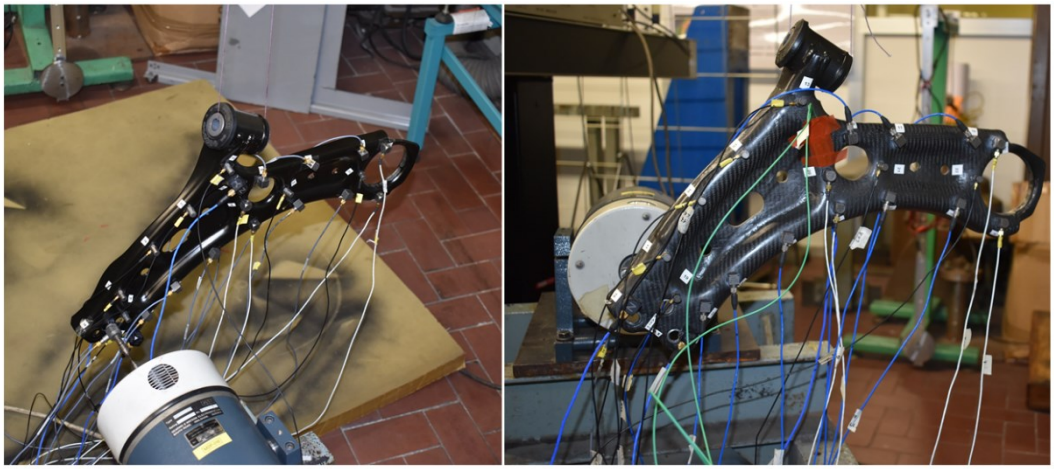

Figure 7.3 – Experimental set up for the modal analysis for baseline (left) and hybrid (right) arms

7.2. Model parameters extraction algorithm

The LIPEZ method has been adopted as model parameters extraction algorithm using the Rational Fraction Polynomials (RFP) representation of the Frequency Response Function (FRF) and, with the aim of defining a small and well-conditioned set of linear equations, expounds a total least square method in the Z-domain [92]. In the following lines is a detailed description of LIPEZ methodology mathematical principles. For a linear and time invariant system with n degrees of freedom, the FRF H (ω) can be expressed by:

$$H_k = \sum_{r=1}^{2n} A_r \frac{z_k}{z_k - z_r} \tag{7.1}$$

And:

$$H_k = H(i\Omega_k) \tag{7.2}$$

$$\Omega_k = (k-1)\Delta\Omega = (k-1)2\pi\Delta f = \pi f_s (k-1)/(N-1) \tag{7.3}$$

$$i = \sqrt{-1} \tag{7.4}$$

Where:

A_r are the modal constants, Δf is the frequency resolution, f_s is the sampling frequency, N is the number of spectral lines, k = 1 · · ·N. The terms related to the Z-transform are:

$$z_r = e^{s_r \Delta t} \tag{7.5}$$

$$z_k = e^{i(k-1)\Delta\Omega\Delta t} = e^{i\pi(k-1)(N-1)} \tag{7.6}$$

Where the poles s_r are linked to the natural angular frequencies ω_r and damping ratios ξ_r by the expression:

$$s_r = -\xi_r \omega_r + i\omega_r \sqrt{1-\xi_r^{\,2}} \tag{7.7}$$

The sum in Eq. (7.1) can be converted in the following RFP expression:

$$H_k = \frac{b_1 z_k + \cdots}{a_0 + a_1 z_k + \cdots} \qquad z_k^{2n-1} + z_k^{2n} \tag{7.8}$$

Where: the 4n unknown coefficients $a_0,\cdots$ and $b_1,\cdots$ are real valued. Eq. (7.8) can be written for N spectral lines to get:

$$\begin{Bmatrix} H_1 & H_1 z_1 & \cdots & {}^{N-1} \\ H_2 & H_2 z_2 & \cdots & {}^{N-1} \\ \vdots & \vdots & \ddots & \vdots \\ H_N & H_N z_N & \cdots & {}^{N-1} \end{Bmatrix} \begin{Bmatrix} a_1 \\ a_2 \\ \\ a_{2N-1} \end{Bmatrix} - \begin{bmatrix} z_1 & z_1^2 & \cdots & b_1 \\ z_2 & z_2^2 & \cdots & b_2 \\ \vdots & \vdots & \ddots & \vdots \\ z_N & z_N^2 & \cdots & b_{2N} \end{bmatrix} \begin{Bmatrix} H_1 z_1^{2N} \\ H_2 z_2^{2N} \\ \vdots \\ H_N z_N^{2N} \end{Bmatrix} \tag{7.9}$$

Or, in a more compact form:

$$[A - B]\begin{Bmatrix} a \\ b \end{Bmatrix} = w \tag{7.10}$$

This algorithm Eq. (7.10) can be easily extended when considering a number NFRF of FRFs, because vectors **a** and **b** remain unchanged as well as matrix **B** (because it depends on the system poles only).

The systems Eq. (7.10) can be therefore assembled in the form:

$$\begin{bmatrix} A_1 \\ \vdots \\ A_{NFRF} \end{bmatrix} \begin{bmatrix} -B & \cdots & b_1 \\ \vdots & \ddots & \vdots \\ 0 & \cdots & b_{NFRF} \end{bmatrix} \begin{Bmatrix} w_1 \\ \vdots \\ w_{NFRF} \end{Bmatrix} \tag{7.11}$$

In which each line represents a system of N equations.

The linear system of Eq. (7.11) has $2n(NFRF+1)$ unknowns, i.e. the elements of the vectors a and b_m, and can be solved if $N \geq 2n(1+\frac{1}{NFRF})$. The above procedure is indeed correct but can be time consuming while implementing, especially when large data sets are analyzed *(NFRF ≫1)* and n has to vary (e.g. to define a stabilization chart). It is possible to develop a least square procedure to solve Eq. (7.11) with very good numerical performances. The problem boils down to:

$$Ra = r \tag{7.12}$$

Matrix $R \in \Re^{2n \times 2n}$ and vector $r \in \Re^{2n \times 1}$ contains the information of all the measured FRFs but a system of only 2n real linear equations has to be solved.

Moreover, because of the formulation in the Z-domain, matrix **R** is well conditioned and the solution vector **a** is very reliable. The poles $s_r = \ln z_r / \Delta t$ can then be obtained by using the equation:

$$a_0 + a_1 z + \cdots \qquad ^{2n-1} + z^{2n} = 0 \tag{7.13}$$

Any vector b_m and the related modal constants A_r, and eventually the mode shapes, can then be recovered from Eq. (7.10).

7.3. Experimental data processing

In Figure 7.4 is reported the procedure scheme adopted from experimental test to virtual data correlation. The experimental modal analysis has been carried out from a SIMO system. Firstly, the component positioning and the attachments of the force transducer and the accelerometers has been prepared and, secondly, the system has been excited and the results recorder. Subsequently, the coherence has been used as experimental reliability index:

$$\gamma_{xy}^2(\Omega) = \frac{\left|S_{xy}\right|^2}{S_{xx} * S_{yy}} \tag{7.14}$$

Where:

- $S_{xy}(\Omega)$ is the cross-spectrum between the input (forcing function) and the output (displacement measured by the accelerometers);
- $S_{xx}(\Omega)$ is the power spectral density of the input;
- $S_{yy}(\Omega)$ is the power spectral density of the output.

In particular, the coherence should be approximately around 1, except in correspondence of the resonances or anti-resonances of the system. Every single coherence function has been checked for each 22 accelerometers for both the arms. Then, for reason of compactness and to improve the readability of the results, only one example of coherence plot has been reported for both the arm.

At the end, a post process analysis has been done to obtain the frequency response function and compute the modal response of the system. A Matlab code has been implemented to proceed with the identification of modal parameters as the responses of several nodes (define by the accelerometers) to a random frequency excitation. The unknown model order n, is increased from a minimum value of 3 to a maximum of 40, in order to define stabilization charts, with the aim of separating physical and computational modes.

Then, the stabilization diagrams of natural frequencies and damping ratios of the component have been analyzed to identify natural frequencies with their damping. Time domain input and output data have been processed according to the

H_v estimator to produce the FRFs, which are the necessary inputs for the LIPEZ method. The frequency response of each node is defined by the ratio between the acceleration, measured by accelerometer, and the input excitation of the system, that correspond to the inertance (I) of each node. Although the frequency excitation was set between 100 and 1500 Hz, the frequency range of interest has been defined between 100 and 1000 Hz accordingly to the research targets.

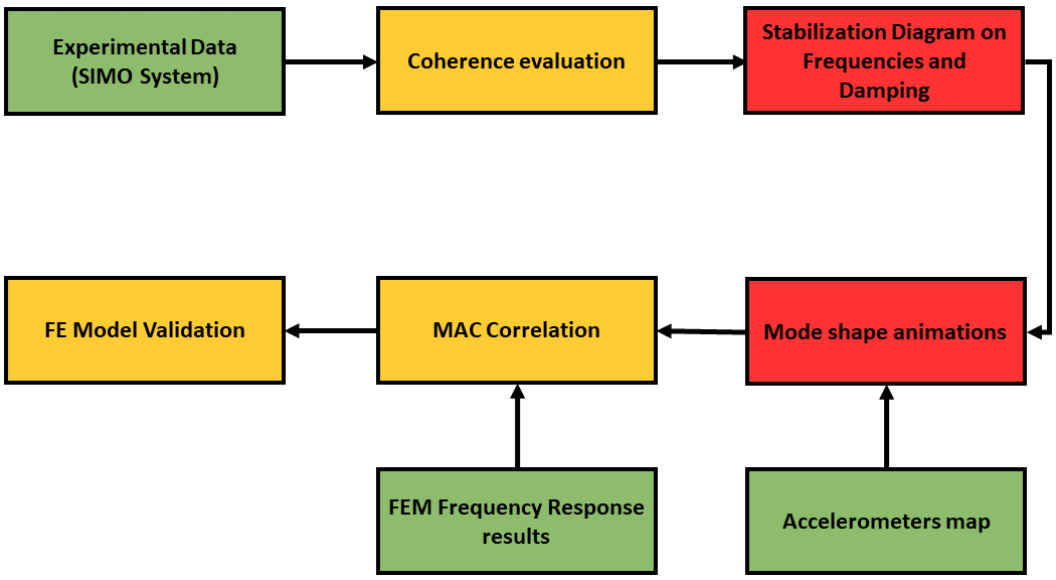

Figure 7.4 – Modal parameters extraction and correlation workflow

6.3.1. Baseline Experimental modal analysis

In Figure 7.11 is reported the power spectral density of the input force on the baseline arm. Although the input signal has a flat spectrum, the PSD function of the input force presents peaks close to the anti-resonance of the system while minimum are at the resonance frequency values. Nevertheless, the evaluation of every single coherence function has confirmed the reliability of the measurement and, as consequence, the validity of the frequency response function.

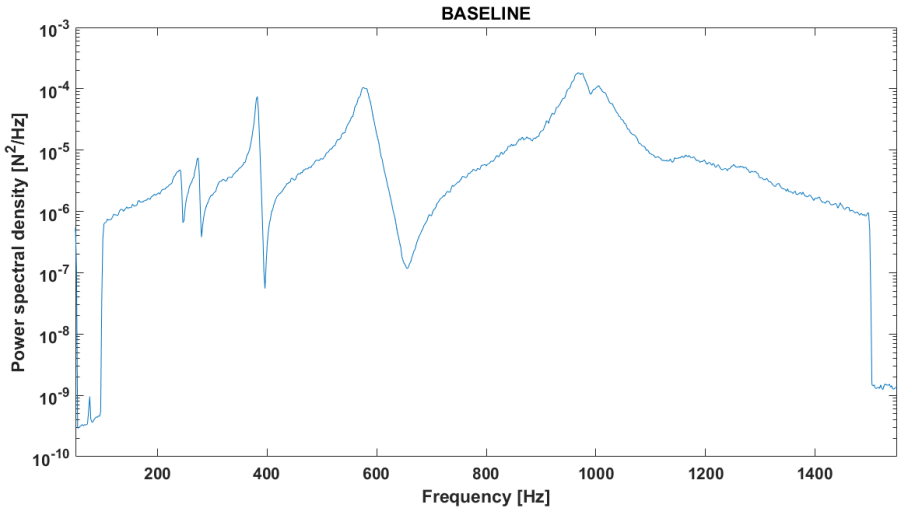

Figure 7.5 - PSD of the input force on baseline LCA

As could be observed in Figure 7.6 very stable frequency lines even at low orders are present, especially for the two peaks at about 400 Hz and 650 Hz. Each "+" corresponds to an estimated frequency in the selected band, given the model order n (ranging from 3 to 40), while in Figure 7.7 has been reported the number of extracted poles for each mode identified.

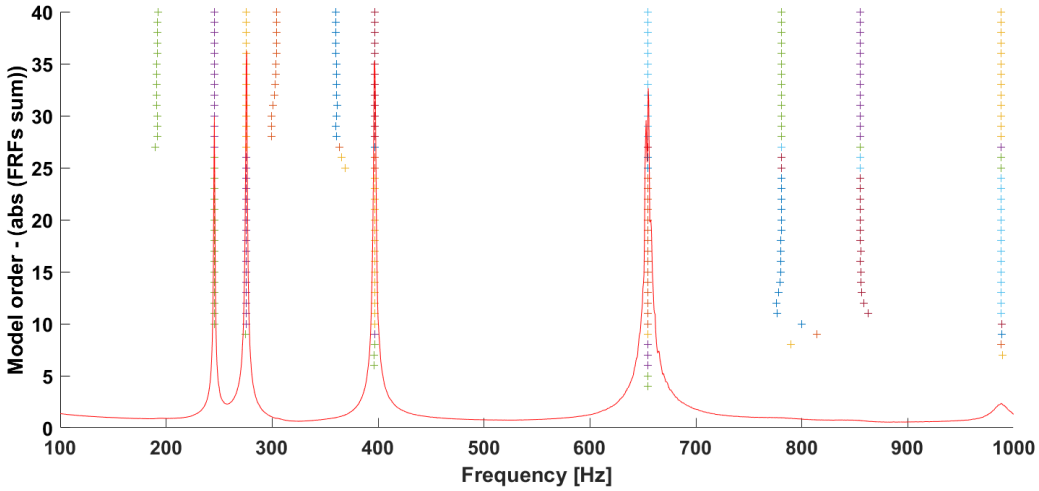

Figure 7.6 – Frequency stabilization diagram for baseline LCA

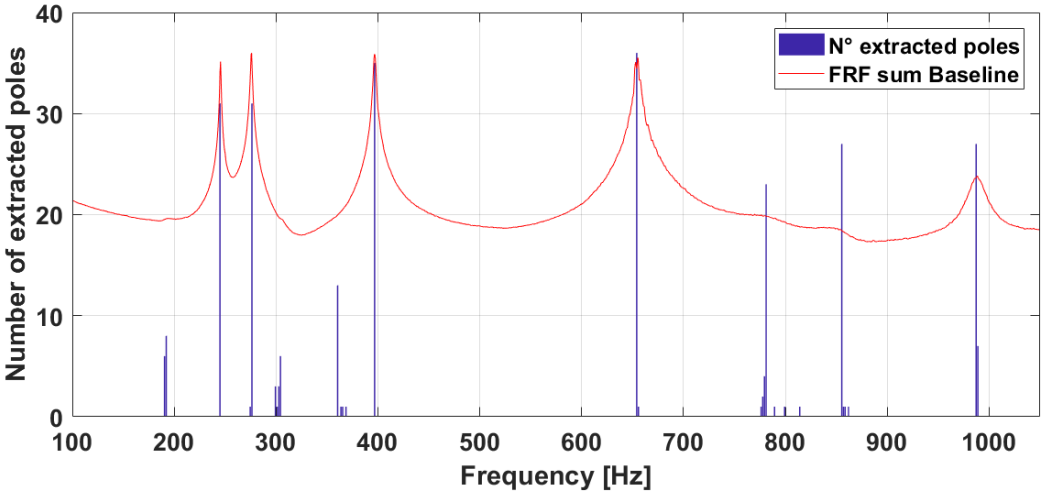

Figure 7.7 – Number of extracted poles for baseline LCA

In Figure 7.8 each "*" corresponds to the pair natural frequency damping ratio, given the model order n. Mode shapes are considered stable when, for a given frequency, damping is concentrated to a certain value for each eigenvalue extracted.

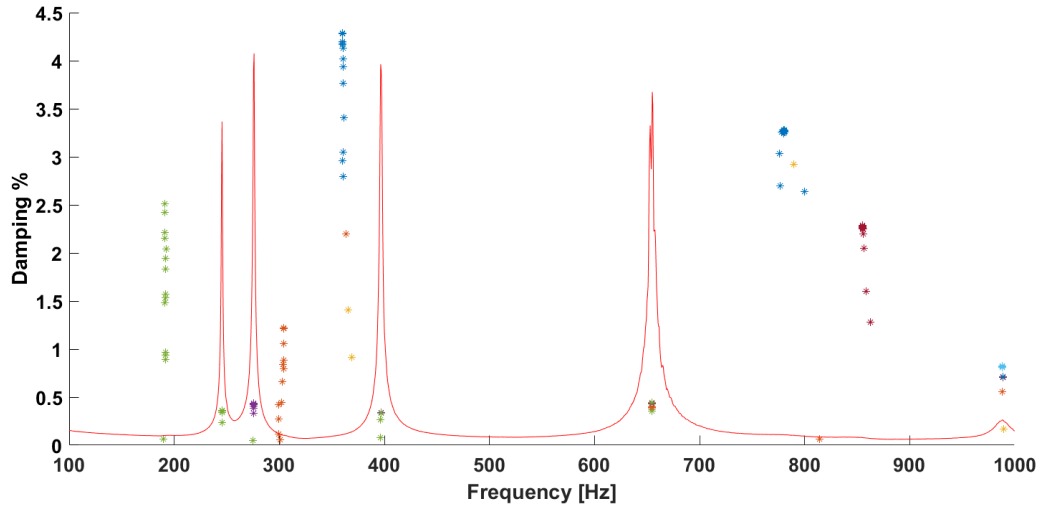

Figure 7.8 – Damping stabilization diagram for baseline LCA

Three computational mode has been observed in the range of 300-400 Hz and before 200 Hz: they have been separated from structural modes considering the physical response of the system, damping value stabilization and number of extracted poles as well. Mode five and six have been considered stable although their peaks are not well defined. This phenomenon was caused by the low excitation of the system due to the input load position that was close to a node of these mode shapes. Experimental data have been validated checking every single coherence index and in Figure 7.9 is shown for instance the plot regarding accelerometer n°9 that is located as in Figure 7.10.

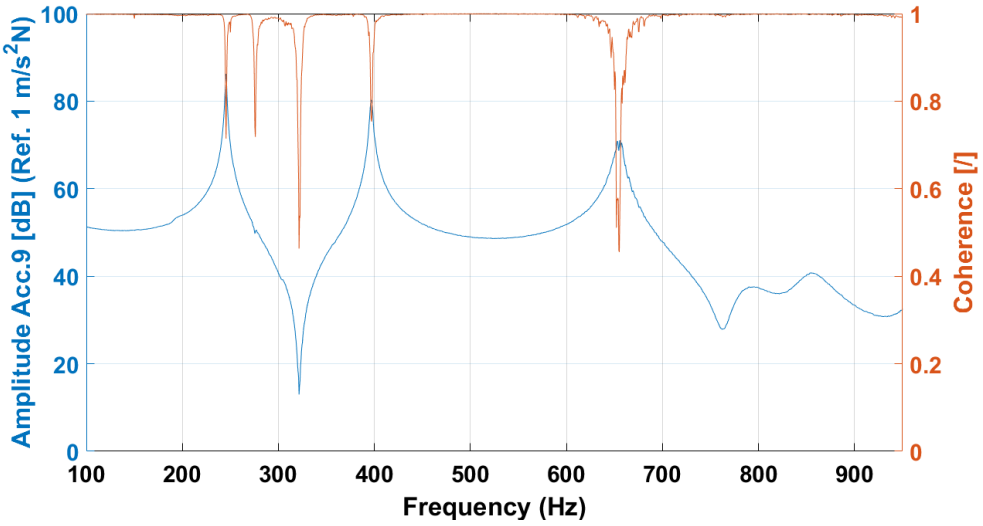

Figure 7.9 – Coherence plot of accelerometer n°9 of baseline LCA

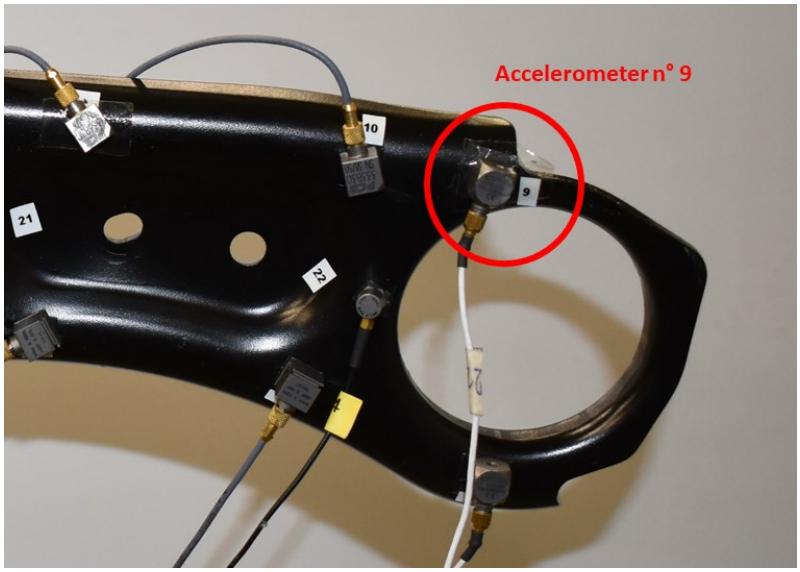

Figure 7.10 - Accelerometer n°9 position on baseline LCA

6.3.2. Hybrid experimental modal analysis

In Figure 7.11 is reported the power spectral density of the input force on the hybrid arm. As for the baseline one, the PSD function of the input force presents peaks close to the anti-resonance of the system while minimum are at the resonance frequency values. Even in this case, the evaluation of every single coherence function has confirmed the reliability of the measurement and, as consequence, the validity of the frequency response function.

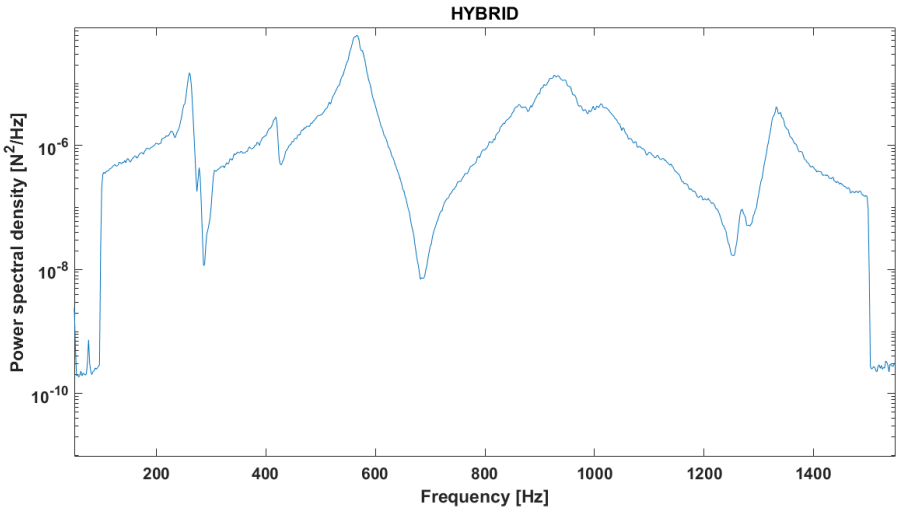

Figure 7.11 - PSD of the input force on hybrid LCA

In Figure 7.12 is presented the stabilization diagram of the hybrid LCA. Three main peaks from 250 Hz to 700 Hz are very stable from low orders, in particular the 2nd and the 4th are those with the higher energetic contribution, while in Figure 7.13 has been reported the number of extracted poles for each mode identified.

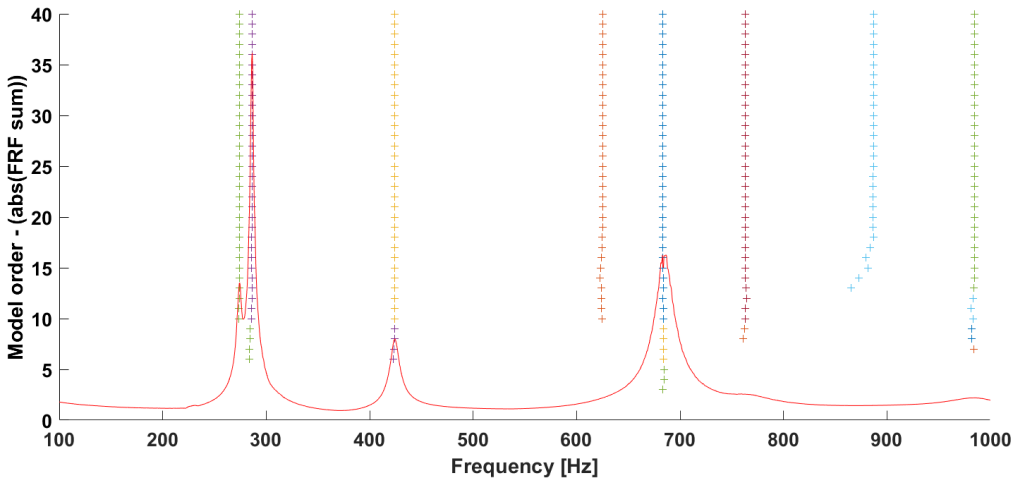

Figure 7.12 - Frequency stabilization diagram for hybrid LCA

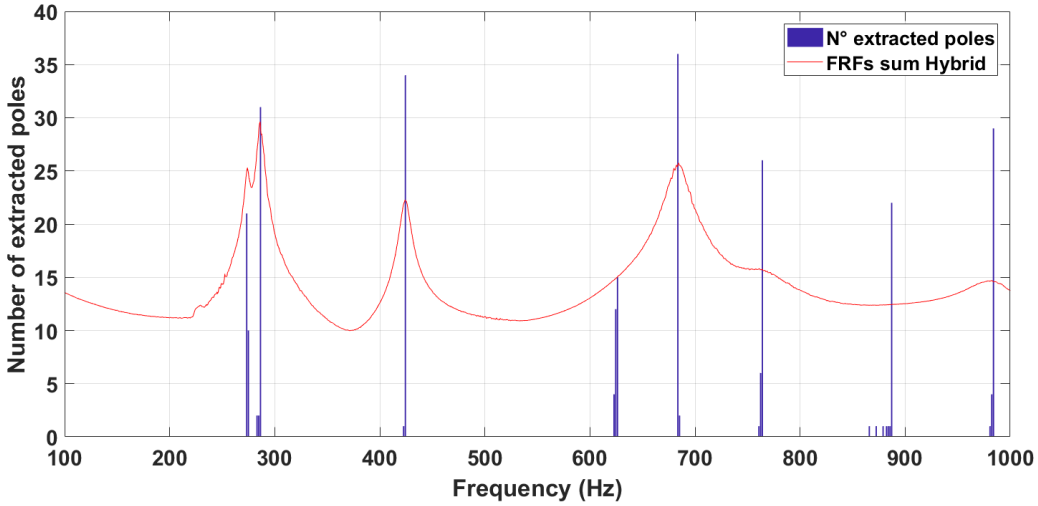

Figure 7.13 - Number of extracted poles for hybrid LCA

In this case, two computational mode has been found: one around 630 Hz and the other around 900 Hz. Although their frequency stabilization diagram were quite stable, these two modes have been discarded because their shapes were not plausible and the damping ratios were too high than the average of the other natural frequencies, as shown in Figure 7.14. Therefore, for the hybrid LCA the total number of structural modes extracted are six in the range of 100-1000 Hz.

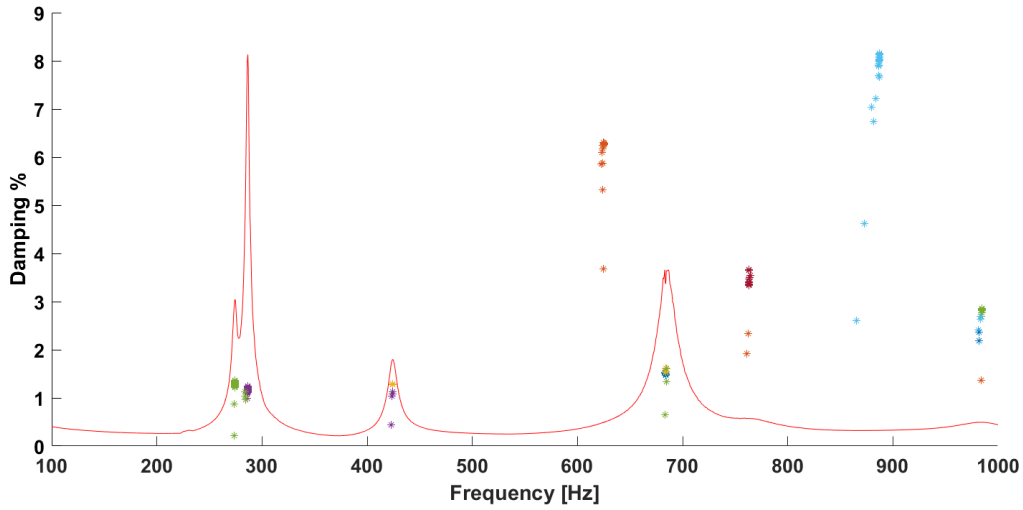

Figure 7.14 - Damping stabilization diagram for hybrid LCA

Finally, in Figure 7.15 has been reported an example of coherence calculated for the accelerometer n°9 that is located as Figure 7.16.

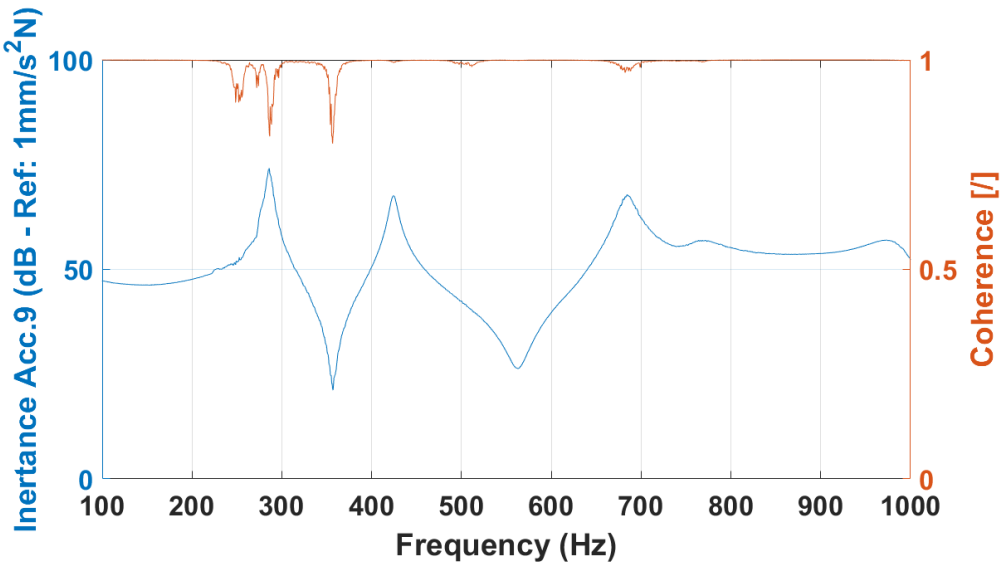

Figure 7.15 - Coherence plot of accelerometer n°9 of hybrid LCA

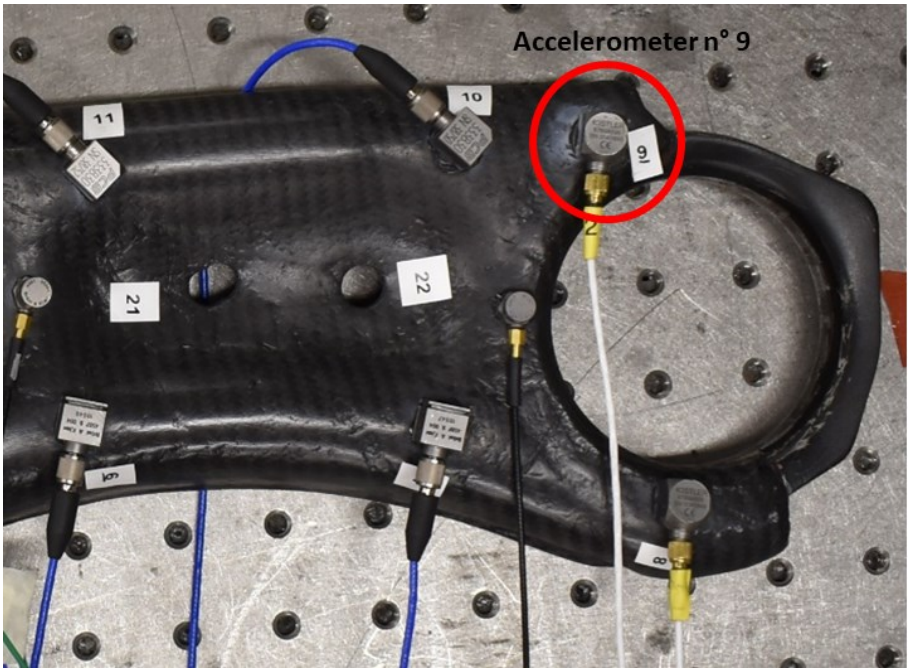

Figure 7.16 - Accelerometer n°9 on hybrid LCA

6.3.3. Synthesis of experimental modal analysis results

As previously found out in Chapter 5, HVV compound has proved good damping capabilities for specimens. Comparing the experimental results, the hybrid lower control arm shows a sensible improvement in terms of damping performance. In particular, the hybrid LCA damping ratio increased at least of 3,5 times for each eigenmode as shown in Table 7.3, with the exception of eigenmode 5 and 6 where the damping ratio is slightly higher than the baseline.

Eigenmode	Baseline Exp. Frequency [Hz]	Hybrid Exp. Frequency [Hz]	Damping Ratio Baseline [%]	Damping Ratio Hybrid [%]
1	245,43	274,14	0,36	1,28
2	275,69	286,18	0,42	1,23
3	396,78	424,21	0,33	1,29
4	654,62	683,48	0,4	1,5
5	780,18	763,26	3,25	3,39
6	855,55	984,45	2,25	2,76
7	988,09	-	0,82	-

Table 7.3 – Experimental data comparison between baseline and hybrid LCA

The reduced number of eigenmode for the hybrid LCA may have been caused by the presence of HVV material which could have completely smoothed the peak in the range of 800 Hz and 900 Hz. In fact, in Figure 7.17 the comparison of the inertance of the hybrid and baseline arms is plotted and the effect of damping material could be easily appreciated. By comparing the dynamic response between the baseline LCA (in blue) and the hybrid (in red) an efficient vibration reduction is clearly depicted since the first modes, in which smoothing of the peaks are strongly evident. In addition, the combined effect of mass and stiffness variation determined a frequency shifting of maximum 10% for the first mode, whereas for the others is less than 6%. This aspect implies that the original range of natural frequency tuned by the OEM (Original Equipment Manufacturer) for the baseline LCA has been kept also in the hybrid arm, although materials and mass are totally changed.

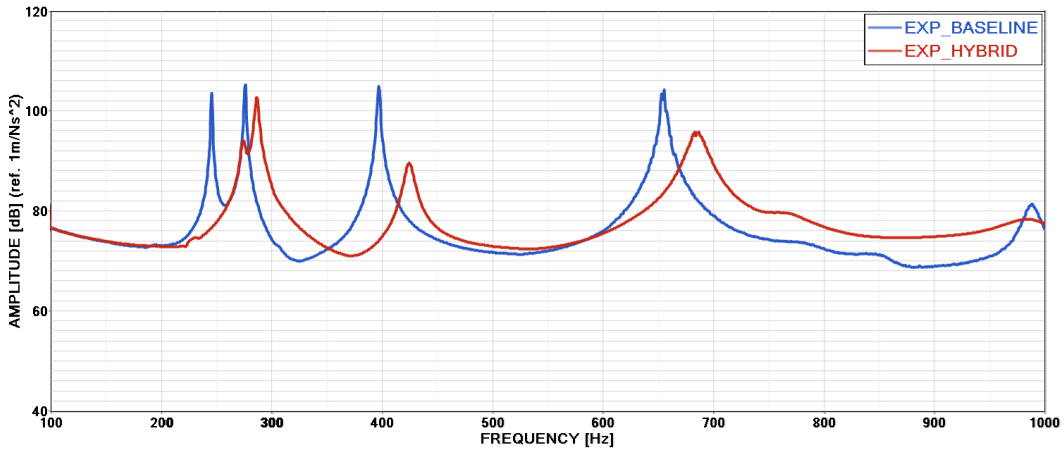

Figure 7.17 – FRF comparison between baseline and hybrid LCA

7.4. FE model for modal analysis

The experimental modal analysis has been reproduced in Optistruct by setting a frequency response simulation, as in the case of the Oberst test correlation. The FEM models developed are defined to replicate as much as possible the real components in order to predict their dynamic behaviour. Modal analysis simulation

are very sensitive to model details: for instance mass distribution is fundamental to get a well correlated FRF as also geometry definition and local stiffness.

For these reasons, baseline and hybrid FE model have been modified before running the frequency response analysis. The most important modification has been consisted in the front bushing, as shown in Figure 7.18, where the geometry has been modelled as the real component shape.

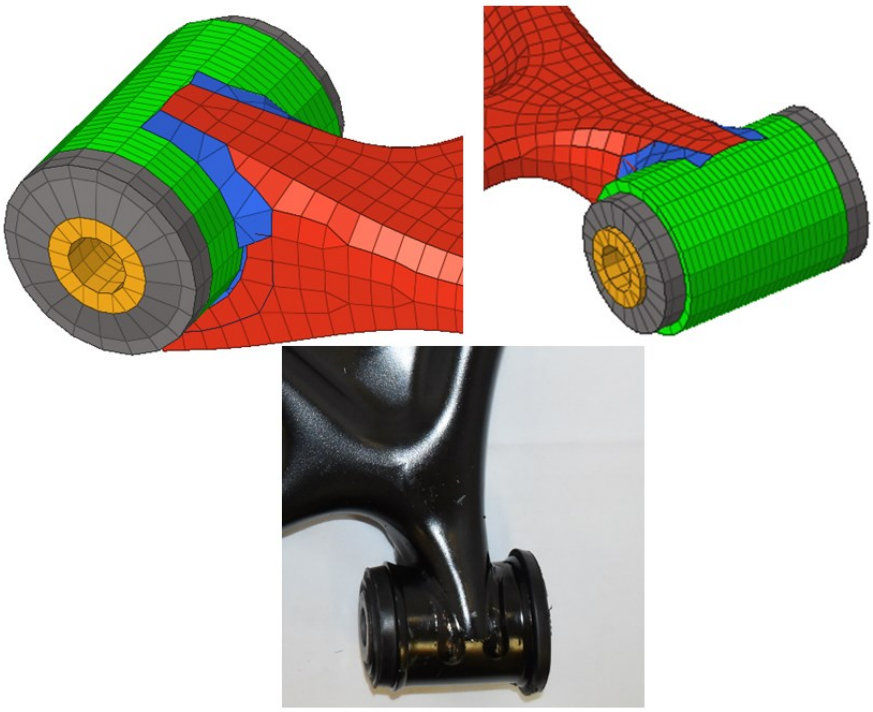

Figure 7.18 – Bushing model improvements: FEM (top), real (bottom)

Then, the accelerometer map has been reproduced on the model according to the experimental position as shown in Figure 7.19. The concentrated mass elements (CONM2) has been used to model the accelerometer mass on each specific node. The total accelerometers mass amount is around 80 g.

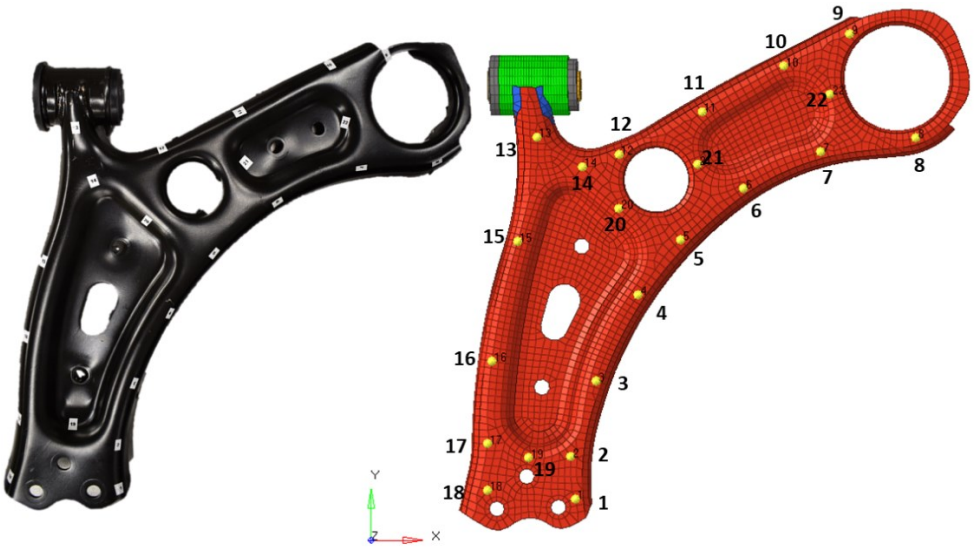

Figure 7.19 – Nodes mapping for accelerations output

As concerns material cards, it has been used the same typology and values adopted for the optimization model in Chapter 7, in which the experimental data were already implemented. In particular:

- *S420MC*: isotropic elastic material law (MAT1) with experimental data fitted for arms metal parts, with loss factor η = 0,003 [93];
- *Carbon fiber materials (GG245T, GG430T an M46J)*: orthotropic material law (MAT8) with experimental data fitted, for carbon fiber laminate;
- *HVV*: isotropic elastic material law (MAT1) with experimental data fitted.

Moreover, for the hybrid model, the structural damping has been defined for each material using USEMAT flag inside the PCOMPP property. In particular, a loss factor curve in function of frequencies has been set for the HVV and GG245T carried out from Oberst test. Finally, the random input has been defined by using DAREA load collector in order to excite in Z direction as shown in Figure 7.20. The simulation output requested consisted in the accelerations of the mapped nodes and the mode shapes.

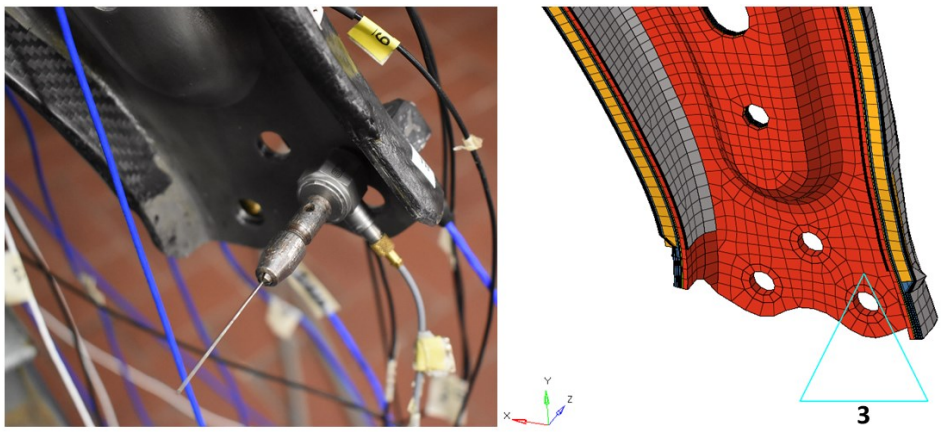

Figure 7.20 – Detail of load cell position on experimental test (left) and FEM (right)

7.5. Correlation on modal analysis

The correlation between virtual model and experimental test has been conducted evaluating the frequency shifting, the trend of the FRF, and the MAC (Modal Assurance Criterion) coefficient. In particular, this coefficient aims at comparing the simulated and experimental modal analysis results. This correlation method needs the calculation of eigenvalues that is already performed by the modal analysis. Therefore, the MAC calculation will compare the experimental and simulated eigenvalues of each analysed nodes related to each normal modes:

$$MAC_{TS} = \frac{\left|\{\psi_T\}^T \{\psi_S\}^*\right|^2}{\left(\{\{\psi_T\}^T \{\psi_T\}^*\}\right)\left(\{\{\psi_S\}^T \{\psi_S\}^*\}\right)} \tag{7.15}$$

Where:

- ψ_T are the theoretical eigenvectors
- ψ_S are the experimental eigenvectors

MAC index is expressed as a matrix of results, in which each simulated modes is compared with all the experimental one and vice-versa. The range covered by this coefficient is from 0 to 1. Two mode shapes can be considered comparable when the MAC is equal or higher than 0.5 / 0.6, instead for lower values two modes are considered different.

As concerns the baseline FEM frequency response function, an excellent correlation in terms of frequency values are observed until 650 Hz as shown in Figure 7.21, where the experimental inertance is reported in blue while the FEM in red. Virtual FRF is perfectly correlated with the experimental behaviour with errors on frequency estimation less than 2%. After 700 Hz, FEM model starts to lose accuracy: errors become higher with a maximum difference of 9% on the six mode.

Nevertheless, FEM solver is not able to find out the mode shape between 800 Hz and 900 Hz. This phenomenon may be related to the accuracy level of the CAD or FEM model. In fact, at lower frequency (200-600 Hz), modes involve the global behaviour of the structure while, at higher frequencies (700-1000 Hz), modes are mainly influenced by local stiffness or geometry variation. Therefore small modification adopted in terms of mesh discretization or geometry simplification may have affected the virtual frequency response function.

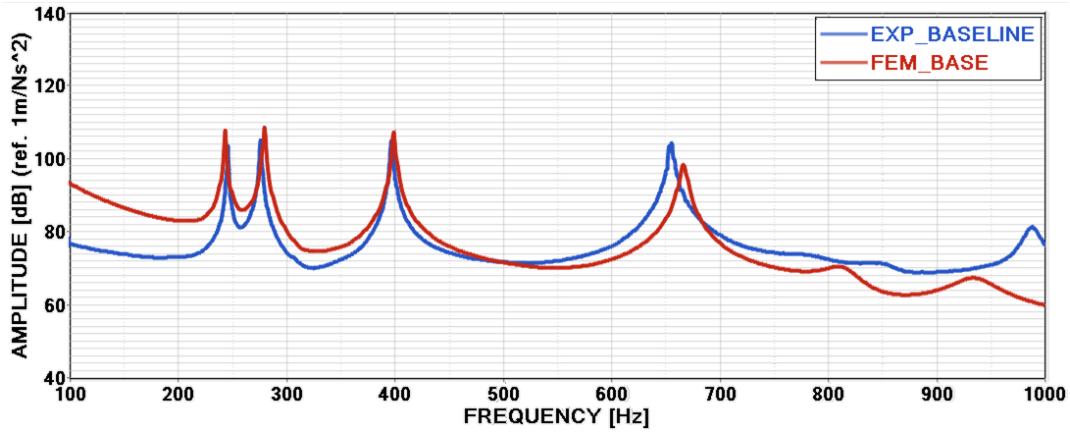

Figure 7.21 – Inertance comparison between EXP and FEM of baseline LCA

This situation is also confirmed by MAC index, in Figure 7.22, which is close to 1 for the first four mode shape while a sensible worsening is highlighted for mode 5 and 6. In particular, virtual mode shape 6 is not comparable with experimental mode shape 6 and according to the MAC matrix could be analogous with experimental mode shape 5. In Table 7.4 is summarized the complete comparison between FEM and experimental test for the baseline arm.

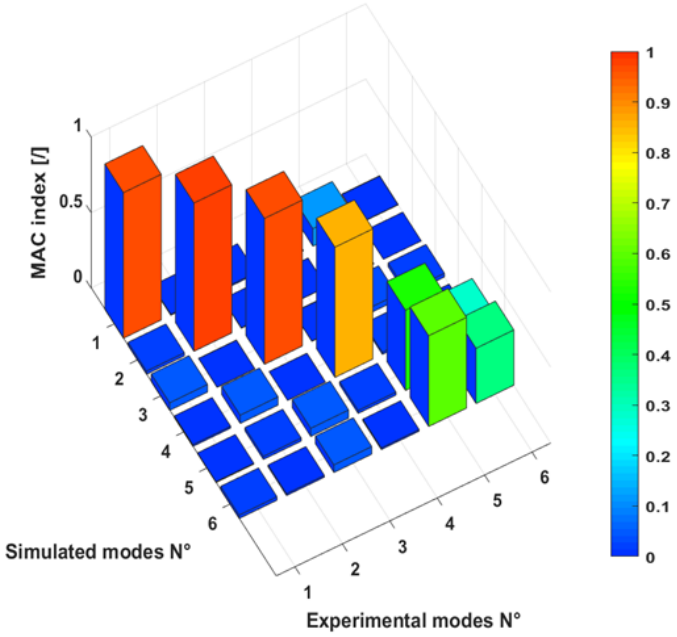

Figure 7.22 – MAC index for baseline LCA

Eigenmode BASELINE	Frequency FEM [Hz]	Frequency EXP [Hz]	Δ Frequency [%]	Diag (MAC)
1	243	245,43	0,99	0,965
2	279	275,69	-1,20	0,982
3	398	396,78	-0,31	0,967
4	666	654,62	-1,74	0,863
5	812	780,18	-4,08	0,520
6	933	855,55	-9,05	0,366
7	-	988,09	-	-

Table 7.4 – Correlation between FEM and EXP data for baseline LCA arm

As concerns the hybrid virtual modal analysis, the trend of the FRF shows a very good correlation in terms of frequencies as could be observed in Figure 7.23, where the experimental inertance is reported in blue while the FEM in red.

In this case, the virtual model is not able to match the first two modes trend although the damping behaviour is very good correlated. In this specific case, the correlation is more sensitive to each single variation due to the lamination process of the hybrid LCA. In fact, some aspects are really difficult to reproduce on the FEM model: two clear examples are the impossibility to control the thickness variation along the arm or the exact fiber orientation of the plies. Despite this, the difference between the frequencies is less than 5% except for the first mode which is about 7%.

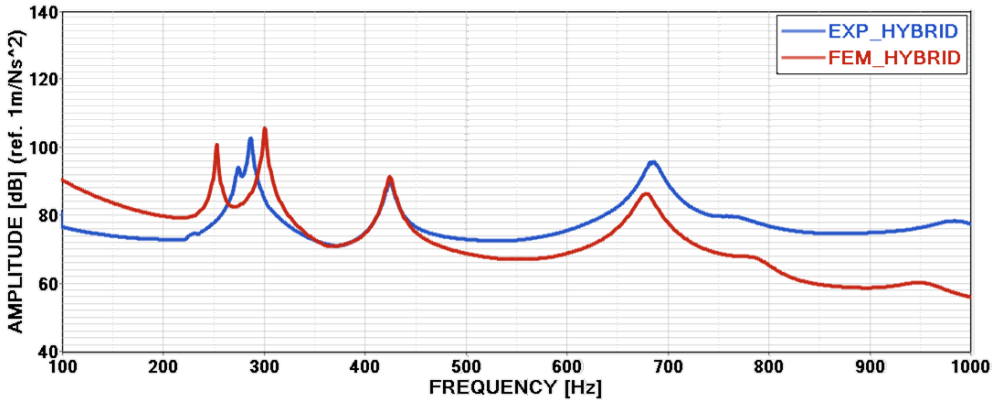

Figure 7.23 - Inertance comparison between EXP and FEM for hybrid LCA

However, MAC index in Figure 7.24 confirms the goodness of the overall correlation because is close to 1 for the first four mode shape as in the case of the baseline arm. The situation worsening for mode shape 5 and 6 that not comparable with the experimental ones. In particular virtual mode 5 has a poor level of correlation while experimental mode 5 and 6 have low analogies with simulated mode 4. In Table 7.5 is summarized the complete comparison between FEM and experimental test for the hybrid arm.

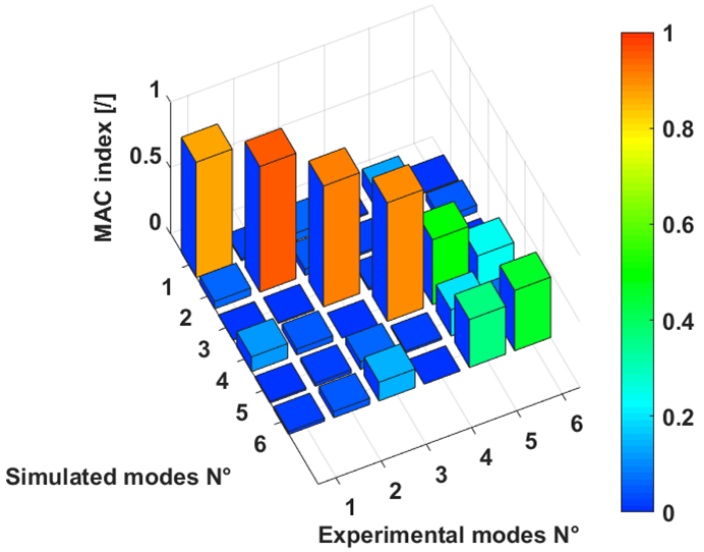

Figure 7.24 - MAC index for hybrid LCA

Eigenmode HYBRID	Frequency FEM [Hz]	Frequency EXP [Hz]	Δ Frequency [%]	Diag (MAC)
1	253	274,14	-7,71	0,873
2	300	286,18	4,83	0,952
3	424	424,21	-0,05	0,916
4	678	683,48	-0,80	0,899
5	787	763,26	3,11	0,199
6	952	984,45	-3,30	0,457

Table 7.5 - Correlation between FEM and EXP data on hybrid LCA

In conclusion, the experimental tests highlight the excellent damping vibration properties of the hybrid lower control arm that are for the first four modes 3,5 times higher than to the baseline component. Although FEM models are very sensible to geometric or stiffness variation on the real component, a very good correlation has been obtained between virtual and experimental test. For this reason the design procedure from Oberst test characterization to components modal analysis both virtual and experimental has been considered validated.

7.6. Strength analysis: bending load case

In order to complete the performance evaluation on the arms a strength analysis has been conducted and correlated. The strength test has a double function that is to verify the experimental stiffness value and to find out the characteristic curve of force displacement. For this reason, the bending load case has been chosen as representative test of the most common LCA working condition. In this case, the test has been limited to a maximum load value of 10 kN in order to preserve the structural integrity of both the LCAs, especially because only one hybrid lower control arm has been manufactured. The maximum load value has been decided according to the results obtained on virtual analysis carried out in Chapter 3 and 7, in which the stress state of the components were far from yield limit or failure.

The main test output consists in the evaluation of the longitudinal stiffness K_x of the swinging arms. Then an appropriate test apparatus has been design for this specific test as depicted in Figure 7.25. The LCA were placed over a calibrated plateau where two thick steel plates hold them in vertical position (purple and brown colors). The original rubber bushings have been replaced with two solid steel shafts have been fitted inside the bushings seats and fastened at four triangular support (green and red colors). In so doing, the bushings stiffness contribution has been removed from the total compliance of the system. The vertical alignment between the two bushings has been guaranteed by using a couple of calibrated spacers on the bottom supports.

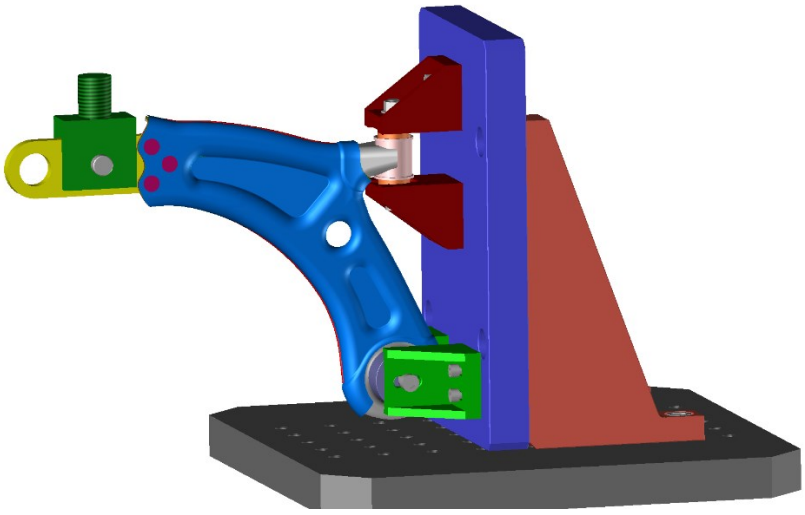

Figure 7.25 – Bending test analysis apparatus

The test has been conducted inside the DISEG (Department of Structural, Geotechnical and Building Engineering) department of Politecnico di Torino. In Figure 7.26 is illustrated the MTS hydraulic piston installed on a frame portal with a 100 kN load cell that has been used as testing machine.

Figure 7.26 – Testing machine for bending strength analysis

A set of five strain gauges (HBM LY-48-3/350 Ohm) have been distributed on the arm surfaces in order to monitor local deformations close to critical areas during the test. In Figure 7.27 are reported the strain gauge position on the LCAs: A1, B2, C3, D4 and E5 are the external strain gauges while the interlaminar sensor F6 and G7 are placed only in the hybrid LCA. In the hybrid LCA, the strain gauges have been attached on the outer surface in order to be aligned with the local orientation of fiber.

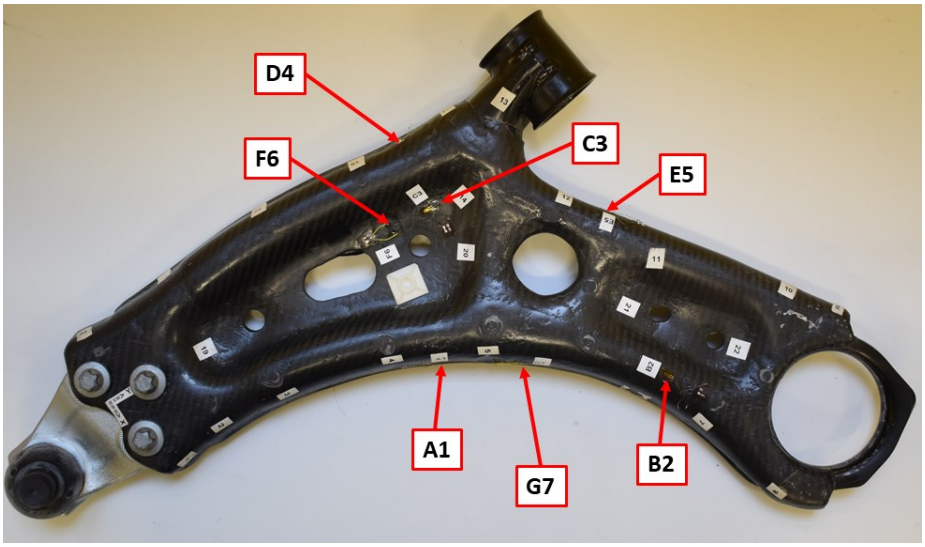

Figure 7.27 - Strain gauge map on hybrid LCA

However, the correlation with virtual results has been focused only on the force-displacement curve obtained as output from the testing machine. Finally, in Figure 7.28 are reported the test set up for baseline (left) and hybrid (right) lower control arm for the longitudinal strength test.

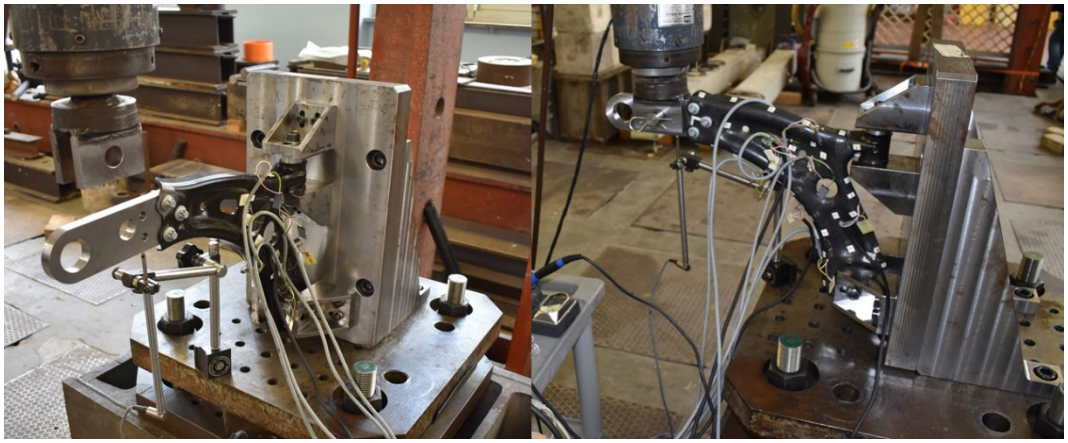

Figure 7.28 – Test set-up for baseline (left) and hybrid (right) LCA

7.7. RADIOSS FE model

The RADIOSS lower control arm model is illustrated in Figure 7.29. In order to reproduce as much as possible the physical behavior of the test, the principal apparatus components have been created on the virtual environment. For this reason, the FEM model counts about 22000 elements between shell and solids with an average size of 4 mm.

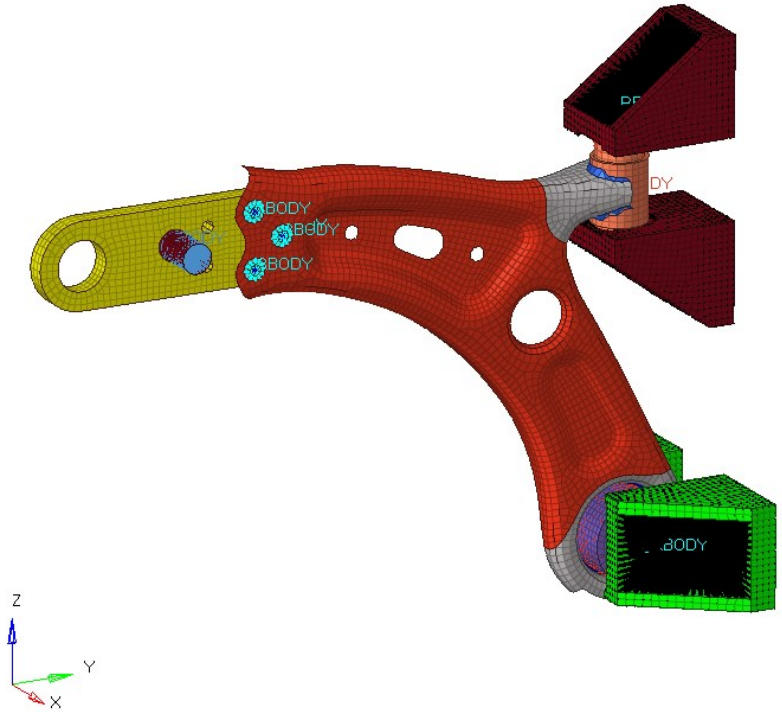

Figure 7.29 – RADIOSS LCA model

In particular, the four steel supports have been created as rigid components and fully constrained both top and bottom in their loops as shown in Figure 7.30. Instead, the purple screws have been modelled as deformable components in order to simulate the right stiffness contribution of the bolts. The screw ends have been fixed in position with a spider of rigid elements.

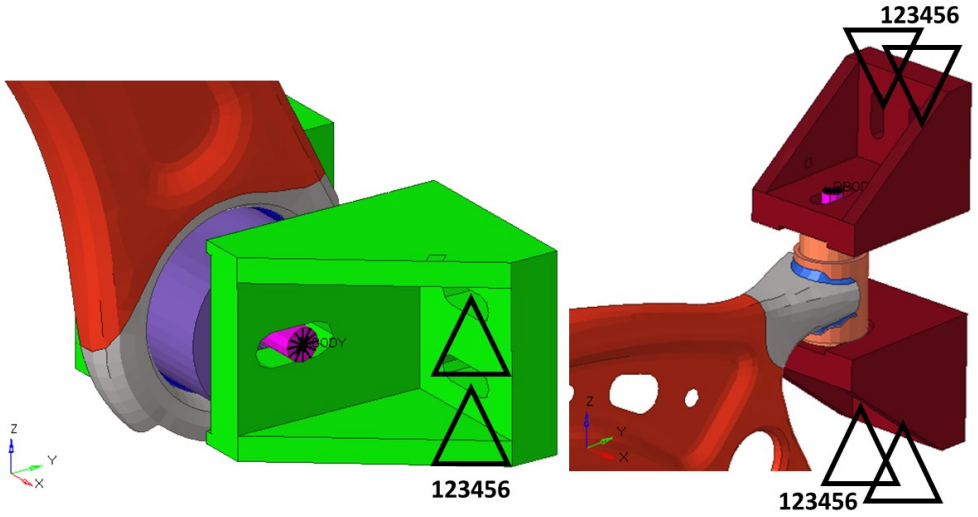

Figure 7.30 – Details of top and bottom LCA supports

The same approach has been used for the lower ball joint screws (green and blue) and the yellow plate on Figure 7.31. Even in this case, the ends of the screw have been fixed to the arm by a spider of rigid elements. The applied force of 10 kN has been set as an imposed displacement to the dark red pin, modelled as rigid body, to simulate the behavior of the hydraulic piston.

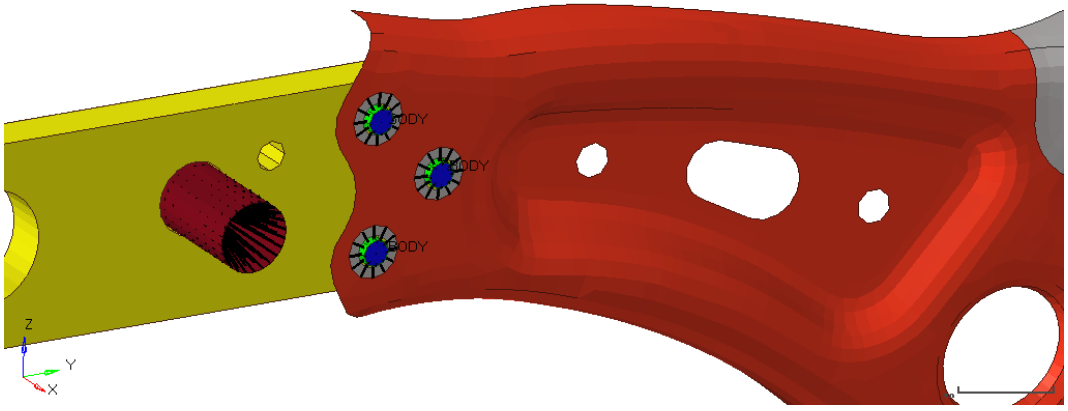

Figure 7.31 – Model detail of the mechanical assembly to the testing machine

A general node-to-surface interface (TYPE7) has been defined to simulate contact condition through all components. As concerns the material properties, it has been considered the value obtained from the experimental correlation activity found out in Chapter 6. In particular:

- *S420MC*: isotropic elasto-plastic material law (M36_PLAS_TAB) with experimental data fitted, for arms metal parts;

- *C40 Steel*: isotropic elasto-plastic material law (M2_PLAS_JOHNS) with nominal datasheet values (E=210 GPa, ν=0,3, σ_y=540 MPa, σ_{max}=700 MPa, ε_{max}=0,06), for yellow plate;
- *Steel for bolts (8.8 class)*: isotropic elasto-plastic material law (M2_PLAS_JOHNS) with nominal datasheet values (E=210 GPa, ν=0,3, σ_y=640 MPa, σ_{max}=800 MPa, ε_{max}=0,12);
- *Carbon fiber materials (GG245T, GG430T an M46J)*: orthotropic material law (LAW25 (COMPSH) with CRASURV formulation) with experimental data fitted, for carbon fiber laminate;
- *HVV*: isotropic elastic material law (M1_ELAST) with experimental data fitted.

Finally, the element properties has been defined as follow:

- *Steel shell components*: P1_SHELL with QEPH element formulation;
- *Steel solid components*: P14_SHELL with HPEH element formulation;
- *Composite laminate component*: P51_STACK and P19_PLY with QBAT element formulation.

7.8. Experimental results and correlation

As can be easily to expect, the mechanical performance of the arms during the bending test have been affected by the compliance of the entire system. Bolts and the other mechanical connections have notably decreased the total stiffness of the LCAs compared to the virtual estimation made in Chapter 3 and Chapter 7, in which the joint were modelled as completely rigid. Then, a couple of preliminary cycle have been done at 5 kN before applying maximum load in order to settle the mechanical test apparatus and reducing mechanical gap and friction on the assembly. Subsequently, the arms have been submitted to two tests of load and unload cycle at 10 kN.

Notwithstanding, some binding effects have been found between mechanical connections as can be observed in Figure 7.32, especially in the case of the baseline LCA which tends to increase its stiffness after 6 kN. However, the experimental difference between the baseline (blue) and the hybrid (red) curve is very low. In particular, the baseline longitudinal stiffness K_x is equal to 3,6 kN/mm while the hybrid K_x is 3,4 kN/mm, that means a difference of 6%.

Another important aspect to be mentioned is the remarkable energy dissipation of the hybrid LCA compared to the baseline. This effect is the combination of the viscoelastic properties of the CFRP matrix and, above all, the HVV material that confirms its high energy dissipation characteristics. In addition, the two couple of test conducted on the arms present a perfect repeatability.

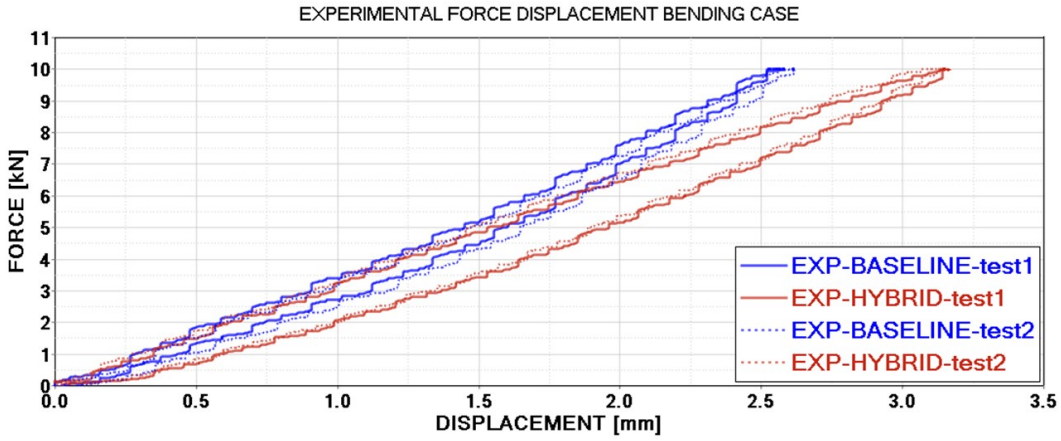

Figure 7.32 – Experimental strength curves for baseline and hybrid LCA

Moreover, the strain analysis confirm this trend. In Figure 7.33 and Figure 7.34 are reported the strain sampled in function of time for both the tests, for each LCA. Particularly, for the baseline arm, it can be seen the deformation increasing after 35 s on the strain gauge D4. This sensor is placed near the front bushing seat, hence it may be possible that the binding phenomenon was due to bushing friction with the upper support.

On the contrary, on the hybrid arm all the strain curves are linear and no stiffening effects are present. Unfortunately, one of the interlaminar sensor (F6) has been damaged probably during the surface finishing and no data have been logged. In the end, the experimental values of the strain are in the order of 0,001 mm/mm and no residual deformations are reported, therefore the elastic conditions are observed.

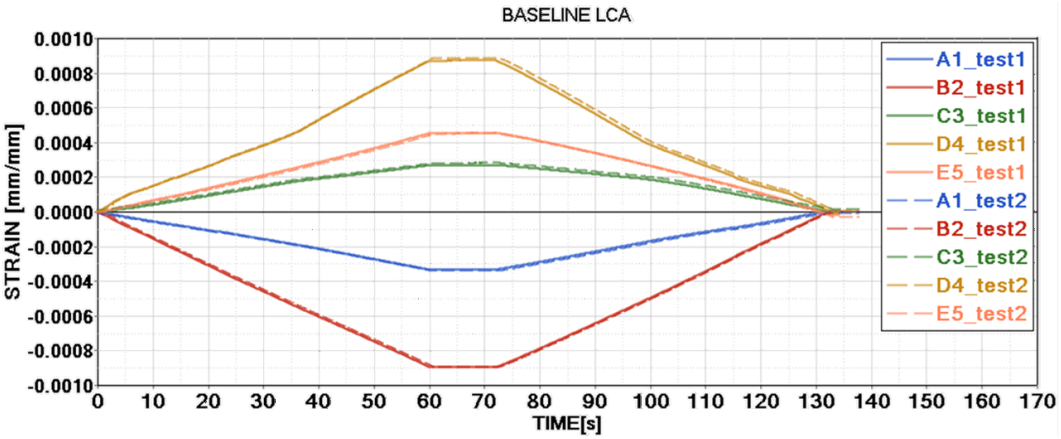

Figure 7.33 - Experimental strain curves of baseline LCA

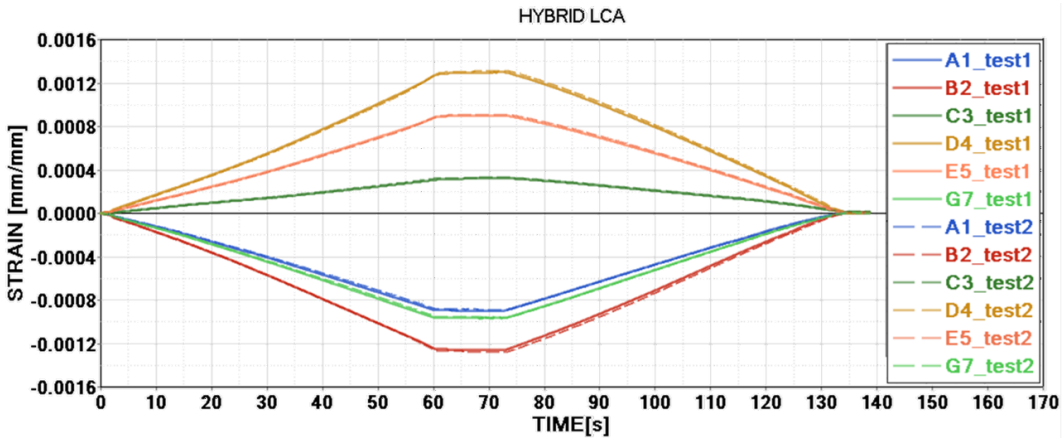

Figure 7.34 - Experimental strain curve of hybrid LCA

7.9. Correlation on strength tests

Then, the RADIOSS models have been correlated with the experimental results. As highlighted in Figure 7.35, the baseline FEM force-displacement curve shows a very good level of correlation: at the beginning, FEM model underestimates the experimental stiffness of 7% until 4 kN while after is perfectly aligned with the experimental curve trend.

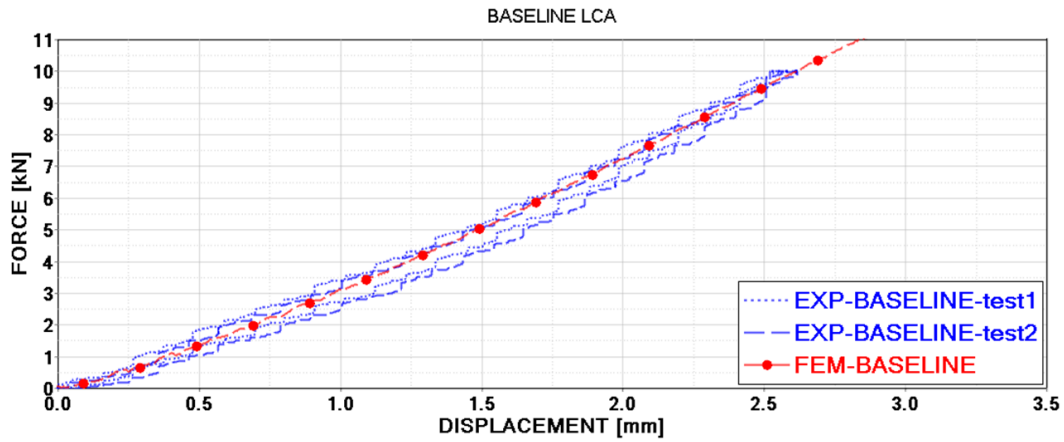

Figure 7.35 – Correlation results for baseline LCA bending test

In the case of hybrid lower control arm in Figure 7.36, the behavior is similar of the baseline because FEM underestimate the initial stiffness of 4% until 7 kN while after becomes aligned with the experimental curve. At 10 kN, the virtual curve deviates with a stiffness increasing of about 7%. This difference may be linked to the FEM joint modellization: in fact, the rigid spiders at the end of the screws can cause local stiffening effect after a certain load, reducing the components deformation due to the compliance of the real system.

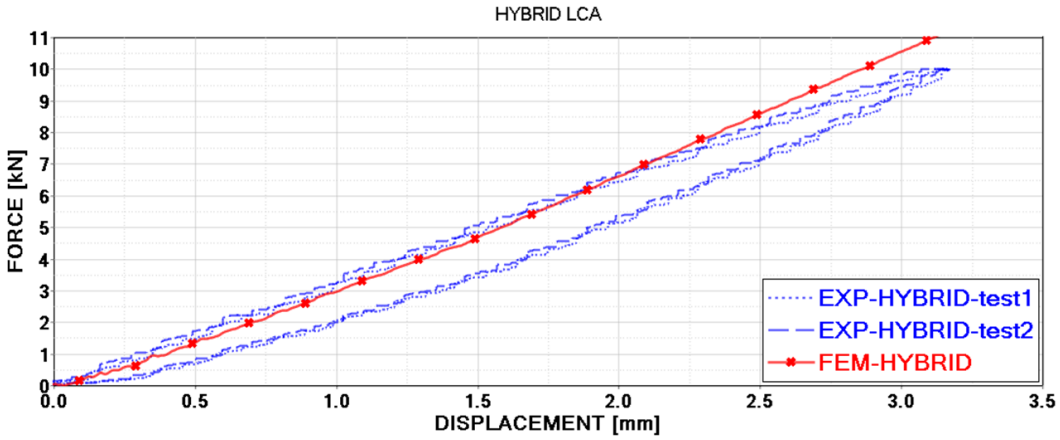

Figure 7.36 - Correlation results for hybrid LCA bending test

In conclusion, the strength test for the longitudinal case has highlighted a low difference in performance between the two swinging arm. In fact, it has been experimental demonstrated that the longitudinal stiffness of the hybrid LCA is just 6% less than the baseline one.

The analysis of the experimental strains had shown no residual deformation on both the components after two tests of load and unload cycle at 10 kN. As consequence, no plastic deformations have been registered so the arms had remained in elastic field. On the other hand, the RADIOSS FEM models of the baseline and hybrid arm had obtained a high correlation level with their respective experimental tests, with a maximum error on stiffness estimation of 7%.

For these reasons, the results carried out both from experimental and virtual tests had validated the design procedure that involve all the intermediate stage from material specimen characterization to real component test. In Table 7.6 the test summary has been reported including a synthetic comparison between FEM and EXP results.

	EXP Stiffness K_x [kN/mm]	**Δ between EXP [%]**	**FEM stiffness K_x [kN/mm]**	**Δ EXP vs. FEM [%]**
BASELINE LCA	3,6	-	3,35	-7%
HYBRID LCA	3,4	-6%	3,26	-4%

Table 7.6 – Result summary on longitudinal strength tes

Chapter 8

Conclusions

The main goal of this thesis is the study, the development and testing a multi-material lower control arm of a McPherson suspension for a C segment vehicle (Fiat 500X). An innovative viscoelastic material has been used to join carbon fiber with steel that works as passive constrained layer damper and adhesive simultaneously. Therefore, the hybrid technology applied has been focused to reduce the LCA mass, diminishing the steel thickness and adding a CFRP tailored cover without compromising the global mechanical performance. In particular, it has been developed a specific methodology that combines both virtual and experimental procedures to face the hybridization challenges of mechanical coupling, damping and lightweight. In addition, particular attention has been paid on the investigation of the dynamic response in terms of vibration reduction especially in the range of structure-borne frequencies from 0-600 Hz.

The definition of the load conditions on the lower control arm has been set by considering three different configurations: lateral and longitudinal load for stiffness evaluation, special and misuse events. From the reference vehicle information, a multibody model of the 500X has been created in order to carry out the force acting on the lower control arm. As special events, the simulation performed consisted in skid-pad, maximum acceleration and maximum braking test to evaluate lateral and longitudinal force at grip limit. Instead, as misuse events, the simulation performed consisted in driving over a crossbeam, hump and drain to evaluate lateral and longitudinal force after an impact. The suspension parameters have been carried out from benchmark analysis.

Through a reverse engineering activity, the baseline lower control arm CAD file has been generated and the FEM model created. Then, the FEM stiffness analysis, special and misuse events have been conducted in order to define the reference performance for the hybrid LCA.

The hybrid LCA concept has been also designed to be replaceable with the original component, accomplishing specific constraints such as suspension packaging, mechanical coupling to the wheel and chassis, manufacturing process as well. These requirements have been integrated to the component targets: lightweight, damping and safety by using innovative materials and design procedures defined for this specific case study.

Two viscoelastic materials have been compared in order to evaluate their damping and adhesive properties. These two compounds have been tested in a wide frequency and temperature range (ASTM E756-05 and SAE J1637) and after an aging treatment of 750h (IEC 60068) in order to carry out their Young's moduli and loss factor value at different conditions. Regarding the adhesive capabilities, single lap joint test (ASTM D5868-01) has been conducted to evaluate the joint strength between steel and CFRP. Both toughnesses G_{Ic} (ASTM 5528) and G_{IIc} (ASTM D7905M - 14) have been estimated at 0 h and 750 h (IEC 60068) as also for the single lap joint. Experimental tests have shown that the HVV compound presents the best damping performance especially for its capability to maintain a high constant loss factor even after 750 h of aging. Moreover, because HVV has the highest shear toughness and shear strength, it has been chosen as interlaminar material between steel and carbon fiber.

Dynamic tests in Altair Optistruct have been performed to virtually reproduce the ASTM 756-05 test, to correlate, on specimen geometries virtual and real tests. An optimal correlation has been found-out by using the new feature GE_USEMAT flag in order to define loss factor value in function of frequency inside a multi-material stacking sequence. The results obtained from the Oberst test have allowed to define a specific Optistruct card material able to reproduce virtually the damping effect of the HVV even in the LCA complete model for the frequency response analysis.

Mechanical characterization on hybrid LCA materials have been carried out to investigate the experimental values necessary for FEA card materials in Altair RADIOSS. For carbon fiber materials three typology of test have been conducted, such as tensile (ASTM D3039), compression (ASTM D3410) and bending test (ASTM D790) to evaluate Young's moduli and maximum stress at different orientations (0°/90°/45°). Only tensile test (ASTM E8/E8M-16A) has been conducted for steel. The experimental results have been successfully fitted in RADIOSS both for CFRP and for steel materials by using a specific FEM procedure. The material cards created have been used inside the longitudinal strength simulation. Instead, the elastic values validated in RADIOSS have also been used for the respective linear elastic material card in Optistruct, to perform the optimization and the frequency response analysis.

The optimization analysis on carbon fiber cover has been addressed to find the optimum combination of ply shape, orientation and stacking sequence accordingly

with the multi-material LCA targets of mass reduction and stiffness performance. The simulation has been carried out considering the stiffness load cases of bending and buckling load starting from the maximum arm envelope defined by the packaging analysis. The optimized hybrid LCA achieved a 23% of mass reduction with longitudinal and lateral stiffness diminished of 9% and 7% respectively than the virtual baseline model. Beside all, it is to be highlighted that the stress distribution due to special and misuse events is fully satisfying the safety requirements.

Modal analysis and longitudinal strength test have been conducted on both the arms to compare their experimental performance in terms of damping and stiffness and to validate the methodological design approach by FEM correlation. LIPEZ modal extraction parameters method has been successfully applied to find out the inertance, mode shapes and damping ratios of the two lower control arms.

Hybrid LCA demonstrated excellent damping capabilities due to the application of HVV compound, increasing of 3,5 times the damping ratio for the first four modes between 100-600 Hz. Moreover, the frequency shifting between baseline and hybrid is limited to a maximum of 10% for only the first mode whereas the other are less than 6%. Therefore, the hybrid arm is tuned in the same range of natural frequencies defined by the OEM for the baseline LCA. High correlation levels have been obtained between the experimental modal analysis and the virtual frequency response. FEM models are able to reproduce a very good correlated FRF in terms of frequency and damping, with a high MAC correspondence especially for the first four modes, whose values are over 0,85.

Nevertheless, FEM modal analysis are strongly sensible to the geometry fidelity to the real component. The accuracy of the CAD and FEM models are crucial for the correlation on eigenmodes and eigenfrequencies. In fact, it has been found out that the correlation at higher frequencies (700-1000 Hz) is poor because modes are mainly influenced by local stiffness or geometry variation. Therefore small modification adopted in terms of mesh discretization or geometry simplification may have affected the virtual frequency response function. This effect is more evident in the case of hybrid LCA were the last modes have the MAC index below 0,5.

Experimental longitudinal strength test has highlighted a low difference in performance between the two LCA. The longitudinal stiffness of the hybrid LCA is just 6% less than the baseline one. The analysis of the experimental strains have shown no residual deformation on both the components after two tests of load and unload cycle at 10 kN. As consequence, no plastic deformations have been registered so the arms are remained in elastic field.

Two detailed RADIOSS FEM models have been created in order to reproduce the same scheme and compliance of the test apparatus. The results obtained have demonstrated a high correlation level with their respective experimental tests, with a maximum error on stiffness estimation of -7% and -4% respectively for the baseline and hybrid LCA.

Finally, summing up all the previous results, it is possible to assert that:

- An innovative lightweight and multi-material LCA has been designed and tested, obtaining a mass reduction of 23% and guarantying similar stiffness values;

- The hybrid design proposed integrates innovative solution to face problems of mechanical coupling, dissimilar material joining and safety standard for a complex component such as a swinging arm;

- Vibration reduction has been achieved: hybrid LCA global damping is more than tripled than baseline LCA, due to excellent damping capabilities of the HVV material;

- A complete methodological approach concerning experimental and virtual paths has been studied, correlated and validated at different levels. High correlation has been obtained both on material card fitting and on complete model simulation with two different commercial FEM solvers.

- FEM simulations are a key enabling technology especially for composite design, but high model accuracy is needed to obtain reliable and predictive models both for structural and dynamic analysis;

- Multi-material concepts represent a feasible solution to foster lightweight challenges even though their potential in terms of performance could be limited if adapted to an existing component.

Further activities will be necessary to test both at component and at vehicle level this innovative solution to fully accomplish the safety, durability and misuse requirements typical of the automotive world. In particular, at component level it would be important to investigate the environmental and aging effects (i.e salt spray, UV radiation) on the mechanical performance of the multi-material lower control arm. In addition, impact and fatigue test would be performed to fully validate the LCA hybrid solution in terms of strength and mechanical coupling between carbon fiber and steel.

As concerns the vehicle level, a four poster rig test would be fundamental to evaluate durability due to road like excitation. Moreover, particular attention would be payed to evaluate the suspension performance by doing specific manoeuvres both “dynamic” (i.e step-steer, ISO lane change) and “structural” (i.e poth-hole, crossbeam) on track as well as NVH test on different road profile to evaluate vibration transmissibility on chassis.

References

[1] European automobile Manufacturers Association. *Manifesto for Clean, Safe and Smart Mobility*. 2016.

[2] Climate Action-European Commission. *Proposal for Post-2020 CO2 Targets for Cars and Vans.* 2017.

[3] Mobility and transport - European Commission. *"European Day Without a Road Death": Success for road safety awareness across Europe*. 2016.

[4] C. Lauter, T. Krooss and T Troester. *Manufacturing of hybrid structures by prepreg press technology*, 19th International Conference on Composite Materials, 2013.

[5] Lotus Engineering Inc. *An assessment of mass reduction opportunities for a 2017-2020 model year vehicle program.* 2010.

[6] M. Frantz, C. Lauter and T Troester. *Advanced manufacturing technologies for automotive structures in multi-material design consisting of high-strength steels and CFRP,* 56th International Scientific Colloquium, 2011.

[7] D. Mayer, T. Bein, H. Buff et al. *Enhance lightweight design by composites – results of the eu project enlight*, Technologies for lightweight structures. 2017

[8] https://www.audi-mediacenter.com, Accessed 15 February 2019.

[9] https://www.daimler.com, Accessed 15 February 2019.

[10] https://www.bmwgroup-werke.com, Accessed 15 February 2019.

[11] https://www.press.bmwgroup.com, Accessed 15 February 2019.

[12] N. Lutsey. *Review of technical literature and trends related to automobile mass-reduction technology*. 2010.

[13] D. Richard. *Automotive Suspension System Benefits from Composite.* Reinforced Plastics. 2003.

[14] P. Beardmore and C.F. Johnson. *The Potential for Composites in Structural Automotive Applications*, Composites Science and Technology. 1986.

[15] F. Klaus and A. A. Almajid. *Manufacturing Aspects of Advanced Polymer Composites for Automotive Applications*. Applied Composite Materials. 2013.

[16] K. Wood. *Composite Leaf Springs: Saving Weight in Production*. https://www.compositesworld.com, Accessed 15 February 2019.

[17] https://www.total.com, Accessed 15 February 2019.

[18] https://www.henkel.com, Accessed 15 February 2019.

[19] D. Zhu. *Lightweight @ ZF Friedrichshafen AG*. 2014.

[20] M-Y Chang. *Lightweight Front Suspensions: A Comparison*. Encyclopedia of Automotive Engineering. 2014.

[21] https://www.jato.com/italy/. Accessed 15 February 2019.

[22] Book UNRAE 2017. *Analisi del mercato autoveicoli in Italia*. 2017

[23] https://en.wikipedia.org. *MacPherson Strut*. Accessed 15 February 2019.

[24] G. Genta and L. Morello. *The automotive Chassis*, Springer. 2009.

[25] R. Salloum, P. Töws, S. Schmidt et al. *Vibration Damping of a Composite Control Arm through Embedded Piezoceramic Patches Shunted with a Negative Capacitance*, Smarte Strukturen Und Systeme, 2016.

[26] G. Sheng. *Vehicle noise, vibration, and sound quality*. SAE international. 2012.

[27] W. Xu, *Vehicle Noise and Vibration Refinement - 1st Edition*. Elsevier. 2010.

[28] M. A. Panza. *A Review of Experimental Techniques for NVH Analysis on a Commercial Vehicle.* Energy Procedia. 2015.

[29] R. Salloum, O. Heuss, and D. Mayer. *Global Optimization of Smart Lightweight Structures*, Proceedings of ISMA 2014 including USD. 2014.

[30] S. Cooper. *Joining of composites*. WEMMA, TWI & BCS Lecture. 2017.

[31] R. Jones. *Mechanics of composite materials-2nd edition*. Taylor & Francis. 1998.

[32] G. Kelly. *Joining of Carbon Fibre Reinforced Plastics for Automotive Applications*. 2004.

[33] M. Liu, Y. Guo, J. Wang et al. *Corrosion Avoidance in Lightweight Materials for Automotive Applications*. Npj Materials Degradation. 2018.

[34] M. Tavakkolizadeh and H. Saadatmanesh. *Galvanic Corrosion of Carbon and Steel in Aggressive Environments*. Journal of Composites for Construction. 2001.

[35] M. Eguia, M. Huang and T. Tyan. *Impact Testing of Lower Control Arm for Crashworthiness Simulation*. SAE international. 2005.

[36] M. Huang, M. Eguia and Tau Tyan. *Crashworthiness Simulation of Lower Control Arm Impact Tests*. SAE international. 2005.

[37] M. Eguia, M. Huang and T. Tyan. *Impact Testing of Bushings for Crashworthiness Simulation*. SAE international. 2006.

[38] S. Jayaraman. *Design of Suspension Components for Small Overlap Frontal Impact (SOF) Analysis*, Symposium on International Automotive Technology. 2017.

[39] S. Abrate. *Impact Engineering of Composite Structures*. Springer. 2005.

[40] M. Çallı, M. Kaya, E. Yiğitoğlu and N. Efe. *Development and optimization of a lower control arm (LCA) using high strength steels*, European Altair Technology Conference. 2014.

[41] H. Fuchs and R. Salmon. *Lightweight MacPherson Strut Suspension Front Lower Control Arm Design Development*. SAE International. 2011.

[42] Cetim. *JEC innovation Awards*. 2013.

[43] C. Fagiano, F. Laurin, P. Lapeyronnie et al. *Design of composite structures: from mechanical behaviour characterisation to structural optimisation*, Franco-British Symposium on Composite Materials. 2015.

[44] P. Feraboli, F. Gasco, B. Wade et al. *Lamborghini "forged composite®" technology for the suspension arms of the Sesto Elemento*, ASC conference proceedings. 2011.

[45] http://www.project-enlight.eu/. Accessed 15 February 2019.

[46] T. Bein. *The ENLIGHT Project: Enhanced Lightweight Design*. 2012.

[47] D. Bassan. *Scruitanising manufacturing aspects for innovative lightweight composite components production: EnLight project results*. 2016.

[48] R. Salloum. *Optimization of shunt damped composite structures using negative capacitances*. PhD Thesis. 2016.

[49] R. Salloum, O. Heuss and D. Mayer. *Design of Smart Lightweight Structures: Simultaneous Optimization of Mechanical and Shunt Circuit Parameters*, 25th International Conference on Adaptive Structures and Technologies. 2014.

[50] Book UNRAE. *Immatricolazioni in Italia di autovetture e fuoristrada top ten per segmento*. 2018.

[51] https://www.fiat.it/. Accessed 15 February 2019.

[52] W. Papacz, P. Kuryło and E. Tertel. *The Composite Control Arm – Analysis of the Applicability in Conventional Suspension*. American Journal of Mechanical Engineering. 2013.

[53] S. J. Heo, D. O. Kang, J. H. Lee et al. *Shape Optimization of Lower Control Arm Considering Multi-Disciplinary Constraint Condition by Using Progress Meta-Model Method.* International Journal of Automotive Technology. 2013.

[54] S. H. Yoo, J. Doh, J. Lim et al. *Topologically Optimized Shape of CFRP Front Lower Control Arm.* International Journal of Automotive Technology. 2017.

[55] D. Detwiler, E. Nutwell and D. Lokesha. *Multistage optimization of automotive control arm through topology and shape optimization*, 6th BETA CAE International Conference. 2015.

[56] https://portal.a2mac1.com/. Accessed 15 February 2019.

[57] http://www.optimumg.com/. Accessed 15 February 2019.

[58] A. Ferraris. *Automotive Composite Components Design and Test: A Vibration Reduction Oriented Approach.* PhD Thesis. 2016.

[59] https://www.totalmateria.com/. Accessed 15 February 2019.

[60] R. Kalhor. *Energy Absorption in Metal-FRP Hybrid Square Tubes*. PhD Thesis. 2016.

[61] C. Lauter, J. Niewel, B. Siewers et al. *Crash Worthiness of Hybrid Pillar Structures Consisting of Sheet Metal and Local CFRP Reinforcements*. 15th International Conference on Experimental Mechanics. 2012.

[62] A. Fasana, A. Ferraris, D. Berti Polato et al. *Composite and Damping Materials Characterization with an Application to a Car Door*. Advances in Italian Mechanism Science. 2019.

[63] A. Fasana, A. Ferraris, A. G. Airale et al. *Experimental Characterization of Damped CFRP Materials with an Application to a Lightweight Car Door*. Shock and Vibration. 2017.

[64] A. Fasana, A. Ferraris, A. G. Airale et al. *Oberst and Aging Tests of Damped CFRP Materials: New Fitting Procedure and Experimental Results*. Composites Part B: Engineering. 2018.

[65] W. Liebig, V. Sessner, K. A. Weidenmann et al. *Numerical and Experimental Investigations of the Damping Behaviour of Hybrid CFRP-Elastomer-Metal Laminates.* Composite Structures. 2018.

[66] M. M. Stoll and K. A. Weidenmann. *Materials selection for a fiber-metal-laminate with elastomer interlayers*, 21st International Conference on Composite Materials. 2017.

[67] J. Krollmann, T. Schreyer, M. Veidt et al. *Impact and Post-Impact Properties of Hybrid-Matrix Laminates Based on Carbon Fiber-Reinforced Epoxy and Elastomer Subjected to Low-Velocity Impacts*. Composite Structures. 2019.

[68] M. Stoll, F. Stemmer, S. Ilinzeer et al. *Optimization of Corrosive Properties of Carbon Fiber Reinforced Aluminum Laminates due to Integration of an Elastomer Interlayer*. Key Engineering Materials. 2017.

[69] Us Dept Of Defense. *Composite Materials Handbook-MIL 17: Guidelines for Characterization of Structural Materials*, Volume 1, 1999.

[70] Test Method for Measuring Vibration-Damping Properties of Materials. ASTM International. 2017.

[71] Laboratory Measurement of the Composite Vibration Damping Properties of Materials on a Supporting Steel Bar. SAE International, 2013.
[72] A. D. Nashif, I. David and G. Jones. Vibration Damping. Wiley. 1985.

[73] Environmental testing - Part 2-78: Tests - Test Cab: Damp heat, steady state. IEC webstore, 2012.

[74] Test Method for Lap Shear Adhesion for Fiber Reinforced Plastic (FRP) Bonding. ASTM International. 2014.

[75] Test Method for Apparent Shear Strength of Single-Lap-Joint Adhesively Bonded Metal Specimens by Tension Loading (Metal-to-Metal). ASTM International. 2010.

[76] Test Method for Mode I Interlaminar Fracture Toughness of Unidirectional Fiber-Reinforced Polymer Matrix Composites'. ASTM International. 2013.

[77] A. Monden, M. G. R. Sause and S. Horn. *Surface modified steel/epoxy-based CFRP hybrid laminates under mode I, mode II and mixed-mode load conditions*, ECCM17 - 17th European Conference on Composite Materials. 2016.

[78] Test Method for Determination of the Mode II Interlaminar Fracture Toughness of Unidirectional Fiber-Reinforced Polymer Matrix Composites. ASTM International. 2014.

[79] F. Ausano. *Valutazione Sperimentale Delle Caratteristiche Di Materiali Smorzanti*. 2003.

[80] *Altair OptiStruct User Guide v17*. Altair Engineering. 2017.

[81] Test Method for Tensile Properties of Polymer Matrix Composite Materials. ASTM International. 2017.

[82] Test Method for Compressive Properties of Polymer Matrix Composite Materials with Unsupported Gage Section by Shear Loading. ASTM International. 2016.

[83] Test Methods for Flexural Properties of Unreinforced and Reinforced Plastics and Electrical Insulating Materials. ASTM International, 2017.

[84] Test Methods for Tension Testing of Metallic Materials. ASTM International. 2016.

[85] *Altair Radioss Theory Manual v17*. Altair Engineering. 2017.

[86] Delsart, D., Joly, D., Mahe, M., et al. *Evaluation of finite element modelling methodologies for the design of crashworthy composite commercial aircraft fuselage*, 24th International Congress of the Aeronautical Science. 2004.

[87] European Program "Commercial Design for Crash Survivability-CRASURV". Brite Euram project BRPRCT96-0207, 1996–2000.

[88] M. Carello, A. G. Airale, A. Ferraris et al. Static Design and Finite Element Analysis of Innovative CFRP Transverse Leaf Spring. Applied Composite Materials. 2017.

[89] J.L Batoz, and G. Dhatt. Modeling of Structures by Finite Element. HERMES, 1992.

[90] Jeffrey A Wollschlager. *Introduction to the Design and Analysis of Composite Structures: An Engineers Practical Guide Using OptiStruct*. Mill Creek. 2014.

[91] Z. Hashin and A. Rotem. *A Fatigue Criterion for Fiber Reinforced Materials*. Journal of Composite Materials. 1973.

[92] A. Fasana, *Modal Parameters Estimation in the Z-Domain*. Mechanical Systems and Signal Processing. 2009.

[93] Fasana, A. and S. Marchesiello. *Meccanica Delle Vibrazioni*. Clut. 2006.